ZDR Electron Cooling for RHIC

Table of Contents

References

[III.B.1] This solution was found by J.Kewisch
[III.B.2]D. Janssen, et al., Nucl. Instr. and Meth. A507 (2003) 314.
[III.B.3]D. H. Dowell S. Z. Bethel and K. D. Friddell, NIM A 356, (1995), 167

[III.B.4]R. Calabrese et al. NIM A 340, (1994), 109
[III.B.5]A. Shih et al. J. Appl. Phys. 82, 1860 (1997)
[III.B.6]X.Y.Chang, et al., *Compensation for bunch emittance in a magnetization and space charge dominated beam*, to be published
[III.B.7] *Advanced Energy Systems*, USA.
[III.B.8] Dong Wang et. al., PAC 2003, Portland, May 2003.
[III.B.9] *The MAFIA Collaboration*, MAFIA Version 4.0, CST GmbH, Darmstadt, Germany.
[III.B.10] Paolo Pierini, *Build Cavity Manual*, Milan, Italy.
[III.B.11] J. Sekutowicz, Proceedings of Linear Accelerators Conference, Tsukuba, Japan, 1994.
[III.B.12] *Frequency Structure Simulation (HFSS),* ANSOFT Co., Pittsburgh, PA, USA.
[III.B.13] F. Marhauser et.al., *Numerical Simulations of HOM damped cavity*, PAC 2001.
[III.B.14] Derun Li and Robert Rimmer, *Beam Impedance Calculations and Analysis of HOMs using MAFIA in Time Domain*, PAC 2001, Chicago.
[III.B.15] R. Schuhmann, T. Weiland, PRST-AB, Vol. 3, 122002(2000).
[III.B.16] TDBBU was written by G.A. Krafft at Jefferson Laboratory.
[III.B.17] MATBBU was written by G.A. Krafft at Jefferson Laboratory.
[III.B.18] Y. H. Chin, *ABCI Version 8.1*, CERN, Geneva.
[III.B.19] Chojnacki et. al., Proceedings of the Particle Accelerator Conference, 1997.
[III.B.20] Mike Iarocci, Private Communication.
[III.B.21] J. Sekutowicz, PRST-AB, Vol.2, 062001 (1999).

ZDR for Electron Cooling at RHIC

I. INTRODUCTION

The material presented in this document constitutes a Zero'th order Design Report, or ZDR for the electron cooling of RHIC component of the RHIC II project. The RHIC II project constitutes a luminosity upgrade for RHIC, of which the major element is electron cooling of RHIC and detector upgrades. RHIC II is on the list of "Facilities for the Future of Science" of the DOE Office of Science. The ZDR has been prepared by a large number of persons, mostly in the Collider-Accelerator Department. A list of contributors is included in the document. The ZDR has a number of parts. Following this introduction and an R&D plan, we are introducing the physics and engineering issues of the electron cooler, including electron cooling physics, electron beam dynamics of the cooler and solenoid design. It is followed by a description of the major components of the cooler including superconducting linac cavities designed for Energy Recovery Linac (ERL) operation, a high-current, high-brightness electron beam gun and an ERL-prototype for R&D purposes which is under construction. The WBS, cost and schedule for both the electron cooler and its R&D program, concludes the ZDR.

I.1 The Science of RHIC II

The early measurements at RHIC have revealed a new regime of nuclear matter at extremely high density and temperature—the long-sought medium in which the predictions of QCD can be tested, and new phenomena explored, under conditions where the relevant degrees of freedom over nuclear volumes are those of quarks and gluons, rather than of hadrons. This is the realm of the quark gluon plasma, a state of matter whose existence and properties are now being explored with the RHIC experiments.*

Results to date have shown that detailed exploration of the properties of new matter produced at RHIC can be carried out using experimental probes that carry information directly from the thermal volume of hot matter during its lifetime. Such probes include the spectra of heavy quarks (charm and bottom) that are formed in the earliest stages of the collision, and are so massive that their dynamical properties are not lost to thermalization at the temperatures and densities that prevail in the plasma of light quarks and gluons. Another class of such probes is the measurement and classification of high-momentum jets of particles corresponding to energetically scattered quarks and gluons. Accurate measurements of large samples allow experiments to carry out, in effect, a tomography on the initial dense matter with "beams" of quarks and gluons.

These measurements, and others like them, involve extremely rare phenomena that cannot be fully explored at the present data rates of RHIC. The very small cross sections for these probes require data samples in Au-Au collisions of ~10 nb-1, an order

of magnitude greater the annual yield at the present luminosity. To realize these large data samples, along with the necessary comparison data utilizing lighter ions and varying energies, requires beam collision rates ten times greater than the present RHIC capability. It also requires substantial upgrades to the existing large detectors, to provide enhanced sensitivity to the signatures of these processes and to implement electronic readout, data acquisition, and trigger systems matched to the increased collision rates.

The proposed RHIC II Project consists of major upgrades of the RHIC collider and detectors, to provide this new capability for studying extremely rare processes with high precision in high-energy nucleus-nucleus, proton-nucleus, and proton-proton collisions. Electron cooling of the ion beams provides the key for achieving the luminosity goals.

*For an overview see: "New Discoveries at RHIC", Proceedings of the RIKEN BNL Research Center Workshop, May 14-15, 2004, BNL-72391-2004

I.2 The luminosity of a collider, IBS and electron cooling

The luminosity of a collider is given by following well-known formula

$$L = f_c \cdot \frac{N_1 N_2}{4\pi\sigma^2}$$

where N_1, N_2 are the number of particles in the two colliding bunches, f_c is the collision frequency and σ is the RMS beam size (assuming the two colliding bunches have the same size). The beam size is proportional to the square root of the beam emittance, or, in other terms, the transverse temperature of the particles in the reference frame of the beam. The temperature (emittance) can increase with the time, leading to a reduction of the luminosity. In RHIC, scattering of stored particle beams on each other, a process called Intra-Beam Scattering (IBS), is the main cause of the luminosity reduction.

The strength of the IBS process is proportional to $(Z^2/A)^2$, thus it is particularly detrimental to high-charge (i.e. Z is large), heavy ions such as gold. Since the strength of IBS increases at low energies, it is also a problem for protons at energies that correspond to the low range of eRHIC.

Electron cooling is used to reduce the emittance of an ion beam circulating in a storage ring by transferring the transverse motion (the heat) from a high emittance (hot) ion beam to a low emittance (cold) electron beam. For cooling to occur, the electron beam must have the same velocity as the ion beam and the two beams must merge as they travel through a solenoidal magnetic field for a portion of the storage ring orbit. Since fresh, cool electrons continuously replace the heated electrons while the ion beams continue to circulate, the process leads to a continuous improvement in the quality of the ion beam.

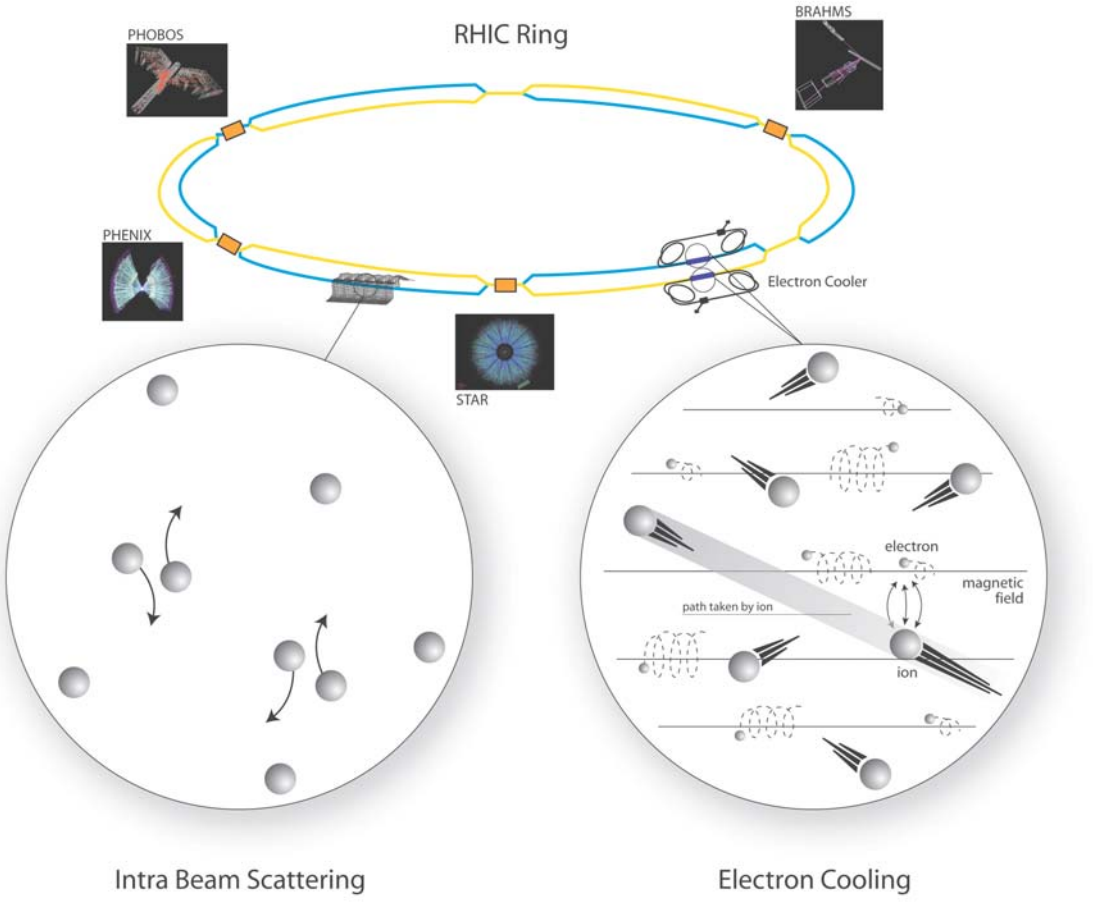

Fig. I.2.1 Electron cooling of RHIC, a pictorial diagram.

Figure I.2.1 shows schematically RHIC's blue and yellow rings, equipped with electron coolers (one each), and depicts the heating and cooling mechanisms.

Intra-Beam Scattering takes place across the whole circumference of each of the rings, while cooling occurs only in the cooling solenoid, where ion and electron beam co-propagate.

IBS is mediated by the focusing fields, which appear as a time-dependent potential in the reference frame of the particles. Under such a potential, the random collisions between ions can lead to an increase in the temperature (random motion in the particle's reference frame) for all three degrees of freedom.

Electron cooling will be applied by two systems (one per ring), tentatively near the 4 o'clock section of RHIC. As seen in the reference frame of the ions (and electrons, which are velocity matched to this frame), the ions have a random distribution of velocities. The electrons have also a random distribution, except that they are confined to move longitudinally by a solenoidal magnetic field, which forces them to move in spirals following the magnetic field lines. An ion interacting with an electron transfers energy to

the electron and thus loses energy. This interaction, repeated with a large number of electrons, appears as friction force acting on the ion, thus leading to a reduction in the temperature of the ions.

I.3 RHIC Parameters

The RHIC lattice allows for simultaneous operation at six different interaction regions, each with a design luminosity of 2 10^{26} cm^{-2} s^{-1} for gold beams. The current machine parameters (as of May 2004) are compared to the RHIC II in Table I.3.1.

Table I.3.1: The luminosity performance of RHIC II in scenarios of Au+Au collisions at 100 GeV/nucleon and polarized proton collisions at 250 GeV per beam.

Gold Collisions (100 GeV/n ×100 GeV/n)	w/o e-cooling	with e-cooling
Emittance (95%) [π·μm]	15 → 40	15 → 10
β-function in IR [m]	1.0	0.5
Number of bunches	112	112
Bunch population [10^9]	1	1 → 0.3
Beam-beam parameter per IR	0.0016	0.004
Peak luminosity [10^{26} cm^2 s^{-1}]	**32**	**90**
Average store luminosity [10^{26} cm^2 s^{-1}]	**8**	**70**
Polarized Proton Collisions (250 GeV × 250 GeV)		
Emittance (95%) [π·μm]	20	12
β-function in IR [m]	1.0	0.5
Number of bunches	112	112
Bunch population [10^{11}]	2	2
Beam-beam parameter per IR	0.007	0.012
Average store luminosity [10^{30} cm^2 s^{-1}]	**150**	**500**

The RHIC spin physics program uses the unique capability of RHIC to accelerate and collide polarized proton beams at a center-of-mass energy of up to 500 GeV and a luminosity of up to 2 10^{32} $cm^{-2}s^{-1}$.

The RHIC II luminosity upgrade is also essential to provide the precision in the electron-ion collider "eRHIC" program, a future upgrade of RHIC. The proton beam intensity can be increased, or the beam emittance can be decreased until the beam-beam limit is reached which corresponds to a *p-p* luminosity approaching 10^{33} $cm^{-2}s^{-1}$. The RHIC electron cooler, to be used at storage for heavy ion operation, could be used at injection energy to achieve this reduction of the proton beam emittance.

I.4 High-Energy Electron Cooling

Electron cooling was developed at the Institute of Nuclear Physics in Novosibirsk, following the lead of G.I. Budker. In the past 35 years of development, electron cooling has been applied successfully to various low energy storage rings found in numerous laboratories around the world.

All electron-cooling systems in operation to date can be classified as low energy systems. These systems use conventional DC high-voltage supplies to bias the electron source with respect to the cooling region, and a continuous longitudinal (solenoidal) magnetic field to confine or focus the electron beam.

The electron beam-cooling scheme proposed for RHIC uses a single pass, energy-recovery superconducting linac to generate the 54 MeV, 100-200 mA electron beam needed to extract the transverse and longitudinal energy spread from the circulating ions. The electron beam is "magnetized" to reduce the cooling time. Generation of the necessary transverse and longitudinal brightness requires the development of a CW laser photocathode RF gun as the injector. The electron accelerator is a superconducting, energy-recovery linac, very similar to an existing, 50 MeV, 5 mA average current CW linac operating for a free electron laser at TJNAF.

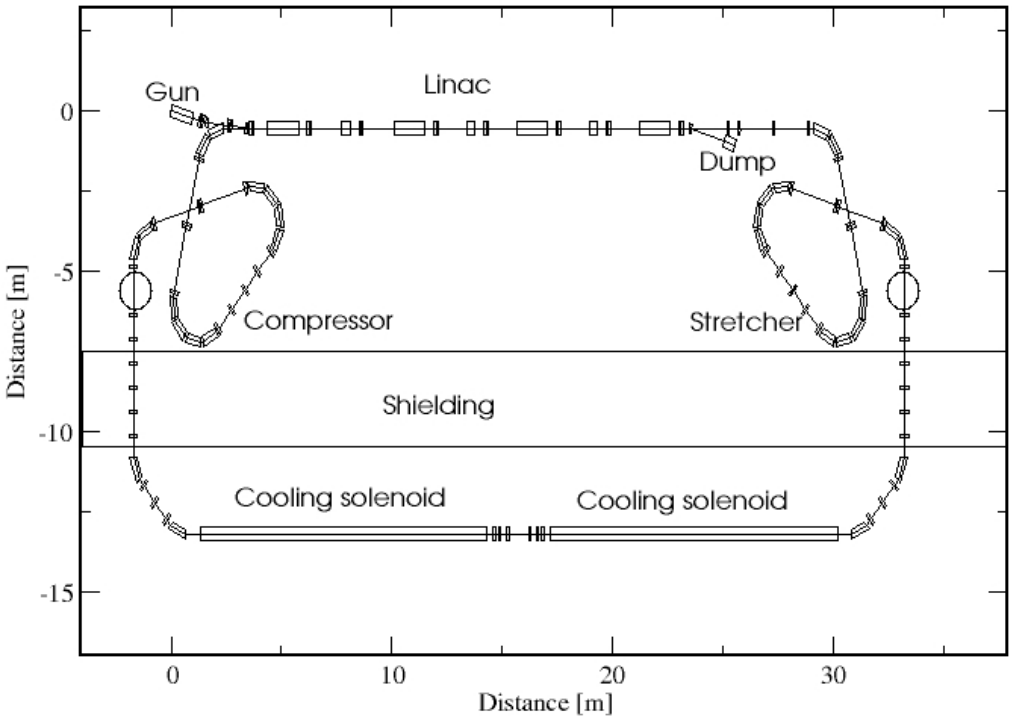

Fig. I.4.1 Layout of the electron accelerator and the cooling solenoid section of RHIC.

Figure I.4.1 shows a schematic layout of one of the electron cooling systems. The electron cooler comprises two major elements: the energy recovery linac (ERL) and the cooling sections. The ERL (see Section III) comprises of the injector, the superconducting RF linac and the ring lattice including the stretcher and compressor. The cooling sections comprises of the matching section where electron merge with the ion beam and solenoid section where the cooling process takes place. Energy transfer between the “cold” electron beam and the “hot” ion beam takes place in a highly uniform solenoidal field to maintain particle alignment. While the electrons are traversing a short (about 30 meter long) section of the ring, they travel along a common path with the ions in a "cooling section" solenoid, the longest available straight section in RHIC.

Before and after entering the ring, the electrons undergo debunching and bunching produced by a combination of spiral optical inserts and cavities. Other components of the system are an electron linac structure, an electron gun and a beam dump. The electron gun’s cathode has to be properly immersed in a solenoidal magnetic field in order to match the size and divergence of the electron beam to the magnetic field strength in the cooling section. The debunching optical insert has to increase the electron bunch length to reduce the electron relative momentum spread to a few parts in 10^4, required for

effective cooling. After deceleration and beam energy recovery the electron beam is dumped at energy of about 3 to 5 MeV.

Electron cooling of the RHIC beams will increase the luminosity of gold-gold collisions in RHIC by an order of magnitude. The luminosity increase will come from two effects: one is a reduction of emittance (a "cooler" ion beam); the other is mitigation of a "heating" mechanism called Intra-beam Scattering (IBS), leading to steady luminosity throughout the life of the beam. The increase is so dramatic that with cooling a gold beam of a billion ions will be consumed in the collision process within a few hours – and that is the ultimate in luminosity.

I.5 R&D requirements for the RHIC electron coolers

Electron cooling for RHIC is an enormous technical challenge. It may be argued that electron cooling has been known for many years and is practiced in many machines around the world. It is also true that the physics of cooling takes place in the reference frame of the ions (and electrons) bunch, which is independent of the energy of the machine. However, there are a number of differences between this electron cooler and any other built so far:

1) The RHIC cooler will be by far the highest energy cooler, requiring electron energy of over 50 MeV as compared to the few hundred KeV of any previously built cooler (the only exception is the recycler cooler of FNAL, which is under construction and will have 4.3 MeV electron energy).
2) The RHIC cooler is the only machine planned for cooling with bunched electron beams.
3) The RHIC II will be the first instance of a directly cooled collider.
4) The RHIC cooler will operate with electrons that are much “hotter” than in previous coolers.
5) The RHIC cooler will use a very long, high-field, ultra-high precision solenoid.

There are various implications stemming from these observations. The first one is rather obvious. The electron beam technology of this cooler will be different than any other, requiring high-energy, high-current and low-emittance (temperature) electron beams. That requires a very bright electron source. The other one becomes obvious when one considers that the cooling solenoid has to provide 5 Tesla field over two 13-meter sections with a precision (angular deviation of the magnetic field) smaller than 8×10^{-6} as measured at any point along the magnet. This is a very challenging magnet. The next point becomes obvious when one considers the electron accelerator, which has to provide a C.W. beam at over 50 MeV and over 0.2 amperes, providing a challenge even to superconducting energy recovery linacs. Finally, all of these considerations put together mean that the present state-of-the-art of electron cooling simulations must be considerably improved.

The Collider-Accelerator Department concluded that R&D should be taken along the following fronts:

1) An electron source based on a 703.75 MHz laser-photocathode RF gun (photo injector) must be developed to demonstrate that the electron beam can be prepared with the required emittance, bunch charge and average current. This research may be broken further down to the following R&D components:

    a. High quantum-efficiency, long-lived photocathode.

    b. High average-power, 9.4 MHz repetition frequency laser.

    c. A high electric field, CW operation RF gun.

The above-mentioned elements must be brought together in an operating gun.

2) Energy recovery linac R&D must be pursued to accelerate (and then decelerate for energy recovery) the electron beam without emittance or energy-spread degradation.

3) A high-precision superconducting solenoid R&D must be carried out.

4) Electron cooling simulation codes, providing better predictions of the performance of electron coolers must be developed.

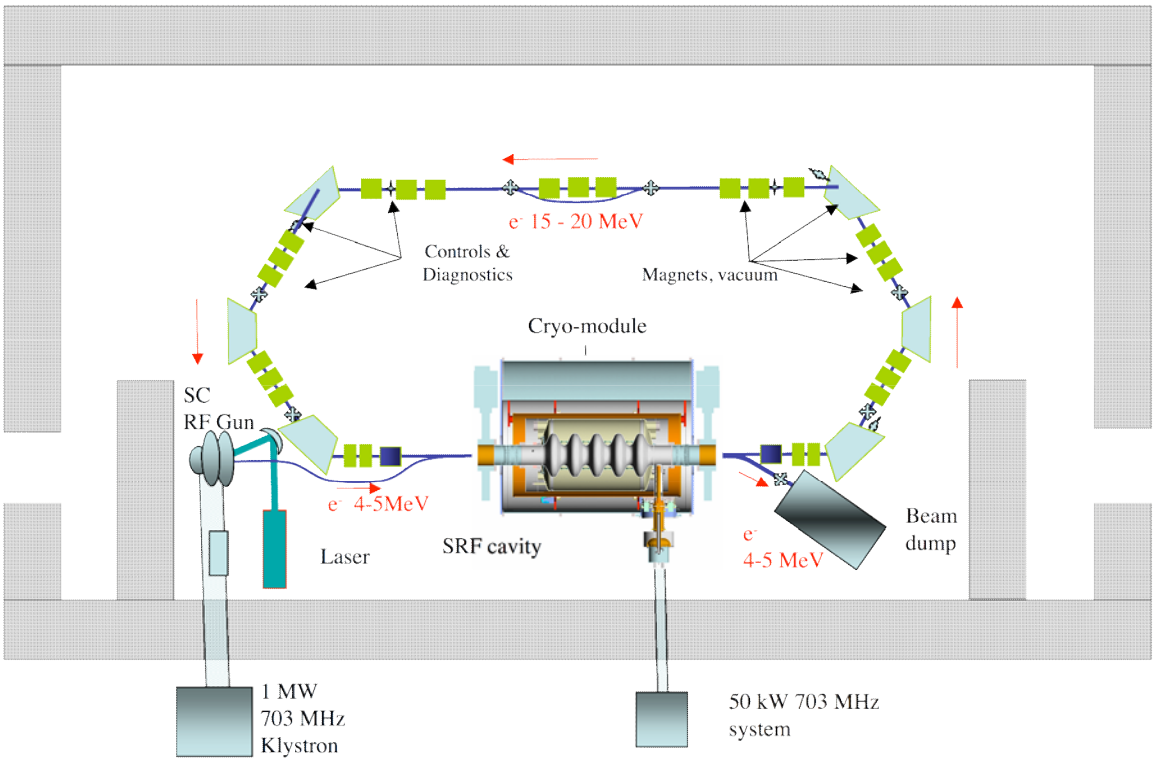

Fig. I.5.1 A schematic layout of the test ERL system inside a shielded vault.

A prototype of the solenoid will be build and tested as the part separately by super-conducting magnet group. The rest of the R&D systems will be assembled and tested as a part of test ERL facility shown in Fig. I.5.1, which will be located in Bldg. 912.

Energy Recovery Linacs based on super-conducting RF cavities is a novel emerging technology which promises to revolutionize many accelerator concepts, including colliders and light sources. The test-ERL we are building at C-AD is very unique being the first ERL based on the Super-conducting RF (SRF) cavity specifically designed to operate very high - 50 fold the present record – average electron beam current. The operation principles of the ERL-prototype are similar to that of the electron cooler ERL: electrons, kicked out from a photo-cathode by a laser beam, are accelerated in a CW electron gun to 3-5 MeV, focused and injected into the main SRF cavity. In SRF cavity electrons gain ~15 MeV of energy and pass through the ring. Finally, electron beam re-enters the cavity in decelerating phase. Decelerating electrons give energy back to the SRF cavity and reach the dump with residual energy 4-5 MeV.

Goals of this test facility are three-fold:

- Demonstration of stable intense CW electron beam with parameters typical for the RHIC e-Cooling project and, potentially, eRHIC;
- Test of novel elements of ERL such as high current CW photo-gun, SRF cavity with HOM dumpers, beam diagnostics, and feedback systems;
- Test stability criteria and it dependence of the ERL lattice (settings of it magnets) used for high current CW ERL.

A detailed R&D plan is presented in this design report. The Collider-Accelerator Department is taking aggressive action to execute this research program. This work is done in close collaboration with other national laboratories such as Jefferson Laboratory, industries such as Advanced Energy Systems in Medford NY and Tech-X in Boulder, CO., and international institution such as the Budker Institute of Nuclear Research in Novosibirsk, Russia, the Joint Institute of Nuclear Research in Dubna, Russia and the Gesellschaft für Schwerionenforschung in Darmstadt, Germany.

II. DESCRIPTION OF THE ELECTRON COOLING AT RHIC II

Electron cooling of the RHIC ion beams either contra-acts the growth of beam emittance caused by IBS or reduces the emittance below its original value (see details in Section III.A), i.e. increases the brightness of the RHIC beams. The brighter ion beams in the RHIC II generate significantly higher luminosity, i.e. the measure of the RHIC efficiency to generated desirable collisions in its four detectors. Electron cooling will increase this efficiency by an order of magnitude. It means that RHIC detectors after anticipated up-grades (which are needed to catch up with the RHIC II productivity) will detect in one year the data worth ten-years of work with the designed luminosity (productivity).

II.1 LAYOUT OF THE RHIC WITH THE ELECTRON COOLER

Present plan for the electron cooling of RHIC beam calls for two electron cooling systems, i.e. both yellow and blue ring will be equipped with individual electron coolers, as shown in Fig. II.1.1. Tentatively the electron coolers will be located near the 4 o'clock IR of RHIC.

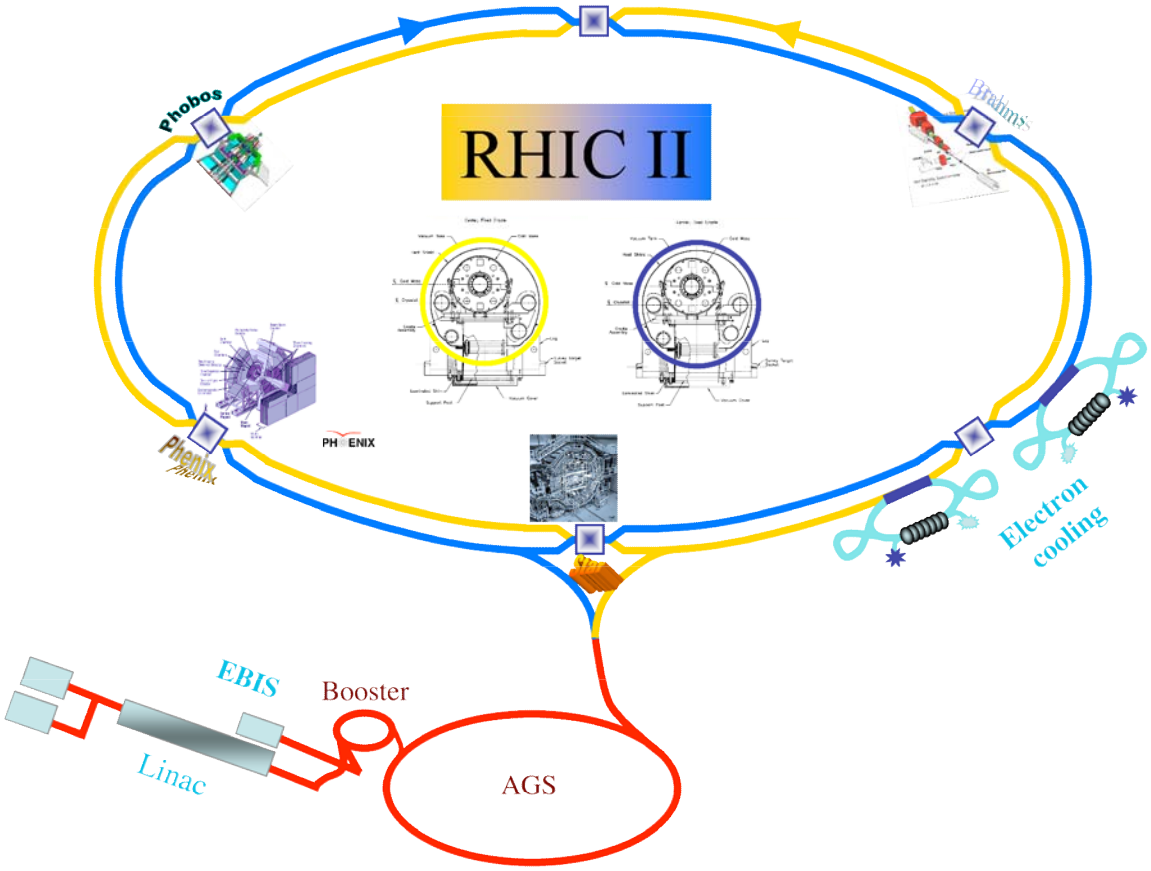

Figure II.1.1. Schematic of RHIC II collider with two electron coolers located at 4 o'clock.

The RHIC II luminosity will reach a practical limit when 50% or more of stored ions would "burned-off" in the collisions occurring in the RHIC detectors. The burn-off rate of the ions during a typical duration of a store (i.e. ~4 hours) is a measure of the RHIC efficiency to generated desirable collisions in its four detectors. At RHIC II, the Star and Phenix detectors will see average luminosity of 7×10^{27} cm^{-2} sec^{-1} during typical four-hour long store when 60% of stored ions will be "burn-off" in the collisions[1].

Furthermore, electron cooling will play important role in reaching very high luminosity in the future eRHIC facility [II.1], where ions and protons will collide with polarized electron beam. The role of electron cooling will be especially critical for the linac-ring eRHIC shown in Fig. II.1.2, which promises 10 times higher luminosity compared with the ring-ring option. eRHIC facility plans to operate with 3 times higher number of ion and proton bunches, compared with RHIC II. It also means that electron coolers have to operate with 3-fold higher beam current when operate for eRHIC (see section II.4).

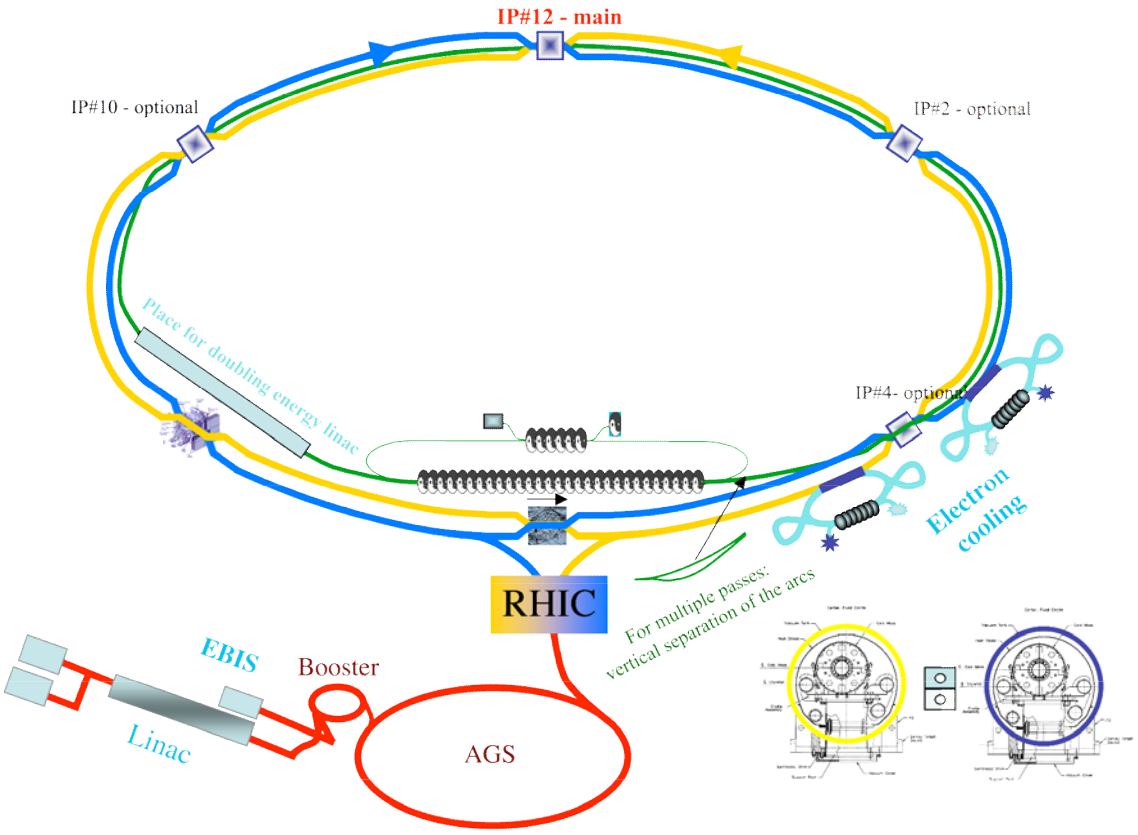

Figure II.1.2. Possible layout of eRHIC II collider with multiple IRs: Two electron coolers play critical role in the 10-fold luminosity enhancement compared with the ring-ring option of eRHIC.

[1] Assuming that Brahms and Phobos operate with 50% of this luminosity, and the RHIC beam parameters listed in Table I.2.1

Electron cooling at RHIC will serve two main purposes:

- it will cool ion beams directly at the energy when they do collide either with another ions, like in the Star or Phenix
- it will pre-cool polarized proton beams for proton-proton and proton-electron collision

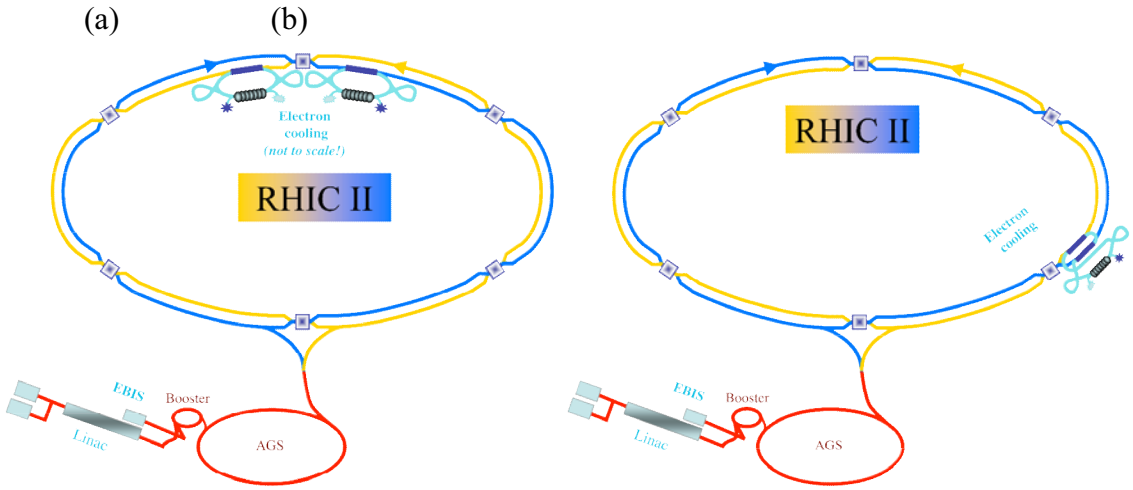

Figure II.1.3. Possible location of the e-coolers at 12 o'clock (a) and a possible layout of a single electron cooler used for cooling two RHIC rings (b).

The location of the electron coolers is rather flexible – they can be located at or around any IR, which has 30 meters of free straight section for installation of the cooler's solenoid. An example of the e-coolers located at 12 o'clock is shown in Fig. II.1.3a.

Furthermore, there is a possibility of using a single electron cooler (see Fig.II.1.3b) for cooling ion beams in both blue and yellow rings. The modifications to the cooler for providing this low cost option are rather modest: after interacting with ions beam in 30m long solenoidal section, the electron beam does not return back to the ERL, but instead is bent by 180^o achromatic arc into the solenoid installed onto the yellow ring. The length of the connecting arc should be chosen to synchronize the electron with the ion bunches:

$$L_{arc} + 2 \cdot L_1 = n \cdot \frac{C_{RHIC}}{N_b}$$

where L_1 is the distance from the end of the arc to the nearest collision point in IR, L_{arc} is the arc length, C_{RHIC} is the RHIC circumference, $n = 1,2,3, \ldots$ is an integer and N_b is total number of buckets in the RHIC ($N_b = 120$ for RHIC II operation, 8 buckets are empty in the abort gap).

RHIC needs some modifications to take full advantage of the electron cooling. One of them is that the cooling sections of RHIC rings should have a smooth horizontal and vertical β-functions with values ~ 60-100 meters. Second is possible increase of the starting luminosity by reducing so-called beta-star in the IR to $\beta^* = 0.5$ *m*. (see section III.c).

The electron cooler is heavily based on modern super-conducting technology: it has superconducting RF cavities and linacs as well as superconducting high precision solenoid. In spite of similarity with RHIC superconducting systems, the electron cooler needs independent cryo-system. There are two main reasons for this solution:

- super-conducting RF system needs a super-fluid liquid helium at temperatures of $2K^{o}$, i.e. well below $4K^{o}$ used for RHIC magnets;
- it is financially sound to use shut-down time of the RHIC facility for tuning of relatively inexpensive electron cooling system, instead of using very valuable and expensive time when RHIC is cold.

II.2 LAYOUT OF THE ENERGY RECOVERY LINAC

One the possible layouts of ERL for the e-cooler is shown in Fig. II.2.1.

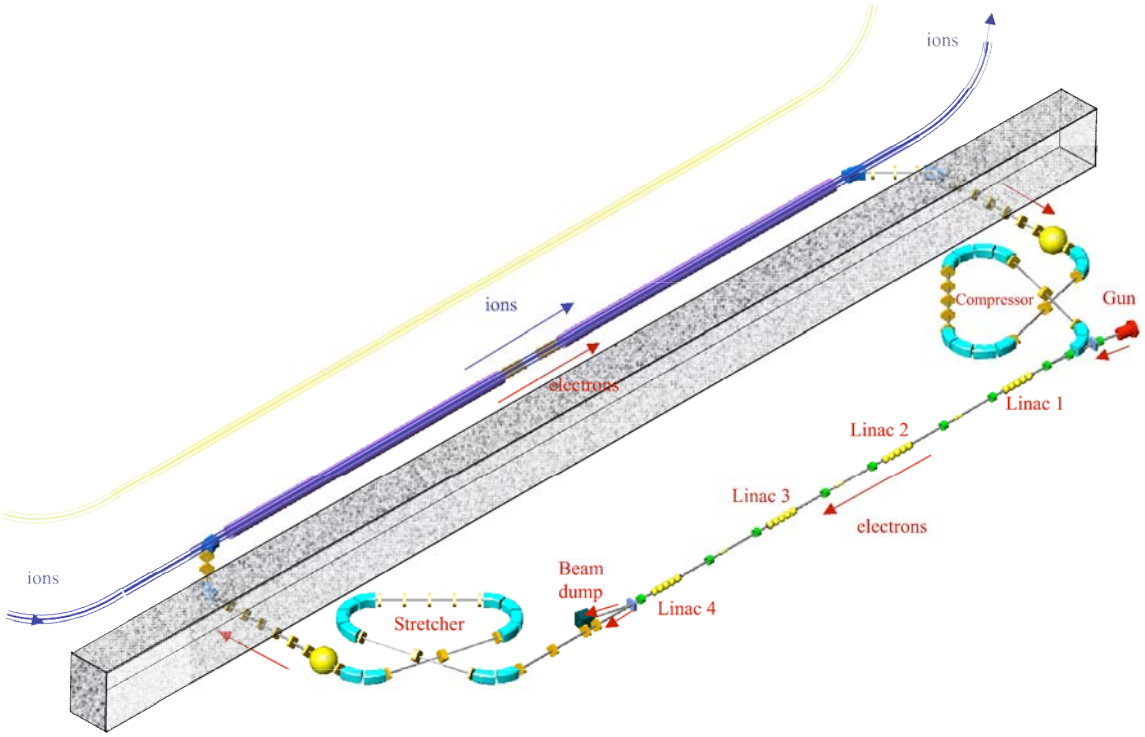

Figure II.2.1. A possible layout of ERL for e-Cooler at RHIC II: the main part of the ERL is located in a dedicated building outside the RHIC shielding wall.

Low energy (~5 Mev) electrons are generated in superconducting RF photo-electron gun, which further accelerated by four superconducting RF linacs to the designed energy of 54 MeV. The main RF frequency systems of the ERL operate at 703.75 MHz , which is 75^{th} harmonic of the RHIC II bunch repetition frequency (9.383 MHz) and on 25^{th} harmonic of that for eRHIC. Energy recovery linac also has a number of auxiliary RF cavities operating at 3^{rd} harmonic and on sub-harmonics of 703.75 MHz.

The 3rd harmonic system is used for linearising the acceleration process in the ERL, while sub-harmonic cavities are used in the compression and decompression process.

Electron bunches generated is the gun and accelerated in the linacs have duration ~ 2 cm, which is much shorter compared with that of the ion bunches in the RHIC with duration ~ 30 cm. The ERL's stretcher is used to match the length of the electron bunch with that of the ion bunch: the linacs of the ERL generate a linear energy chirp ~1%, which cases the electron beam to expand in the stretcher arc. The remaining energy chirp is removed by a low energy cavity before the beam going into the RHIC tunnel.

Electron beam penetrates through the RHIC shielding only to merge with the ion beam in the solenoid cooling section. After cooling the ion bam, electron beam separates from it and leaves the RHIC tunnel. The next process with electron beam is its compression, which is the process exactly opposite to the stretching.

The used electron bunch merges the low energy beam in the linacs section via set of bending magnets. In contrast with a fresh electron bunch, which is accelerated in the linacs, the used bunch comes with 180^{o} phase shift and hence is de-accelerated from 54 to about 5 MeV by the same linacs. Finally, the used beam is separated by a dipole magnet from the fresh accelerated beam and finishes its trip in the beam dump.

Section III.B of this ZDR give a very detailed description of the e-cooling ERL, its systems, lattice and the beam dynamics. It also contains the description of the ERL prototype, which is under construction in Bldg. 912. This prototype facility, shown in Fig. II.2.2 will serve as a test-bed for the most of new technologies incorporated into the RHIC II electron coolers.

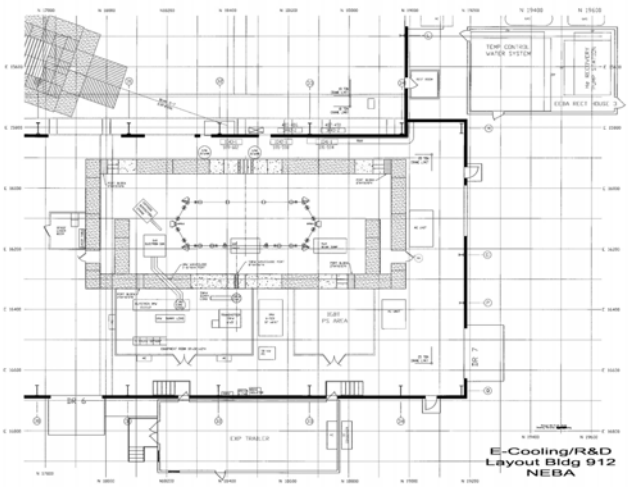

Fig. II.2.2 Layout of the R&D ERL facility: the facility will include the full current photo-electron gun, 15 MeV super-conducting 5-cell linac, 20 MeV re-circulating loop, full set of the beam diagnostics and, naturally, a 1 MW electron beam dump.

The following sections give the main parameters of the electron cooler and its prototype ERL as well technically driven schedule for the e-cooling project.

II.3 TECHNICALLY DRIVEN SCHEDULE

The technically driven schedule for the RHIC II project is as shown in Figure II.3.1.

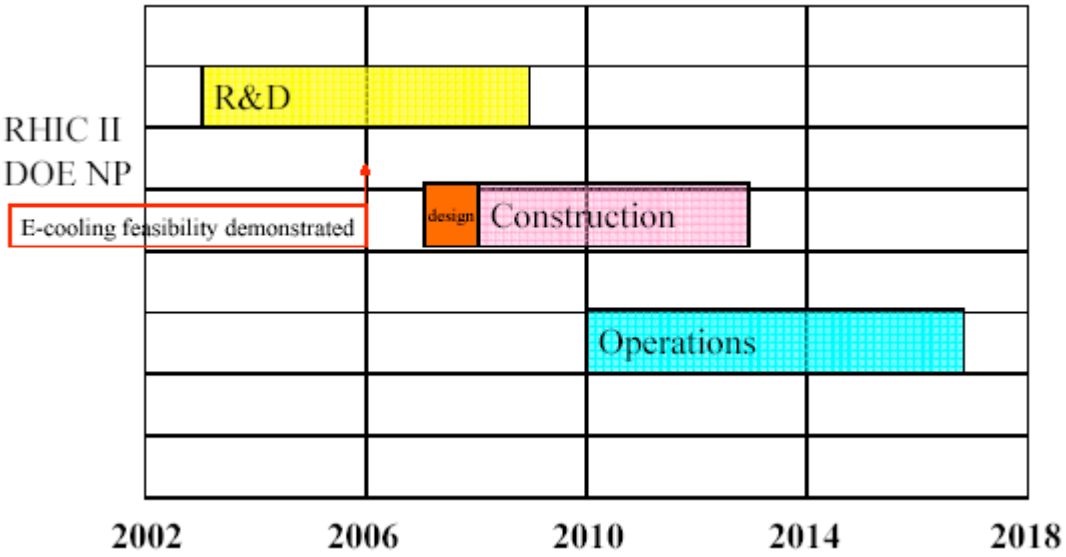

Fig. II.3.1 Technically driven schedule for RHIC II.

II.4 LEVEL-1 PARAMETERS

Main parameters of the electron cooling system and the ERL-prototype are listed in the following tables. Detailed parameters and the parameters of subsystems can be found in corresponding sections of the ZDR.

Table II.4.1. Parameters of the electron cooler

	RHIC II	eRHIC
Injection energy, MeV	**3-5**	
Maximum beam energy, MeV	**54.7**	
Average beam current, mA	***~ 200***	***~500***
Bunch rep-rate, MHz	***9.4***	***28***
Charge per bunch, nC	**up to 20**	
Normalized emittance, mm*mrad	**~50**	
Transverse electron temperature, eV (in beam's reference system)	**~1000**	
Electron bunch length in the cooling section**, cm**	**3-30**	
Electron beam diameter in the cooling section**, mm**	**1-2**	
Magnetic field solenoid, T	**5**	
Efficiency of current recovery	**>99.95%**	

Table II.4.2. Parameters of the prototype ERL in Bldg. 912

	High charge mode	**Low charge mode**
Injection energy, MeV	**3-5**	**3-5**
Maximum beam energy, MeV	**15-20**	**15-20**
Average beam current, mA	**100-200**	**10-200**
Bunch rep-rate, MHz	**9.4**	**9.4-*700***
Charge per bunch, nC	**10 or more**	**~0.3 -1**
Normalized emittance, mm*mrad	**~ 30**	**~1-3**
Efficiency of current recovery	**>99.95%**	**>99.95%**

References

[II.1] eRHIC ZDR, Appendix A, http://www.agsrhichome.bnl.gov/eRHIC/

Contents for ZDR's Section III.A "Theory and simulation of cooling dynamics":

III.A.1 Elements of Cooling Theory

The traditional electron cooling system [Budker1] applied up to now in any existing cooler is based on electron beam generated with electrostatic electron gun in DC operation mode, immersed in a longitudinal magnetic field. The magnetic field is used for electron beam transport through the cooling section from the gun to collector. The field value is determined by condition of electron "magnetization" – radius of the electron Larmor rotation in the transverse plane has to be much less than the beam radius.

Usually an action of electron cooling on the ion dynamics inside a storage ring is described using a few standard simplifications:

1. Angular deviation of the longitudinal magnetic field line is substantially less than the ion beam angular spread.
2. Ion transverse displacement inside the cooling section is substantially less than electron beam radius.
3. Ion beam temperature is substantially larger than electron one and ion diffusion in the electron beam can be neglected.
4. Electron beam has a round shape cross-section and uniform density distribution in the radial direction.

Under these assumptions one can obtain analytic formulas for characteristic cooling times of transverse beam emittances and momentum spread.

For electron cooling of gold ions in RHIC electron energy has to be about 55 MeV and electrostatic acceleration of the electron beam is practically impossible. An RF acceleration of bunched electron beam results in the transverse velocity spread in electron beam orders of magnitude larger than in conventional coolers. Such a large temperature of electron beam needs to be compensated by a strong magnetic field in cooling solenoid thus requiring strong magnetized cooling.

Elementary description of electron cooling could be found in any review article on this subject, for example see Reference [Meshkov1] and references therein. In sections III.A.1.1-III.A.1.4, basic description is taken from report of BetaCool code [BetaCool].

III.A.1.1. Friction force calculation

The friction force acting on an ion is determined by Coulomb collisions with electrons (Fig. III.A.1.1). The electron at velocity $v_{e\_}$ in the PRF colliding with the ion having velocity v_i at impact parameter ρ obtains the transverse momentum $\Delta p_\perp$:

$$p_\perp \equiv \Delta p_\perp = \frac{2Ze^2}{(\vec{v}_i - \vec{v}_e)\rho}, \qquad \text{(III.A.1.1)}$$

where Ze and e are the charges of the ion and electron, respectively. Due to conservation of the total particle momentum $p_\mu = const$ the appearance of the transverse momentum $p_\perp$ of electron leads to the following change of its longitudinal momentum:

$$\Delta p_{II} = p_\mu - \sqrt{p_\mu{}^2 - \Delta p_\perp{}^2} \approx \frac{(\Delta p_\perp)^2}{2p_\mu}. \qquad \text{(III.A.1.2)}$$

The electron energy changes by:

$$\Delta E_e = \frac{\Delta p_\perp{}^2}{2m}, \qquad \text{(III.A.1.3)}$$

which is equal to the change of the ion energy ΔE_i.

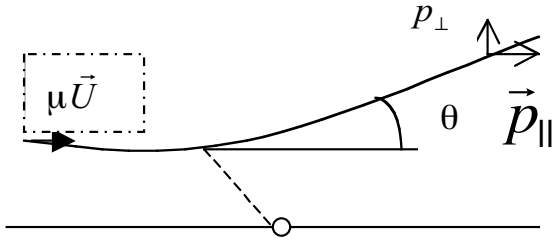

Fig. III.A.1.1 Two-bodies problem

Integration over impact parameter ρ gives us the ion energy loss per unit of the length:

$$\frac{dE_i}{ds} = 2\pi \int_{\rho_{\min}}^{\rho_{\max}} n_e \Delta E_i \rho d\rho, \qquad \text{(III.A.1.4)}$$

Here, n_e is the electron density, ρ_{max} and ρ_{min} – minimum and maximum impact parameters of the collision. Thus the friction force is equal to:

$$F = -\frac{dE_i}{ds} = -\frac{4\pi Z^2 n_e e^4}{m v_i^{\,2}} \ln \frac{\rho_{\max}}{\rho_{\min}}. \qquad \text{(III.A.1.5)}$$

For more accurate estimates one needs to take into account that electrons have finite temperatures and velocity distributions. To obtain corresponding friction force one needs to average over electron velocity distribution function $f(v_e)$ [Meshkov1]:

$$\vec{F} = -\frac{4\pi n_e e^4 Z^2}{m} \int L_c(v_i) \frac{\vec{v}_i - \vec{v}_e}{\left|\vec{v}_i - \vec{v}_e\right|^3} f(v_e) d^3 v_e, \qquad \text{(III.A.1.6)}$$

where $v_{e\_}$, v_i are the electron and ion velocity, L_c – Coulomb logarithm:

$$L_c = \ln \frac{\rho_{\max}}{\rho_{\min}}. \qquad \text{(III.A.1.7)}$$

Since variation of Coulomb logarithm is small one can put it in front of the integral, which gives

$$\vec{F} = -\frac{4\pi n_e e^4 Z^2 L_c}{m} \int \frac{\vec{v}_i - \vec{v}_e}{\left|\vec{v}_i - \vec{v}_e\right|^3} f(v_e) d^3 v_e. \qquad \text{(III.A.1.8)}$$

III.A.1.1.1. Budker's formula

In the case of a uniform Maxwellian distribution of electrons, this is described by the function:

$$f(v) d^3 v = \left(\frac{m}{2\pi T_e}\right)^{3/2} \exp\left(-\mu v_e^2 / 2T\right) v_e^2 dv_e d\Omega, \qquad \text{(III.A.1.9)}$$

the friction force $\vec{F}_M$ is equal to:

$$\vec{F}_M(\vec{v}_i) = -\frac{\vec{v}_i}{v_i^{\,3}} \frac{4\pi n_e e^4 Z^2 L}{m} \varphi\left(\frac{v_i}{\Delta_e}\right),$$
$$\varphi(x) = \sqrt{\frac{2}{\pi}} \int_0^x e^{-y^2/2} dy - \sqrt{\frac{2}{\pi}} e^{-x^2/2}, \qquad \text{(III.A.1.10)}$$

Δ_e - r.m.s. electron velocity in the PRF, $T_e = m\Delta_e{}^2$. The friction force maximum corresponds to ion velocity of about $v_i = 1.36\Delta_e$ (Fig. III.A.1.2).

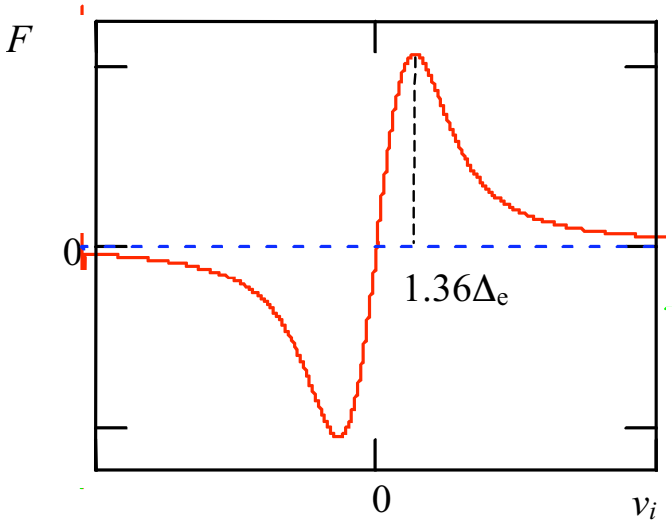

Fig. III.A.1.2. Friction force as a function of ion velocity for uniform Maxwellian distribution function of electrons.

In the LRF the friction force can be expressed by the *Budker's* formula [Meshkov1]:

$$F_{M,\alpha} = -2KL\varphi\left(\frac{\theta}{\theta_e}\right)\frac{\theta_\alpha^*}{\theta^3},\ \alpha = x,\ z,\ s, \qquad \text{(III.A.1.11)}$$

where θ is the full particle velocity inside the electron beam (in units of $\gamma\beta c$, PRF):

$$\theta = \sqrt{(\theta_x^*)^2 + (\theta_z^*)^2 + (\theta_s^*/\gamma)^2}, \qquad \text{(III.A.1.12)}$$

$$\theta_e = \frac{1}{\beta\gamma}\sqrt{\frac{T_e}{m_e c^2}}, \qquad \text{(III.A.1.13)}$$

where the friction force constant K is defined as

$$K = \frac{2\pi r_p r_e}{\beta^4\gamma^5}\frac{Z^2}{A}n_e, \qquad \text{(III.A.1.14)}$$

Here, n_e is electron beam density in LRF, r_p and r_e are the classical proton and electron radii, respectively. For DC electron beam with uniform density distribution it can be expressed by electron beam radius a and current I:

$$K = \frac{2r_p}{\beta^5\gamma^5}\frac{Z^2}{A}\frac{1}{a^2}\frac{eI}{m_e c^3}. \qquad \text{(III.A.1.15)}$$

The Coulomb logarithm L is calculated with the following minimum and maximum impact parameters. The maximum impact parameter

$$R = \min\left\{\sqrt{(\theta_x^2 + \theta_z^2 + \gamma^{-2}\theta_s^2)\frac{m_e c^2 \beta^2 \gamma^2}{4\pi n_e e^2}},\quad \sqrt[3]{\frac{3Z}{n_e}}, a\right\} \qquad \text{(III.A.1.16)}$$

$$\rho_{max} = <|V|>\cdot\tau$$

corresponds to the shielding sphere, where n_e is electron density in PRF. The electron density n_e in PRF and electron current density J in LRF are related as follows:

$$n_e = \frac{J}{e\gamma\beta c}, \qquad \text{(III.A.1.17)}$$

The following value is usually used as the minimal impact parameter:

$$\rho_{\min} = \frac{Ze^2}{m_e}\frac{1}{\beta^2\gamma^2(\theta + \theta_\perp)^2}. \qquad \text{(III.A.1.18)}$$

It corresponds to electron scattering by the angle of $\pi/2$.

III.A.1.1.2. Non-magnetized electron beam with flattened velocity distribution

In the case of electrostatic acceleration of the magnetized electron beam the temperatures of transverse and longitudinal degrees of freedom are different:

$$T_\perp \approx T_{cathode} + T_{optics}, \qquad T_\parallel = \frac{T_{cathode,eff}^2}{\beta^2\gamma^2 mc^2} + e^2 n_e^{1/3}, \qquad \text{(III.A.1.19)}$$

where $T_{cathode}$ is the cathode temperature, T_{optics} describes an additional transverse velocity spread due to distortions during electron beam transportation to the cooling section. The effective cathode temperature used for longitudinal temperature calculation includes a term determined by a ripple amplitude of the accelerating voltage.

In the case of RF electron beam acceleration the transverse and longitudinal temperatures can be calculated from electron beam parameters as follows:

$$T_\perp = mc^2\beta^2\gamma^2\theta^2,$$

$$T_{\|} = mc^2\beta^2\left(\frac{\Delta p}{p}\right)^2, \qquad \text{(III.A.1.20)}$$

where θ is r.m.s. angular spread and $\Delta p/p$ – r.m.s. momentum spread of electrons in the cooling section. The angular spread can be a function of radial co-ordinates due to the drift motion of electrons.

In general case the velocity distribution function can be approximated by Maxwellian distribution with different temperatures of longitudinal and transverse degrees of freedom:

$$f(v)d^3v = \left(\frac{m}{2\pi}\right)^{3/2}\frac{1}{T_\perp\sqrt{T_{II}}}e^{-mv^2{}_\perp/2T_\perp - mv_{II}^2/2T_{II}}\,2\pi v_\perp dv_\perp dv_{II}. \qquad \text{(III.A.1.21)}$$

In the case, when transverse velocity spread of electrons is substantially larger than the longitudinal velocity spread the friction force can be approximated in three ranges of the ion velocity.

I. High velocity $v_i >> \Delta_\perp$:
Here longitudinal and transverse components of the friction force are equal:

$$\vec{F} = -\frac{4\pi Z^2 e^4 n_e L_c}{m}\frac{\vec{v}_i}{v^3}, \qquad \text{(III.A.1.22)}$$

and the friction force shape coincides with the simplest Budker's formula.

II. Low velocity $\Delta_\| << v_i << \Delta_\perp$:
Here the transverse components of the friction force are given by the following expression:

$$\vec{F}_{x,z} = -\frac{4\pi Z^2 e^4 n_e L_c}{m}\cdot\frac{\vec{v}_{i,x,z}}{\Delta_\perp^3}, \qquad \text{(III.A.1.23)}$$

and longitudinal:

$$\vec{F}_s = -\frac{4\pi Z^2 e^4 n_e L_c}{m}\frac{\vec{v}_s}{v_s\Delta_\perp^2}. \qquad \text{(III.A.1.24)}$$

III. Super low velocity $v_i << \Delta_\|$:
Here the transverse component of the friction force is equal to zero, and the longitudinal component is given by:

$$\vec{F}_s = -\frac{4\pi Z^2 e^4 n_e L_c}{m} \frac{\vec{v}_s}{\Delta_{\|} \Delta_{\perp}^2}. \qquad \text{(III.A.1.25)}$$

In the LRF the friction force components are calculated in accordance with:

$$F_{x,z}(\vec{\theta}^*) = K \begin{cases} 2L \dfrac{\theta^*_{x,z}}{\theta^3}, & \{I\} \\ 2L \dfrac{\theta^*_{x,z}}{\theta_{\perp}^3}, & \{II\} \\ 0, & \{III\} \end{cases} \qquad \text{(III.A.1.26)}$$

$$F_s(\vec{\theta}^*) = K \begin{cases} 2L \dfrac{\theta^*_s}{\theta^3}, & \{I\} \\ 2 \operatorname{sgn} \theta^*_s L \dfrac{\gamma}{\theta_{\perp}^2}, & \{II\} \\ 2L \dfrac{\theta^*_s}{\theta_{\perp}^2 \theta_{II} / \gamma}, & \{III\} \end{cases} \qquad \text{(III.A.1.27)}$$

III.A.1.1.3. Magnetized electron beam. Derbenev-Skrinsky-Meshkov formulae

In the magnetized electron beam, when maximum impact parameter is larger than radius of electron Larmor rotation, the magnetized collisions between ion and electron take place. In this case the electron is attracted by the ion, which pulls it along the magnetic field line forth or back, depending on ion position [Derbenev1]. In various ranges of the ion velocity and impact parameter three type of collisions are possible: fast (small impact parameters were the presence of magnetic field is not essential), adiabatic (intermediate impact parameters where multiple repeated passing of electron by the ion is essential) and magnetized (large impact parameters). Summarizing all the possibilities one can write down analytical formulae for friction force. In LRF it can be presented in the following form (for details, see references [Meshkov1-2]):

$$F_{x,z}(\vec{\theta}^*) = K \begin{cases} (2L_F + k_{x,z} L_M) \dfrac{\theta^*_{x,z}}{\theta^3}, & \{I\} \\ 2(L_F + N_{col} L_A) \dfrac{\theta^*_{x,z}}{\theta_{\perp}^3} + k_{x,z} L_M \dfrac{\theta^*_{x,z}}{\theta^3}, & \{II\} \\ 2(L_F + N_{col} L_A) \dfrac{\theta^*_{x,z}}{\theta_{\perp}^3} + L_M \dfrac{\theta^*_{x,z}}{(\theta_{II} / \gamma)^3}, & \{III\} \end{cases} \qquad \text{(III.A.1.28)}$$

$$F_s(\vec{\theta}^*) = K\begin{cases} (2L_F + k_s L_M + 2)\dfrac{\theta_s^*}{\theta^3}, & \{I\} \\ 2\,\mathrm{sgn}\,\theta_s^* \cdot (L_F + N_{col}L_A)\dfrac{\gamma}{\theta_\perp^2} + (k_s L_M + 2)\dfrac{\theta_s^*}{\theta^3}, & \{II_a\} \\ 2(L_F + N_{col}L_A)\dfrac{\theta_s^*}{\theta_\perp^2\theta_{II}/\gamma} + L_M\dfrac{\theta_s^*}{(\theta_{II}/\gamma)^3}, & \{II_b + III\} \end{cases} \qquad \text{(III.A.1.29)}$$

The Coulomb logarithms are defined by the formulae:

$$L_M = \ln\frac{R}{\langle\rho_\perp\rangle},\ L_A = \ln\frac{2\langle\rho_\perp\rangle}{\rho_F},\ L_F = \ln\frac{\rho_F}{\rho_{\min}}. \qquad \text{(III.A.1.30)}$$

Note that if argument of a logarithm is less than 1, then the logarithm value has to be set to zero. It means that the corresponding type of collisions is absent at given parameters. The Larmor radius of electron rotation is:

$$\langle\rho_\perp\rangle = \frac{\beta\gamma\theta_\perp mc^2}{eB}, \qquad \text{(III.A.1.31)}$$

the intermediate impact parameter

$$\rho_F = \langle\rho_\perp\rangle\frac{|\theta + \theta_{II}/\gamma|}{\theta_\perp}. \qquad \text{(III.A.1.32)}$$

The number of multiple collisions in the super low velocity range:

$$N_{col} = 1 + \left[\frac{\theta_e}{\pi|\theta_e + (\theta_{II}/\gamma)|}\right]. \qquad \text{(III.A.1.33)}$$

The electron longitudinal velocity spread is calculated from the temperature of the longitudinal degree of freedom in accordance with:

$$\theta_{II} = \frac{1}{\beta}\sqrt{\frac{T_{II}}{m_e c^2}}. \qquad \text{(III.A.1.34)}$$

III.A.1.1.4. Magnetized electron beam. Parkhomchuk's empiric formula

In Reference [Parkhomchuk1], a semi-empirical formula was proposed for calculation of the friction force with magnetized electron beam. In LRF and notations similar to the rest of Section III.A.1.1 (which are notations from the BetaCool Report [BetaCool]), it can be expressed as:

$$\vec{F}\left(\vec{\theta}\right) = \frac{2K}{\pi} L_P \frac{\vec{\theta}}{(\theta^2 + V_{effe}^2)^{3/2}}, \qquad \text{(III.A.1.35)}$$

$$L_P = \ln\left(\frac{R_{\max} + \rho_{\min} + \langle \rho_\perp \rangle}{\rho_{\min} + \langle \rho_\perp \rangle}\right), \qquad \text{(III.A.1.36)}$$

where V_{eff} is effective electron velocity spread.

III.A.1.2 Cooling time estimates

An order of magnitude estimate of cooling time can be obtained using expressions for the cooling force. For example, using the non-magnetized expression for the force, we can write cooling time for transverse beam emittance:

$$\frac{1}{\tau} = \frac{F}{mv} = \frac{4\pi Z^2 r_p r_e n_e c \eta}{A\gamma^2} \frac{\Lambda_c}{v^3} = \frac{4\pi Z^2 r_p r_e n_e c \eta \Lambda}{A\gamma^2} \left[\frac{\beta_i}{\gamma \varepsilon_i}\right]^{3/2} \qquad \text{(III.A.1.37)}$$

here A and Z are the ion atomic and charge numbers, γ and c are relativistic factor and the speed of light, β_i is the beta-function in the cooling section, η is the length of the cooling region divided by the ring circumference, Λ_c is the Coulomb logarithm, r_e and r_p are the classical electron and proton radii, n_e is electron beam density in the laboratory frame and ε_i is the normalized ion beam emittance.

The expression in Eq. (III.A.1.37) for cooling time is very approximate (it does not take into account electron transverse temperature, betatron and synchrotron ion motion, etc.) but it can give an order-of-magnitude estimate for the cooling time. Note that one obtains similar formula for magnetized cooling as well, if the Parkhomchuck's formula is used for the cooling force. In this case longitudinal cooling time will be shorter than transverse only because longitudinal spread of ion velocities is initially smaller than transverse for ion energy of 100 GeV at RHIC. If instead one uses analytic expression for the cooling force, derived in an approximation of infinite magnetic field (D-S-M formula), the resulting longitudinal cooling time is faster than the transverse.

For typical parameters of RHIC the cooling time of Au ions at 100 GeV is of the order of 1000 sec, which is much longer than the typical cooling time of about 0.1 sec in standard low-energy coolers. As a result, an order of magnitude accuary in cooling time prediction at RHIC becomes unacceptable. In addition, such a long cooling time becomes

comparable to other characteristic times in RHIC like beam diffusion due to the intrabeam scattering within the ion bunch. An accurate estimate of the cooling times thus requires a detailed calculation of the cooling process which takes place simultaneously with various diffusive mechanisms in RHIC. Such calculations are described in Section 4.

The task of getting accurate estimates of cooling times is further complicated by many unexplored effects of high-energy cooling in a collider:

1. Cooling needs to be done with a bunched electron beam.
2. Transverse and longitudinal temperatures of electron beam are orders of magnitude larger than the temperatures of electron beam used in existing coolers.
3. For practical values of magnetic field in cooling solenoid, the Coulomb logarithm of magnetized cooling force is very close to unity, which may require either very accurate expressions for the cooling force in such a regime or numerical calculation of the friction coefficients.
4. Due to high energy, typical angular spread of the ion beam in RHIC is of the order of 10^{-5}, which requires straightness of magnetic field lines in cooling solenoid to be a few times better than such a value. Formation of the magnetic field at such an accuracy level is a complicated technical task.
5. The major goal of cooling in a collider is to increase the luminosity, which depends on the details of ion beam distribution. Rapidly cooled ion core requires detailed calculations of other processes for such "collapsed" ion distribution, for example, it requires more accurate treatment of the intrabeam scattering, rather than the standard treatments based on rms parameters of beam distribution.
6. The ultimately achieved luminosity will depend on ion beam dynamics for such cooled distribution, which requires an accurate treatment of beam-beam effect, collective instabilities, etc.

All these effects can be studied by means of numerical calculations which are discussed in following sections.

III.A.2. Intrabeam scattering

Charged particle beam are stored in circular accelerators for a long time. The phenomenon when particles within the beam are scattered from one another via Coulomb scattering is called Intra-Beam Scattering (IBS). Such a process is typically separated in two effects:

1. Scattering on a large angle so that the particles can be lost from a bunch as a result of a single collision – such an effect is called the Touschek effect.

2. Scattering on small angles can randomly add together which can cause beam dimension to grow – such effect is called the Intra-Beam Scattering.

III.A.2.1 General models

The process of IBS is very similar to collisions in a plasma (ionized gas), which govern gas relaxation towards equilibrium. The corresponding simple diffusion coefficients can be derived. The case of charged particle beam is in fact very similar to the plasma case when the longitudinal motion is transformed away by going into the Particle-Rest-Frame (PRF) which moves along the storage ring at the nominal beam velocity. The scattering events now appear exactly as in the plasma case, the only difference is that the distribution function is now given in terms of generalized coordinates which describe particle motions in circular accelerator . In circular accelerator, curvature of the orbit produces a dispersion, and due to the dispersion a sudden change in energy results in a change of betatron amplitudes. Such a coupling makes an important difference between small-angle Coulomb collisions in plasma (Gas-Relaxation) and in circular accelerators (IBS).

A theory of IBS for protons beams was proposed by Piwinski [Piwinski1], who calculated growth of beam dimensions in all three directions. In the original theory, beam dimensions were estimated as an average around the circumference of the ring. For this purpose, the ring lattice functions were also averaged. This model was later extended by a CERN team in collaboration with Piwinski to include variations of the lattice function around the ring. An improved model was later described in a detailed report by Martini [Martini1] and is sometimes referred to as Martini's model. Similar results were also obtained with a completely different approach of S-matrix formalism by Bjorken and Mtingwa [Bjorken1].

III.A.2.2 IBS at high energy

Calculation of the IBS growth rates using Piwinski's, Martini's or Bjorken-Mtingwa's models is very time consuming due to numerical integration at every lattice element. Therefore, a variety of more approximate but simpler formulations of IBS were developed over the years, for example by Parzen [Parzen1] and Wei [Wei1]. One should note that at very high particle energy, which is of interest for colliders, another effect which results in a collapse of distribution function (longitudinal velocity spread becomes much smaller than transverse) in PRF becomes more important than coupling. As result, one can have satisfactory representation of Coulomb collisions by using gas-relaxation formulas derived for a collapsed distribution function in velocity space [Sorensen1, Fedotov1]. Detailed study of growth-rates using G-R formula and various models of IBS was recently conducted [Fedotov2]. Various models of IBS (accurate calculation at lattice elements and simpler approximations) were implemented in one of the beam dynamics codes BETACOOL [BetaCool] which is used for cooling studies at RHIC. Comparison of IBS growth rates calculation between various formulas was also performed [Fedotov3].

III.A.2.3 IBS for ion beam distribution under electron cooling

Standard models of IBS discussed above are based on the growth of rms beam parameters for the Gaussian distribution. However, as a result of electron cooling, the core of beam distribution is cooled much faster than the tails. A simple use of standard rms-based IBS approach would significantly underestimate IBS for beam core. A detailed treatment of IBS, which depends on individual particle amplitudes, was recently proposed by Burov [Burov1], with an analytic formulation done for a Gaussian distribution. However, during the cooling process beam distribution quickly deviates from a Gaussian profile. Due to an extreme importance of understanding of degree of a core collapse (which directly impacts luminosity in a collider), a simple "core-tail" model, based on a different diffusion coefficient for beam core and tails was proposed by the BNL team [Fedotov4]. The beam distribution under cooling can be well approximated by a bi-Gaussian. In addition, the standard IBS theory was recently reformulated for rms parameters growth of a bi-Gaussian distribution by Parzen [Parzen2]. Such a formulation provides a possibility for further improvements of a "core-tail" model of IBS, which is presently used in simulation of RHIC cooling.

The above formulations, which attempts to calculate IBS for a beam distribution changing under electron cooling, are implemented in beam dynamics codes BetaCool and SimCool, which are used for cooling studies of RHIC and will be discussed in following section on numerical simulations.

III.A.2.3.1 IBS growth rates for bi-Gaussian distribution

The following section summarizes results for the intrabeam scattering growth rates for a bi-Gaussian distribution [Parzen2]. The calculation is done based on the treatments given by Bjorken and Mtingwa [Bjorken1]. The bi-Gaussian distribution is defined below as the sum of two Gaussians in the particle coordinates x,y,s,p_x,p_y,p_s. The Gaussian with the smaller dimensions produces most of the core of the beam, and the Gaussian with the larger dimensions largely produces the long tail of the beam. The final result for the growth rates are expressed as the sum of three terms which can be interpreted respectively as the contribution to the growth rates due to the scattering of the particles in the first Gaussian from themselves, the scattering of the particles in the second Gaussian from themselves, and the scattering of the particles in the first Gaussian from the particles in the second Gaussian.

<u>The Gaussian distribution</u>

Before defining the bi-gaussian distribution, the gaussian distribution is reviewed. $Nf(x,p)$ gives the number of particles in d^3xd^3p, where N is the number of particles in a bunch.

For a gaussian distribution, f(x,p) is given by

$$f(x,p) = \frac{1}{\Gamma}\exp[-S(x,p)]$$

$$S = S_x + S_y + S_s$$

$$S = \frac{1}{\bar{\varepsilon}_x}\varepsilon_x(x_\beta, p_{x\beta}/p_0$$

$$x_\beta = x - D(p - p_0)/p_0$$

$$p_{x\beta}/p_0 = p_x/p_0 - D'(p - p_0)/p_0$$

$$\varepsilon_x(x,x') = \gamma_x x^2 + 2\alpha_x xx' + \beta_x x'^2$$

$$S_y = \frac{1}{\bar{\varepsilon}_y}\varepsilon_y(y, p_y/p_0)$$

$$\varepsilon_y(y,y') = \gamma_y y^2 + 2\alpha_y yy' + \beta_y y'^2$$

$$S_s = \frac{1}{2\sigma_s^2}(s-s_c)^2 + \frac{1}{2\sigma_p^2}\left((p-p_0)/p_0\right)^2$$

$$S_s = \frac{1}{\bar{\varepsilon}_s}\left(\frac{1}{\beta_s}(s-s_c)^2 + \beta_s((p-p_0)/p_0)^2\right)$$

$$\beta_s = \sigma_s/\sigma_p$$

$$\bar{\varepsilon}_s = 2\sigma_s\sigma_p$$

$$S_s = \frac{1}{\bar{\varepsilon}_s}\varepsilon_s(s-s_c,(p-p_0)/p_0)$$

$$\Gamma = \int d^3x d^3p \exp[-S(x,p)]$$

$$\Gamma = \pi^3 \bar{\varepsilon}_x \bar{\varepsilon}_y \bar{\varepsilon}_s p_0^3 \qquad \text{(III.A.2.1)}$$

$$\bar{\varepsilon}_i = \ < \varepsilon_i(x,p) > \quad i = x,y,s$$

Here, D is the horizontal dispersion and D'=dD/ds. Symbol <> indicates an average over all the particles in a bunch.

The bi-Gaussian distribution

The bi-Gaussian distribution is assumed to have the form given by the following. Nf(x,p) gives the number of particles in $d^3x d^3p$, where N is the number of particles in a bunch.

For a bi-Gaussian distribution, f(x,p) is given by

$$f(x,p) = \frac{N_a}{N}\frac{1}{\Gamma_a}exp[-S_a(x,p)] + \frac{N_b}{N}\frac{1}{\Gamma_b}exp[-S_b(x,p) \qquad \text{(III.A.2.2)}$$

In the first Gaussian, to find G_a,S_a then in the expressions for G,S, given above for the Gaussian distribution, replace $\bar{\varepsilon}_x, \bar{\varepsilon}_y, \bar{\varepsilon}_s$ by $\bar{\varepsilon}_{xa}, \bar{\varepsilon}_{ya}, \bar{\varepsilon}_{sa}$. In the second Gaussian, in the expressions for Γ ,S, replace $\bar{\varepsilon}_x, \bar{\varepsilon}_y, \bar{\varepsilon}_s$ by $\bar{\varepsilon}_{xb}, \bar{\varepsilon}_{yb}, \bar{\varepsilon}_{sb}$. In addition, N_a+N_b=N. This bi-Gaussian has 7 parameters instead of the three parameters of a Gaussian.

Growth rates for a Bi- Gaussian distribution

In the following ,the growth rates are given in the Rest Coordinate System, which is the coordinate system moving along with the bunch. Growth rates are given for $<p_i\ p_j>$. From these one can compute the growth rates for $<\varepsilon_i>$ as well [Parzen2].

$$
\begin{aligned}
\frac{1}{p_0^2}\frac{d}{dt} < p_i p_j > &= N \int d^3\Delta\ C_{ij}[\left(\frac{N_a}{N}\right)^2 \frac{exp(-R_a)}{\Gamma_a} + \left(\frac{N_b}{N}\right)^2 \frac{exp(-R_b)}{\Gamma_b} \\
&\quad +2\frac{N_a N_b}{N^2}\frac{\Gamma_c}{\Gamma_a \Gamma_b} exp(-T)] \\
C_{ij} &= \frac{2\pi}{p_0^2}(r_0/2\bar{\beta}^2)^2(|\Delta|^2\delta_{ij} - 3\Delta_i\Delta_j)2\bar{\beta}c\ \ ln[1+(2\bar{\beta}^2 b_{max}/r_0)^2] \\
\bar{\beta} &= \beta_0\gamma_0|\Delta/p_0| \\
r_0 &= Z^2e^2/Mc^2 \\
\frac{1}{\bar{\epsilon_{ic}}} &= \frac{1}{2}\left(\frac{1}{\bar{\epsilon_{ia}}} + \frac{1}{\bar{\epsilon_{ib}}}\right)\quad i = x, y, s \\
\frac{1}{\bar{\epsilon}_{id}} &= \frac{1}{2}(\frac{1}{\bar{\epsilon}_{ia}} - \frac{1}{\bar{\epsilon}_{ib}}) \\
r_0 &= Z^2e^2/Mc^2 \\
\Gamma_a &= \pi^3\bar{\epsilon_{sa}}\bar{\epsilon_{xa}}\bar{\epsilon_{ya}}p_0^3 \\
R_a &= R_{xa} + R_{ya} + R_{sa}s \\
R_{xa} &= \frac{2}{\beta_x\bar{\epsilon_x}}[\gamma^2D^2\Delta_s^2 + (\beta_x\Delta_x - \gamma\tilde{D}\Delta_s)^2]/p_0^2 \\
\tilde{D} &= \beta_x D' + \alpha_x D \\
R_{ya} &= \frac{2}{\beta_y\bar{\epsilon_y}}\beta_y^2\Delta_y^2/p_0^2 \\
R_{sa} &= \frac{2}{\beta_s\bar{\epsilon_s}}\beta_s^2\gamma^2\Delta_s^2/p_0^2 \\
T &= T_x + T_y + T_s \\
T_x &= R_{xc} - R_{xd} \\
T_y &= R_{yc} - R_{yd} \\
T_s &= R_{sc} - R_{sd} \\
R_{xd} &= 2\{[-\gamma D\bar{\Delta}_s \\
&\quad +(\beta_x\bar{\Delta}_x - \gamma\bar{D}\bar{\Delta}_s)\alpha_x]^2 \\
&\quad +[(\beta_x\bar{\Delta}_x - \gamma\bar{D}\bar{\Delta}_s)]^2\} \\
&\quad /(\beta_x\bar{\epsilon}_{xd}^2/\bar{\epsilon}_{xc}) \\
R_{yd} &= \frac{2\beta_y}{\bar{\epsilon}_{yd}^2/\bar{\epsilon}_{yc}}\bar{\Delta}_y^2 \\
R_{sd} &= \frac{2\beta_s}{\bar{\epsilon}_{sd}^2/\bar{\epsilon}_{sc}}\bar{\Delta}_s^2
\end{aligned}
$$

(III.A.2.3)

Here, R_a ,R_b, R_c are each the same as R_a except that $\bar{\varepsilon}_i$ in these expressions is replaced by $\bar{\varepsilon}_{ia}, \bar{\varepsilon}_{ib,} \bar{\varepsilon}_{ic}$ respectively.

III.A.2.3.2 Core-tail model of IBS for ion distribution changing under cooling.

A core of beam distribution is cooled much faster than the large-particle amplitudes. If cooling is not strong enough than only small portion of particles in a core is being cooled while the rms parameters of beam distribution may stay practically unchanged, as shown in Figs. III.A.2.1 –III.A.2.2 for transverse rms emittance and beam profiles, respectively. In such a case, applying IBS diffusion coefficients based on the rms beam parameters does not describe IBS for a beam core correctly [Burov1]. As a result, the standard "rms-based IBS approach" underestimates diffusion of beam core due to IBS which results in an unrealistic collapse of beam core distribution due to cooling as shown in Fig. III.A.2.3.

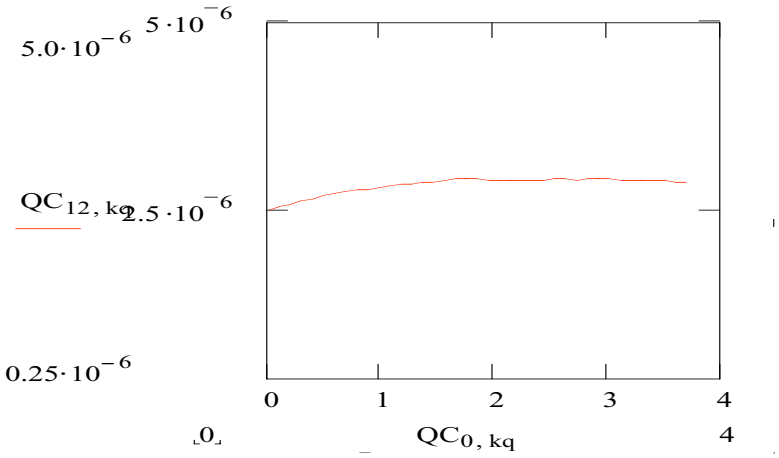

Fig. III.A.2.1 Time evolution of transverse rms emittance for typical cooling parameters of Au ions at 100 GeV energy. Horizontal axis: time [hours]. Vertical axis: ε_{in} [m rad].

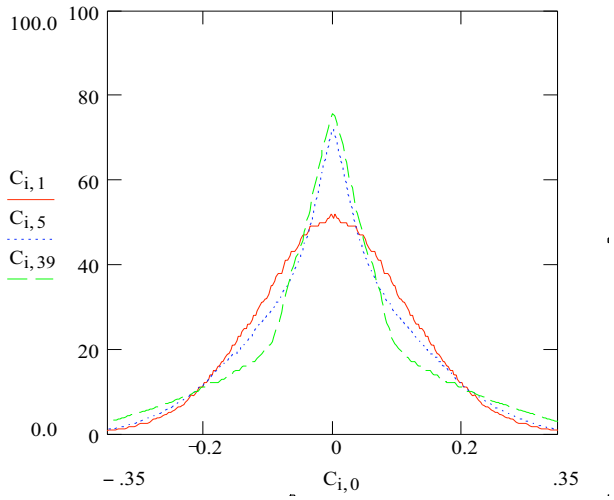

Fig. III.A.2.2 Transverse beam profile at various time steps for "core-tail" model of the IBS.Red: initial, blue: after 30 minutes of cooling, green: after 4 hours of cooling at 100 GeV.

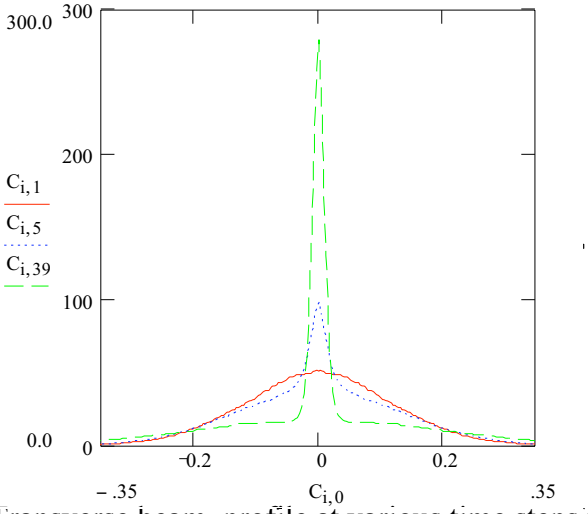

Fig. III.A.2.3 Transverse beam profile at various time steps for the rms model of the IBS.Red: initial, blue: after 30 minutes of cooling, green: after 4 hours of cooling.

The purpose of simple "core-tail" model was to have an estimate of the diffusion of beam core which is rapidly shrinking as a result of cooling process. For that purpose, the core was defined by a Full-Width-Half-Maximum of the distribution. The diffusion kick was then applied differently for particles in the core and outside of the core [Fedotov4].

For example, the longitudinal diffusion coefficient, using the gas-relaxation formula expressed in terms of the rms beam parameters in circular accelerator, can be written as:

$$D_{zz} = \frac{2Nr^2c}{(\gamma\beta)^3}\frac{\Lambda_{ibs}}{\varepsilon^{3/2}\sqrt{\beta_a}(\sqrt{2\pi})\sigma_s}, \qquad \text{(III.A.2.4)}$$

where ε is the transverse rms beam emittance, σ_s is rms bunch length, β_a is the average beta-function over the ring lattice, Λ_{ibs} is the Coulomb logarithm for IBS, and N is the total number of particles in a bunch.

For the distribution changing under cooling, particles in the core will receive a kick according to

the diffusion coefficient $D_{zz,core}$:

$$D_{zz,core} = N_{core} \frac{C}{\varepsilon_f^{3/2} \sigma_{sf}} + (N - N_{core}) \frac{C}{\varepsilon^{3/2} \sigma_s}, \qquad \text{(III.A.2.5)}$$

where ε_f and σ_{sf} are the transverse emittance and bunch length corresponding to FWHM of transverse and longitudinal distribution, respectively. Here, constant C incorporates all the parameters in the diffusion coefficient which are not changing with time. Particles in the core receive a kick according to overall rms parameters of beam distribution:

$$D_{zz,tails} = N \frac{C}{\varepsilon^{3/2} \sigma_s}, \qquad \text{(III.A.2.6)}$$

The accuracy of this model is determined by finding N_{core} inside the distribution given by a Gaussian with σ_f corresponding to FWHM with an appropriate numerical factor.

To improve accuracy of simplified (based on FWHM) core-tail model, a numerical procedure is presently being employed by fitting two Gaussian distributions to a real distribution observed in simulations for each time step of the calculation [Eidelman3]. The amplitude and width of fitted Gaussians provide more accurate parameters which are used instead of ε, ε_f, σ_s, σ_{sf} in the diffusion coefficients for core and tails of the beam distribution, in expressions (III.A.2.4-III.A.2.6).

Transverse diffusion coefficients are expressed through the longitudinal coefficient using the dispersion function of the ring [Fedotov4].

Presently, the core-tail model implemented in the SimCool code is based on the Gas-Relaxation rates to represent the kick on individual particles in the velocity space due to IBS. The core-tail model is also implemented in the BetaCool code which allows the use of more realistic IBS rates based on standard formulas from the IBS theory, including detailed dependence on lattice functions and their derivatives.

III.A.3 Equilibrium between IBS and electron cooling

III.A.3.1 Estimates for critical number of electrons

One can roughly estimate the number of electrons required to reach equilibrium between cooling and IBS. The cooling rate using empiric formula for the friction force by Parkhomchuk is

$$\frac{1}{\tau_{cool}} = \frac{2\ N_e r_i r_e c \eta}{\pi \gamma^5 \beta^3 \varepsilon^{5/2}} \frac{\Lambda_c \sqrt{\beta_i}}{\sigma_s \sqrt{2\pi}}, \qquad \text{(III.A.3.1)}$$

where γ, β and c are relativistic factors and the speed of light, β_i is the beta-function in the cooling section, η is the length of the cooling region divided by the ring circumference, Λ_c is the Coulomb logarithm, r_e and $r_i=(Z^2 r_p)/A$ are the classical electron and ion radii, n_e is electron beam density in the laboratory frame, N_e is the number of electrons in the bunch, σ_s is the rms bunch length. Here, the transverse rms electron beam size σ was expressed in terms of the beam emittance ε.

Using the heating rate due to IBS based on the Gas-Relaxation formula

$$\frac{1}{\tau_{ibs}} = \frac{2\ N_i r_i^{\ 2} c}{\gamma^3 \beta^3 \varepsilon^{3/2} \sqrt{\beta_i}} \frac{\Lambda_{ibs}}{\sigma_p^{\ 2} \sigma_s \sqrt{2\pi}}, \qquad \text{(III.A.3.2)}$$

where σ_p is an rms momentum spread ($\Delta p/p$), N_i is number of ions and Λ_c is the Coulomb logarithm due to IBS, the equality of heating and cooling rates gives

$$N_{ec} = \pi \frac{r_i}{r_e} \frac{N_i}{\eta} \frac{\Lambda_{ibs}}{\Lambda_c} \frac{1}{g_f}, \qquad \text{(III.A.3.3)}$$

where g_f is the flatness parameter of ion distribution defined as

$$g_f = \left(\frac{v_{longitudinal}}{v_{tranverse}} \right)^2 = \frac{\sigma_p^{\ 2}}{\gamma^2 (\varepsilon / \beta_i)}. \qquad \text{(III.A.3.4)}$$

Note that expression for N_{ec} above is just an order of magnitude estimate. In fact, depending on which formula is used for the cooling force or for the IBS, the factor π in Eq. (III.A.3.3) may be replaced by some other factor. Also, in the case of equilibrium between detailed IBS and cooling [Burov1] one gets a factor of 2 instead of π in Eq. (III.A.3.3), for example.

Taking the following parameters of RHIC: $N_i=1*10^9$, $\eta=0.0078$, $\Lambda_{ibs}=20$, $g_f=0.24$ (for Au ions at storage energy of 100 GeV), and assuming that the cooler will have magnetized cooling logarithm $\Lambda_c=2$ (value of magnetized cooling logarithm will be discussed in following sections) one gets about $N_{ec}=3*10^{11}$.

Keeping in mind that this is an order of magnitude estimate, one should expect that number of electrons in a bunch in the range $N_{ec}=1 - 5*10^{11}$ may be required to reach an equilibrium between cooling and IBS, for RHIC parameters.

III.A.3.2 Numerical simulations of critical number at 100 GeV

Numerical simulations which include many effects such as the finite strength of the magnetic field and finite temperatures of the electron beam show reasonably good agreement for the critical number obtained with an order of magnitude estimates based on Eq. (III.A.3.3). Figures III.A.3.1 –III.A.3.8 show the rms emittances and beam profiles for $N_{ec}=1.2$, 2.4, 3.0, $3.6*10^{11}$ electrons, respectively. Simulations are done with the BetaCool code [BetaCool].

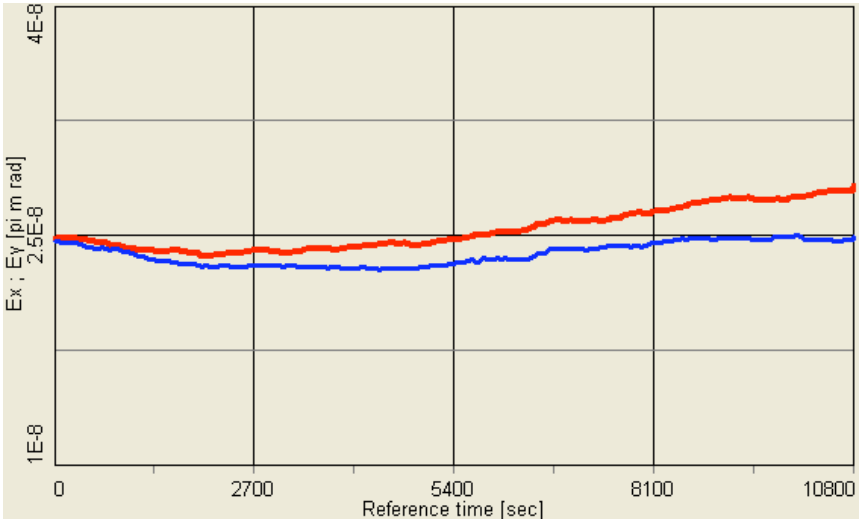

Fig. III.A.3.1 Time evolution of unnormalized rms emittances at 100 GeV with number of electrons $Ne=1.2*10^{11}$.

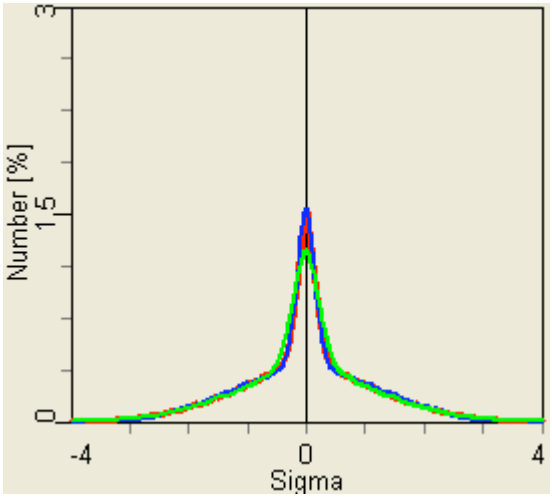

Fig. III.A.3.2 Beam profiles after 4 hours of cooling (x,y: red, blue; s: green) for cooling with Ne=1.2*10^{11} .

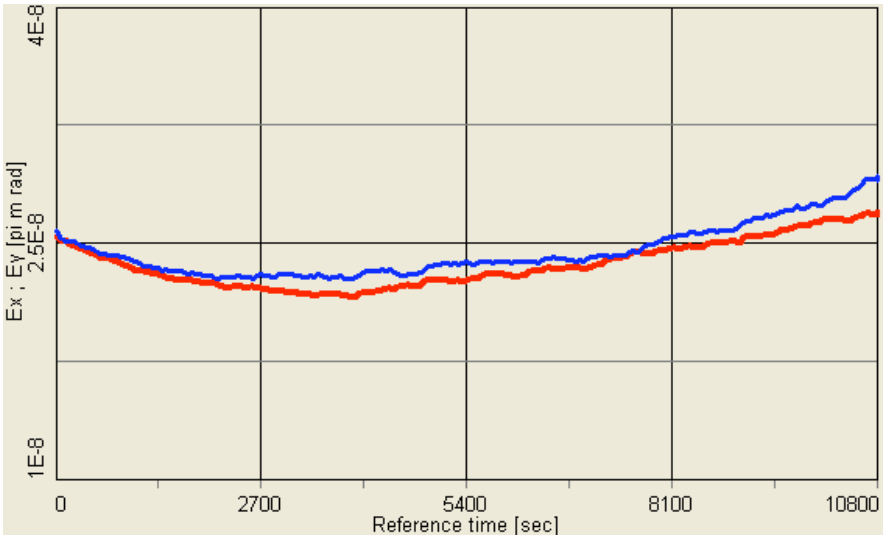

Fig. III.A.3.3 Time evolution of unnormalized rms emittances at 100 GeV with number of electrons Ne=2.4*10^{11} .

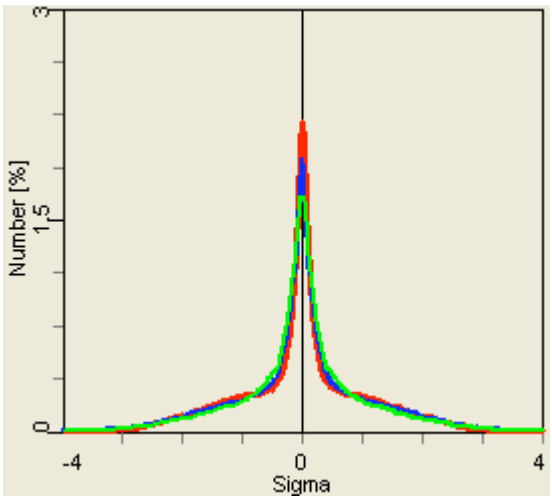

Fig. III.A.3.4 Beam profiles after 4 hours of cooling (x,y: red, blue; s: green) for cooling with Ne=2.4*10^{11} .

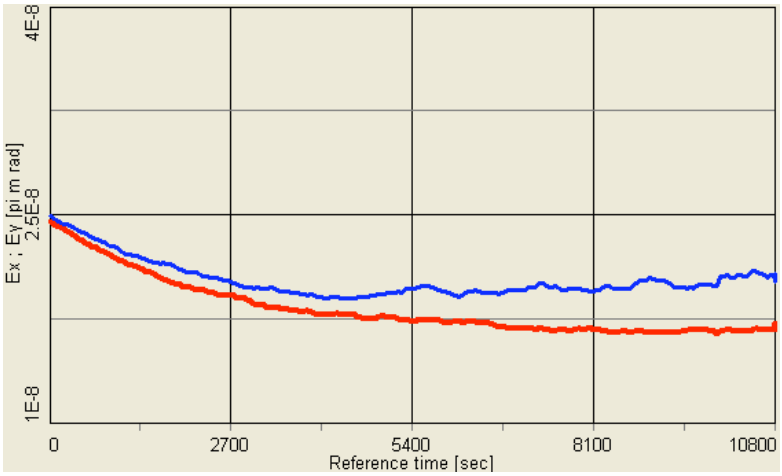

Fig. III.A.3.5 Time evolution of unnormalized rms emittances at 100 GeV with number of electrons Ne=3.0*10^{11} .

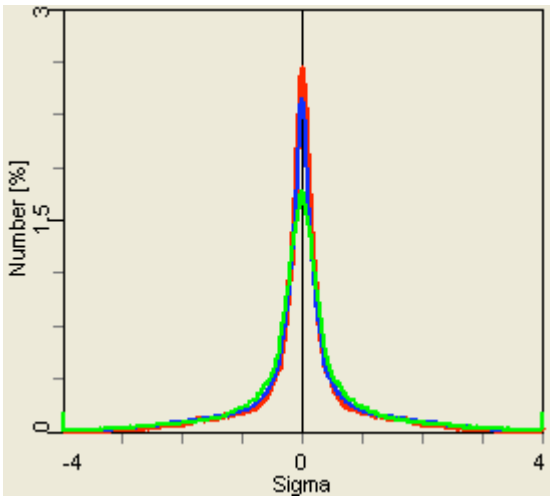

Fig. III.A.3.6 Beam profiles after 4 hours of cooling (x,y: red, blue; s: green) for cooling with Ne=3.0*10^{11} .

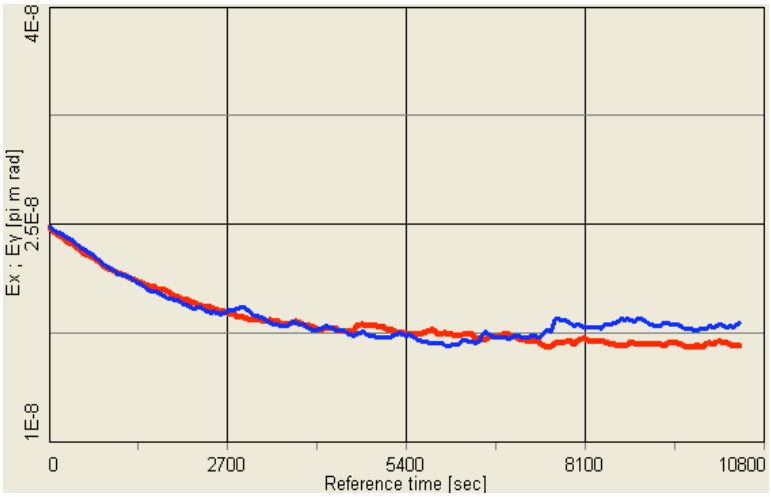

Fig. III.A.3.7 Time evolution of unnormalized rms emittances at 100 GeV with number of electrons Ne=3.6*10^{11} .

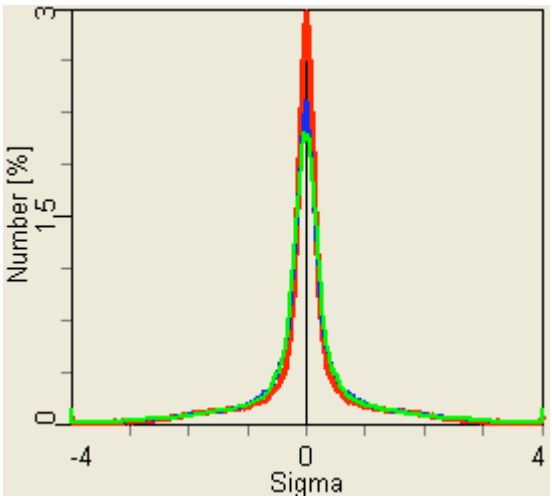

Fig. III.A.3.8 Beam profiles after 4 hours of cooling; Ne=3.6*10^{11}

One can see that (for present baseline parameters of the cooler) an equilibrium is reached at a critical number of electrons which is surprisingly in good agreement with very rough estimate of N_{ec}=3*10^{11}, based on formula in Eq. (III.A.3.3). At N_{ec}=3.6*10^{11} , an equilibrium between cooling and IBS is reached already after one hour of cooling. Further cooling results in reduction of rms beam parameters as, for example, is needed for the eRHIC project [eRHIC].

III.A.3.3 Numerical simulations of critical number at 30 GeV

At lower energy, cooling is much faster due to strong dependence on relativistic γ factor. In addition, one can expect smaller critical number due to the flatness parameter of the ion beam distribution which is shown in Eq. (III.A.3.4).

Figures III.A.3.9–III.A.3.11 show the rms emittances, the bunch length and beam profiles for N_{ec}=1.2*10^{11} electrons, respectively. One can see that an equilibrium with a significant reduction of an rms emittance is already reached within one hour of cooling.

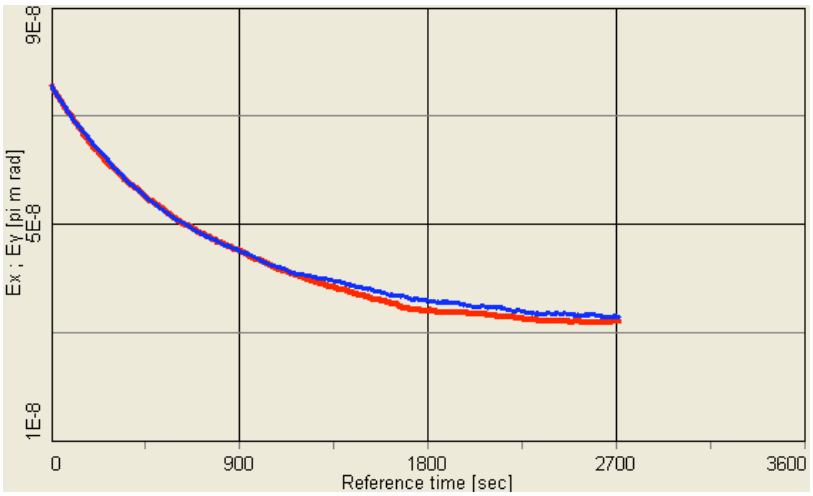

Fig. III.A.3.9 Time evolution of unnormalized rms emittances at 30 GeV with number of electrons Ne=1.2*10^{11} .

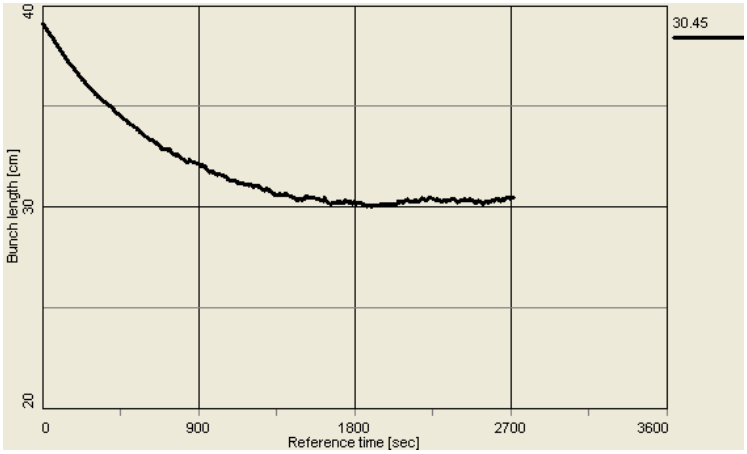

Fig. III.A.3.10 Cooling of bunch length at 30 GeV with Ne=1.2*10^{11}

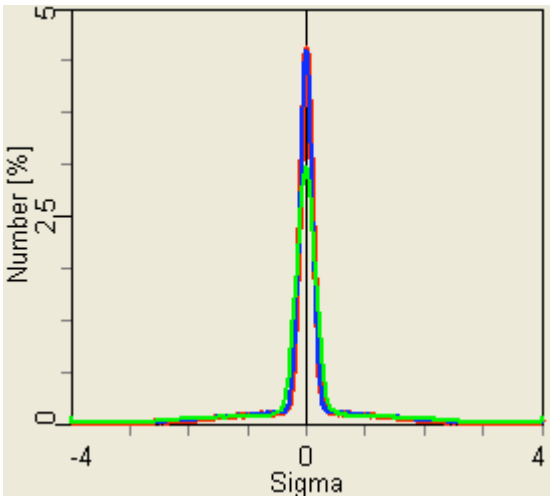

Fig. III.A.3.11 Beam profiles after 2700 seconds of cooling at 30 GeV with Ne=1.2*10^{11}

Based on the critical number N_{ec} needed at 100 GeV and expression for the flatness parameter, one can estimate that as low as Ne=3.6*10^{10} may be sufficient to reach an equilibrium between IBS and cooling at 30 GeV energy. Such an estimate is in good agreement with numerical simulations shown in Fig. III.A.3.12.

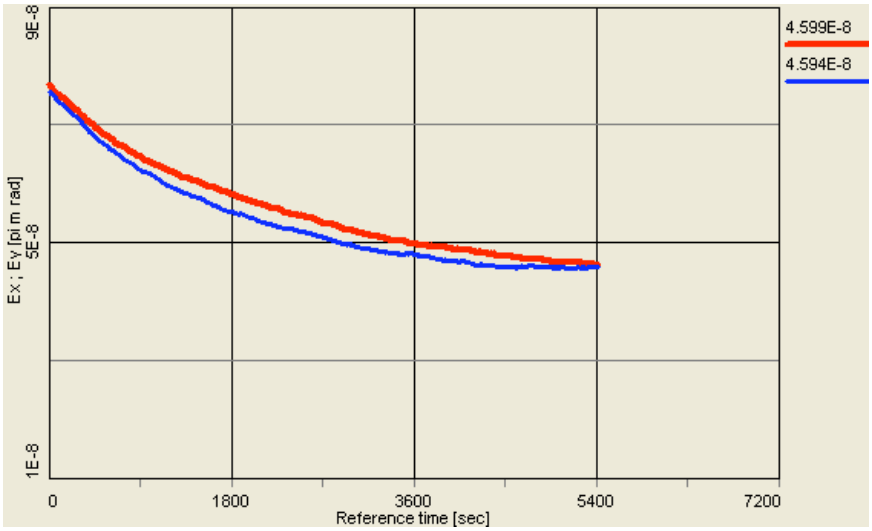

Fig. III.A.3.12 Transverse emittances for cooling at 30 GeV with Ne=3.6*10^{10}

III.A.4 Detailed calculation of cooling dynamics

III.A.4.1 Numerical simulation of the friction force

The first step towards accurate calculation of cooling times is to use an accurate description of the cooling force. The large temperatures of electron beam, which results due to RF acceleration of a bunched beam to high energy, can not be fully compensated by the magnetic field in a solenoid for practical reason. As a result achievable magnetized cooling logarithm is not very large so that available formulas, derived in logarithmic approximation becomes questionable. In addition, in some parameter regimes there is a significant discrepancy between available analytic formulas.

The uncertainty in the magnitude of the magnetized friction force has been acceptable for existing electron coolers, all of which operate at very low energy which result in short cooling time making order-of-magnitude estimates sufficient. In contrast, electron cooling in RHIC will be done in a completely new regime which sets very strict accuracy requirements on various aspects of cooling dynamics, starting with the friction force. For this reason the ParSec project [Bruhwiler1] at Tech-X company is being used to develop a parallel code capability based on the VORPAL code [VORPAL] to simulate from first principles the friction force and diffusion coefficients for parameters directly relevant to RHIC [Bruhwiler2].

The friction force can be numerically calculated based on the inter-particle Coulomb forces directly.
When all pair wise forces are computed directly the numerical approach becomes intensive in the extreme. Primitive N-body simulations were found to be unacceptably noisy due to the problem of artificially close collisions. In an artificially close collision, two charged particles approach one another very closely due to a finite time step which results in an unrealistically large collision. The Particle-In-Cell method avoided this problem at the expense of losing close Coulomb collisions altogether. However, it is these close particle collisions which are essential for correct modeling of the physics of electron cooling. To address these issues a 4^{th} –order Hermite algorithm with aggressive variable time-stepping was implemented in the VORPAL code. The goal of the VORPAL code is to provide reliable simulation of the RHIC cooling section, including both space charge forces and, critically important, friction forces and diffusion coefficients due to Coulomb collisions of the ion and electron beam.

The on-going simulations with the VORPAL show great promise for resolving ambiguities in the theoretical understanding of the magnetized friction force under idealized conditions [Bruhwiler2]. The goal is also to determine quantitatively the effect of complicated factors, such as bulk space-charge electric fields, variations of electron

density, the effect of nearby trajectories of other ions, impact of errors in the solenoidal magnetic field.

The primary goals of VORPAL simulation for the RHIC cooling project can be summarized as follows:

- Resolve differences in analytic calculations (approximations of uniform electron density,
  no space charge, infinite magnetic field, etc.)
- Determine validity of Z^2 scaling for friction force (non-linear plasma effects in magnetized plasma Debye shielding).
- Understand the effects of space charge and diffusion dynamics
- Understand the effects of magnetization (from strong to weak magnetization, magnetic field errors)
- Accurate calculations of friction force in the regime of small Coulomb logarithm due to magnetized collisions.
- If the friction force for RHIC regime significantly deviates from description based on simple formulas, provide a numerical Table of friction coefficients to be used in dynamics codes.

Preliminary studies with VORPAL found good agreement with available formulas in some parameters regimes and deviate in the other. For a regime similar to RHIC with a small Coulomb logarithm a relative good agreement with empiric formula by Parkhomchuk was found. However, to accurately simulate RHIC regime, massively parallel computation are required which is presently underway.

III.A.4.2 Development of dynamics simulation codes for high energy cooling

Reliable predictions of cooling times at high energies of a collider with a corresponding increase of the luminosity require detailed simulation of many effects acting together: friction force which ions experience by passing through the cooling section, diffusion due the intrabeam scattering which ions in a bunch undergo during their passage over ring circumference, diffusion due to beam-beam effects, ion recombination in the cooling sections, solenoid imperfections, etc. To address these aspects of cooling in a collider two cooling dynamics codes (SimCool and BetaCool) are presently being developed for the RHIC project.

III.A.4.2.1 The SimCool code

The first code SimCool was originally developed at BINP in Novosibirsk. It is presently being developed by the BNL team with on-going modifications/improvements being made to address specifics of electron cooling at RHIC [Eidelman1-2]. Some of the recent modification to the code include synchrotron motion, more accurate treatment of longitudinal and transverse diffusion due to the IBS based on an rms beam parameters, development of core-tail model for the IBS treatments which takes into account different diffusion coefficients for particle in the core of beam distribution and tails of beam distribution, etc.

An important feature of the SimCool code is a direct modeling of ion beam distribution using the macro-particle approach, which allows for particle distribution to change with time. The time evolution of the distribution is modeled using the Monte Carlo approach with one time step corresponding to a large number of turns in the ring ($\sim 10^5 - 10^6$). On each time step ion particle undergoes random kick due to the friction and diffusions coefficients in the cooling sections and kicks due to the IBS in the ring. The friction force kicks are applied based on the empiric cooling force in Eq. (III.A.1.35). The IBS kicks are presently applied based on the Gas-Relaxation formula [Fedotov1] and, therefore, have no dependence on variation of lattice functions around the ring. Such treatment of IBS is very approximate and was found to overestimate diffusion for RHIC compared to a more accurate IBS models [Fedotov2].

The modeling of dynamics in the SimCool code allows for beam distribution to change as a result of both cooling and IBS which leads to a beam distribution with a pronounced (collapsed) beam core. Formation of a dense core is the most important feature for cooling in a collider since the luminosity directly depends on details of particle distribution. In fact, even for cooling parameters which may not be sufficient to cool an average beam parameters (rms emittance stays unchanged or may even increase) formation of a dense core can lead to a strong luminosity increase. However, an accurate treatment of other effects which may depend on such a dense core becomes extremely important.

III.A.4.2.2 The BetaCool code

The second code for cooling dynamics BetaCool is being developed at JINR in Dubna [BetaCool]. The original version of the code which was based on rms beam parameters was shown to be not sufficient for simulation of high-energy cooling in a collider where changing beam distribution is of crucial importance. As a result, a new model (called "Modeled beam") based on the SimCool approach was recently implemented. Presently, development of many effects in BetaCool code goes in parallel with the SimCool development. A detailed benchmarking between the two codes ensures accuracy of the models being implemented.

The present version of the BetaCool code allows performing dynamic simulation using three different algorithms:

1) rms beam dynamics (evolution of rms beam parameters for a Gaussian distribution)
2) Modeled beam (modeling of beam with macro-particles similar to the SimCool)
3) Tracking – particle dynamics over the ring elements using techniques from Molecular Dynamics.

Many of recent developments in the code are directly aimed to address specific question of high-energy cooling at RHIC. Such developments include:

1. More accurate treatments of IBS under cooling: detailed model of IBS; core-tail model of IBS.
2. Solenoid errors in the cooling section.
3. Possibility to change cooling parameters dynamically to achieve better cooling performance. 4. Accurate treatment of particle losses: due to collision, acceptance, loss from the bucket.
5. Various calculations of beam emittances: rms parameters, Courant-Snyder invariants, Full-Width-Half-Maximum, and emittance percentiles.

The program is object oriented and its structure permits to use:

- different formulas for the cooling force calculation (presently, several formulas are implemented including an empiric formula used in the SimCool code)
- allows to read in tabulated coefficients for the friction force calculated by other codes, for example, by the Vorpal code described above
- includes different analytic models for IBS growth rate calculations (models by Piwinski, Martini, Wei and Gas-Relaxation)
- various models of the electron beam
- allows to take into account errors in the cooler geometry
- allows to change position of bunched electron beam with respect to bunched ion beam both transversely and longitudinally.

III.A.4.3 Ion beam dynamics in realistic RHIC environment

Because of the novelty and complexity of the bunched electron cooling approach, model-based analysis plays an import role in the design and commissioning of the RHIC electron cooling system. To enhance the accuracy and overall impact of beam dynamics studies, the associated theoretical models will be integrated with the RHIC off-line simulation facility. Its structure is shown in Figure III.A.4.1:

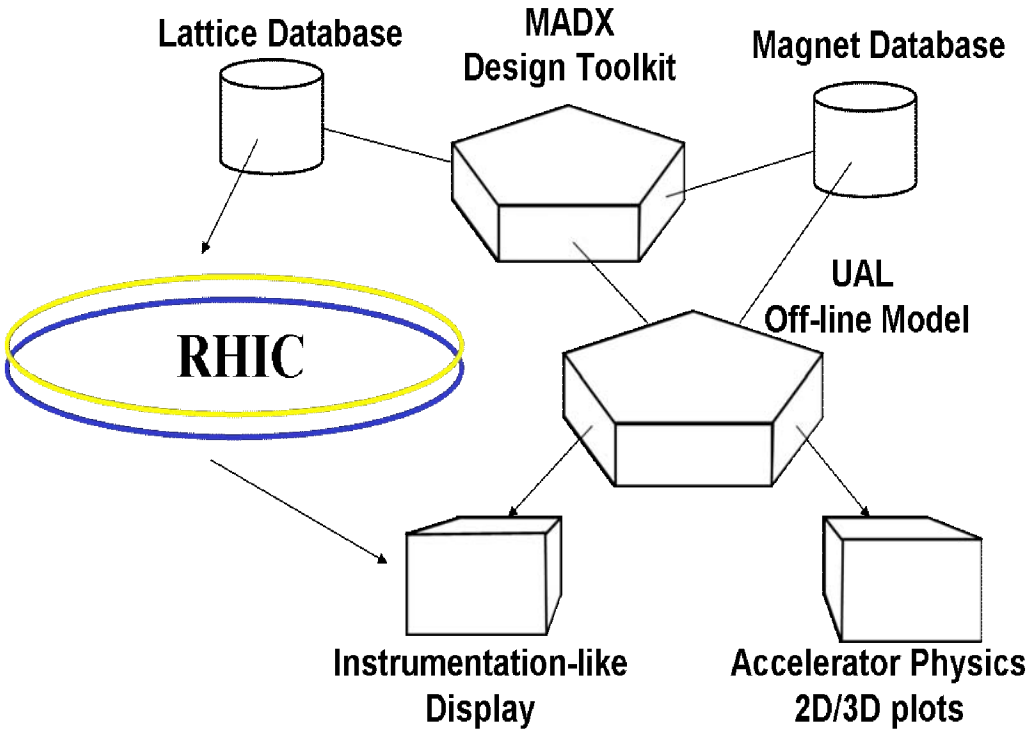

Figure III.A.4.1: RHIC off-line simulation facility.

The facility is built from three major components: MAD-X, UAL, and ROOT. The MAD-X toolkit deals with all design issues associated with changes of lattice optics, such as beta squeeze, upgrade of interaction regions, etc. The various simulation applications are based on the UAL framework and an open catalog of tracking algorithms [UAL]. Finally, the ROOT toolkit facilitates the analysis of simulation results and their comparison with operational data. The development of the RHIC off-line simulation facility was driven by and associated with dedicated beam experiment studies. In 2003-2004, its prototype was applied to the analysis of operational non-linear correction schemes and to measure multipole fields operationally for comparison (and discrepancy identification) with the magnet database. There is a plan to continue and extend these studies with beam-beam applications in the following year.

The core component of the described RHIC off-line simulation facility is an Off-line Model (Virtual Accelerator) based on the Unified Accelerator Libraries (UAL) environment. UAL was introduced in 1996 to perform realistic beam dynamics studies including complex combinations of physical effects and dynamic processes. This goal was achieved by developing an open infrastructure where diverse accelerator approaches are implemented as collaborative C++ libraries connected together via common accelerator objects (such as Element, Twiss, Particle, etc.). By this time, it has been successfully applied to different projects and accumulated several accelerator libraries

(see Figure 2). Recently, the UAL flexible infrastructure has been significantly enhanced and consolidated with the Accelerator Propagator Framework (APF), which provides a consistent mechanism for developing new tracking algorithms and connecting

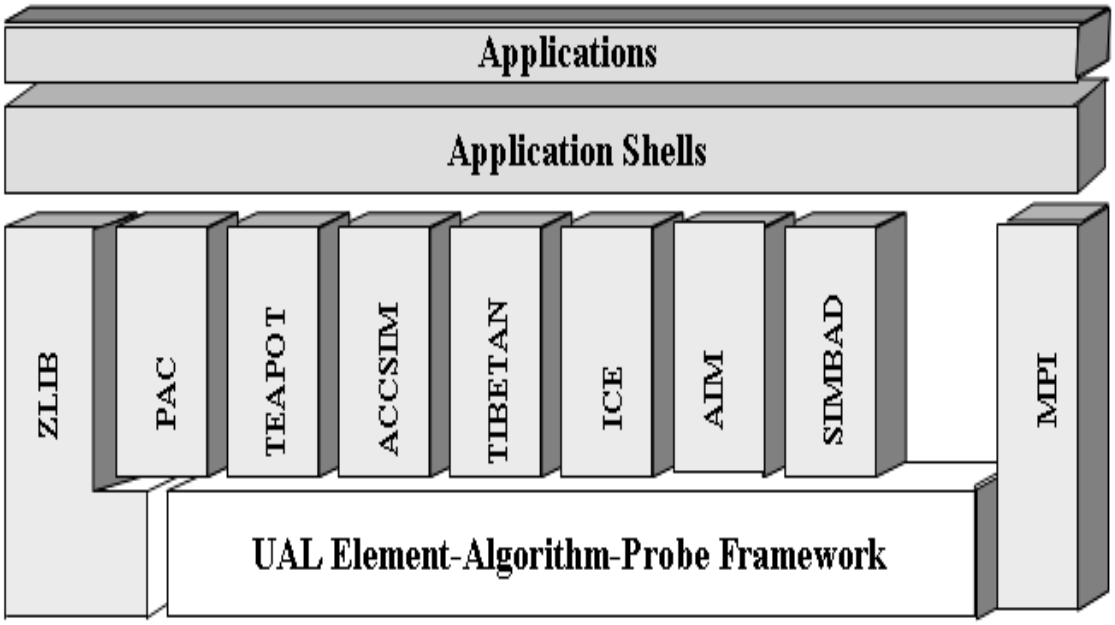

Figure III.A.4.2: UAL architecture

them with selected accelerator elements. In this framework, accelerator tracking programs, such as SIMCOOL and BetaCOOL, will be plugged via small adapters and used together with other propagators for complex beam dynamics studies. Moreover, such integration will simultaneously connect electron cooling applications with the present RHIC off-line model and post-processing analysis and diagnostics toolkit.

III.A.4.4 Cooling logarithm

In the presence of magnetic field, one can generally describe Coulomb interactions of heavy ions with electrons by considering three different regions of impact parameters:

Small impact parameters:

$$\rho_a = V_a/\omega_L > \rho > \rho_{min}\,, \qquad \text{(III.A.4.1)}$$

where $V_a=V-V_{e,long,}$ and ρ_{min} is given by scattering on $\pi/2$ angle. Such collisions are referred to as "fast". In such an interaction, collision is not influenced by magnetic field because the collision time is much shorter than the Larmor revolution period of electrons.

Intermediate impact parameters:

$$r_L=V_e/\omega_L > \rho > \rho_a ,$$

(III.A.4.2)

such collisions are referred to as "adiabatic". In such collisions, during the time of interaction electron has several Larmor rotations.

Large impact parameters:

$$\rho_{max} > \rho > r_L ,$$

(III.A.4.3)

such collisions are referred to as " magnetized". In such a case, electron has so many Larmor rotations that the heavy particle essentially interacts with the Larmor circle, which can move along the magnetic field line.

The empiric formula by Parkhomchuk makes unification of all these three contribution for practical purposes. Here, this formula is repeated for the PRF:

$$\vec{F}(v)=\frac{4e^4 n_e Z^2}{A} L_P \frac{v}{(v^2+v_{eff}^2)^{3/2}}$$

(III.A.4.4)

$$L_P=\ln\left(\frac{\rho_{max}+\rho_{min}+r_L}{\rho_{min}+r_L}\right).$$

(III.A.4.5)

Such a cooling logarithm allows estimating required parameters of the cooler for a good magnetization, and finding at which parameters there is a transition into the bad magnetization regime. For RHIC case, transition into bad magnetization region would suppress cooling because of a very high transverse temperature of electrons. In fact, because the transverse temperatures of electron beam are so high, it becomes essential to offset such temperatures with a large magnetic field in cooling solenoid.

The condition where magnetized cooling, for RHIC case, is suppressed is then given by $\rho_{max}/r_L=1$.

For effective magnetized cooling, one needs to choose magnetic field values at a level which makes the ratio $\rho_{max}/r_L >> 1$ (To ensure at least some safety margin, the minimum of this ration should be restricted to at least 2). Maximum impact parameter is typically given by a dynamic Debye shielding $\rho_D=V_i/\omega_p$, where V_i is relative thermal velocity of an ion. However, it should be always compared with the time of flight through the cooling section. Presently, there are several approaches for cooling at RHIC with different parameters of electron beam. For the baseline parameters where electron beam is stretched the maximum impact parameter is given by the flight time: $\rho_f=V_i \cdot \tau$.

For RHIC e-cooler parameters, the cooling logarithm is a small number. As a result, the ratio of ρ_{max}/r_L under logarithm can significantly change the value of the cooling logarithm Lp itself and the cooling rate subsequently. Presently, parameters of the cooler are designed to have a value of Lp=2 which also ensures effective magnetized cooling.

In its present design the cooling solenoid is split into two halves 13 meters each, for technical reasons. If the direction of magnetic field in each half goes into opposite directions (which compensates introduced coupling), each part of the solenoid acts as independent for the cooling process with ρ_f now determined by the flight through only 13 meters. On the other hand, if the field in each solenoid goes in the same direction then one may expect that two part of solenoid will acts effectively as one piece of 26 meters length. This assumption will be studied with the Vorpal code, an in principle should include realistic imperfections, alignments of solenoid halves, fringe fields, etc.

From the practical point of view, and to stay on the safe side, it is reasonable to make a design based on the assumption that solenoids halves will act independently (but have in mind that there is possibility to have a bigger effective length provided that the field in each half does not go in the opposite direction).

Figures III.A.4.3 and III.A.4.4 show required magnetic field and emittance of electron beam to achieve cooling logarithm Lp=2 for the case with effective solenoid length of 26 and 13 meters, respectively.

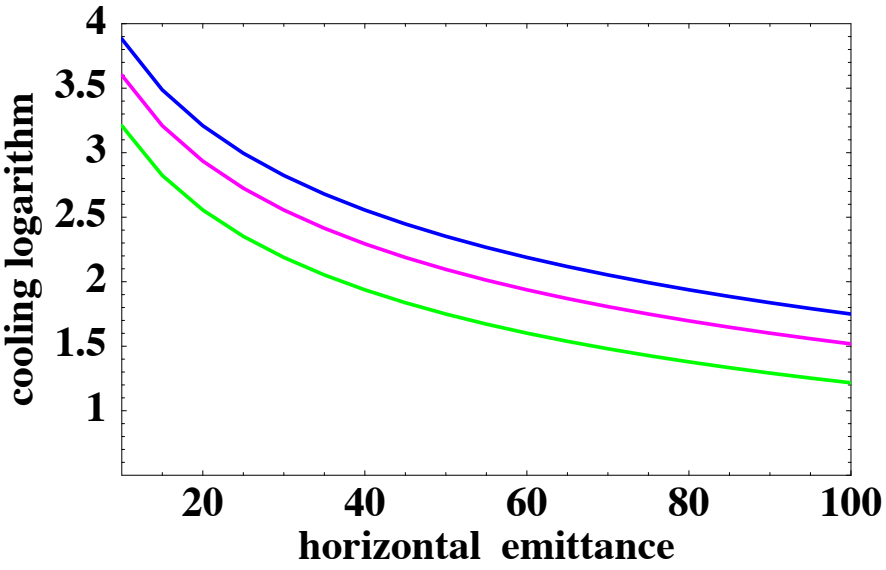

Fig. III.A.4.3. Effective length of solenoid is 26 meters. Different strength of magnetic field: 1) Green: 2T, 2) Pink: 3T, 3) Blue: 4T.

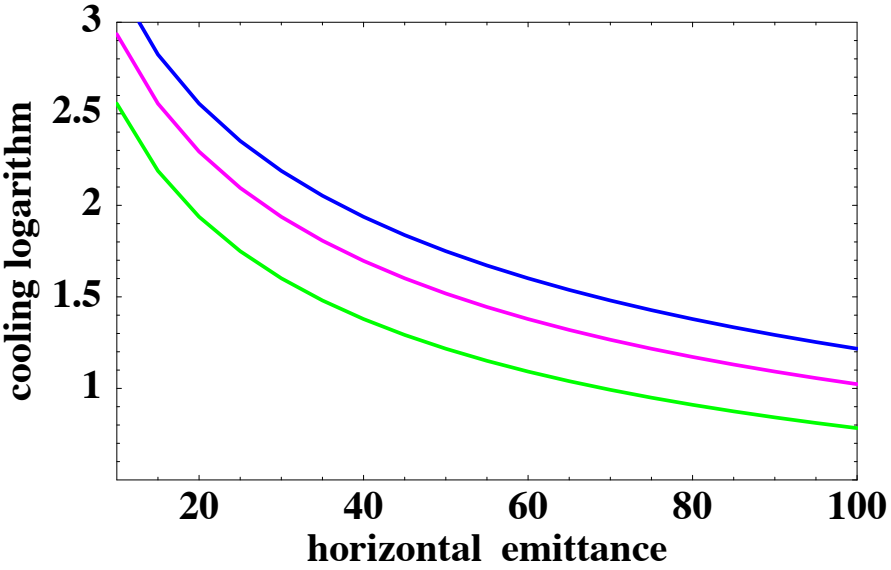

Fig. III.A.4.4 Effective length of solenoid is 13 meters. Different strength of magnetic field: 1) Green: 2T, 2) Pink: 3T, 3) Blue: 4T.

For an rms normalized emittance of electron beam around ε_x= 40-50 [π mm mrad] one needs to have B=4T to approach Lp values of 2, with an effective cooling length of 13 meters. For the effective solenoid length (two halves) of 26 meters, the magnetic field strength of B=3T becomes sufficient.

To ensure some margin (accuracy of computer models, etc.) and to provide desired luminosity increase this argues for magnetic field values in the cooling solenoid in the range of 4-5 T. Presently, two solenoids with the length 13 meters and magnetic field 5 T are being designed.

III.A.4.5 Requirements on transverse emittance of electron beam

To have sufficient magnetized cooling logarithm:

Transverse temperatures of bunched electron beam are several orders of magnitude higher than similar parameters of a DC electron beam in present low-energy coolers. To have an effective cooling with such a "hot" beam one needs to rely on magnetized cooling where transverse temperature is effectively suppressed by a strong magnetic field. As discussed in previous section, for a magnetic field of 4-5 T, the requirements on electron beam transverse emittance are around 40 [π mm mrad]. To upset the IBS and to obtain required increase in integrated luminosity at the RHIC complex, the charge of an electron beam is presently chosen at 20nC.

To avoid significant losses from recombination:

One of the impacts of electron beam on ion beam is ion losses through electron-ion recombination in the cooling section. If recombination lifetime is too short it can significantly affect achievable Luminosity under cooling. In fact, it would be desirable to limit recombination losses to a minimum. As described in Section III.A.8.1, efficiency of ion capture is inversely proportional to the transverse velocity of the electrons, which sets requirement on the low limit of transverse temperature of electrons.

Below, Figs. III.A.4.5- III.A.4.6 show loss of ions due to recombination for different temperatures of electron beam, which gives guidelines for electron beam emittance as well.

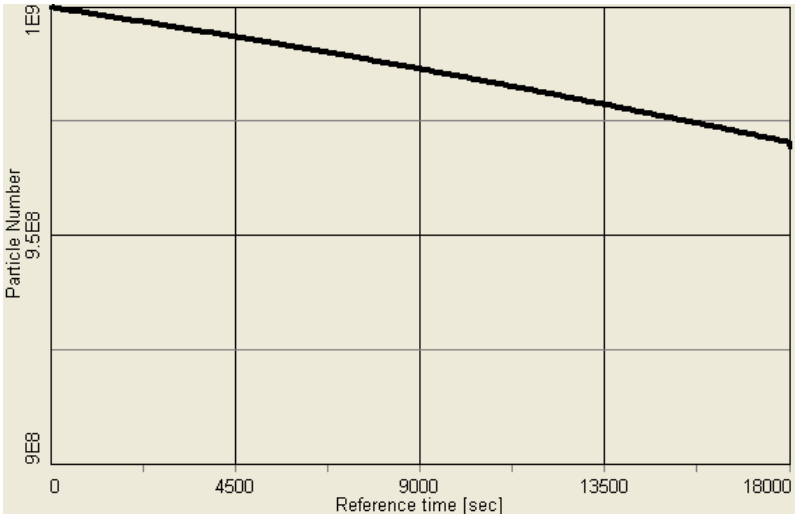

Fig. III.A.4.5 Number of ions lost due to recombination in 5 hours (Te=800eV)

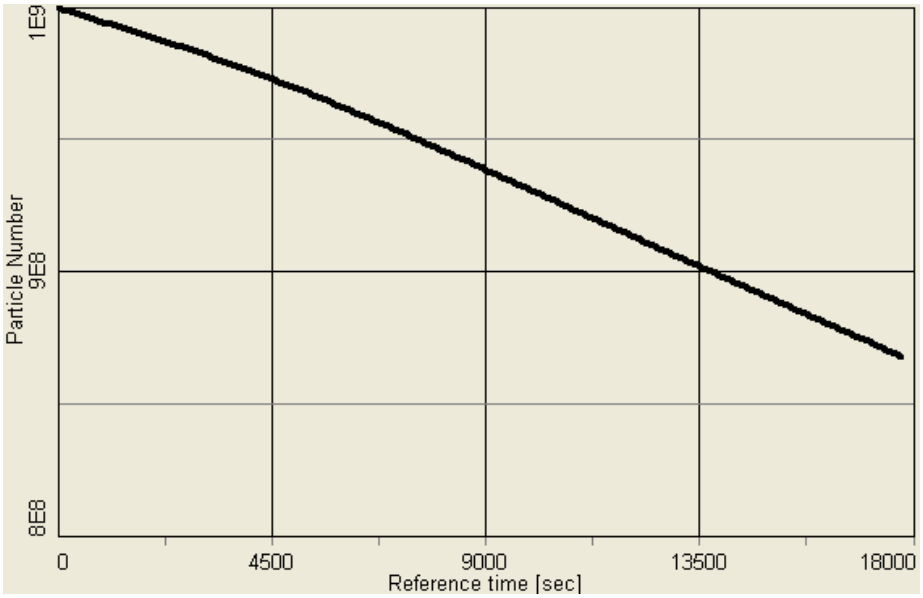

Fig. III.A.4.6 Number of ions lost due to recombination in 5 hours (Te=100eV). With $\varepsilon x < 15\ \pi$ (for other parameters of electron beam as before) one gets more than 10% loss of particle due to recombination.

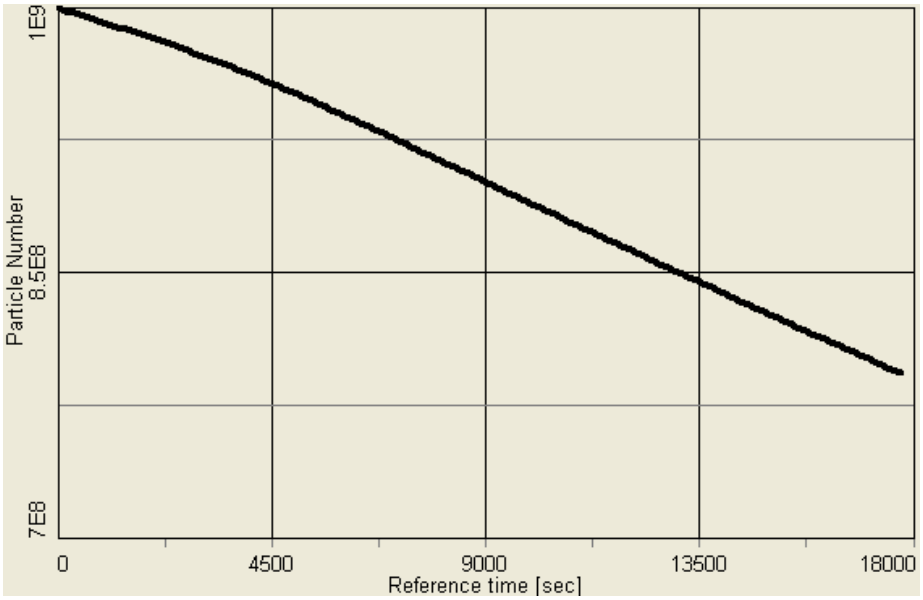

Fig. III.A.4.7 Number of ions lost due to recombination in 5 hours (Te=50eV). With εx = 5 π (for other parameters of electron beam as before) one gets 20% percent loss of particle due to recombination which clearly unacceptable.

Figure III.A.4.7 shows that with Te=50eV (which corresponds for ε_x = 5 π μm with transverse rms size of electron beam σ_e=1mm, or ε_x=2.5 π with σ_e=0.5mm, for example) loss due to recombination becomes comparable with the loss due ion-ion disintegration. Such low transverse temperatures of ion beam should be avoided. Electron beam emittance and beam size should correspond to transverse temperatures > 100 eV. As a result, on one side transverse emittance should me minimized to improve magnetized cooling while one the other hand it should be too small to avoid addition ion losses from recombination.

One should note, that exact value of transverse emittance is not very critical (logarithmic dependence), provided that one has sufficient magnetized cooling with a cooling logarithm not close to a unity (as discussed in Section III.A.4.4). For present parameter of e-cooler, one then gets that rms emittance ε_x should be in the range 10-50 π μm.

III.A.4.6 Requirements on longitudinal momentum spread of electron beam

For magnetized cooling, the maximum of the cooling is determined by the longitudinal temperature of electron beam. In the case of RF acceleration such temperature is determined by the energy spread in electron beam. For RHIC case, it is also significantly larger than in typical low-energy coolers. After the linac the electron beam is stretched to reduce rms momentum spread δ_e to $1*10^{-4}$
level, which corresponds to $T_{e,long}$=5meV or $V_{Te,long}=3*10^4$ m/sec.

However, due to the fact that there are random error in solenoid magnetic field lines they introduce "effective temperature" of Larmor circles or "effective" velocity of electrons $V_{eff.}$ The present requirement on solenoid error $\Delta\theta_s=0.8*10^{-5}$ corresponds to $V_{eff}=2.4*10^5$ m/sec. As a result, the effective longitudinal temperature is presently limited by solenoid imperfections. In fact, with such solenoid errors larger momentum spread up to $\delta_e=5*10^{-4}$ can be also tolerated.

III.A.4.7 Tolerance on magnetic field errors

Requirements on the straightness of magnetic field lines in cooling solenoid becomes more strict with energy increase and is given by angular divergence of the ion beam

$$\Delta\theta_i = \sqrt{\frac{\varepsilon_{in}}{\gamma\beta_i}}, \qquad \text{(III.A.4.6)}$$

which gives, for the normalized rms emittance of $\varepsilon_{in}=2.5\ \pi$ mm mrad and beta-function in the cooling section βi=60 m, ion angular spread $\Delta\theta_i=1.6*10^{-5}$. Required straightness of magnetic lines should be better than the ion angular spread. Taking into account that ε_{in} is further reduced during cooling process, requirement on $\Delta\theta_s$ (defined as the ratio of transverse magnetic field component to the longitudinal one) is presently set at $\Delta\theta_s=0.8*10^{-5}$.

In addition to random errors in magnetic lines straightness, one should pay very careful attention to the systematic component of magnetic field line with a strict requirement on systematic component as well, which requires long correction coils.

Simulations of the cooling process in the presence of random and systematic errors are discussed in Section III.A.4.8.

III.A.4.8 Cooling dynamics under various effects

The performance of RHIC can be simulated taking into account various effects, for example: IBS, electron cooling, beam dissociation at IP and ion beam recombination in the cooling section.

In the following sections, simulations are performed for the parameters corresponding to the RHIC-II upgrade (see Section II). Also, since electron cooling can prevent increase of rms emittances due to the IBS, this allows operation with lower beta* from the beginning which results in higher integrated luminosity. Simulations with both beta*=1 meter (which is RHIC set-up without electron cooling) and beta*=0.5 meters are presented below.

III.A.4.7.1 RHIC performance without cooling

Without cooling:

a) There is an emittance increase of about factor of 2 during the store time of 5 hours which results in a significant luminosity loss. This is shown in Fig. III.A.4.5-III.A.4.8 (simulation) and Fig. III.A.4.9 (Run-2004 experimental data).

b) There is a significant growth of bunch length which leads to particle loss from the bucket. In addition, with such a long bunch length only central portion of longitudinal beam distribution can effectively contribute to counts in the detector which result results in an addition loss of effective luminosity up to a factor of 2.

With cooling:

Electron cooling can take care of both unwanted effects described above. It counteracts IBS and prevents transverse emittance from growing (or even decrease emittance to a required level, as in eRHIC design [eZDR]). It also prevents rms bunch length from growing thus significantly increasing effective luminosity at the detector.

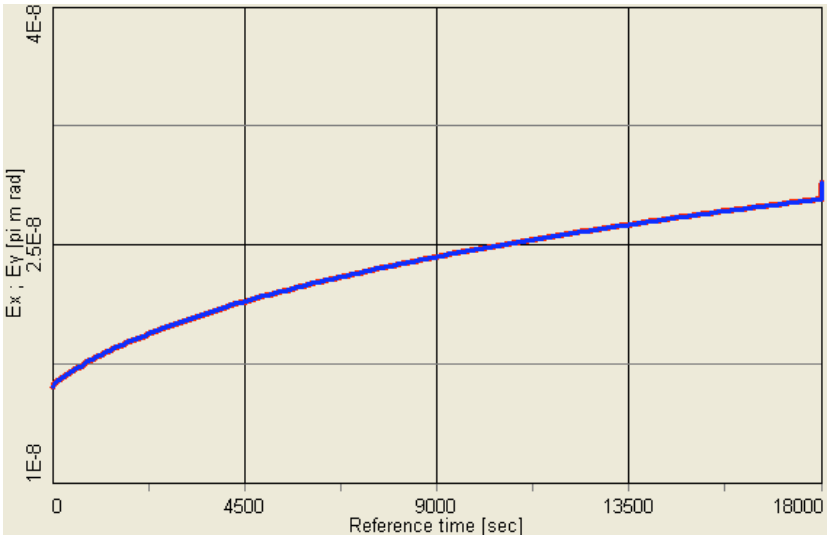

Fig. III.A.4.5 Time evolution of unnormalized rms emittance without cooling for RHIC-II (initial 95% normalized emittance ε_x=10 [π mm mrad]).

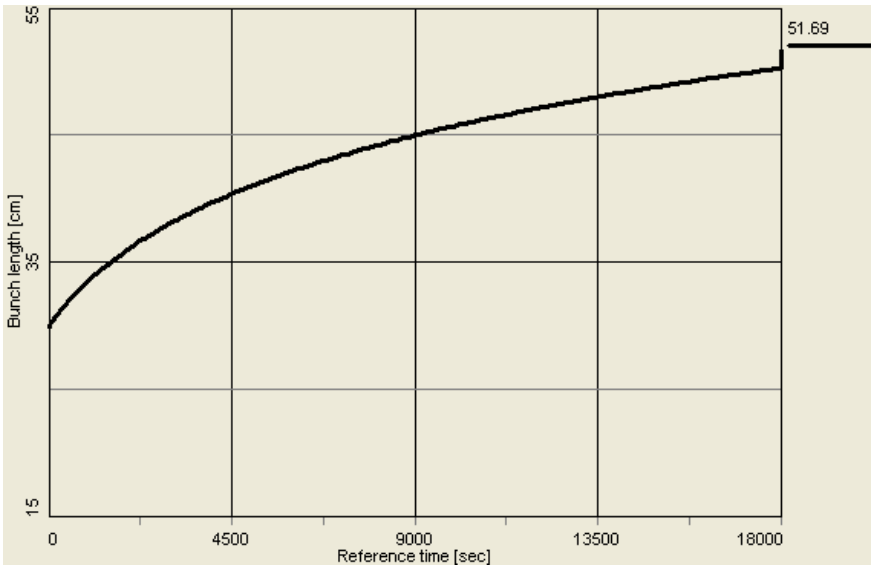

Fig. III.A.4.6 Example of expected bunch length increase without cooling for RHIC-II, ε_x=10 π mm mrad (5 hours).

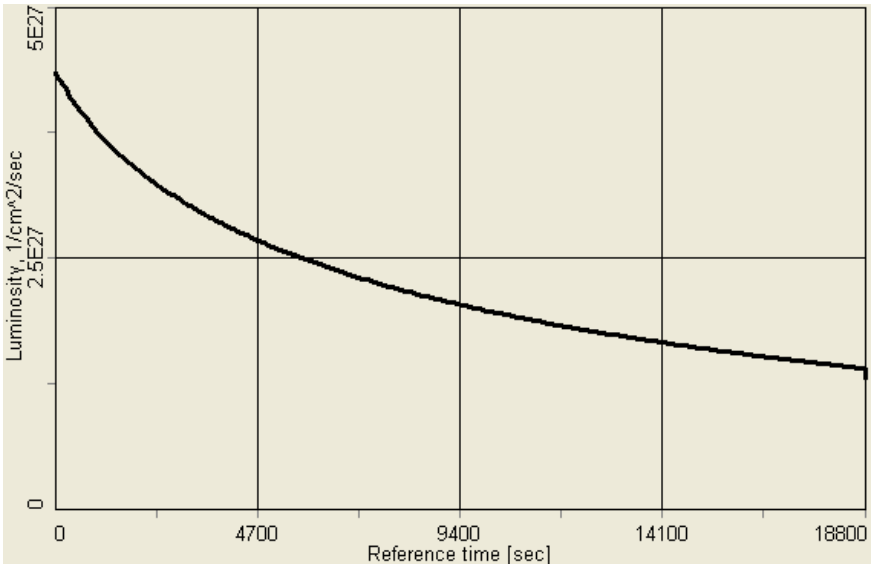

Fig. III.A.4.7 Example of expected luminosity decrease without cooling for RHIC-II, ε_x=10 π mm mrad, 112 bunches (5 hours).

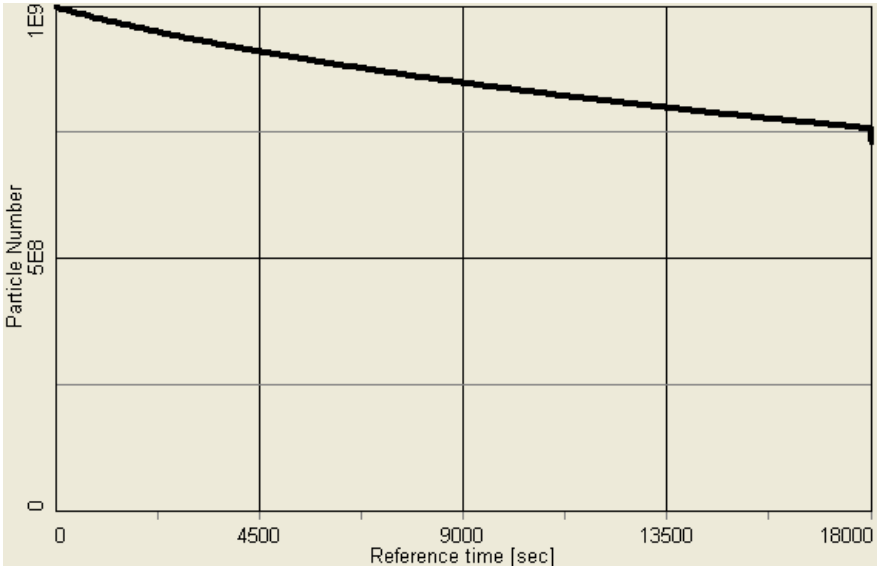

Fig. III.A.4.8 Number of lost particles without cooling for RHIC-II (5 hours)

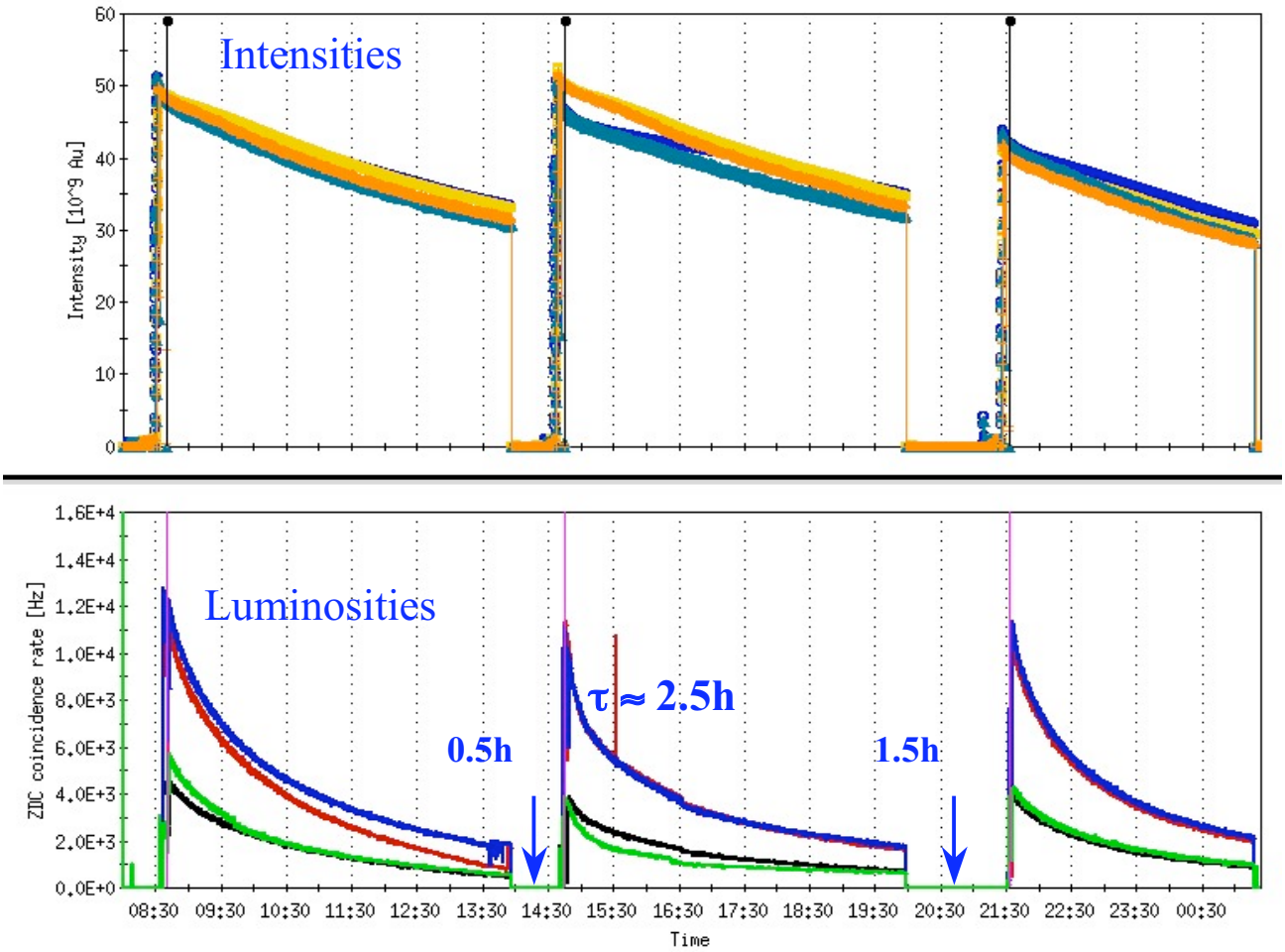

Fig. III.A.4.9 Run-2004 experiment (40 bunches).

III.A.4.7.2 Cooling with present β*=1 meter at IP

As a result of cooling, one obtains fast increase in luminosity with a subsequent decay due to losses of ions from ion disintegration by ion-ion collisions.

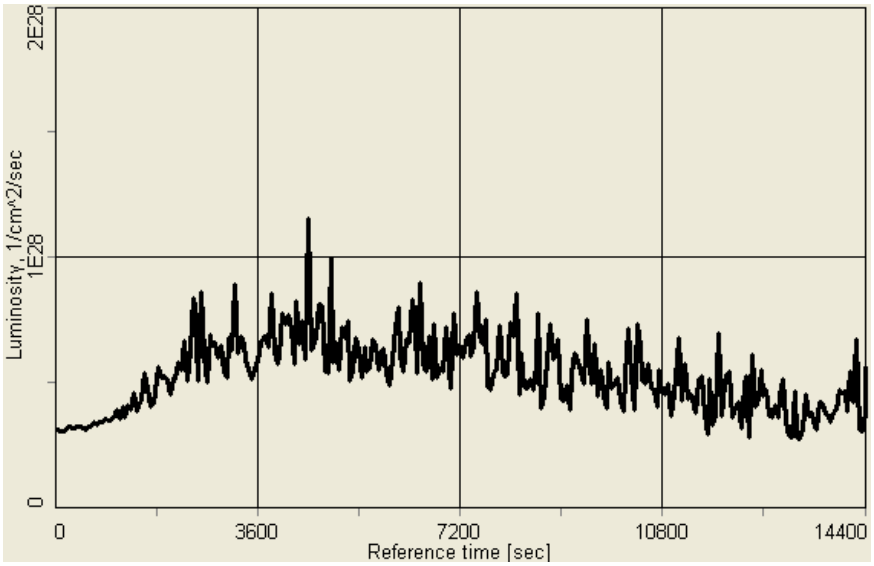

Fig. III.A.4.13 Luminosity: number of bunches N_b=112, number of ions per bunch Ni=1*10^9, beta*=1m; electron beam: Ne=1.2*10^{11}, σ_e=1mm, ε_x=40 π [mm mrad].

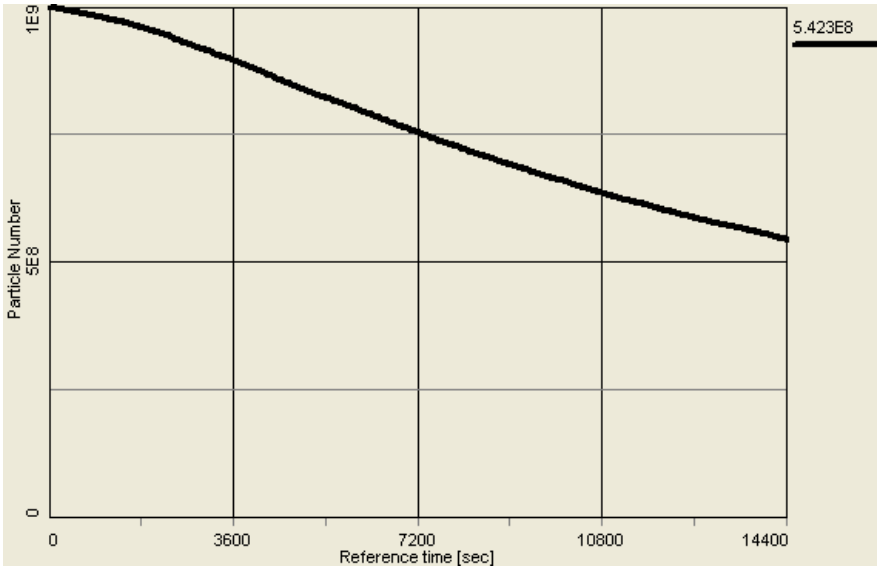

Fig. III.A.4.14 Beam loss due to burnoff: 46% of beam is burned in 4 hours <L>=5*10^{27}

When cooling of the core is too strong and one gets significant increase of the luminosity it may come not for free. An important parameter to watch in such a case is the beam-beam parameter. Limitation due to beam-beam parameter are discussed in detail in Section III.A.7.

III.A.4.7.3 Cooling with β*=0.5 meter

If cooling is sufficiently strong, one can reduce rms beam parameters to a required level as is planned for the electron-ion collider eRHIC at BNL [eZDR]. However, when cooling only keeps rms parameters from growing this can give an additional boost in luminosity increase just by starting with smaller beta* at the interaction region. In present RHIC operation without cooling, the beta* is limited to about 1 meter (or slightly less) due to the fact that emittance is increased by a factor of 2 because of the IBS. Further reduction of the beta* with such an increase of emittance would lead to a significant angular spread and beam loss. On the other hand, keeping rms emittance constant (with cooling), allows to start with smaller beta* (for example by a factor of 2) and thus have significantly larger luminosity from the start.

In this section, such a scenario for RHIC upgrade with the beta*=0.5 is explored.

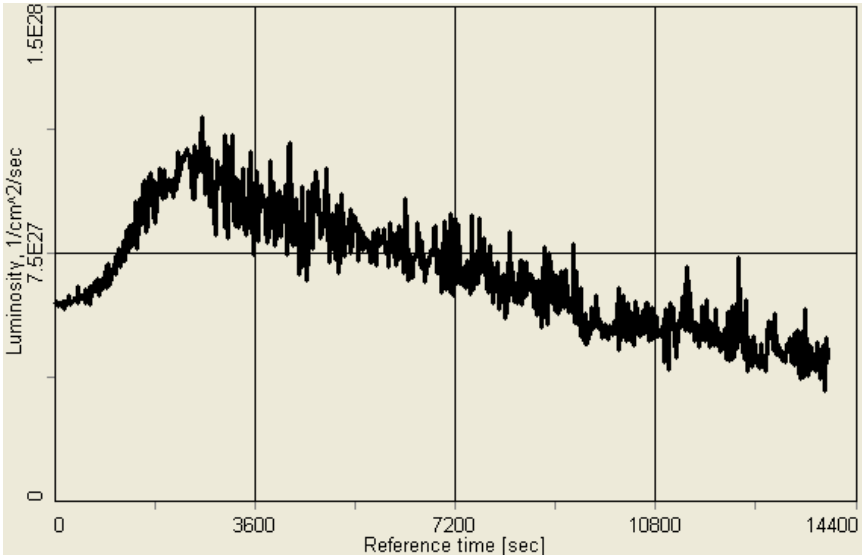

Fig. III.A.4.15 Luminosity for beta*=0.5m.

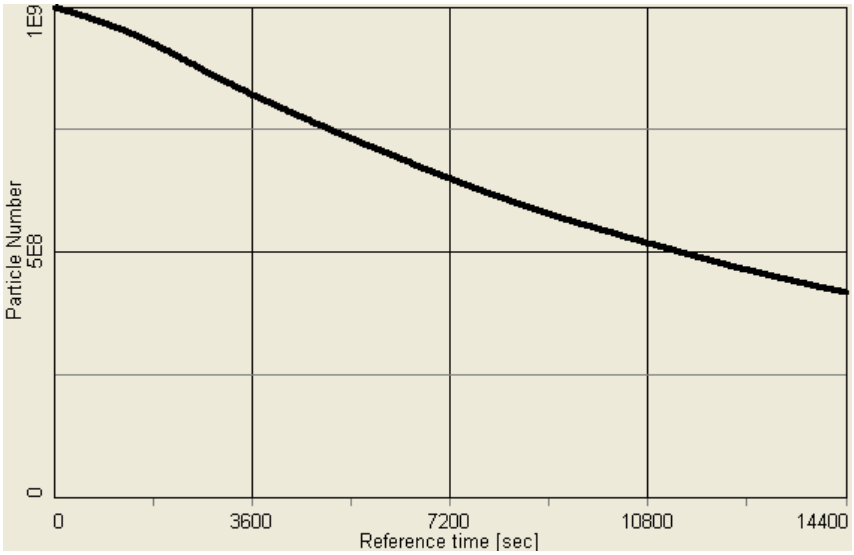

Fig. III.A.4.16 Number of particles for beta*=0.5m (60 % of beam is burned in 4 hours, $<L>=7*10^{27}$).

Note that in the case with beta*=0.5 meters, the beam-beam parameters still exceeds the beam-beam limit of ξ=0.005-0.007 per IP, as shown in Fig. III.A.4.17.

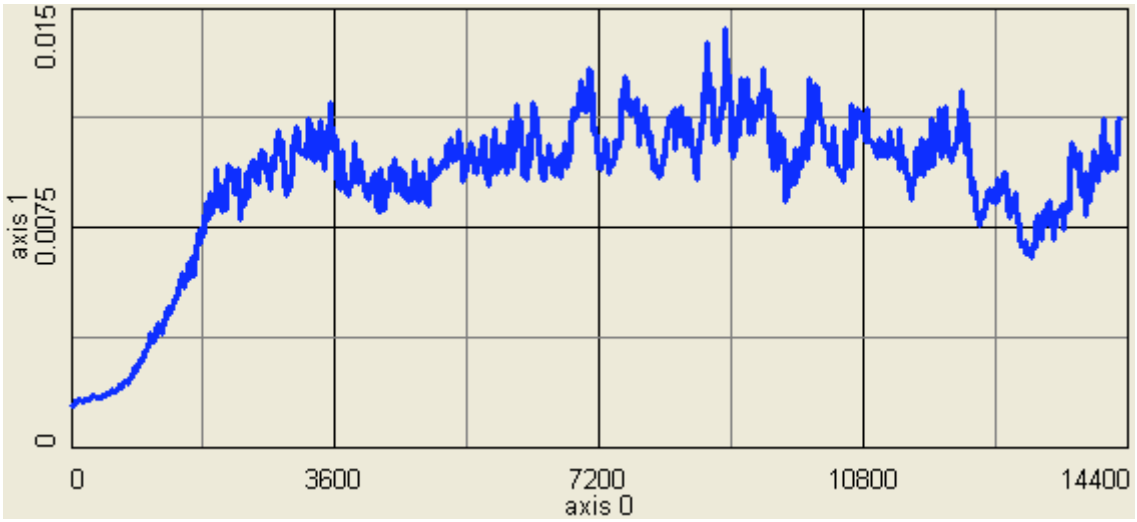

Fig. III.A.4.17 Beam-beam parameter , beta*=0.5m.

What are the allowed values for the beam-beam parameter in the presence of electron cooling will require self-consistent simulation for the ion beams as discussed in Section III.A.7. However, when large values of beam-beam parameter become a problem, it seems feasible to control beam-beam parameter with the electron beam distribution (see Section III.A.7).

III.A.4.7.4 Effect of random errors in solenoid based on effective velocity

Random misalignment of solenoid field lines in cooling solenoid can be regarded as an effective temperature of Larmor circulars. To account for such imperfections, an effective velocity Veff can be introduced in the expression of the cooling force. As a result, the maximum of the cooling force does not happen at the longitudinal velocity of electron beam given by the energy spread but instead at "effective" velocity Veff (provided that Veff is higher than the longitudinal rms velocities of electron beam). The values of solenoid imperfections is thus determine cooling of the core of beam distribution.

Below, an impact of solenoid errors on cooling of the beam core is presented based on Veff in the empiric formula for the friction force. This is later compared with the random errors directly introduced in the solenoid magnetic field in the BetaCool code.

β*=1 meter:

1) $\Delta\theta_s=1.6*10^{-5}$ (T_{eff}=1.5 eV)

Figure III.A.4.18 shows that an error of magnetic field (twice bigger than design value of $\Delta\theta_s=0.8*10^{-5}$) lines effectively slows down cooling of a beam core, so that luminosity approximately stays at the initial level. As a result, an average luminosity is significantly reduced from <L>=$5*10^{27}$ to only <L>=$3.5*10^{27}$ for the same parameters of electron cooler.

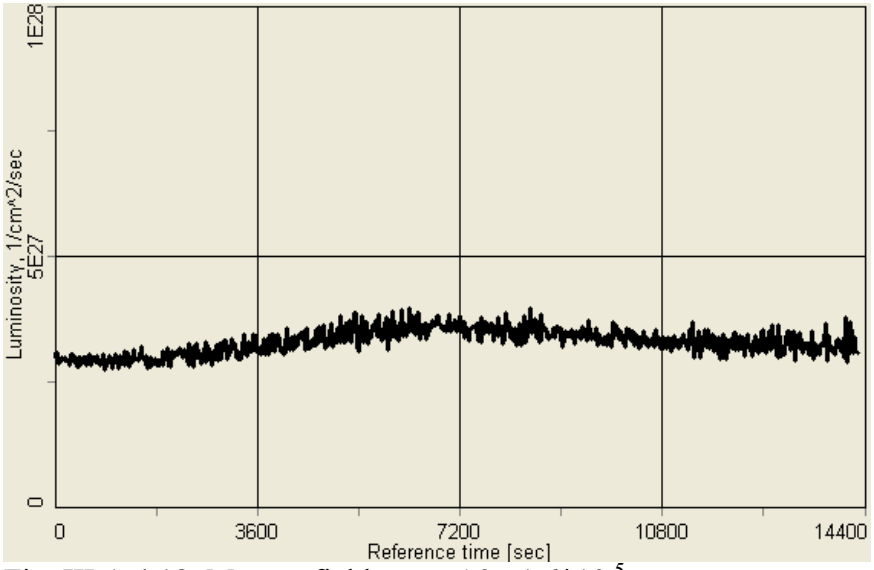

Fig. III.A.4.18 Magnet field error $\Delta\theta_s=1.6*10^{-5}$.

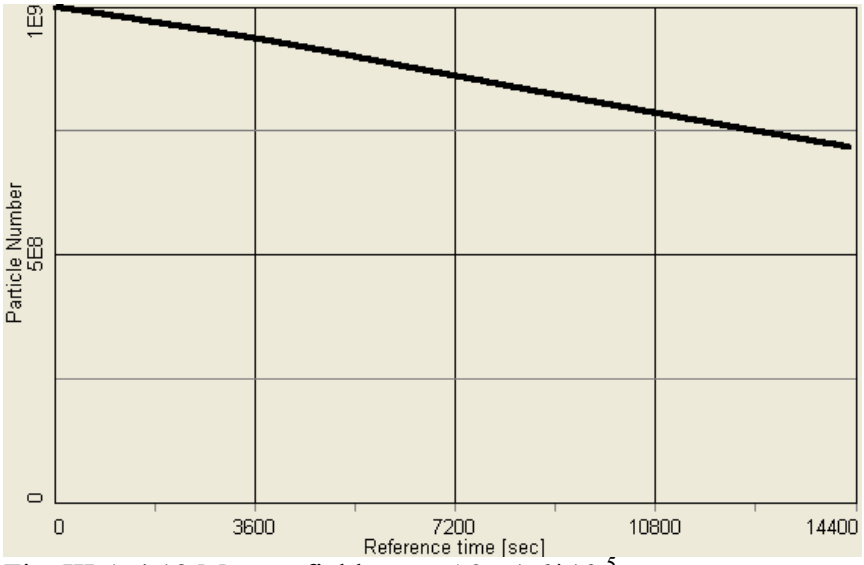

Fig. III.A.4.19 Magnet field error $\Delta\theta_s=1.6*10^{-5}$

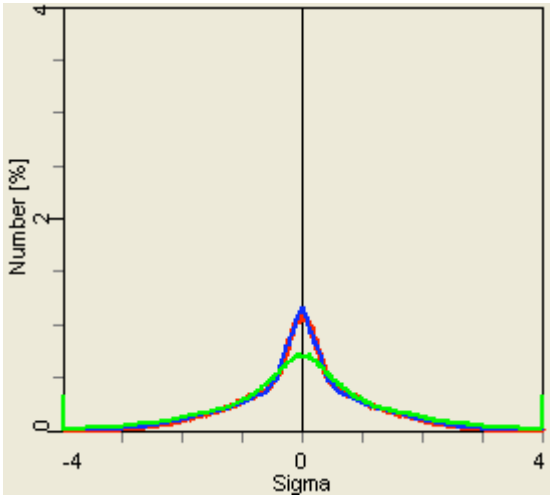

Fig. III.A.4.20 Beam profile after 4 hours: magnet field error $\Delta\theta_s=1.6*10^{-5}$

β*=0.5 meters:

1) Solenoid imperfection $\Delta\theta_s=1.6*10^{-5}$ (T_{eff}=1.5 eV)

Figures III.A.4.22-23 shows that for the beta*=0.5 m cooling of the core with the solenoid imperfections at such a level is not sufficient. In this case, only 43% of the beam is burned by ion-ion collisions during 4 hours which corresponds to $<L>=5*10^{27}$.

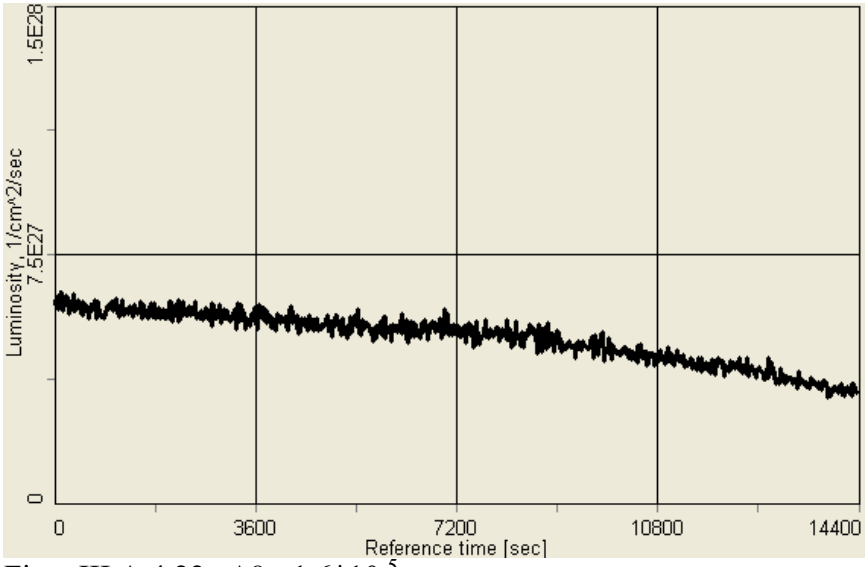

Fig. III.A.4.22 $\Delta\theta_s=1.6*10^{-5}$

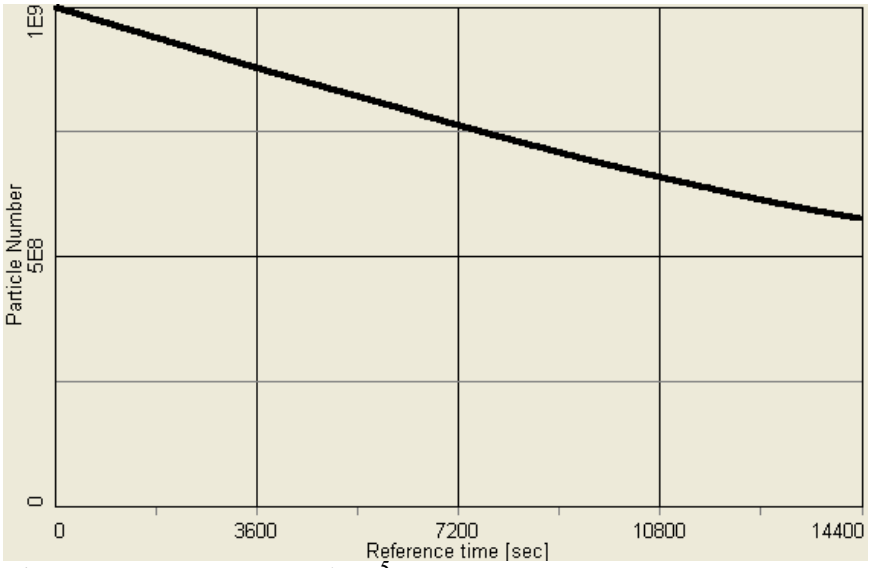

Fig. III.A.4.23 $\Delta\theta_s=1.6*10^{-5}$

2) $\Delta\theta_s=1.3*10^{-5}$ (T_{eff}=1.0 eV)

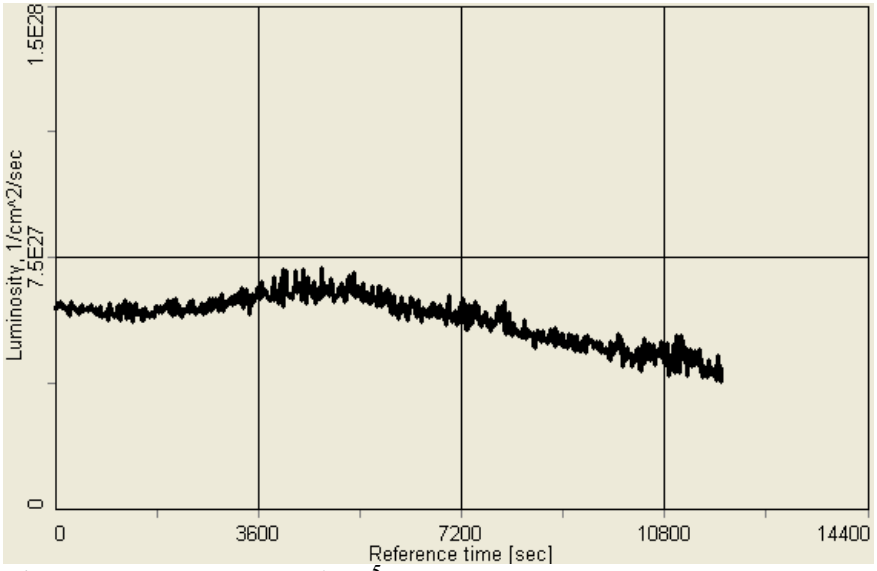

Fig. III.A.4.24 $\Delta\theta_s=1.3*10^{-5}$

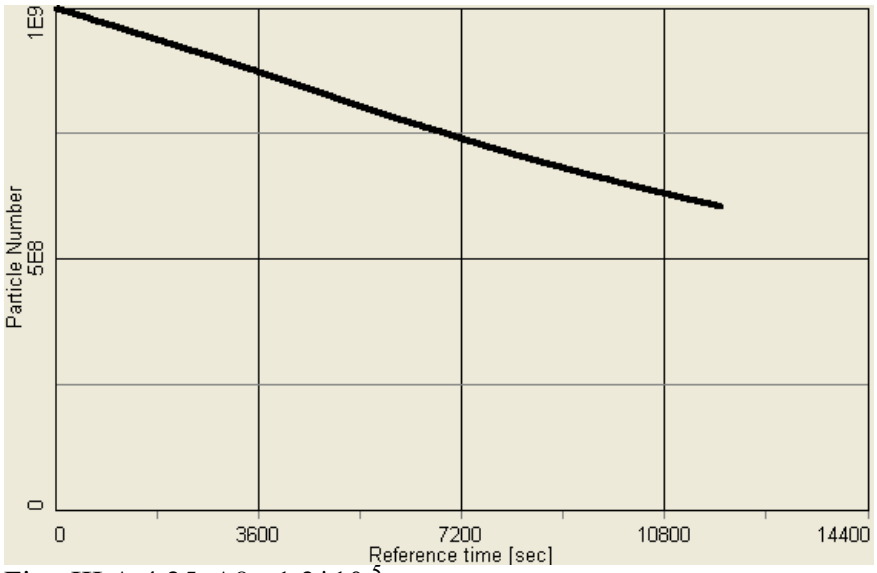

Fig. III.A.4.25 $\Delta\theta_s=1.3*10^{-5}$

3) $\Delta\theta_s=1.0*10^{-5}$ (T_{eff}=0.6 eV)

Even with the solenoid error of $\Delta\theta_s=1.0*10^{-5}$, which is slightly higher than design requirement ($\Delta\theta_s=0.8*10^{-5}$), cooling of the beam core is slowed down which results in lower average luminosity, as shown in Fig. III.A.4.26. In this case, <L> in 4 hours is $6.2*10^{27}$.

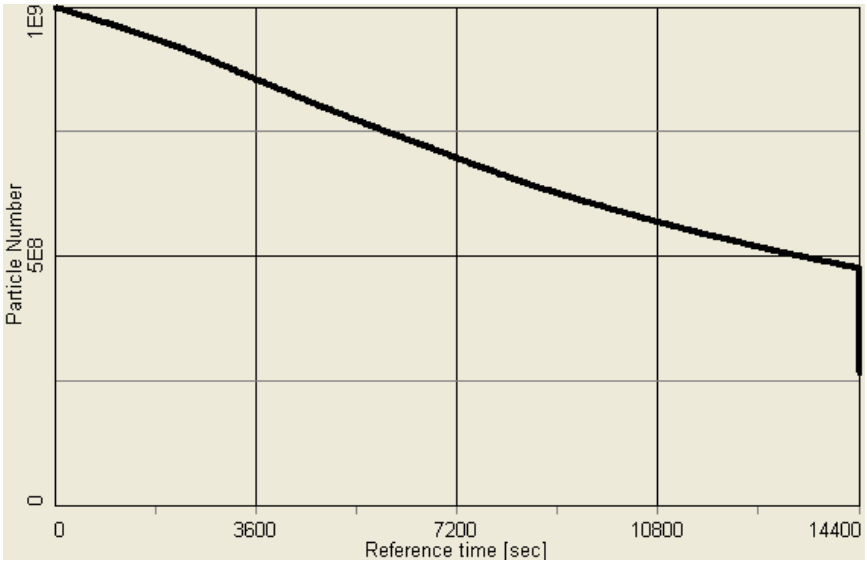

Fig. III.A.4.26 $\Delta\theta_s=1.0*10^{-5}$

3) $\Delta\theta_s=0.4*10^{-5}$ (T_{eff}=0.095 eV)

Improving solenoid errors, for example by a factor of 2, speeds up cooling of the core particles, but an overall gain in the luminosity over 4 hours period is not significant. For the example which is discussed above, with the solenoid imperfections of $\Delta\theta_s=0.4*10^{-5}$, one gets an average luminosity of $<L>=7.2*10^{27}$ compared to $6.7*10^{27}$ for the baseline design error of $\Delta\theta_s=0.8*10^{-5}$, as shown in Fig. III.A.4.27 for the ion loss due to the burnoff process.

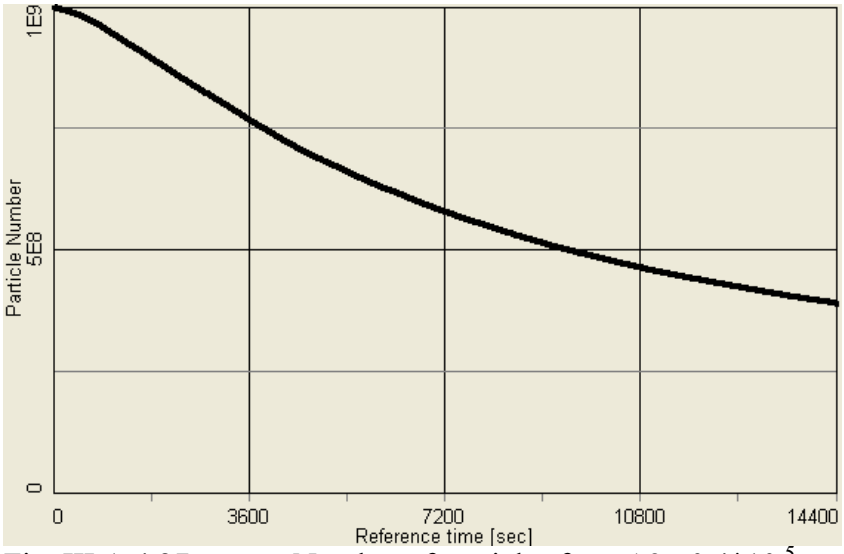

Fig. III.A.4.27 Number of particles for $\Delta\theta_s=0.4*10^{-5}$

4) $\Delta\theta_s=0.4*10^{-5}$ (T_{eff}=0.095 eV), 15 nC

Since further increase in solenoid accuracy does not significantly impact average luminosity this does not allow to reduce charge of electron beam substantially. For example when solenoid imperfections at reduced by a factor of 2 (compared to the baseline), decrease of electron charge to 15 nC already does not allow to recover desired level of an average luminosity.

III.A.4.7.5 Effect of systematic errors in solenoid

Effect of systematic errors in solenoid may be even more pronounced. A detailed compensation of such errors is required. For example, a systematic error of $1.0*10^{-5}$ just in a single plane significantly effects beam distribution and does not allow to reach required luminosity increase. Figure III.A.4.28-III.A.4.29 shows for example beam profile after 2 hours of cooling and corresponding luminosity for the case with beta*=0.5 meters (compare with ideal case without error in Fig. III.A.4.15).

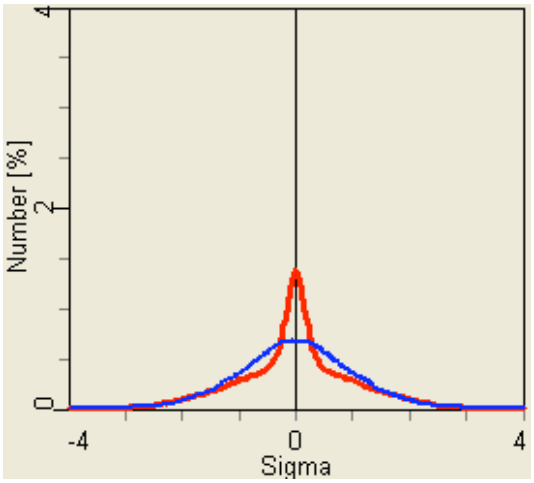

Fig. III.A.4.28 Beam profiles after 2 hours, systematic error $1*10^{-5}$.

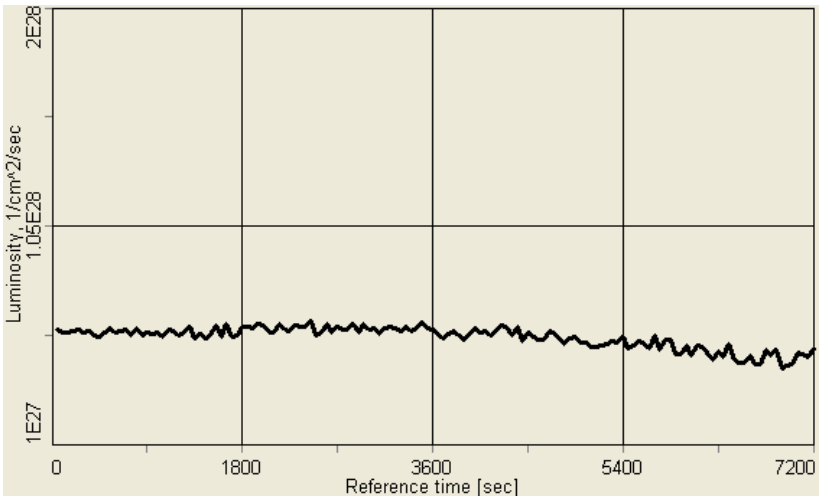

Fig. III.A.4.29 Luminosity for beta*=0.5 with systematic error $1.0*10^{-5}$.

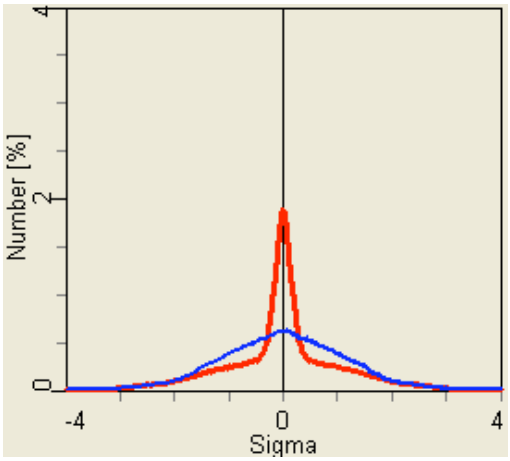

Fig. III.A.4.30 Beam profiles after 3 hours, systematic error $5*10^{-6}$

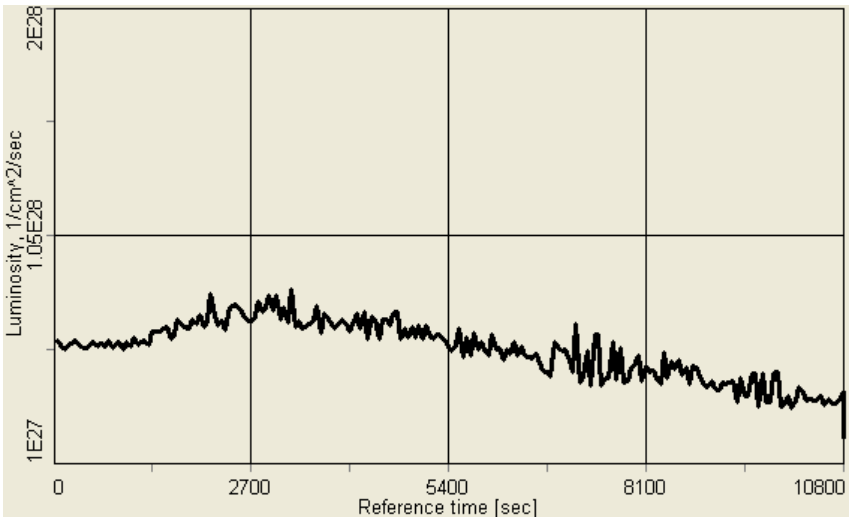

Fig. III.A.4.31 Luminosity, systematic error $5*10^{-6}$

To recover the desired luminosity such systematic errors should be kept at $1.0*10^{-6}$ level, as shown in Figs. III.A.4.32-III.A.4.33 for beam profiles and luminosity, respectively. One then recovers the luminosity increase as in the ideal case (Fig. III.A.4.15). More error studies will be done in the future.

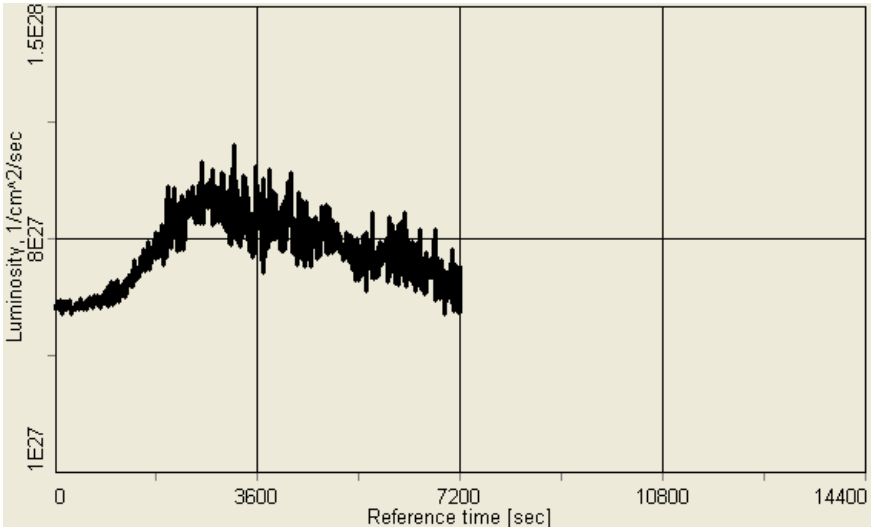

Fig. III.A.4.32 Luminosity for beta*=0.5 m with systematic error $1.0*10^{-6}$

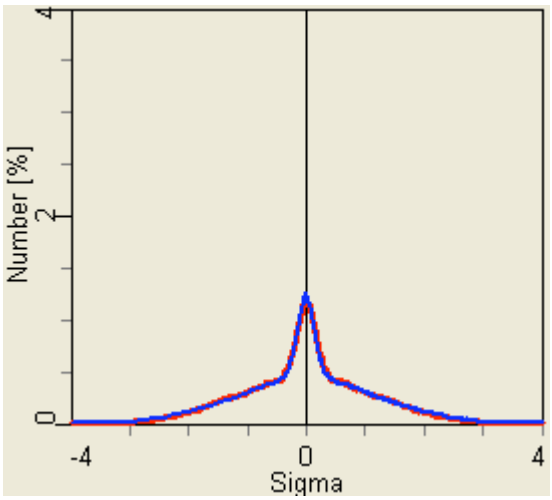

Fig. III.A.4.33 Beam profiles after 2 hours, systematic error $1.0*10^{-6}$

--- Studies with solenoid errors are very preliminary ---

III.A.5 Cooling optimization

Major parameters which affect beam cooling are:

1. Length of cooling section – directly impacts cooling speed (see expression for cooling time)
2. Cooling current – directly impacts cooling speed
3. Dependence on beta-function in the cooling solenoid – partially offset by ion beam size increase – corresponding increase of electron beam size leads to reduction of electron density
4. Alignment of electron-ion beam
5. Non-homogeneity of magnetic field lines in cooling solenoid

In addition, cooling can be significantly altered with optimization of electron beam parameters. For example, changing radius of electron beam affects cooling of beam core. As a result, smooth increase of electron beam radius after maximum instantaneous luminosity is reached allows to sustain high luminosity for some extra time which results in larger average luminosity than without cooling optimization.

Both effective cooling and control of ion beam distribution (to prevent overcooling of beam core) requires full control of an electron beam. To achieve these goals various techniques can be employed, such as modulations of electron beam velocity distribution, electron beam energy modulations, "painting" with electron beam, etc. [Benzvi1].

III.A.6 Scenarios of cooling at RHIC

There are various possibilities of using electron cooling at RHIC. Direct cooling at 100 GeV can be considered as a base line approach for RHIC-II approach. However, for eRHIC for example, it is important that cooling is fast enough and sufficient to have rms beam parameters cooled as well, especially the rms bunch length. In such a case, pre-cooling at low energy becomes very attractive due to a very strong dependence of the cooling time on energy. For the same reason, cooling is very effective for scenarios with collisions at low energy.

III.A.6.1 Cooling at full energy

Direct cooling of Au ions at storage energy of 100 GeV requires allows to reach desired increase in the integrated luminosity for the RHIC upgrade (see section III.A.4.7). However, it requires using very high charges of electron beam. For the present parameters of electron beam cooling is below the critical number which prevents cooling of the whole ion beam distribution and results in a distribution with very dense beam core (see section III.A.3). Stability of such "bi-Gaussian" distribution becomes of concern and requires careful study.

III.A.6.2 Pre-cooling at low energy

Although some time is lost from effective luminosity integral, pre-cooling at low energy becomes very attractive. This is due to the fact that cooling is much faster at lower energy as well as that required charge of electron beam to cool at low energy is much smaller as discussed in section III.A.3.3. In addition, pre-cooling at low energy provides also reduction of rms transverse beam emittances and bunch length, which is critical for the eRHIC upgrade of RHIC complex [eRHIC]. Also, pre-cooling at low energy allows to employ cooling not just for Au ions but also for protons. In the present report, we explored pre-cooling above the transition energy to avoid instabilities of cooled beam near transition (Section III.A.3.3).

III.A.6.3 Cooling at various collision energies

It was shown (see Section III.A.3.3) that one can pre-cool beam at a low energy, in fact using significantly low charge of electron beam. Such a fast cooling also opens a possibility of collisions at low energy, which is also under consideration for RHIC-II and eRHIC.

However, faster cooling of beam core immediately brings beam-beam problems when beamsare put into collisions. What is the tolerable beam-beam parameter at low energy is not clearsince relatively slow beam-beam diffusion may be now compensated by a fast more affectively than at high-energy. This requires accurate computer simulations of cooling together with beam-beam diffusions which is planed in the future.

Here, simulations were done without beam-beam diffusions, taking into account only IBS, electron cooling and collisions at 3 IP. For 30 GeV Au ions used in simulation the IP beta* was taken to be 5 meters. Assuming that the beam-beam parameter should still stay in the range of 0.007 per IP, one needs a full control of electron beam to keep luminosity at a constant level and prevent the beam-beam parameter from exceeding the limit. Such control may be very challenging in a real cooler since it requires that the quality of electron beam stays at satisfactory level while beam radius or charge in the electron bucnh is varied. Figures III.A.6.1 – III.A.6.2 show example of such control with an electron beam. Radius of electron beam and charge were dynamically changed to keep beam-beam parameter at constant level shown in Fig. III.A.6.2. Resulting luminosity is shown in Fig. III.A.6.1.

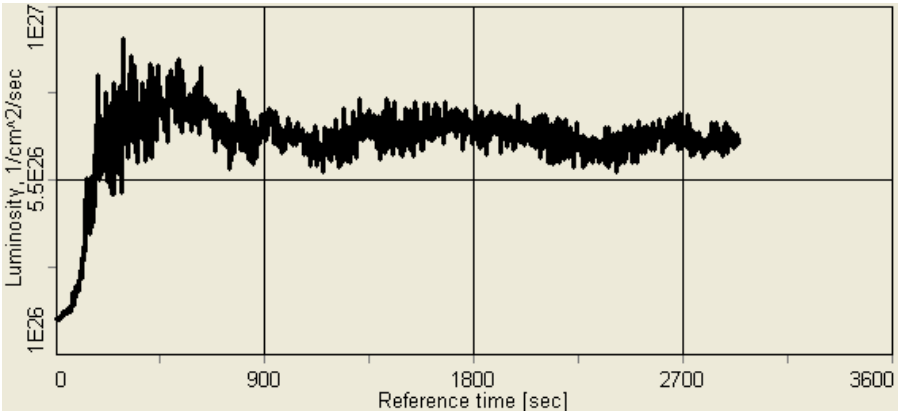

Fig. III.A.6.1 Luminosity for collisions at 30GeV with electron beam control.

III.A.7 Luminosity limitations under cooling

III.A.7.1 Incoherent beam-beam effects

The electro-magnetic force field of a moving bunch produces a force which acts on individual particles in another bunch moving in the opposite direction. Such a force acting on individual particles is referred to as incoherent beam-beam force. One can integrate this force over the collision to obtain the incoherent beam-beam kick.

Beam-beam kick for head-on collision

One typically starts consideration of beam-beam effects with calculation of an increment of transverse particle momentum change after crossing the encounter bunch, considering "strong-weak" approximation of beam-beam interaction [Katayama1]. In this model it is assumed that particles of the weak-beam (index 2) are influenced by a strong electromagnetic field of the opposite bunch (index 1), while the strong bunch does not feel any field of the weak bunch. Assume that opposite bunch with N_1 particles has the Gaussian space charge density distribution with r.m.s. bunch size σ_x, σ_z, σ_s:

$$\rho(x,z,s,v_1,t) = \frac{q_1 N_1}{(2\pi)^{3/2}\sigma_x\sigma_y\sigma_z}\exp\left(-\frac{x^2}{2\sigma_x^2}-\frac{z^2}{2\sigma_{zy}^2}-\frac{(s-v_1 t)^2}{2\sigma_{sz}^2}\right). \qquad \text{(III.A.7.1)}$$

where $V_1 = \beta\cdot c$ is the average velocity of the strong beam particles. In the reference frame moving with V_1 velocity (noted as prime coordinate system), the longitudinal position of a weak beam particle is :

$$s' = \gamma(s - v_1 t). \qquad \text{(III.A.7.2)}$$

Similarly, the strong beam density distribution is

$$\rho'(x,z,s') = \frac{N_1}{(2\pi)^{3/2}\sigma_x\sigma_z(\sigma_s\gamma)}\exp\left(-\frac{x^2}{2\sigma_x^2}-\frac{z^2}{2\sigma_z^2}-\frac{s'^2}{2\sigma_s^2\gamma^2}\right). \qquad \text{(III.A.7.3)}$$

Electrostatic potential of the Gaussian bunch is [Kellogg1, Takayama1]:

$$U'(x,z,s') = \frac{q_1 N_1}{4\pi^{3/2}\varepsilon_0}\int_0^\infty \frac{\exp\left[-\frac{x^2}{(2\sigma_x^2+w)}-\frac{z^2}{(2\sigma_z^2+w)}-\frac{s'^2}{(2\sigma_s^2\gamma^2+w)}\right]}{\sqrt{(2\sigma_x^2+w)(2\sigma_z^2+w)(2\sigma_s^2\gamma^2+w)}}dw, \qquad \text{(III.A.7.4)}$$

where q_1 is the electric charge of the "1" particle, gives us the transversal components of electrostatic field in the moving reference frame: differentiation of the potential (III.A.7.4) $E'_x = -\partial U'/\partial x$, $E'_z = -\partial U'/\partial z$:

$$E_x = -\frac{q_1 N_1 \gamma}{2\pi^{3/2}\varepsilon_0}\int_0^\infty \frac{\exp\left[-\frac{x^2}{\left(2\sigma_x^2+w\right)}-\frac{z^2}{\left(2\sigma_z^2+w\right)}-\frac{\gamma^2\left(s-v_1 t\right)^2}{\left(2\sigma_s^2\gamma^2+w\right)}\right]}{\left(2\sigma_x^2+w\right)^{3/2}\sqrt{\left(2\sigma_z^2+w\right)}\sqrt{\left(2\sigma_s^2\gamma^2+w\right)}}dw\ , \qquad \text{(III.A.7.5)}$$

with analogous expression for E_z component. Moving bunch of charged particles creates magnetic field:

$$B_x = -\beta_1 \frac{E_z}{c},\ B_z = -\beta_1 \frac{E_x}{c} \qquad \text{(III.A.7.6)}$$

The equations of the test particle transverse motion are

$$\frac{dp_x}{dt} = q_2\left[E_x - \left(-v_2 B_z\right)\right] = q_2 E_x\left(1+\beta_1\beta_2\right),$$
$$\frac{dp_z}{dt} = q_2\left[E_z - \left(-v_2 B_x\right)\right] = q_2 E_z\left(1+\beta_1\beta_2\right). \qquad \text{(III.A.7.7)}$$

To define a change of particle momentum after crossing the encounter bunch, the equations (III.A.7.7) have to be integrated along the time of interaction. Assuming that particle position and Lorentz force are not changed during test particle crossing the encounter bunch (thin lens approximation) one gets

$$\Delta p_x = q_2\left(1+\beta_1\beta_2\right)\int_{-\infty}^{\infty} E_x dt = -\frac{q_1 q_2 N_1 (1+\beta_1\beta_2)}{2\pi^{3/2}\varepsilon_0\left(v_2-v_2\right)} x\int_0^\infty \frac{\exp\left[-\frac{x^2}{\left(2\sigma_x^2+w\right)}-\frac{z^2}{\left(2\sigma_z^2+w\right)}\right]}{\left(2\sigma_x^2+w\right)^{3/2}\sqrt{\left(2\sigma_z^2+w\right)}}dw, \qquad \text{(III.A.7.8)}$$

and similar for Δp_z.

In the linear approximation, the integral in Eq. (III.A.7.8) can be evaluated analytically:

$$\int_0^\infty \frac{\exp\left[-\frac{x^2}{\left(2\sigma_x^2+w\right)}-\frac{z^2}{\left(2\sigma_z^2+w\right)}\right]}{\left(2\sigma_x^2+w\right)^{3/2}\sqrt{\left(2\sigma_z^2+w\right)}}dw \approx \int_0^\infty \frac{dw}{\left(2\sigma_x^2+w\right)^{3/2}\sqrt{\left(2\sigma_z^2+w\right)}} = \frac{1}{\sigma_x\left(\sigma_x+\sigma_z\right)}, \qquad \text{(III.A.7.9)}$$

which gives:

$$\Delta p_x = -\frac{q_1 q_2 N_1\left(1+\beta_1\beta_2\right)}{2\pi\varepsilon_0\left(\beta_2+\beta_1\right)\sigma_x\left(\sigma_x+\sigma_z\right)} x. \qquad \text{(III.A.7.10)}$$

Let us introduce the value of beta-function at the interaction point $\beta_x^*,\ \beta_z^*$. Then the change of slope of particle trajectory in linear approximation can be written as follows:

$$\Delta\frac{dx}{ds}=\frac{\Delta p_x}{p_s}=4\pi\frac{\xi_x}{\beta_x^*}x,\ \Delta\frac{dz}{ds}=\frac{\Delta p_z}{p_s}=4\pi\frac{\xi_z}{\beta_z^*}z, \qquad \text{(III.A.7.11)}$$

where $\xi_x,\ \xi_z$ are beam-beam parameters, which have a meaning of linear part of betatron tune shift due to beam-beam collision [Katayama1]:

$$\xi_x=N_1\frac{\beta_x^*}{4\pi}\frac{q_1q_2}{4\pi\varepsilon_0 m_2c^2}\frac{(1+\beta_1\beta_2)}{\gamma_2\beta_2(\beta_1+\beta_2)}\frac{2}{\sigma_x(\sigma_x+\sigma_z)}, \qquad \text{(III.A.7.12)}$$

$$\xi_z=N_1\frac{\beta_y^*}{4\pi}\frac{q_1q_2}{4\pi\varepsilon_0 m_2c^2}\frac{(1+\beta_1\beta_2)}{\gamma_2\beta_2(\beta_1+\beta_2)}\frac{2}{\sigma_z(\sigma_x+\sigma_z)}. \qquad \text{(III.A.7.13)}$$

For collisions of the particles at equal velocities ($\beta_1 = \beta_2 = \beta$), charge numbers ($q_1 = q_2 = Z$) and atomic numbers the beam-beam parameters can be simplified:

$$\xi_x=\frac{\beta^*}{4\pi}\frac{Z^2}{A}r_p\frac{N(1+\beta^2)}{\beta^2\gamma\sigma_x(\sigma_x+\sigma_z)}, \qquad \text{(III.A.7.14)}$$

$$\xi_z=\frac{\beta^*}{4\pi}\frac{Z^2}{A}r_p\frac{N(1+\beta^2)}{\beta^2\gamma\sigma_z(\sigma_x+\sigma_z)}. \qquad \text{(III.A.7.15)}$$

For the relativistic factor $\beta=1$ one has

$$\xi=\frac{\beta^*}{2\pi}\frac{Z^2}{A}r_p\frac{N}{\gamma\sigma_z(\sigma_x+\sigma_z)} \qquad \text{(III.A.7.16)}$$

Stability of linear incoherent motion

In the linear approximation, the motion of a test particle in the presence of the other beam is stable if the absolute value of the trace of the one-turn transfer matrix is less than 2.

Such stability criteria gives very large attainable linear beam-beam tune shifts, which indicates that much smaller experimentally achieved beam-beam parameters are not due to this stability mechanism.

III.A.7.2 Coherent beam-beam effects

Coherent beam-beam effects arise from the forces which an exciting bunch exerts on a whole test bunch during collision. The corresponding coherent kick is obtained by integrating incoherent beam-beam kick over the charge distribution of the test bunch. In ideal case, due to symmetry, the coherent beam-beam kick vanishes for head-on collisions.

III.A.7.2.1 Linear tune shift

The linear coherent beam-beam tune shift can be calculated and becomes just one half of the linear incoherent shift ξ :

$$\Xi = \frac{\beta^*}{4\pi}\frac{Z^2}{A} r_p \frac{N}{\gamma\sigma_x\left(\sigma_x + \sigma_z\right)} \qquad \text{(III.A.7.17)}$$

Stability of linear coherent motion

Coherent oscillation of two beam under certain condition can lead to an instability. With one bunch per beam to modes are possible, the 0-mode, where both beam oscillate in phase and π-mode where both beam oscillate out of phase. With m bunches per beam, one gets $2m$ modes of oscillation, correspondingly.

The stability of the system can be also calculated in the linear matrix theory. Although the threshold is now significantly lower then in the incoherent case it is still well above the experimentally observed beam-beam limits.

III.A.7.3 Nonlinear effects and beam-beam limit

III.A.**7.3.1** **Non-linear tune spread and resonances**

The nonlinear variation of the beam-beam force with radius in a round Gaussian beam causes a tune shift of individual particles to have dependence on particle oscillation amplitude. For the distribution of particles within the beam this results in a tune-spread in the beam. In addition the beam-beam force drives non-linear resonances.

Experimental beam-beam limit is usually attributed to excitation of non-linear resonances. Overlapping of resonances results in stochastic particles motion with corresponding particle loss. The strength of nonlinear beam-beam resonances can be related to the incoherent beam-beam parameter which allows to use its value to describe

beam-beam limit. In principle, an estimate of the real beam-beam limit should include nonlinear resonances excited by the magnet imperfections which then makes beam-beam limit to be machine dependent.

In lepton machines, the beam-beam tune spread is much high than in hadron machine. As a result, many nonlinear resonances are crossed. However, diffusion caused by a very high-order nonlinear resonance is compensated by intrinsic damping mechanism of lepton machines which is the synchrotron radiation.

In the absence of damping mechanism diffusion even by a very high-order resonances can have significant effect on particles losses, which is believed to be the case for hadron machine. Introduction of additional fast damping mechanism, such as e-cooling can offset diffusion due to high-order resonance, at least partially, and thus lead to higher values of beam-beam parameters. Due to very slow cooling rates at high energy, this damping mechanism may not lead to compensation of beam-beam diffusion. However, this question of equilibrium between beam-beam and cooling requires very careful computational study, especially for the distribution with a dense beam core which appears for high-energy cooling at RHIC (see Sections III.A.3-4).

III.A.7.4 Beam-beam parameter for cooled distribution

For present parameters of electron cooling at 100 GeV only particles in the core of beam distribution are cooled effectively. The rms parameters of beam distribution may in fact stay approximately constant during the cooling time (as shown in Section III.A.4). As a result, the beam-beam parameter based on rms beam values becomes irrelevant and one needs to consider beam-beam parameters of real beam distribution with a dense core.

In simulations shown in Section III.A.4.7.2 with an average luminosity of $<L>=7*10^{27}$ during the 4 hours stores, the beam-beam parameter corresponding to the maximum linear part of the tune shift in fact exceeds the beam-beam limit of 0.005-0.007 per IP as shown in Fig. III.A.7.1.

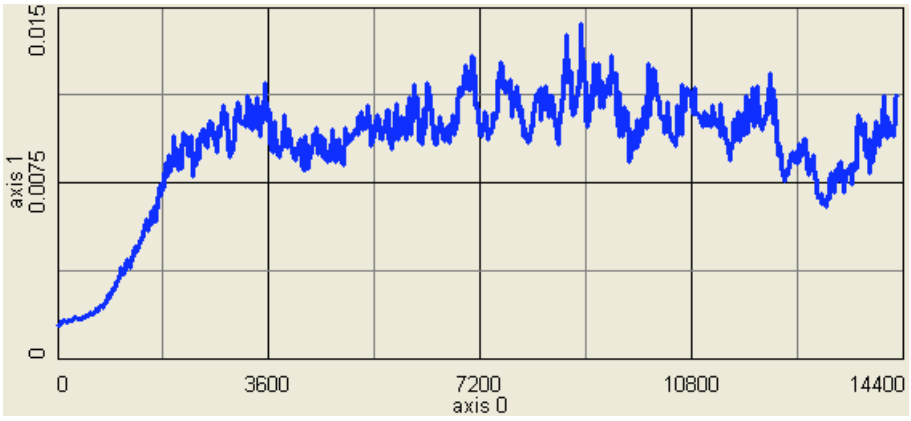

Fig.III.A.7.1 Beam-beam parameter for beta*=0.5 meters without optimization of electron beam (corresponding to <L>=7*10^{27} of 4 hours stores).

One way to minimize the time when beam-beam parameter exceeds the limit is to start even with smaller values of the beta*. For example, when beta*=0.3 meters is used instead of 0.5 meters, the beam-beam parameter exceeds the limit for significantly shorter period of time due to a rapid ion-ion disintegration for such high luminosities, as shown in Figs III.A.7.2-3 for the luminosity and beam-beam parameter, respectively.

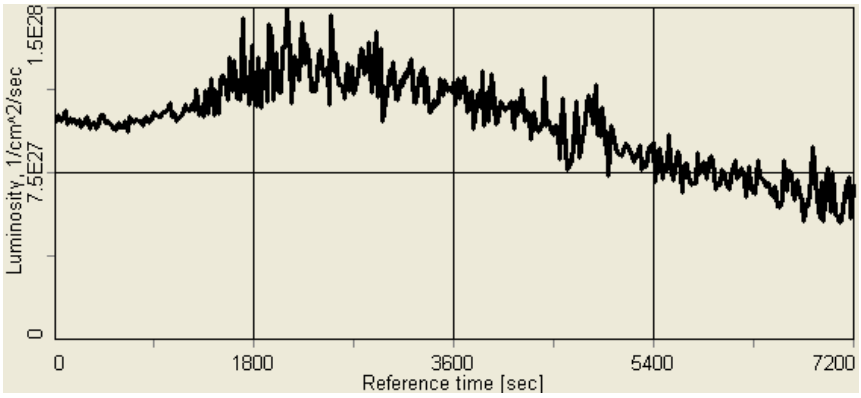

Fig. III.A.7.2 Luminosity for beta*=0.3 meters

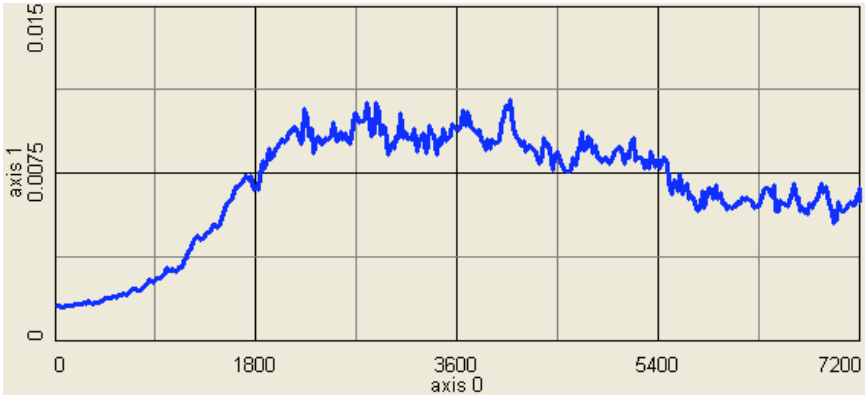

Fig. III.A.7.3 Beam-beam parameter for beta*=0.3 meters.

Further reduction of beam-beam parameter can be achieved by an additional control with the electron beam distribution. For example, in Fig. III.A.7.4 the radius of electron beam was dynamically changed to control the cooling of ion beam core and keeping the beam-beam parameter on average around 0.006 per IP.

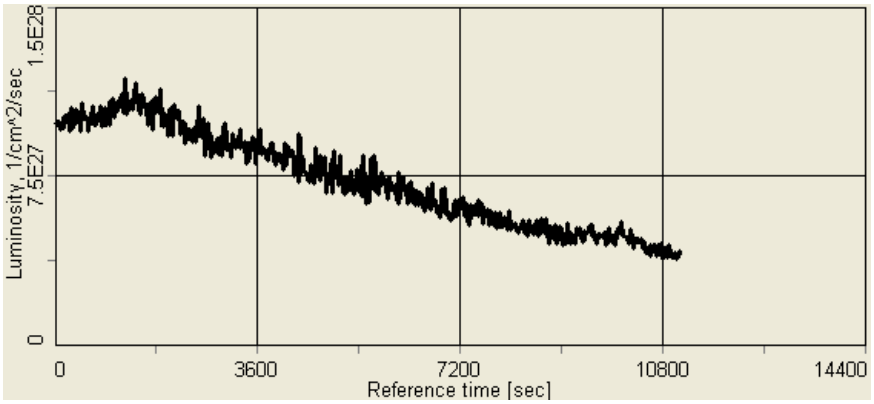

Fig. III.A.7.4 Luminosity for beta*=0.3 meters with additional optimization of electron beam.

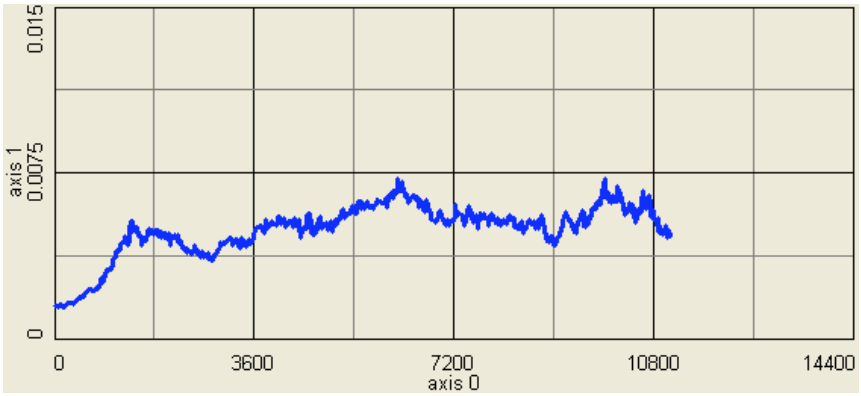

Fig. III.A.7.5 Beam-beam parameter for beta*=0.3 meters and optimization of electron beam.

For typical present parameters of electron cooler. control of the beam-beam parameter by changing electron beam distribution and further decrease of the beta* to 0.3 meters allow to achieve an average luminosity of $7*10^{27}$ during the 4 hours store.

In present simulation, control of beam-beam parameters with the electron beam starting with beta*=0.5 or higher gives an average luminosity of about $6*10^{27}$.

What are the allowable values of beam-beam parameter for the distribution under cooling and thus what are the maximum realistic values of achievable luminosity will be explored via simulations discussed in Sections III.A.7.5-6.

III.A.7.5 Simulation for double-Gaussian beam

Electron cooling together with intra-beam scattering is believed to result in a transverse distribution that can best be described by a sum of two Gaussians, one for the high-density core and one for the tails of the distribution. Simulation studies are being performed to understand the beam-beam interaction of these double-Gaussian beams. Here we report the effect of low-frequency random tune modulations on diffusion in double-Gaussian beams and compare the effects to those in beam-beam interactions with regular Gaussian beams and identical tune shift parameters.

The beam-beam tune shift parameter ξ for round Gaussian beams is defined as

$$\xi = \frac{N_p r_p \beta^*}{4\pi\gamma\sigma^2}, \qquad \text{(III.A.7.18)}$$

with N_p being the number of protons in the oncoming bunch, $r_p = 1.54 * 10^{-18} m$ the classical proton radius, β^* the β-function at the interaction point (IP), γ=267 the Lorentz factor of the beam, and σ the rms beam size of the oncoming beam.

In the case of a bi-Gaussian beam with beam sizes σ_1 and σ_2, and corresponding populations N_1 and $N_2=N_p-N_1$, the resulting beam-beam tune shift $\xi_{1,2}$ is just the sum of the two tune shifts resulting from these two contributions,

$$\xi_{1,2} = \xi_1 + \xi_2 = \frac{N_1 r_p \beta^*}{4\pi\gamma\sigma_1^2} + \frac{N_2 r_p \beta^*}{4\pi\gamma\sigma_2^2}. \qquad \text{(III.A.7.19)}$$

The luminosity L of two identical round Gaussian beams is

$$L = \frac{f}{\pi}\frac{N_p^2}{\sigma^2}. \qquad \text{(III.A.7.20)}$$

In the case of two identical bi-Gaussian beams, the resulting luminosity $L_{1,2}$ can be written as

$$L_{1,2} = \sum\sum \frac{f}{\pi} \frac{N_i N_j}{\sigma_i^2 \sigma_j^2}. \qquad \text{(III.A.7.21)}$$

We can therefore compute the beam size _ of a regular Gaussian beam with identical intensity $N=N_1+N_2$ which provides the same luminosity $L=L_{1,2}$ as

$$\sigma^2 = \frac{f}{\pi}\frac{N_p^2}{L} = \frac{f}{\pi}\frac{N_p^2}{L_{1,2}} = \frac{N_p^2}{\sum_{i=1,2}\sum_{j=1,2}\frac{N_i N_j}{\sigma_i^2 + \sigma_j^2}}. \qquad \text{(III.A.7.22)}$$

Inserting this result into the equation for the tunes hift yields the beam-beam tune shift for this equivalent beam,

$$\xi = \frac{N_p r_p \beta^*}{4\pi\gamma\sigma^2} = \frac{r_p \beta^*}{4\pi N_p \gamma}\sum_{i=1,2}\sum_{j=1,2}\frac{f}{\pi}\frac{N_i N_j}{\sigma_i^2 + \sigma_j^2}. \qquad \text{(III.A.7.23)}$$

The following figure shows a contour plot of the resulting normalized beam-beam tune shift $\xi_{1,2}/\xi$ as a function of the intensity fraction N_1/N_p in the central core and the ratio of the rms widths of the two Gaussian components, σ_2/σ_1 :

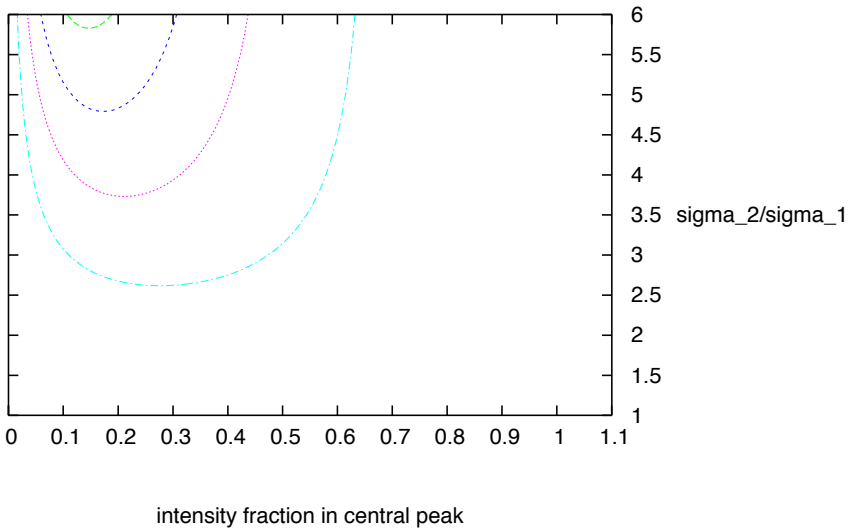

Figure III.A.7.6: Beam-beam contour plot.

To study the beam-beam interaction effect of a double-Gaussian distribution, a weak-strong simulation code was used. The accelerator lattice is described by a linear matrix, with a chromaticity of $\chi_x = \chi_y = 2.0$. Longitudinal motion was included with parameters close to the RHIC case, as listed in the following table:

$N_p = 2.5*10^{11}$
$N_1 = 1.4*10^{11}$
$N_2 = 0.6*10^{11}$
$\sigma = 66\mu m$
$\sigma_1 = 50\mu m$
$\sigma_2 = 150\mu m$
$\xi = -0.007$
$\gamma = 266$
$\gamma_t = 23$
$U_{RF} = 2MV$
harmonic number $h = 2520$
one IP

In the transverse planes, a random tune fluctuation with rms variation of $\sigma_Q = 3*10^{-5}$ and a coherence length $n_c = 10^4$ turns was added to the model. This random drift is modeled as

$$d_{n+1} = \frac{n_c}{1+n_c} d_n + \frac{1}{1+n_c} k_n \qquad \text{(III.A.7.24)}$$

where k_n is a random white noise signal with unit standard deviation and zero mean, and n is the turn number. n_c determines the correlation time of the random drift in terms of revolutions. Using the random drift signal $d_{n,}$ the drift of the tunes is simulated as

$$Q_n = Q + \frac{\delta Q * d_n}{\sqrt{< d_0^2 >}}, \qquad \text{(III.A.7.25)}$$

where

$$d_0 = \frac{k_0}{\sqrt{1+n_c}} \qquad \text{(III.A.7.26)}$$

is the initial condition, and

$$< d_0^2 >= \frac{1}{1+n_c}. \qquad \text{(III.A.7.27)}$$

This random tune fluctuation is assumed to be caused by power supply ripple, vibrations of non-linear magnetic elements, etc.

To study the effect of beam-beam interactions of beams with a double-Gaussian distribution, 1000 particles were launched with specific initial phase space distributions and tracked over $3*10^6$ turns. The total transverse emittance was averaged over 997 turns and recorded. For comparison, the interaction of two regular Gaussian beams with the same beam-beam tune shift parameter $\xi = -0.007$ as in the double-Gaussian case was also studied. Three different working points have been investigated, indicated by their respective tune footprints:

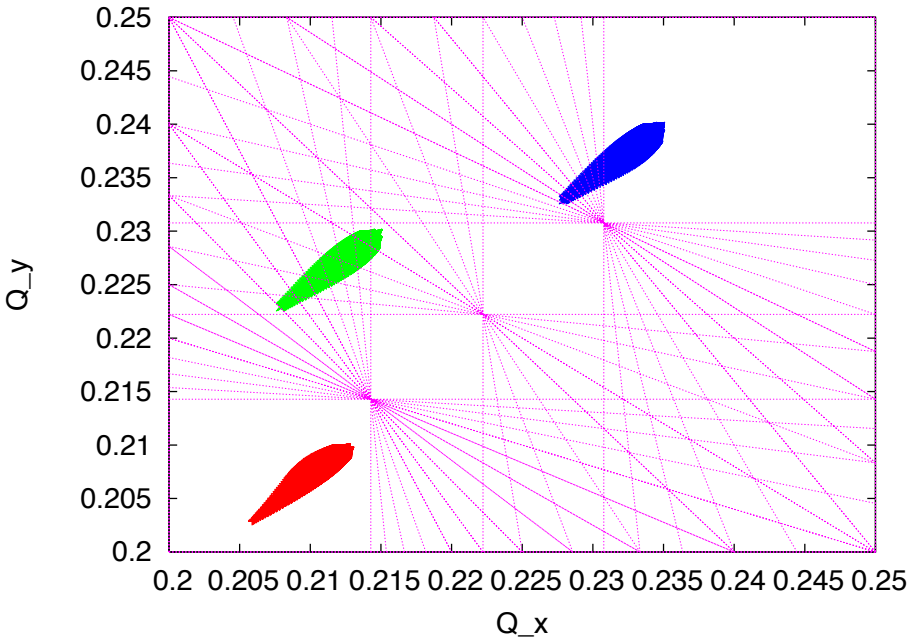

Figure III.A.7.7: Sum resonances up to 14th order and tune footprints of the three working points studied here. The colors are consistent with those in the following figures.

In the regular case, the particles were launched with a Gaussian phase space distribution in both transverse planes, as well as in the longitudinal direction. No significant emittance growth was observed:

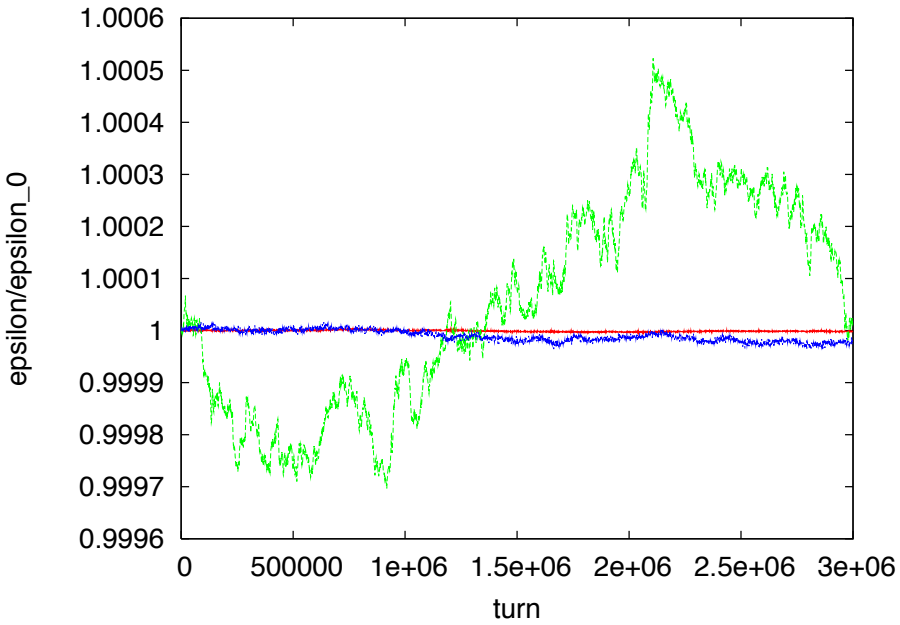

Figure III.A.7.8: Normalized beam emittance in the regular case of two Gaussian beams. The three colors indicate the three working points shown in Fig. III.A.7.7.

In the bi-Gaussian case, the particles were launched according to the rms width σ_2 of the tails of the distribution. In the longitudinal plane, initial phase space coordinates were chosen such as to resemble a beam with 20 cm rms bunch length.

As in the regular case, they were tracked for 3 million turns, and the sum emittance was averaged over 997 turns and written to file every 997 turns. In this case, a significant emittance blow-up occurs:

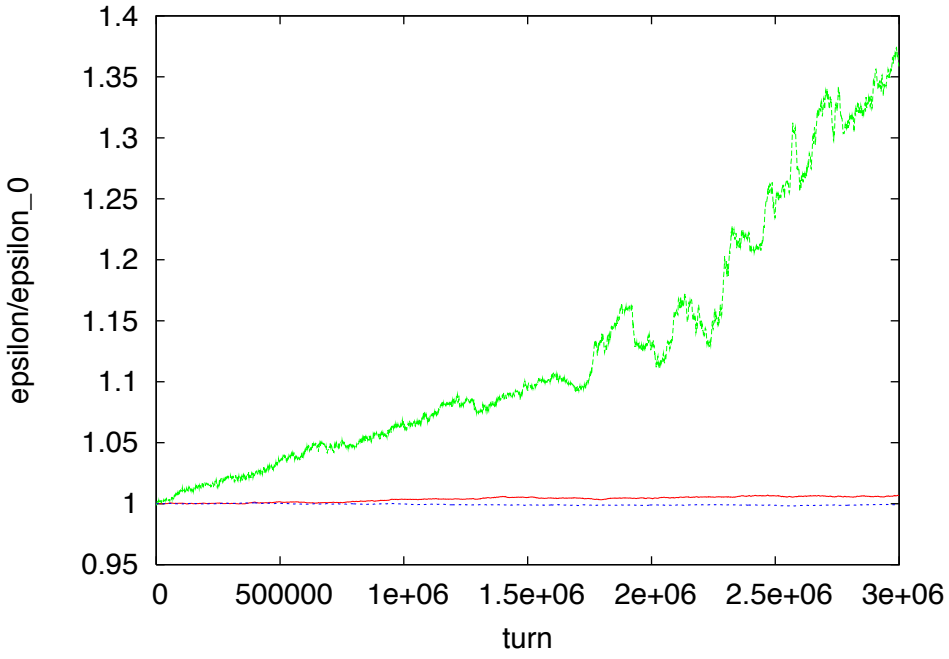

Figure III.A.7.9: Normalized emittance of the 3σ transverse tails, for particles in the longitudinal core. The colors indicate the three different working points.

The observed emittance growth becomes even more pronounced when the longitudinal phase space coordinates resemble the tails of the distribution in this plane, with an rms bunch length of 60 cm This is shown in the following Figure.

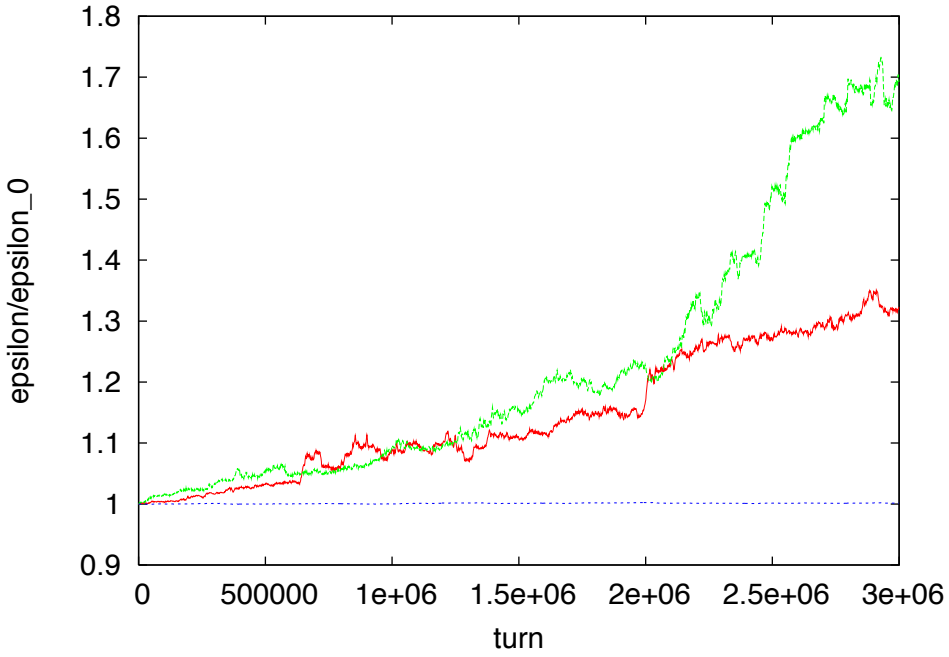

Figure III.A.7.10:

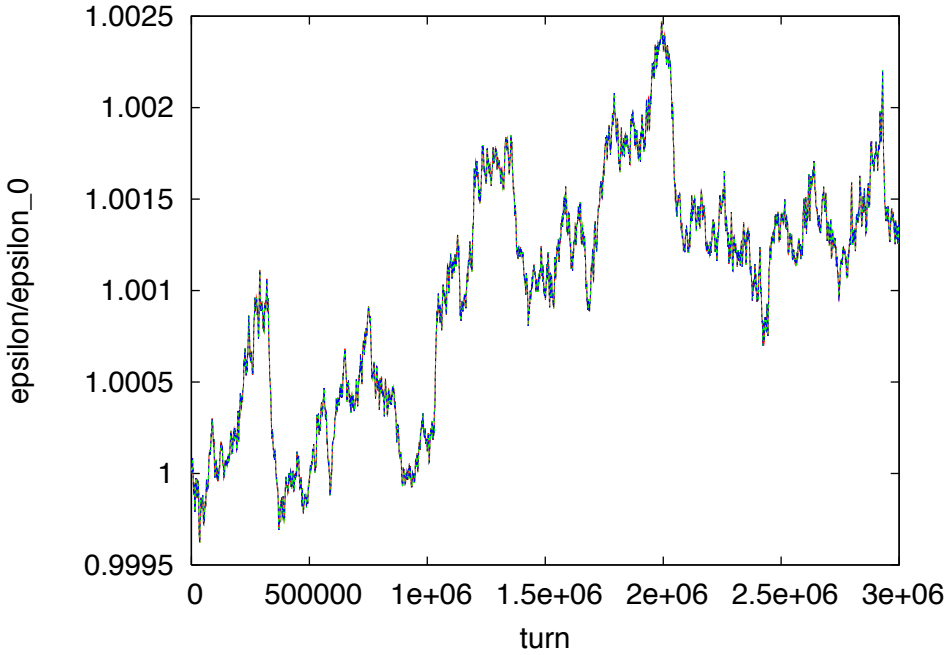

Figure III.A.7.11: Normalized emittance of the 3_ transverse tails, for particles in the longitudinal tail. The bottom picture is a zoomed-in plot of the blue line in the top picture.

Particles launched according to the rms width σ_1 of the beam core do not show emittance blow-up:

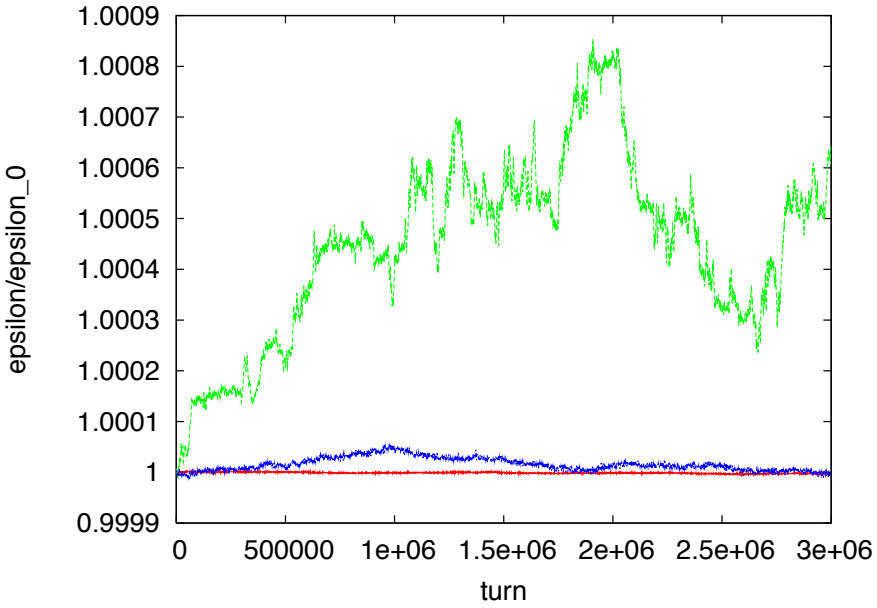

Figure III.A.7.12: Normalized emittance of the core of the double-Gaussian beam, for particles in the longitudinal core.

When the double-Gaussian strong beam is replaced by a regular Gaussian beam providing the same beam-beam tune shift, no significant difference between this case and the double-Gaussian case was observed for the transverse 3σ tails of the weak beam. This indicates that the observed effect is mostly due to the mismatched beam sizes and not due to the fact that the strong beam has a double-Gaussian distribution.

When we expand the exponential term in the beam-beam kick into a polynomial,

$$\Delta x' = \frac{2N_p r_p}{\gamma x}\left(1-\exp\left(\frac{-x^2}{2\sigma^2}\right)\right)$$
$$= \frac{2N_p r_p}{\gamma}\left(\frac{x}{2\sigma^2}-\frac{x^3}{8\sigma^4}+\frac{x^5}{48\sigma^6}-\ldots\right) \qquad \text{(III.A.7.28)}$$

and

$$\Delta x' = \frac{2N_1 r_p}{\gamma x}\left(1-\exp\left(\frac{-x^2}{2\sigma_1^2}\right)\right)+\frac{2N_2 r_p}{\gamma x}\left(1-\exp\left(\frac{-x^2}{2\sigma_2^2}\right)\right)$$
$$= \frac{2N_1 r_p}{\gamma}\left(\frac{x}{2\sigma_1^2}-\frac{x^3}{8\sigma_1^4}+\frac{x^5}{48\sigma_1^6}-\ldots\right)+\frac{2N_2 r_p}{\gamma}\left(\frac{x}{2\sigma_2^2}-\frac{x^3}{8\sigma_2^4}+\frac{x^5}{48\sigma_2^6}-\ldots\right), \qquad \text{(III.A.7.29)}$$

all nonlinear terms in the double-Gaussian case are smaller than in the regular, Gaussian case, while the linear quadrupole terms are identical. However, for the parameters chosen

in these studies, the nonlinear terms differ by less than five percent, which explains the lack of a significant difference in emittance blow-up for the two cases.

For a distribution with $\sigma_2 = 10 * \sigma_1$, $N_2 = 100 * N_1$, and a total beam-beam tune shift parameter of $\xi = 0.007$, nonlinear terms are completely dominated by the core and differ by a factor of two from the regular Gaussian case with the same linear tune shift. In this case, the strong regular Gaussian beam results in a significantly faster emittance blow-up of the weak beam tails:

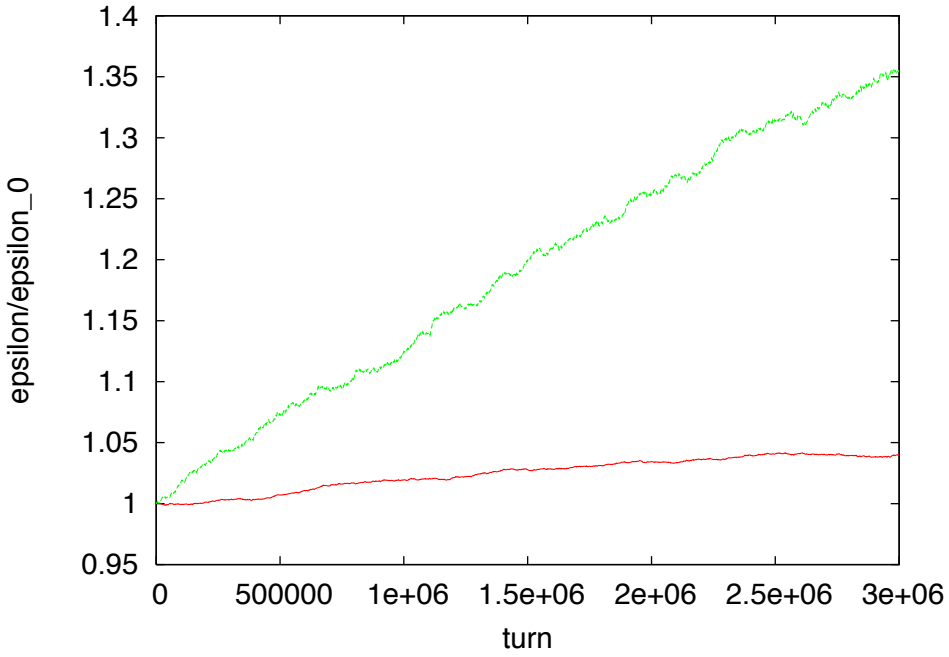

Figure III.A.7.13: Emittance of the 10σ tail when colliding with a regular Gaussian strong beam (green line), and when colliding with a double-Gaussian strong beam (red curve), for equal linear beam-beam tune shiftts. The emittance growth is much faster when colliding with the regular Gaussian strong beam due to the twice larger nonlinear terms in the beam-beam kick.

Though this requires more detailed studies, the broad Gaussian tail of the distribution blows up due to the beam-beam interaction, and may eventually get lost at collimators. If there is significant exchange of particles between core and tail due to electron cooling and IBS, this may result in a significant lifetime reduction of the entire beam.

III.A.7.6 Beam-beam simulations for ion beam under cooling

It is extremely important to treat beam-beam effects for the ion beam while the cooling is present. The main purpose of cooling is to counteract diffusion of ion beam which may be caused by various effects. For accurate treatment, dynamic simulation code should include both cooling and diffusion sources, including intrabeam scattering and beam-beam diffusion. As a simple model, one can describe beam-beam effects with a diffusion coefficient, based on beam-beam space-charge force. Such a coefficient, either approximate analytic or empiric (based on real measurements in RHIC) can be used in dynamic simulation code like BetaCool or SimCool. Simulations of beam cooling including beam-beam diffusion are planned in the nearest future.

As a result of beam-beam force one has two major effects: excitation of beam-beam resonances and tune spread. Because of the tune spread many non-linear imperfection resonances can be crossed which results in a significant beam diffusion and in so called empiric beam-beam limit. The only accurate and reliable way to account for beam-beam effects and to have a reasonable description of achievable beam-beam limit is to include non-linear optics of the machine (imperfection resonance) into account. Such more accurate simulations of beam-beam effects and cooling are planned in the framework of UAL simulation [UAL]. In addition, the UAL based simulation should describe both incoherent and coherent effects in a self-consistent manner.

Taking beam-beam diffusion and e-cooling damping into account in a self-consistent way may show the extent to what degree one can counteract beam-beam diffusion, at least partially, with the cooling which may result in higher achievable beam-beam limit with a subsequent increase in the luminosity.

III.A.7.7 Beam life time due to collisions

High value of the luminosity leads to substantial particle losses due to Coulomb dissociation in Au-Au collisions. For ion beam with Gaussian distribution the ion lifetime due to collisions can be calculated in accordance with the formula:

$$\frac{1}{\tau_{life}} = -n_{IP} L \sigma_{reaction}, \qquad \text{(III.A.7.?)}$$

where n_{IP} is the number of interaction points, L - luminosity calculated for single interaction point and $\sigma_{reaction}$ is a cross-section of the process determining the life-time. These type of losses are good losses and how effectively the beam are “burned” by collision (this type of losses is referred to as a “burnoff” process).

For RHIC storage energy of 100GeV/nucleon the cross section has be estimated [Baltz1] to be σ=212 b. Such a large cross section limits maximum achievable integrated

luminosity. The optimum average luminosity then requires short storage cycles of about 4 hours as shown in Section III.A.4.

III.A.8. Effects of electron beam on ion beam dynamics

III.A.8.1 Recombination in the cooling section

For calculation of ion life time due to electron capture in the cooling section the following formula is usually used:

$$\frac{1}{\tau_{life}} = \frac{1}{N_i}\frac{dN_i}{dt} = -\frac{\alpha_r n_e \eta_L}{\gamma^2}, \qquad \text{(III.A.8.1)}$$

where n_e is the electron density in LRF, $\eta_L = l_{cool}/C$ is the part of the ring circumference C occupied by the cooling section. Recombination coefficient α_r calculated under assumption that ion velocity in PRF is substantially less than electron one and flattened electron velocity distribution is given by the formula [Wolf1]:

$$\alpha_r = A \cdot Z^2 \sqrt{\frac{1}{T_\perp}}\left[\ln\left(\frac{11.32Z}{\sqrt{T_\perp}}\right) + 0.14\left(\frac{T_\perp}{Z^2}\right)^{1/3}\right],\ A = 3.02\cdot 10^{-13}\,\frac{cm^3}{s} \qquad \text{(III.A.8.2)}$$

here $T_\perp$ is measured in eV.

For present baseline parameters the recombination lifetime is of the order of 20 hours and can change significantly depending on parameters of the electron beam.

It is important to remember that such ion losses are additional losses which should be minimized to a minimum. As a result, it seems beneficial to keep transverse temperature of electron $T_\perp$ above 100 eV, as shown in Section III.A.4.

III.A.8.2 Tune shifts

The ions will be submitted to a tune shift due to either their own space charge which increases when cooling proceeds, or due to an electron beam which acts like a lens.

III.A.8.2.1 Ion beam space charge

For an ion beam with Gaussian distribution one has

$$\Delta Q_{SC} = \frac{ZN_i r_i C_r}{4\pi\beta^2\gamma^2\varepsilon_{in}\sigma_{is}\sqrt{2\pi}} \qquad \text{(III.A.8.3)}$$

where C_r is ring circumference, ε_{in} is the normalized rms emittance and σ_{is} the rms bunch length.

For typical parameters of Au ion beam at 100 GeV one gets ΔQ_{sc} about 1*10-3.

As a result of cooling, such tune shift will be increased and at some point may become a problem which should be carefully taken into account.

III.A.8.2.2 Tune shift due to electron beam

Electron beam also acts like a focusing lens on positive Au ions which produces an additional tune shift of ion particles:

$$\Delta Q_e = \frac{Zn_e r_i l_c \beta_i}{2\beta^2\gamma^3} \qquad \text{(III.A.8.4)}$$

where l_c is the length of the cooling section, n_e is the density of electron beam in the laboratory frame and β_i is the average beta-function in the cooling section.

For baseline cooler parameter ΔQ_e is also at 10^{-3} level.

III.A.8.3 Coupling of transverse phase-space plane

The solenoid longitudinal magnetic field causes the ion to execute a cyclotron rotation around the longitudinal axis at frequency:

$$\omega_i = \frac{ZeB}{m_i} \qquad \text{(III.A.8.5)}$$

As a result, at each passage, the solenoid magnetic field will twist the ion beam by

$$\delta\theta = \frac{ZeBl_c}{m_i v_o} = \frac{ZeBl_c}{p_0} \qquad \text{(III.A.8.6)}$$

This will introduce a coupling between the horizontal and vertical planes.

To compensate this drawback, a solenoid producing a field in the opposite direction must be installed somewhere in accelerator. Alternatively, one can also use skew quadrupoles.

For the presently proposed magnetic field of 5T, the most practically solution seems to have magnetic field in the opposite direction in the two of the cooling solenoids.

III.A.8.4 Collective instabilities for ion distribution under cooling

A careful study of collective instabilities becomes a critical issue for beam under cooling at least for two reasons:

- tune spread and momentum spread decreases which may result in insufficient Landau damping

- direct space-charge field increases at the beam cools done with a formation of dense core.

III.A.8.5.1 Requirements on coupling impedance after cooling

For the longitudinal stability a rough condition is

$$\left|\frac{Z}{n}\right| \le F_L \frac{A}{Z_i^2} \frac{\beta^2 \gamma \left(m_p c^2 / e\right) |\eta|}{I_0} \left(\frac{\Delta p}{p}\right)^2_{FWHM} \qquad \text{(III.A.8.9)}$$

where the longitudinal form factor depends on the distribution and approximately F_L=1. Here,
I_0=e$Z_i f_0$N is the average ion beam current for a coasting beam. For a bunched beam, one can roughly use the local peak current I_p=eZ_iβc/l_b.

For low-energy cooling, cooling above transition becomes a problem due to the space-charge contribution to the impedance which results in a significant tune shift. For RHIC energies, the space-charge impedance in negligible so that stability will be simply governed by a degree of a collapse of momentum spread Δp/p. The process of cooling should be carefully controlled to avoid large decrease in Δp/p.

For the transverse stability, the requirement on the transverse impedance is given by

$$Z_t \le 4F_T \frac{A}{Z_i^2} \frac{\gamma\left(mc^2/e\right)}{I_0} \frac{Q}{R} \left(\Delta Q\right)_{FWHM} \qquad \text{(III.A.8.9)}$$

where full tune-spread ΔQ_{FWHM} is given by

$$\left(\Delta Q\right)_{FWHM} = \left[\left(\left(n-Q\right)\eta + Q'\left(\Delta p/p\right)\right)^2 + \left(\left(\partial^2 Q/\partial a^2\right)a^2\right)^2\right]^{\frac{1}{2}} \qquad \text{(III.A.8.10)}$$

The first term in Eq. (III.A.8.10) is due to the revolution frequency, the second term is due chromaticity Q' and the third term is due to the nonlinear tune spread with octupoles.

A study of the longitudinal and transverse stability of cooled ion beam in RHIC, with a dense-core distribution, will begin in the nearest future.

III.A.8.5.2 Coherent ion-electron interactions

A simple description of such interaction can be done via the model of two oscillators [Parkhomchuk1]. Even with such simple model one can get that for high electron densities and long cooling section the net effect of ion-electron interaction can result in "heating" of the ion beam rather than cooling.

For the baseline parameters of RHIC cooler and region of electron densities under consideration such a heating of ion beam is not expected [Benzvi1]. However, this topic will be studied in detail using numerical simulation.

III.A.9 REFERENCES

[Baltz1] A.J. Baltz et al., Phys. Rev. E 54, 4233 (1996).
[Benzvi1] I. Ben-Zvi and V. Parkhomchuk, Tech. Report C-AD/AP/47 (2001).
[BetaCool] I.Meshkov, A.Smirnov, A.Sidorin, G.Trubnikov, E.Syresin, Description of software
for BETACOOL program, Joint Institute for Nuclear Research, Dubna, Report 2003.
[Bjorken1] J. Bjorken and S. Mtingwa, Particle Accel. 13 (1983), p.115.
[Bruhwiler1] D. Bruhwiler et al., "ParSEC- Parallel simulation of electron cooling".
[Bruhwiler2] D. Bruhwiler et al., "Simulating Electron Cooling Physics with VORPAL"

(2003-2004), unpublished.
[Budker1] G.Budker, Proc. Intern. Symp. Electron and Positron Storage Rings, Saclay, 1966.
[Burov1] A. Burov, "Electron cooling against IBS", FNL-TM-2258 (2003).
[Derbenev1] Derbenev Ya.S., Skrinsky A.N., Fyzika plasmy, 1978. v.4, p.492
[Eidelman1] Yu. Eidelman, I. Ben-Zvi, A. Fedotov and V, Litvinenko, Recent developments in
the SimCool code (2004), unpublished (Tech. Note)
[Eidelman2] Yu. Eidelman, A. Fedotov, Description of the SimCool code (2004), unpublished
[Eidelman3] Yu. Eidelman et al., Numerical algorithms for IBS treatment for ion distribution
changing under cooling (2004), unpublished (Tech. Note)
[eZDR] "eRHIC Zeroth-Order Design Report", BNL C-A/AP Note 142 (2004)
http://www.agsrhichome.bnl.gov/eRHIC/eRHIC_ZDR.htm
[Fedotov1] A. Fedotov, Comments on simplified treatment of Intrabeam scattering using
plasma approach (January 2004), unpublished (Tech. Note)
[Fedotov2] A. Fedotov, A. Sidorin, A. Smirnov and G. Trubnikov, Benchmarking of the gas-relaxation vs IBS formulas (May 2004), unpublished (Tech. Note)
[Fedotov3] A. Fedotov and G. Trubnikov, Benchmarking of IBS formulas for RHIC parameters (November 2003), unpublished (Tech Note)
[Fedotov4] A. Fedotov, Yu. Eidelman and V. Litvinenko, Core-tail model for intrabeam scattering of ion distribution changing during cooling (January 2004), Tech. Note
[Katayama1] T.Katayama et al. MUSES Conceptual Design Report, RIKEN, May 1999.
[Kellogg1] O.D. Kellogg, Foundations of Potential Theory (Dover, New York, 1953).
[Martini1] M. Martini, CERN PS/84-9 (AA), 1984.
[Meshkov1] I.Meshkov, Phys. Part. Nucl., 25, 1994, 631.
[Meshkov2] I.Meshkov, Physics and Technique of Electron Cooling, RIKEN-AF-AC-2, 1997
[Parzen1] G. Parzen, Nuc. Inst. Meth. A256, p.231 (1987).
[Parzen2] G. Parzen, Tech. Notes C-AD/AP/144, C-AD/AP/150 (2004).
[Piwinski1] A. Piwinski, Proc. of 9th Intern. Conf. High Energy Accelerators (1974) 405.
[Sorensen1] A. Sorensen, Proc. of CERN Accel. School, CERN 87-10 (1987).
[Takayama1] K.Takayama, Lettere al Nuovo Cimento, Vol.34, No.7,p.190 (1982).
[UAL] N. Malitsky, R. Talman, "Unified Accelerator Libraries", AIP 391 (1996).
[VORPAL] C. Nieter, J. Cary, J. Comp. Phys. 196 , p.448 (2004).
[Wei1] J. Wei, Particle Accel Conference (1993), p. 3651.
[Wolf1] A.Wolf, et al., Recombination in electron coolers, NIM A 441(2000), 183

III.B ELECTRON RECOVERY LINAC FOR RHIC II e-COOLER

The energy recovery linac (ERL) is the heart of the electron cooling facility for RHIC II. The ERL is a complex accelerator system, which generates a high quality magnetized electron beam, accelerates it to the operational energy (54.7 MeV for 100 GeV/u gold ions), matches it (both transversely and longitudinally) into the cooling section of the RHIC II and, finally, decelerates and disposes of the used e-beam. The ERL is based on novel emerging technology of super-conducting RF (SRF) cavities and is a very complex and challenging accelerator. Hence, the C-AD is building a prototype ERL in Bldg. 912 with energy ~ 20 MeV to test all system whose performance is critical for full-scale 54-MeV e-cooler ERL. The prototype ERL is also a very unique accelerator being the first ERL based on the SRF cavity specifically designed to operate with extremely high beam currents.

This chapter contains the description of the main subsystem and the electron beam kinematics and dynamics in both ERLs.

III.B.1 MAIN SYSTEMS OF THE ERL

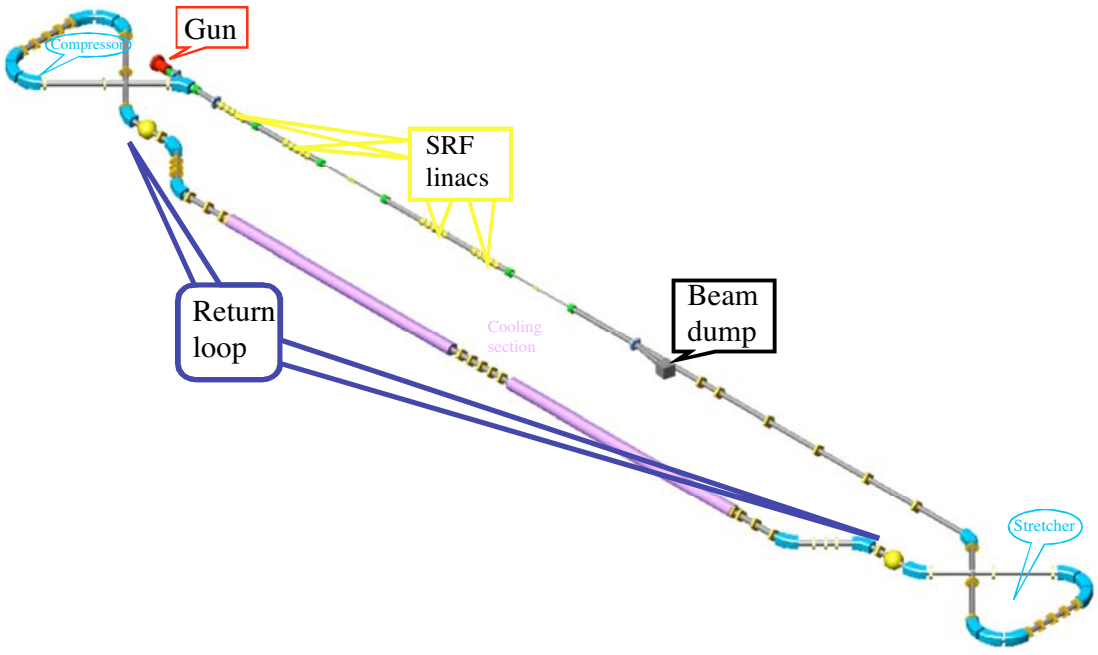

Figure III.B.1.1. Schematic layout of the ERL for electron cooling at RHIC III based on two so called SRF super-structures. The return loop of the ERL is rather sophisticated and includes the stretcher and compressor, the cooling section and miscellaneous matching optics.

The main functional parts of ERL for electron cooling and ERL-prototype are shown in Fig. III.B.1.1 and Fig. III.B.1.2, correspondently: the gun-injector, the SRF linacs, the beam dump and the returning loop.

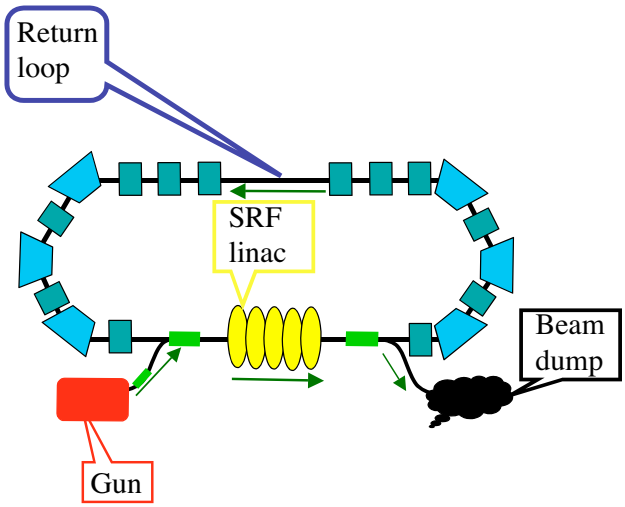

Figure III.B.1.2. Schematic layout of the ERL-prototype based on 5-cell SRF linac. The return loop of the prototype ERL is looking rather simple but includes all necessary "bells and whistles" for studying the electron beam dynamics is ERLs: the arcs are achromatic with tunable longitudinal dispersion (R_{56}) and the lattice provides for full control of the phase advances and the optics in both *x* and *y* directions.

There are also some noteworthy differences between two ERLs:

- The prototype ERL will operate mostly with un-magnetized electron beam, while the ERL for the e-cooler will operate only with strongly magnetized beam
- The prototype ERL will have only 703.75 MHz RF system, while the e-cooler will be equipped also with 3rd harmonic RF system and low frequency RF as well as a special lattice sections for stretching and compressing the beam
- Using the magnetized beam (i.e. an electron beam generated in the axial magnetic field) for cooling significantly improves the cooling efficiency, but is also adds additional conditions for the matching of the electron beam transport between the gun and the solenoid
- The beam should be properly matched into the cooling solenoid to minimize the transverse temperature of the electron beam and to optimize the cooling – this condition is not applicable to the ERL prototype.
- The present e-cooler scheme comprises the RHIC cooling section with two 13-m solenoids with opposite field direction for compensating the coupling for the RHIC ion beam. This configuration requires the matching between two solenoids, which can be done using unit and minus unit matrices in *x* and *y* directions correspondently (see Fig. III.B.1.3)

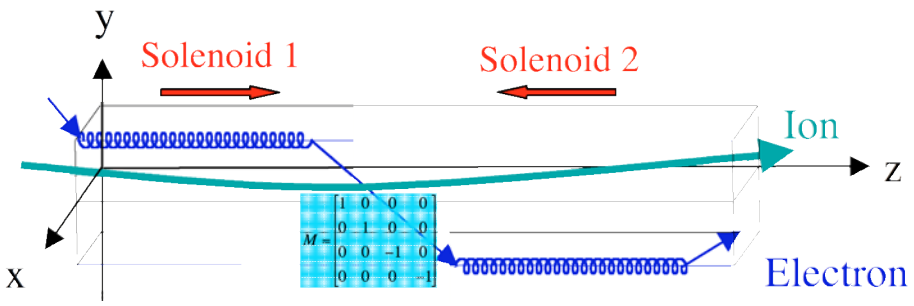

Figure III.B.1.3. The matching conditions between two solenoids with opposite direction of the field: the use of the above matrix changes the sign of the angular momentum of the electron $M_z = [\vec{p} \times \vec{r}]_z = p_x \cdot y - p_y \cdot x \Rightarrow -M_z$, hence matches it into the opposite sign of solenoidal field.

III.B.2 ERL INJECTION SYSTEM

The injection system of the ERL comprises of the source of electrons (photocathode) placed inside the accelerating field (SRF gun cavity), focusing elements (solenoids, magnets), the third harmonic RF cavity (absent in the prototype) and a compensated magnetic system (chicane, dog-leg or their modification) to merge the low -few MeV- energy injector-beam with high – few tens of MeV- energy beam re-circulated in the ERL. The working concept of the injector for the R&D ERL is showing in Fig. III.B.2.1, while the injection concept of the e-cooler ERL is under development,

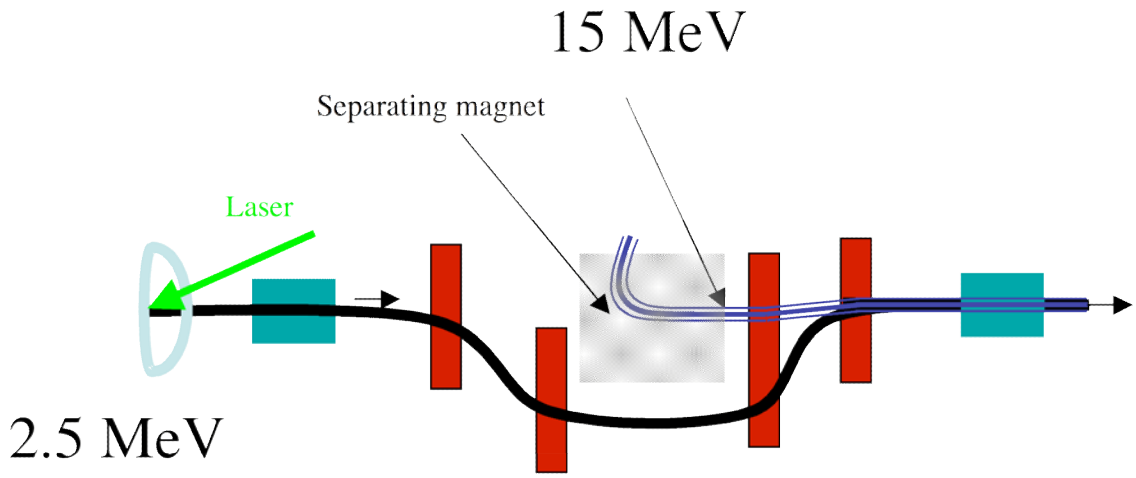

Fig. III.B.2.1. Working concept of the ERL injector: the electrons generated by the laser beam at the photocathode immersed into a half-cell SC RF gun are accelerated to about 2.5 MeV. The generated beam merges with high-energy e-beam (~15 MeV) via a short compensated (vertical) chicane. The 15 MeV beam comes to the chicane via a Lambertson-type septum magnet, which bends its trajectory in horizontal plane.

Present e-cooler design calls for the use of 1.5 cell gun, while the prototype ERL with operate with a half-cell for 703.75 MHz Super-conducting RF gun. The three major elements of ERL injector will be discussed in the next three sections: The electron gun, the photocathode and laser system and injectors beam line elements.

III.B.2.1 Super-Conducting RF Gun

The electron gun is required to produce a CW stream of electron bunches with a high charge (up to 20 nC), low emittance (below 40 microns normalized rms) and a high repetition rate (9.383 MHz). The average current is thus about 200 mA, and the beam power of the order of one megawatt. In addition, the electron beam has to be magnetized, to a value of about 1.5×10^{-5} Weber. This combination is unique in many respects and presents various difficulties. The solution adopted for the electron gun of the electron cooler of RHIC is a superconducting RF (SRF) gun, in which the resonant cavities making up the gun accelerating structure are made of niobium and operated at a low temperature of about 2 degrees K. The frequency of the gun, as that of the ERL, will be 703.75 MHz, or the 75^{th} harmonic of the 9.383 MHz bunch spacing frequency of RHIC II.

The maximum available RF power from a single klystron tube at 703.75 MHz is about 1 MW. Assuming that we power the gun by one klystron, that power is sufficient to accelerate electrons in the gun up to 5 MV, assuming the average current is 0.2 amperes. A higher current would lead to a lower energy at the output of the gun. Electron beam dynamics simulations show that even at a lower energy good injection to the energy recovery linac can be obtained, however the higher the injection energy the better is the beam quality.

The R&D ERL plan to use a half-cell SRF cavity – a prototype of the 1 and 1/2 cell for the e-cooler – which will be limited in accelerating electron to about 2.5 MeV.

In a SRF gun, practically all the amplifier power is available for accelerating the beam. For comparison, in a normal-conducting gun producing only 0.1 amperes at energy of about 2.5 MeV, the gun cavity consumes about 750 kW, thus wasting most of the klystron power. Under these conditions the peak RF field on the cathode of the gun is about 9 MV, and this relatively low field results in an emittance of over 50 microns. At 0.2 amperes the fraction of the field that would be required for the beam would be larger, reducing the field on the cathode and leading to unacceptable performance.

DC guns are limited to about half the field of the normal-conducting gun by breakdown issues, and the beam quality would be even worse. A DC gun operating at a very low peak current must be followed by a low frequency bunching-accelerating system. The performance of such a system is unknown and the resulting accelerator is somewhat complex. Such a gun system is considered as a backup alternative to the SRF gun and will be investigated.

III.B.2.1.1 Structure of the gun

The form of the gun is, naturally, dictated by its function. In this case the three main functional elements are:

1. The function of superconductivity, requiring cooling the gun by liquid helium, thus necessitating a cryostat and affecting the design of elements that connect to the gun such as the photocathode insertion and the fundamental power coupler.
2. The function of a photocathode operating in the gun, which leads to a complex cathode insertion mechanism.
3. The function of delivering a very high CW power into the gun, making it necessary to provide a complex fundamental power coupler.

Surprisingly, the gun cavity may be the simplest element in the photo-injector complex.

As will be described below (section III.B.2.1.2) the photocathode is a critical element of the gun. The secondary-emission enhanced cathode using a diamond window looks promising for an SRF gun, since the diamond window will protect the SRF cavities from the deleterious effects of the cathode material. Whatever the cathode that is being used, the SRF gun must accommodate a cathode insertion mechanism that must serve several functions:

- The cathode insertion must not affect significantly the Q of the gun cavity by either
  - exposing it to too much normal-conducting surface area,
  - generating significant resistive or multipactoring losses at the 2° K helium reservoir, or
  - conduct significant fundamental power out of the cavity.
- The insertion must be heat sinked such that the heat developed in the cathode will not load the 2° K helium system.
- The insertion must allow replacement of the cathode without damage to the gun cavity.
- The insertion must be positioned with some precision.
- For certain types of cathodes, the assembly of the cathode into the gun must be done under good vacuum conditions, thus some form of load-lock mechanism must be available, connecting the insertion mechanism, gun and a cathode storage or fabrication chamber under ultra-high vacuum.

The first SRF gun developed with a successful insertion mechanism is the KFR gun [III.B.2]. This gun is shown in Fig. III.B.2.1.1. The gun is a single cell at 1.3 GHz, and the figure shows the rather complex cathode insertion mechanism, comprising a choke cell and multiple RF filters isolating the fundamental power of the gun from leaking disastrously through the insertion device. The single accelerating cell and the smaller choke cell are superconducting (shown in blue in the figure), and the rest of the insertion

mechanism (shown in red) is cooled by liquid nitrogen. The gun operated successfully and demonstrated a peak electric field of 22 MV/m over the cathode area.

The KFR gun was designed for a relatively low beam current. The RHIC electron cooling gun will operate at a much larger beam power and thus require a rather sophisticated Fundamental Power Coupler (FPC), capable of providing 1 MW CW power to the gun. In addition, the gun HOMs must be well damped.

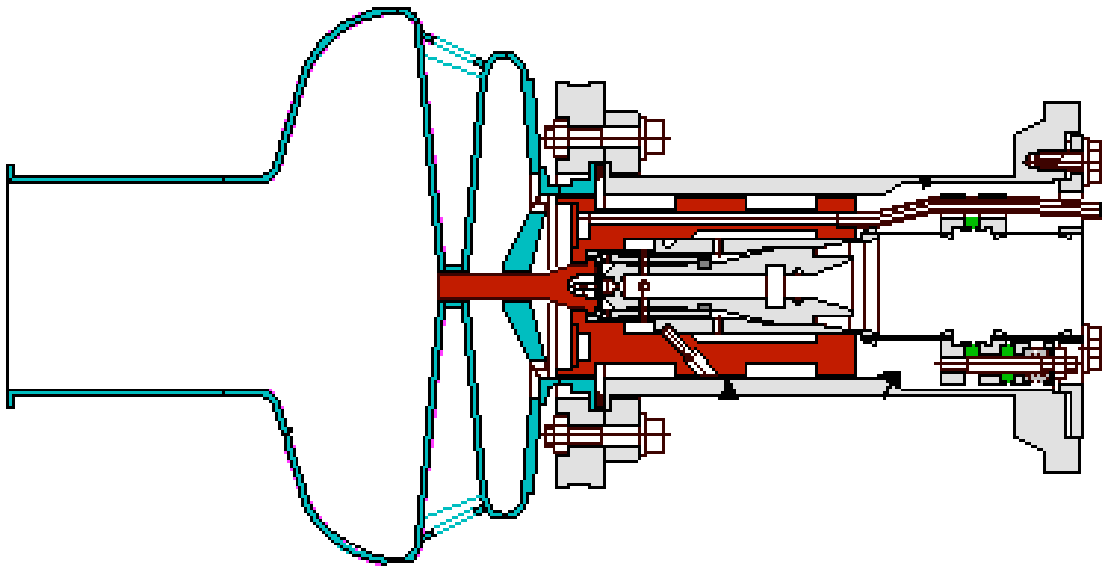

Fig. III.B.2.1.1 The SRF gun developed by the FZ-Rossendorf, in Dresden, Germany, in collaboration with other institutions.

The FPC represents a large perturbation of the field in the gun, and thus will be symmetrized by the application of two opposing couplers. This approach actually makes the design of the FPC easier, since each of the two couplers will carry half the power.

Figure III.B.2.1.2 shows a drawing of a MW FPC. The figure is taken from reference [III.B.2.1.2], the APT high-power coupler for a superconducting cavity operating at 700 MHz. It is rather fortunate that this coupler, designed to deliver the highest power on record to a superconducting cavity, has been designed for a frequency which is so close to the frequency of the RHIC electron cooler. This FPC has been thoroughly tested and was extremely successful. The coupler and its window assemblies have transmitted power up to 1 MW, CW and have handled full reflected 850 kW, CW over a limited standing-wave phase range. This coupler was also adjustable, a nice feature but one which may be traded against the elimination of the bellows, which proved to be the weakest link in this highly successful coupler.

The complexities of the design of a couplers was described in an excellent tutorial on couplers in the 2003 SRF Workshop in Lubek, Germany. The tutorial included a nice assembly of the APT FPC, shown in Fig. III.B.2.1.3.

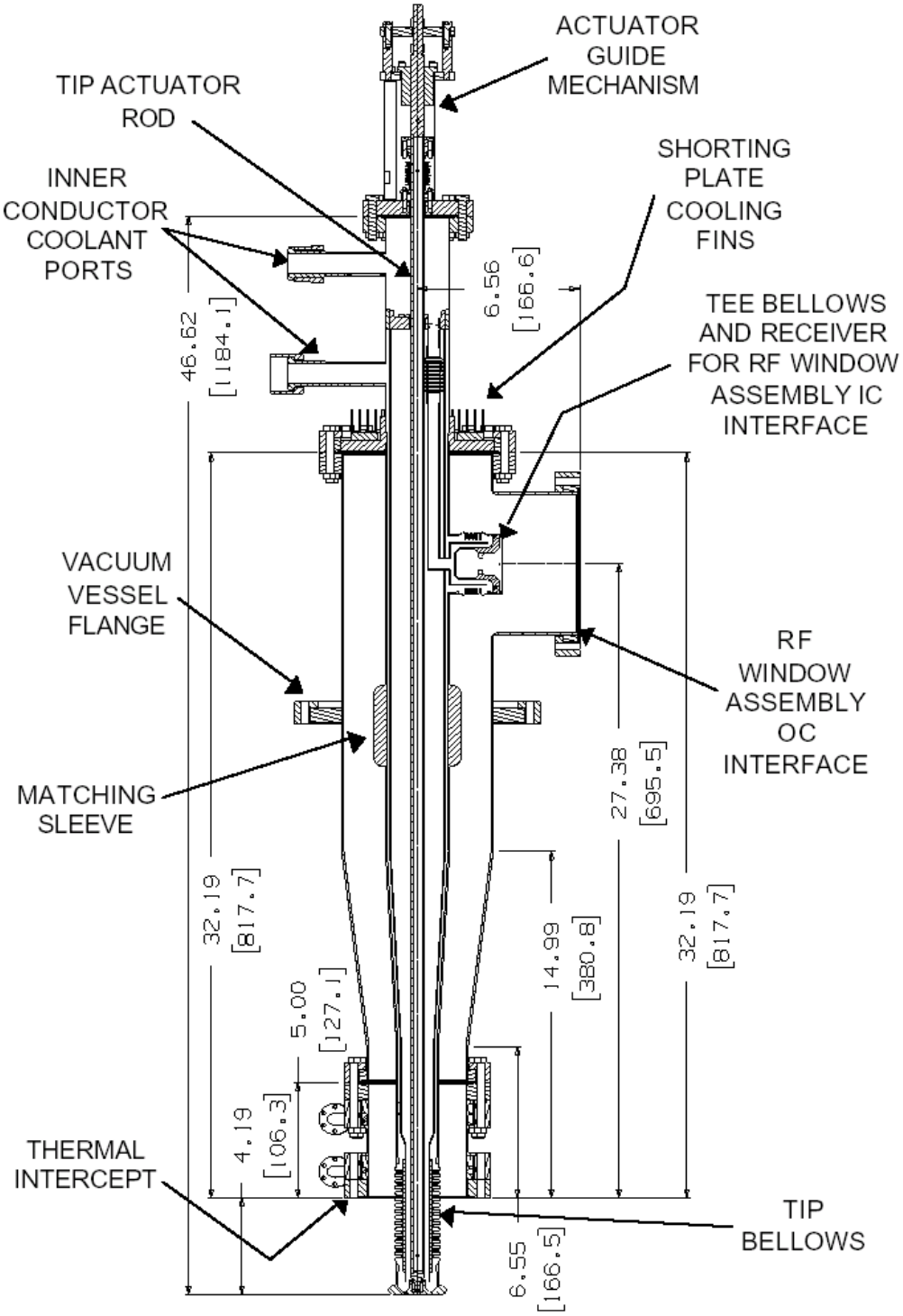

Fig. III.B.2.1.2 .The straight section insert of the APT Fundamental Power Coupler.

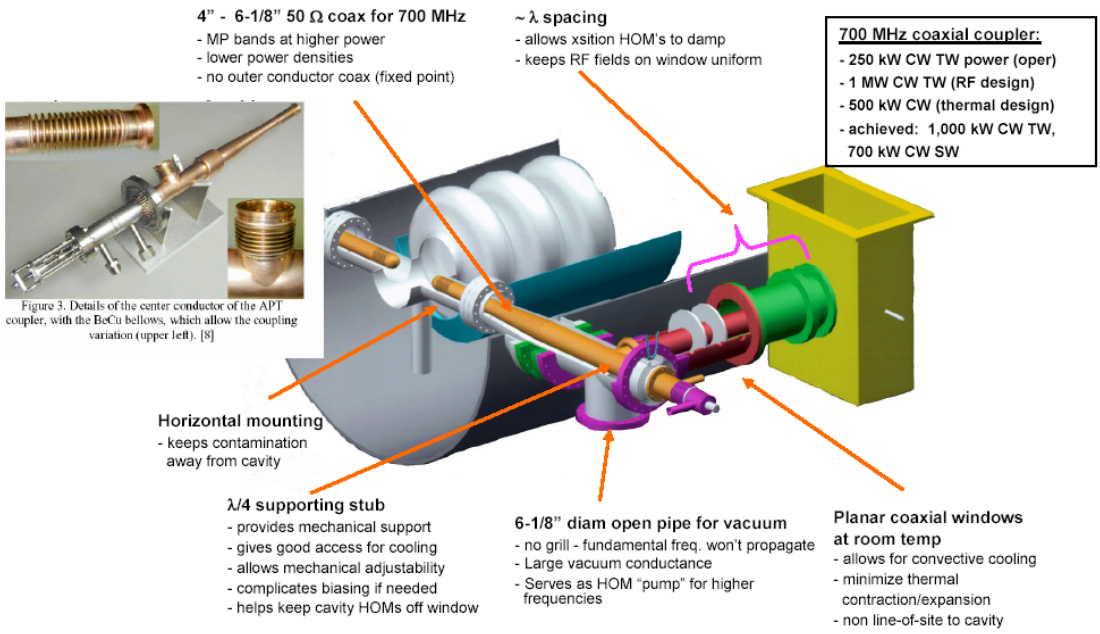

Fig. III.B.2.1.3 The complete assembly of the APT Fundamental Power Coupler.

A final element is necessary in the photoinjector as much as in the linac, and that is a frequency tuner.

An envelope of the SRF gun, which will be used for the R&D ERL, is shown in Fig. III.B.2.1.4

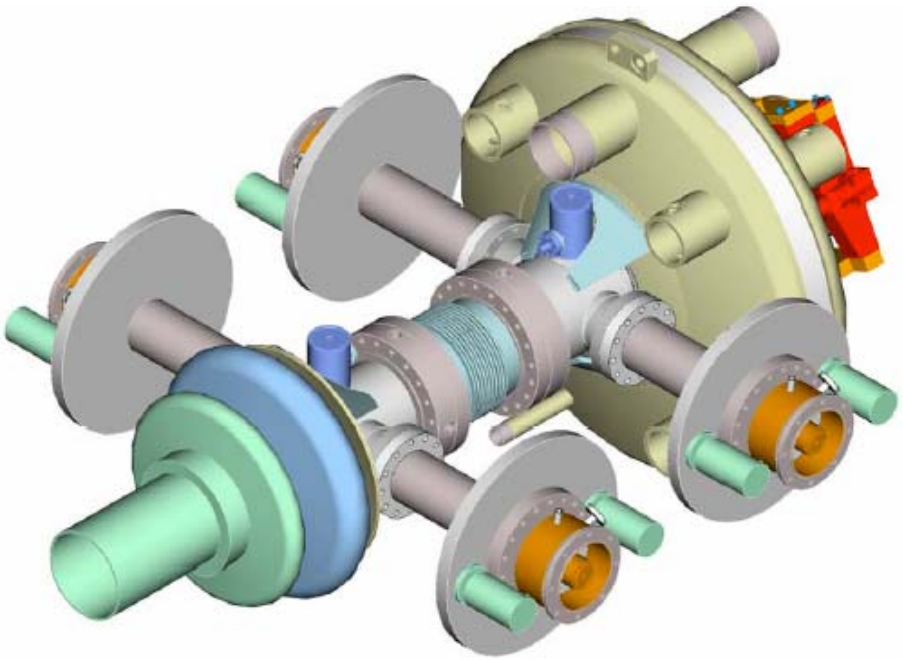

Fig. III.B.2.1.4 A preliminary drawing of the half-cell 703.75 MHz gun.

III.B.2.1.2 Design of the SRF gun cavity and its performance.

The performance of a superconducting gun has been studied using the computer program Superfish (to calculate the electric and magnetic fields) and Parmela (to calculate the beam dynamics of the magnetized electrons.

Figure III.B.2.1.4 shows the Superfish calculation of the electromagnetic fundamental more of a simple model of a "1 1/2 cell" SRF cavity.

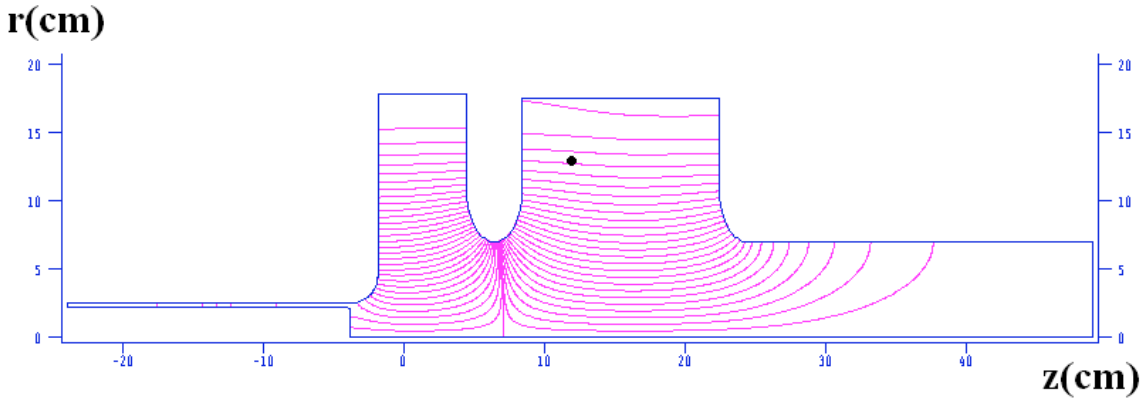

Fig. III.B.2.1.4 Electric field contours of a 1 1/2 cell gun cavity. The cathode insertion is on the left side of the gun.

The design has a few notable features. First, the cathode insertion is recessed. While this reduces the peak electric field on the cathode, it provides RF focusing of the beam, an essential feature for overcoming the defocusing produced by the space-charge forces. The other notable feature is the large iris diameter and even larger beam pipe.

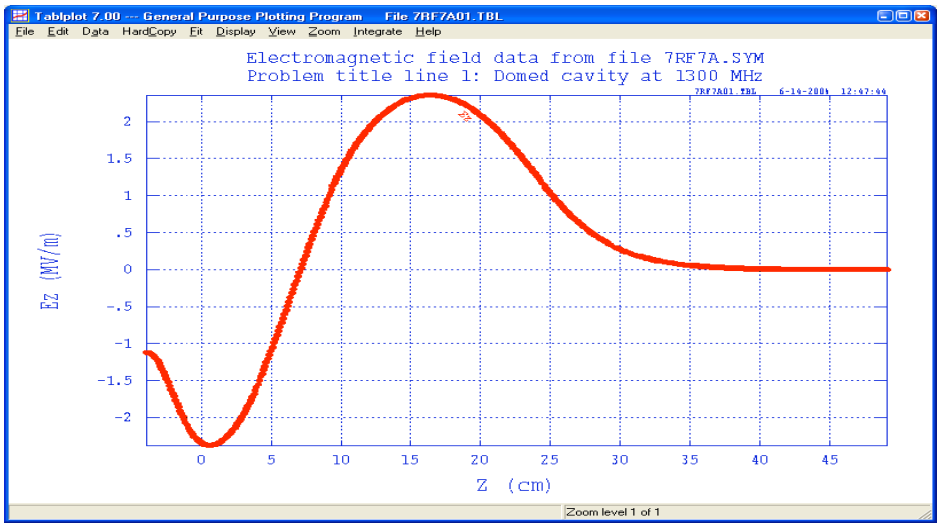

Fig. III.B.2.1.5 The profile of the longitudinal on-axis electric field in the 1 1/2 cell gun cavity. The cathode insertion is on the left side of the gun.

This design is aimed at damping High Order Modes (HOMs), which would propagate down the beam pipe and will be absorbed by a ferrite microwave absorber in the beam line outside the cryostat. The square shape of the cells is a computational convenience, which does not seriously affect the beam dynamics. The actual shape will be calculated separately and will be the customary elliptical shape of superconducting cavities 9see Fig. III.B.2.1.4), a feature that eliminates multipactoring that otherwise will take place near the corners of the square cell. The profile of the longitudinal electric field on axis is plotted in Figure III.B.2.1.5.

The R&D ERL main mode of operation with used a conventional electron beam, i.e. without magnetization. The magnetized beam will be used in the R&D ERL mostly for test of the emittance compensation and transport of magnetized beam. Magnetized beam for electron cooling is created by immersing the cathode in an uniform solenoidal field. A preliminary schematic of such a system compatible with SRF gun and Superfish simulation of the magnetic field are shown in figure III.B.2.1.6. Since the cavity stem enclosing the cathode is superconducting, the magnetic field (which would be turned on only after the cavity has been cooled down) does not penetrate the wall but is confined in the stem. The field on the wall is about 50% higher than the peak field on the center of the cathode area, hence the field is not uniform across the cathode. A more elaborate scheme may be needed to satisfy the uniformity of the field required for the e-cooler. Nevertheless, this preliminary studies demonstrated that the desirable values of magnetic field at the cathode ~200 Gauss will cause a rather low field ~300 Gauss at the SRF gun surface, which are acceptable.

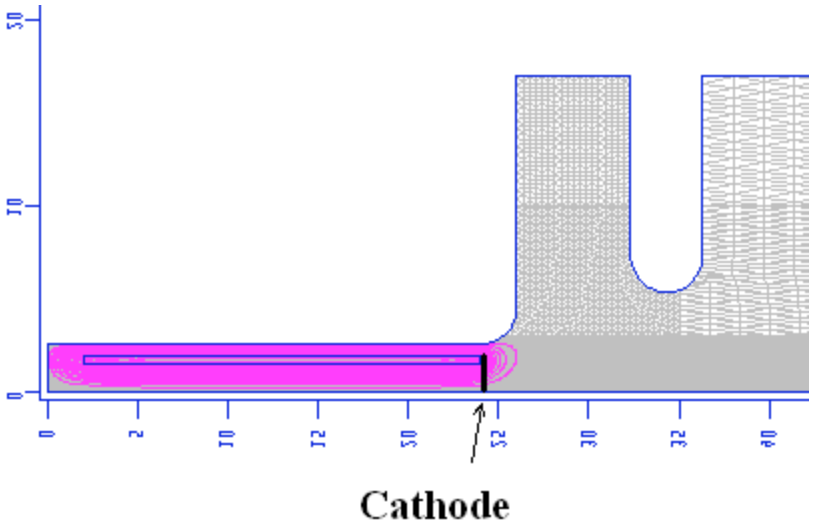

Fig. III.B.2.1.6 The Superfish simulation of the DC magnetic field at the cathode.

The graph of the on-axis longitudinal magnetic field is shown in Figure III.B.2.1.7. The amplitude of the magnetic field drops rather fast from peak value of -160 gauss to few Gauss at about 7 cm from the surface of the cathode.

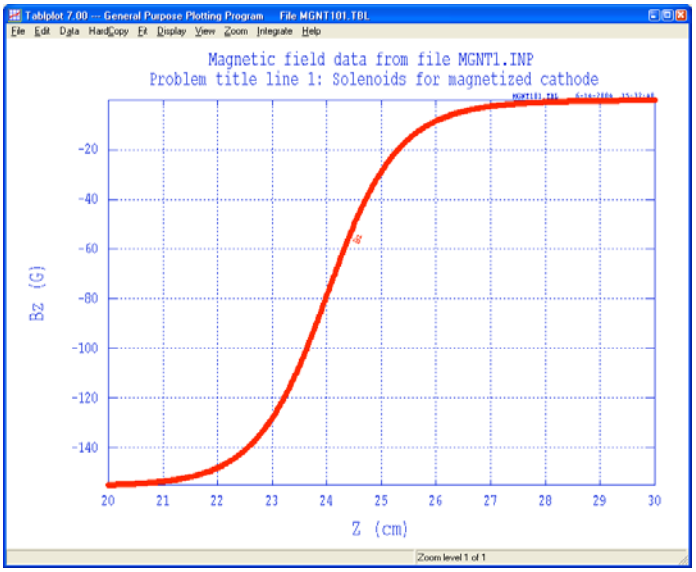

Fig. III.B.2.1.7. The longitudinal profile of the on-axis DC magnetic field in the SRF gun. Z=20 cm correspond to the front surface of the cathode.

The summary of one set of Parmela simulation of electron beam generated in the this gun and propagated through the cavity is given in Table III.B.2.1.1.

Table III.B.2.1.1.

The maximum field on axis E_{axis}	E_{axis} = 29.5MV/m.
The maximum field on cathode E_c	E_c = 13.9MV/m
The maximum field on wall E_{wall}	E_{wall} = 48MV/m
The maximum magnetic field on wall B_{max}	$B_{max} = \mu_0 * H_{max}$=1015 Gs
Laser transverse distribution	Uniform
Beam radius on cathode R_c	R_c = 1cm
Laser longitudinal distribution	Gaussian, σ = 16ps, Full length = ±32ps
Initial phase	35 degrees
Charge/bunch	20 nC
Bunch length after gun exit	σ_z = 5.8mm, Full length = 24mm
Solenoid field on cathode Bc	Bc = 204G
Energy at gun exit E_G	E_G = 4.9MeV
Energy at linac exit E_L	E_L = 55MeV
Normalized Horizontal Emittance at 55MeV	ε_x = 39 mm·mrad
Normalized Vertical Emittance at 55MeV	ε_y = 37 mm·mrad

It is worth noticing that increasing the radius of iris tip can reduce E_{wall}, a change which will not significantly affect the beam dynamics.

III.B.2.2. Photocathode System

The laser and photocathode system for the energy recovery linac must deliver an average current > 100 mA at 9.4 MHz with a pulse duration for ~10 ps, and be built to operate for an extended period of time without need for repair, modification or adjustment. Photoinjectors with photoemitter embedded in the wall of an RF cavity excited by a suitable laser has been shown to deliver very high brightness electron beams. Average currents of ~ 25 mA have been delivered using RF cavities operating at 433 MHz with CsK_2Sb cathode irradiated by 532 nm laser beam [III.B.3]. However, the life time of the cathode was limited significantly due to contamination in normal operating conditions. Cesiated GaAs cathode, another candidate investigated in CW injectors, is limited by the total extractable charge as well as its sensitivity to contamination [III.B.4].

In designing a system that meets the requirements of the ERL several challenges need to be met. The choice of the cathode material is dictated by its ability to deliver the current with high quantum efficiency (QE), lifetime, reliability and ease of preparation. The laser system must be designed to meet the energy requirements mandated by the quantum efficiency, pulse duration and energy density matched to optimum beam transport for low emittance and repetition rate suited for the interaction.

Several R&D projects are underway investigating the best approach to generating the desired current while building a reliable system that can be operated at the most reasonable cost both in terms of dollars spent as well as manpower required to operate and possible downtime due to repair and maintenance. The research is focused on two main aspects of the injector, the photocathode and the laser, with additional thought being given to the interface of the photocathode to the photoinjector.

The cathode required for the ERL must meet some very stringent requirements which previously have been very difficult to obtain. The design parameters require a cathode with a long lifetime (months of continuous operation) and high quantum efficiency (~5 %) at an easily attainable laser wavelength (532nm, 355 nm). High QE and long lifetime have been mutually exclusive in the past and as such it is even more important to properly design all components of this system.

III.B.2.2.1 Multialkali cathode

Cathodes usually fall into two different categories, long lifetime, low QE, (i.e. Cu, Mg, Nb) or short lifetime, high QE (multialkali, cesiated metal/semiconductor). The work function of the metal cathodes is in the range of 4-5 eV, requiring UV photons for photoemission. Laser systems that meet the energy and power requirement of such a cathode will be very complicated and prohibitively expensive even if it can be designed and built. Due to the high average current of the ERL, a significant amount of laser power may be required, even with a high QE cathode. Table III.B.2.2.1 shows a list of possible cathodes for the ERL along with the QE at the given wavelength and the laser power needed to obtain the desired current based on equation (III.B.1).

$$QE[\%] = \left(\frac{I}{P}\right) * E_{ph} * 100 \qquad \text{(III.B.1)}$$

where I is the current from the photocathode, P is the laser power and E_{ph} is the laser photon energy in eV.

Table III.B.2.2.1. Review of high QE cathode materials and relevant parameters

Cathode Material	Desired current	Average QE (%)	Laser Wavelength (nm)	Laser power needed
CsK_2Sb[a]	200 mA	3	532	15.5 W
CsK_2Sb[a]	200 mA	9	355	7.7 W
Cs_3Sb[a]	200 mA	2	532	23 W
Cs_2Te[b]	200 mA	10	266	9.3 W
Cs-GaAs[c]	200 mA	10	765	3.0 W (Long decay time)

a) experiments carried out at BNL by authors
b) http://ucq.home.cern.ch/ucq/cathodes_alcalines.htm#telluride
c) R. Calabrese et al. NIM A 340, (1994), 109

The photocathode research projects for the ERL are focused on multialkali cathodes and their derivatives, specifically on CsK_2Sb. This research will be in parallel to the ongoing investigation of GaAS-Cs cathode at TJNAF on DC injectors.

A three chamber UHV deposition system capable of maintaining vacuum levels of 10^{-11} has been designed, and built with a deposition, storage and test chamber. Preliminary measurements are aimed at establishing the operating parameters of the cathode, such as the QE, lifetime, surface current uniformity, ability to deliver high current density and high current. A number of CsK_2Sb cathodes on molybdenum substrates have been fabricated and their QE are shown in Figure III.B.2.2.1 while Figure III.B.2.2.2 shows the uniformity of emission over the cathode diameter.

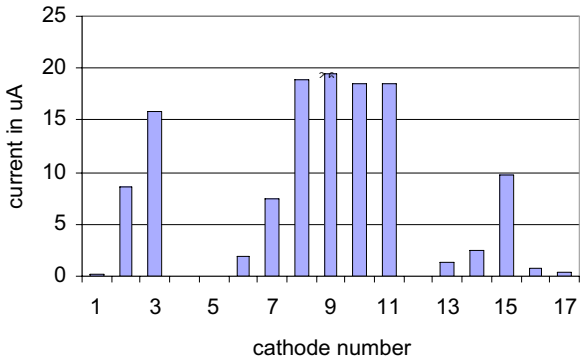

Figure III.B.2.2.1 Reproducibility and QE of the CsK_2Sb cathode at 545 nm.

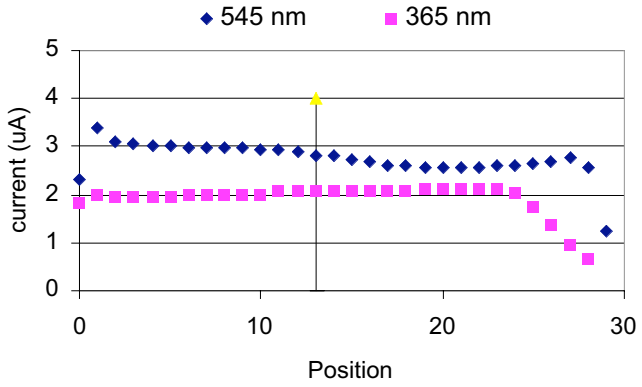

Figure III.B.2.2.2 Emission uniformity of the CsK_2Sb cathode at 545 nm and 365 nm.

Both the CsK_2Sb and GaAS-Cs cathodes are sensitive to contamination and their performance degrades rapidly in pressure > 10^{-9} Torr. As shown in Figure III.B.2.2.3, our present research shows that in a test stand with $2x10^{-10}$ Torr vacuum a CsK_2Sb cathode can maintain its initial QE for over two months. In addition, the QE does not degrade even with the emission of >1400 C/mm^2 thus suggesting that if similar vacuum conditions are met in the injector, life time would not be a limiting factor.

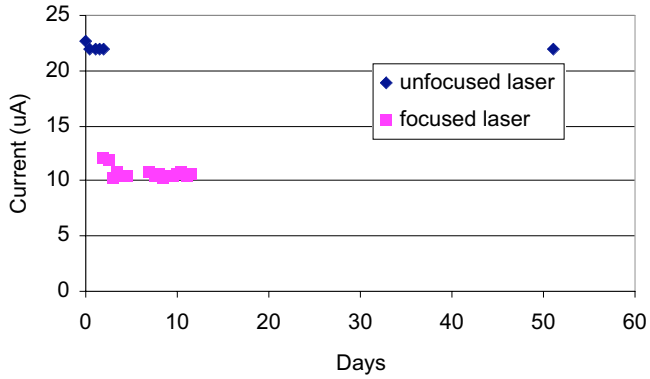

Figure III.B.2.2.3 Lifetime studies of the CsK2Sb cathode using both focused and unfocused laser light at 545 nm.

The second consideration in choosing a cathode material is the wavelength at which photoemission is achieved. Figure III.B.2.2.4 shows the dependence of QE on the wavelength. The QE at either 532 nm or 355 nm is quite good and both these wavelengths with desired powers can be generated by frequency multiplying the output from commercial Yttrium based lasers to deliver 100-200 mA current. The role of the substrate material and the sensitivity to out gassing will be the focus of future research on

this system. Since all the preliminary measurements are encouraging, the base line design of the ERL will assume CsK_2Sb cathode and 535 or 355 nm radiation.

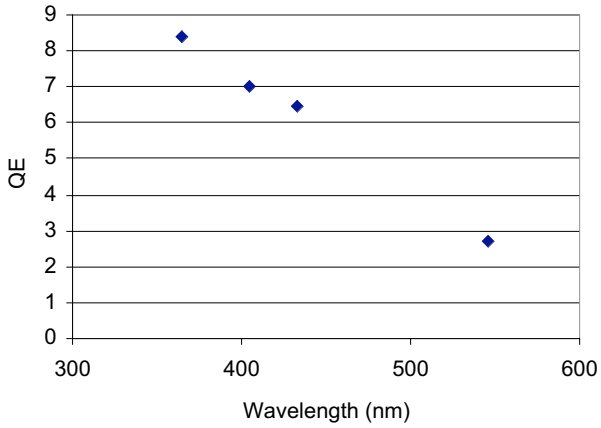

Figure III.B.2.2.4 The QE of the CsK_2Sb cathode as a function of wavelength using a monochromator and Hg arc lamp.

III.B.2.2.2 Diamond Secondary Emission

As seen from Table III.B.2.2.1, even with reproducible 3% QE of CsK_2Sb under 532 nm, the laser power required to deliver 200 mA is rather high and although attainable, the laser system producing this power is complicated and expensive. One alternative to reducing the laser power is to use an electron amplifier such as a high yield secondary emitter. In this approach, the primary and secondary emitters are part of the RF injector. The laser irradiates the primary emitter to release primary electrons that are accelerated to a few keV by the RF field. These electrons impact the secondary emitter, which amplifies the number of electrons. The secondary electrons then drift towards the cavity guided by the RF field, and are emitted into the cavity for further acceleration. Figure III.B.2.2.5 shows a schematic of how this system would work.

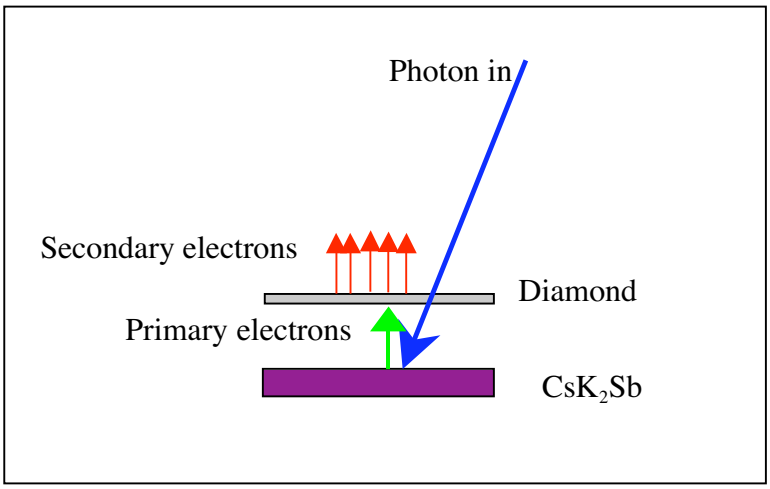

Figure III.B.2.2.5. A schematic representation of the secondary emission process in diamond

This scheme has several advantages over the conventional design of a photocathode in the RF cavity. In addition to reducing the laser power requirements significantly, the secondary emitter isolates the sensitive cathode from the cavity, thereby minimizing the contamination of one by the other. If the two emitters can be encapsulated in vacuum, then the need for complicated load lock system for cathode preparation and insertion can be eliminated. In either case, assembly and construction of a UHV system for either the assembly of a capsule or for the load-lock and interface to the RF injector will require significant engineering and design time.

Table III.B.2.2.2. The diamond secondary emission test plan.

Tests planned	**Primary electron source**	**Significance**	**What outcome will tell us**
Study diamond SE in reflection mode for 20_m and 200_m samples	Electron gun	Confirm operation of test stand	System works
Study diamond SE in transmission mode for 20_m and 200_m samples	Electron gun	Measure SE as a function of sample thickness and voltage bias in a mode similar to that which will be used in the injector	Feasibility of using diamond as a secondary emitter.
Transmission mode studies with cryogenic cooling of diamond	Electron gun	SE as a function of temperature, thermal analysis of diamond and secondary electrons	Further research into use in a SCRF gun that operates at 2 K
Transmission mode studies with cryogenic cooling of diamond and metal	Laser irradiated metal cathode	SE as a function of temperature, thermal analysis of diamond and secondary electrons using	Time dependence of SE as a function of laser pulse duration, moves closer to ERL

cathode		laser irradiation	system
Transmission mode studies with cryogenic cooling of diamond and CsK_2Sb cathode	Laser irradiated cathode	SE as a function of temperature, thermal analysis of diamond and secondary electrons using laser irradiation of actual cathode	Final test stand set-up with real cathode. Make or break for use in injector

This project is still in its infancy but initial research on baseline measurements of different diamond samples is commencing. Specially prepared diamond has shown to be a very effective secondary emitter, with yields up to 100 times the primary electron.[III.B.2.2.3] Preliminary design for the emitter, based on the excellent thermal conductivity, structural strength, ease of boron doping, and favorable electron transport of the bulk diamond is complete. A test chamber to investigate the relevant parameters is being assembled. Table III.B.2.2.2 shows a tentative list of some of the major experiments planned and their significance to using diamond as a secondary emitter in a photoinjector.

If the results are promising, a serious engineering project will have to be planned and executed to design a system of forming a capsule of a thin diamond film over a CsK_2Sb cathode. Even though such a capsule is not necessary for the success of the project, the ability to insert the cathode without a deposition/load lock system simplifies the design of the RF injector and cryostat significantly. The preliminary idea for the capsule design is to have a thin piece of diamond metalized on the edges and then electron beam welded to 1mm spacers and then to the photocathode under ultra high vacuum. By deposition a thin layer of gold or titanium on the diamond surface as well as the spacers there will not be charge buildup on the diamond and if titanium is used it will act as a getter inside of the capsule. Figure III.B.2.2.6 shows a rough sketch of how this capsule may look. This capsule is a key item if the load-lock is forgone since the photocathode cannot be exposed to vacuum of less than 10^{-10} Torr if good performance is expected.

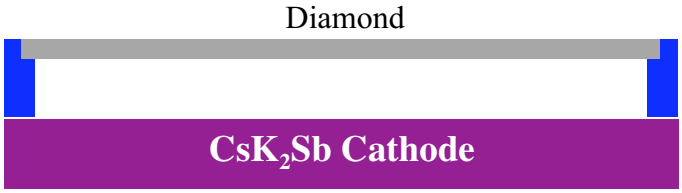

Figure III.B.2.2.6. A CsK_2Sb cathode with a diamond window for secondary emission.

III.B.2.3 Laser System

The laser system that will be required for the ERL will take one of several possible forms based on the photocathode R&D as well as the final decision on which different modes of operation will be carried out with the ERL. The ERL operation entails two modes, one at a low (~100 Hz) repetition rate for tuning the system and executing high charge measurements, and a second mode for routine operation at 9.4 MHz. The laser system should then be capable of delivering a few μJ at ~100 Hz for producing 10 nC as

well as ~ 8 W at 9.4 MHz for producing 100 mA. In addition, it should be upgradeable to at least twice the power for electron cooler.

Discussions with laser vendors (Time Bandwidth Products Inc) point to the following design. The general system will likely be comprised of an oscillator operating at 9.4 MHz followed by a pulse selector for reducing the frequency to the desired 94 Hz for the low current operation of the ERL. This oscillator will be followed by a series of modular pre and power amplifiers. The oscillator will be locked to the RF frequency with a phase stability corresponding to ~ 1 ps. The laser output will then be frequency doubled or tripled depending on the decision to use 532 or 355 nm radiation for photoemission. If the diamond secondary emitter approach is successful, the amplifiers will not be needed. Table III.B.2.3.3 shows a compilation of the possible amplification using diamond and how this affects the laser system.

Table III.B.2.3.3. Laser parameters based on secondary emission from diamond.

Oscillator wavelength	Oscillator freq and power	QE	SEY	QE with SEY	Laser power required with SEY
355 nm	9.4 MHz .4W	9%	30	270%	0.25W
532 nm	9.4 MHz 1W	3%	30	90%	0.52W
355 nm	9.4 MHz .4W	9%	100	900%	0.77W
532 nm	9.4 MHz 1W	3%	100	300%	0.155W

The laser system will be located in the laser room outside the radiation area. The laser room needs to be climate controlled to maintain the temperature (75 +/- 2º F) and humidity (60% +/- 5%) with no turbulent airflow and air cleanliness of ~ 1000 ppm. The beam will be transported to the injector through evacuated beam tubes to minimize exposure to air currents, humidity and dust. The beam trajectory will be monitored using cameras and video monitors, and adjusted using motorized mirror holders. The laser energy irradiating the cathode will be monitored using calibrated photodiodes along the beam line. The position, spot size and profile of the beam on the cathode will be monitored and measured by imaging a fraction of the main beam on a CCD camera a location equivalent to the photocathode.

The entire laser system can be commercially purchased, although custom work will be required by the vendor. The vendor estimates the delivery time to be ~ 10-12 months ARO along with another 6 months allocated for laser installation and testing, transport to the gun and diagnostics. Due to the reliance of the laser system on the approach (primary emitter vs. primary & secondary emitter combination) and the long lead time of the laser system, it is critical that decision on the approach be made by the end of the fiscal year.

III.B.2.4 Third Harmonic (2111 MHz) Cavity for the Injector

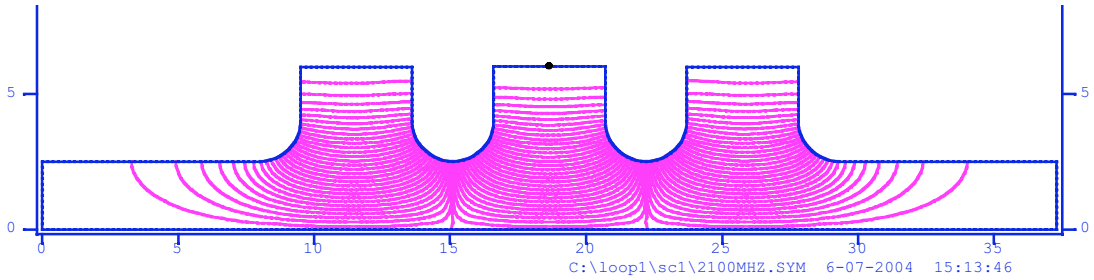

Figure III.B.2.4.1: SUPERFISH output for the SRF 2111 MHz cavity.

Because of the sine-wave dependence of the accelerating field in the gun cavity, the longitudinal kinematics of the electron beam is intrinsically non-linear. Strong space charge forces only increase this non-linearity. We plan using a 2.111 GHz super-conducting RF cavity operating at third harmonic of the gun frequency. This cavity will provides the necessary means to linearise the longitudinal motion and to reduce the energy spread.

One potential advantage of using third harmonic cavity provides for a possibility of using a very primitive merge system comprising of a single dipole magnet (see next section). This option provides of a reasonable degradation of the beam emittance in the direction of the turn by minimizing the energy spread as well an the transverse beam size in the dipole.

The prototype ERL will not use 3-rd harmonic RF system and instead will study a use of more elaborate lattice of the merging system, which preserve transverse emittances for a space charge dominated beams. If this design proves to be successful, it may eliminate the need for 3-rd harmonic cavity in the injector.

In any case, the 3-rd harmonic cavity can be used to minimize the energy spread in the e-cooler and remains a part of the studies for the e-cooling project. Fig. III.B.2.4.1 shows the SUPERFISH calculation of a prototype 3-cell 2111 MHz cavity .

III.B.2.5 System for focusing and merging beams

A critical part of the injection line into the linac is the merge of the low energy bunches coming from the gun to be accelerated in the linac and the high energy bunches coming from the cooling section to be decelerated. As the low energy beam is strongly affected by space charge the merge must be designed to minimize the degradation of the emittance. A typical system of this type has two properly spaced focusing solenoidal magnets used for the emittance compensation. A significant ratio ~ 10 between energies of merging beams allow a rather straight-forward system of dipoles and solenoids.

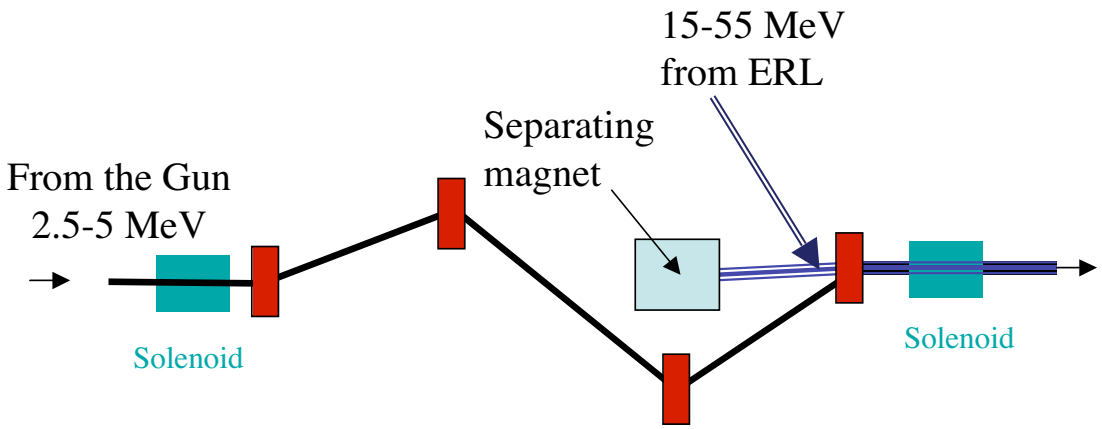

Figure III.B.2.5.1 A merging system comprised of four chevron-type magnets, which is compensate the dispersion effects for space charge dominated beam. Parmela simulations for 3.9 MeV beam from 1 1/2 cell gun with1 nC per bunch shows equal x and y normalized emittances at the level of 2.5-3 mm·mrad at the exit of this merging system.

Focusing of the bending magnets in the merging section has significant effect on the low energy electrons. Hence, the use of chevron magnets with equal focusing strength in x- and y- direction is preferable. One of possible merging schemes, which preserves the emittance of the low energy is shown in Fig. III.B.2.5.1. This system provides a minimum set of elements (4 magnets) for this compensation. A more sophisticated systems with additional focusing solenoid. The principle of this system is based on cancellation of four correlation functions *{x,E},{x',E},{x.t}* and *{x',t}* at the exit of the merging system (chicane).

Since the particle energies change rather dramatically in the ERL's linac, it is very desirable that the effect of the magnets on the e-bema to be compensated locally. This is the current direction for the R&D ERL.

The present design of the merging system e-cooling ERL is based on the simplest device to -a dipole magnet that bends the low energy beam by ~ 30 degrees, while bending the high energy beam by a few degrees. This dipole is the source of dispersion in the low energy beam transport, which degrades the horizontal emittance. In this case the focusing after the first dipole is done by a pair of solenoids with opposing fields instead of a single solenoid. This avoids any coupling of the horizontal dispersion into the vertical direction. A strong septum magnet bends the high energy beam in the place where the separation of the beams is 7 cm.

This is the design where harmful effect of the emittance degradation caused by a single magnet is simply ignored and it is heavily relies on using the 2111 MHz cavity for reducing the energy spread of the beam when it crossing the dipole magnet. This method has additional requirement that the electron beam will have a very narrow waist in the merging dipole. These strict requirements limit the chose of the emittance compensations schemes and can limit performance of the gun. In addition, it will most probably limit range of the beam parameters (such as charge per bunch) this system can tolerate. It also

force on to focus the beam well before the optimal position, i.e. the entrance of the accelerating linacs (see explanation in the following section).

A simple-minded application of known compensated chicanes and other achromatic lattices used for a low intensity beam to the ERL where space charge dominates the beam dynamics is very limited. For example, one of the known achromatic turn is a two dipoles with a focusing solenoid in the middle does not work to the space charge dominated beam where the energy spread changes along the beam line. In addition, the need to focus beam sharply (focal length of the solenoid is only one fourth of the distance between the magnets) cases a very small waist of the beam and dramatically increase the nonlinear space charge effects.

Overall, the design and the development of the merging system for a low emittance, large charge and low energy beam remains the part of the e-cooling R&D program.

III.B.2.6 Emittance Compensation

Emittance compensation is a well known method to improve the beam quality of photo cathode guns. Due to space charge and time dependent fields the longitudinal slices of the bunch experience different focusing and therefore different phase advance. By focusing the beam into a waist the emittance compensation scheme utilizes the space charge to reverse this process. At the point where the phase advance of the slices lines up the beam is accelerated by the linac cavities so that the space charge becomes negligible and the emittance is “frozen”. Fig. III.B.2.6.1 illustrates the development in phase space.

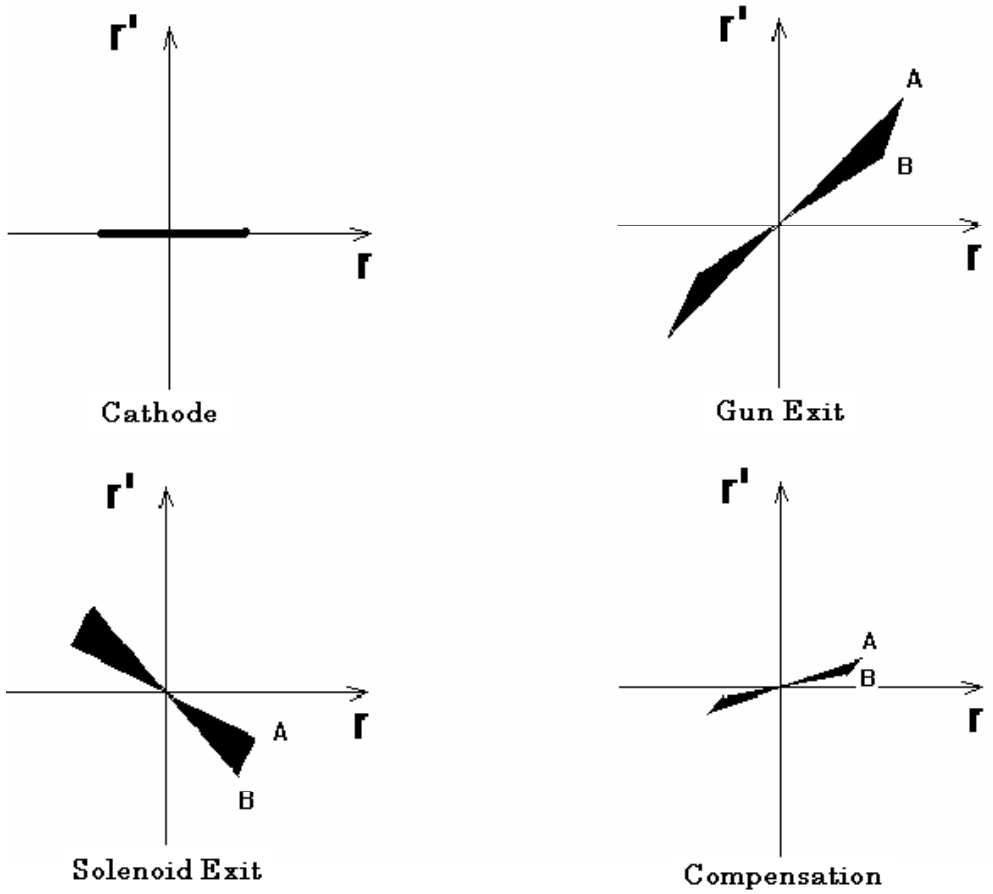

Figure. III.B.2.6.1: Phase-space evolution of a bunch from a RF photocathode gun.

For magnetized beams the emittance compensation scheme must be extended. The emittance relevant to cooling is the emittance inside the cooling solenoid. The fringe field stops the rotation of the beam around the longitudinal axis. Since the rotation speed is dependent on the change of the bunch cross section it is important to keep this change constant over the length of the bunch, so that the fringe field stops the rotation for all longitudinal slices. Fig. III.B.2.6.2 illustrates how in a magnetized beam the emittance increases without proper compensation.

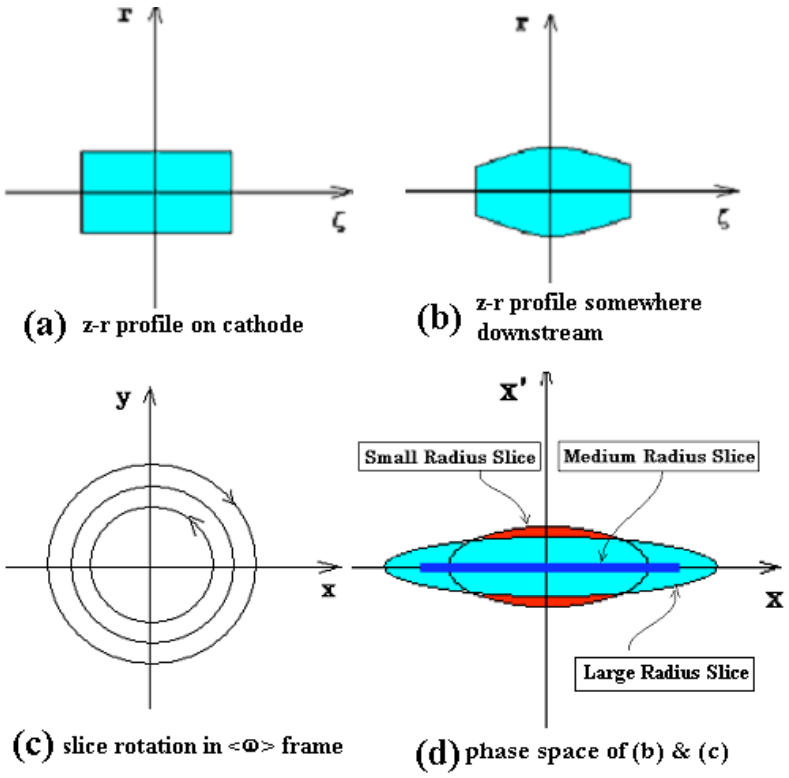

Figure. III.B.2.6.2: (a): ζ-r profile on cathode. The distribution of transverse-charge density is assumed to be uniform; the longitudinal charge-density distribution can be Gaussian. (b): ζ-r profile after some transport. The change in shape is caused by the longitudinal charge distribution. (c): Rotation of longitudinal slices in the frame of average rotation (<???> frame). (d): Phase space in the <???> frame ignoring the radial motion.

The proper compensation scheme for magnetized beam is described in [III.B.5]. Fig. III.B.2.6.3 shows the emittances in the rotating frame. The propagation of the magnetized beam has some specific consequences: The strong space charge and the fringe field of the cathode solenoid lead to a strong divergence of the electrons inside the gun. It is not possible to use magnetic focusing of the beam inside the gun. However, it is possible to get some focusing from the electric field. This is done in two ways:

1. By shaping the cavity in the cathode area a gradient of the radial field is created. This is especially effective because the electrons still have low energy in this area. The drawback is that the field gradient on the cathode is lowered by this method.

2. At the end of the first (half) cell is a defocusing gradient, followed by a focusing gradient in the beginning of the second cell. By choosing the phase so that the electrons pass the defocusing while the field is close to zero the defocusing is minimized and the focusing is enhanced. Some of the acceleration (and emittance) is sacrificed with this method.

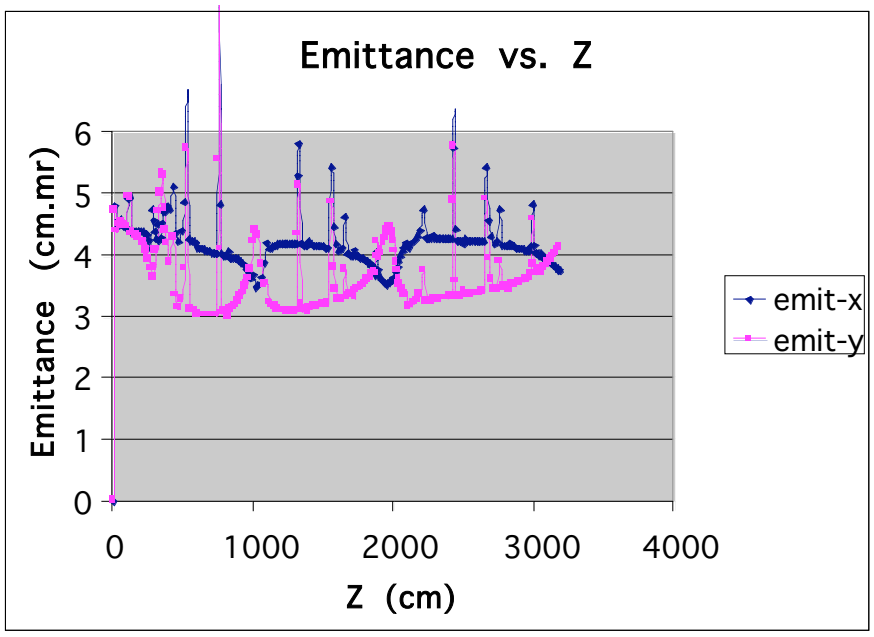

Figure III.B.2.6.3: Horizontal and vertical emittance in the frame of average beam rotation from the gun to the linac. The spikes are artifacts of the PARMELA tracking calculation. The difference between horizontal and vertical emittance comes from the dispersion introduced by the merging magnet.

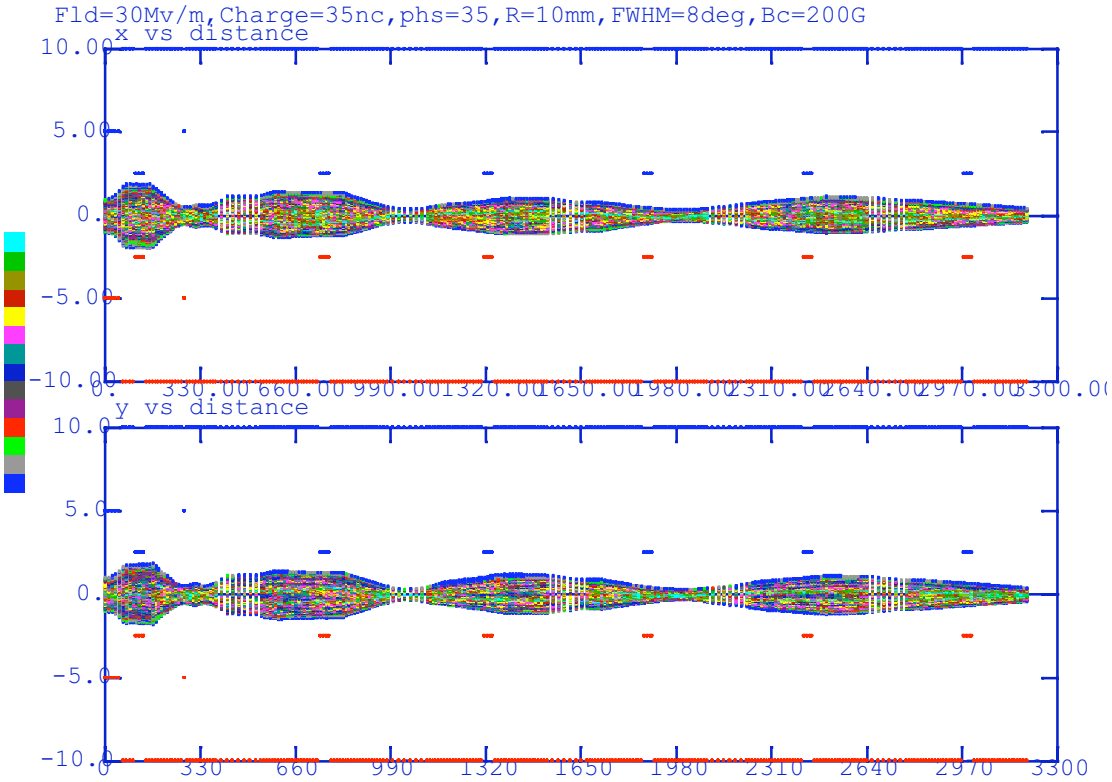

Figure III.B.2.6.4. Parmela calculation of the beam envelope from the gun to the linac

Figure III.B.2.6.4 shows the envelope calculated with PARMELA. In this calculation the spot radius on the cathode is 1 cm and the field is 200 Gauss. This corresponds to a 2 Tesla field and a 1 mm beam radius in the cooling solenoid.

III.B.2.7 Back-up Options for the Gun

A 2 and 1/2 cell normal conducting RF gun powered by a 1MW 700 MHz klystron is considered as a possible back-up option. The advantage of the normal-conducting (copper) gun is that the beam can be focused inside the gun by immersing the gun in a solenoidal field. The disadvantage is the low gradient on the cathode, which limits the bunch charge.

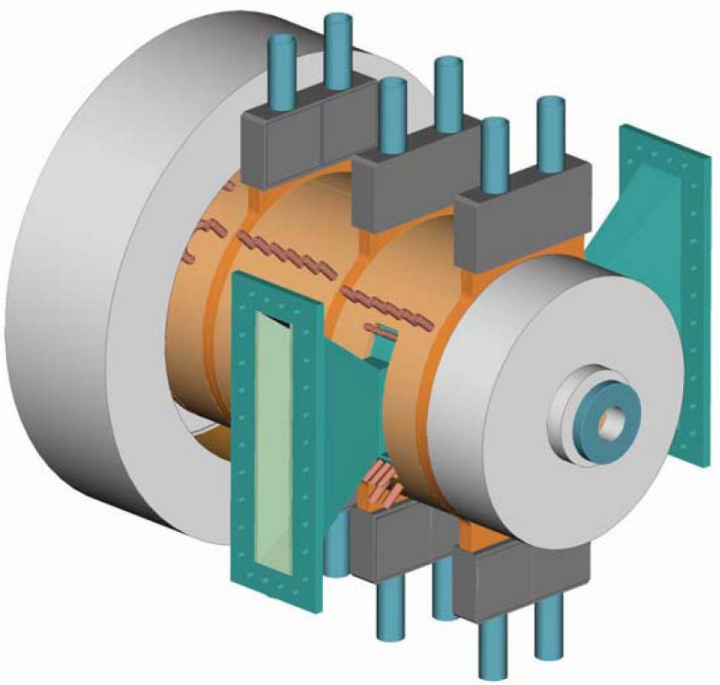

Figure III.B.2.5.1 A room-temperature CW 703.75 MHz gun developed by LANL.

The normal-conductive 2.5 cell gun was designed by AES for LANL. Due to the resistance of the wall 750 kW of RF power is dissipated in heat, leaving 250 kW to power the beam. With a bunch charge of 10 nC (100 mA) the electron energy at the exit of the gun is 2.5 MeV. The peak field in the gun is limited by the available power; the field on the cathode is 9 MV/m. The SUPERFISH calculation of the fields is shown in Fig III.B.2.5.2. The transverse emittance of the beam (in the cooling section) was calculated with PARMELA to be 45 mm mrad.

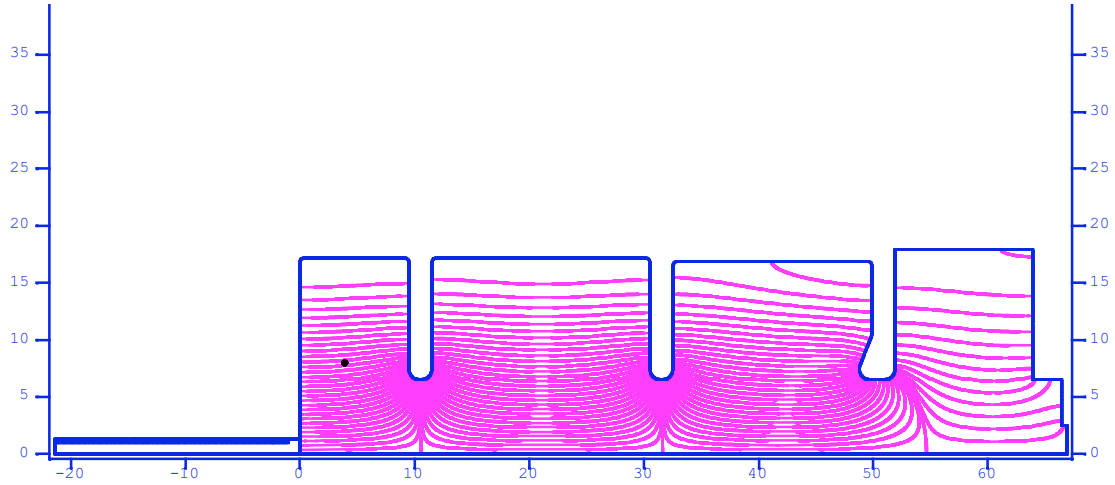

Figure III.B.2.5.2: SUPERFISH calculation of the 2.5 cell normal-conductive gun and the power coupler.

In addition, there is a possibility of using a DC photocathode gun as a back-up (see sketch below). The DC gun developed on similar principle did operated with the CW beam current up to 28 mA at BINP (Novosibirsk). BINP is presently developing a concept of similar gun with average currents ~ 100 mA. The main drawback of this gun is relatively large emittance.

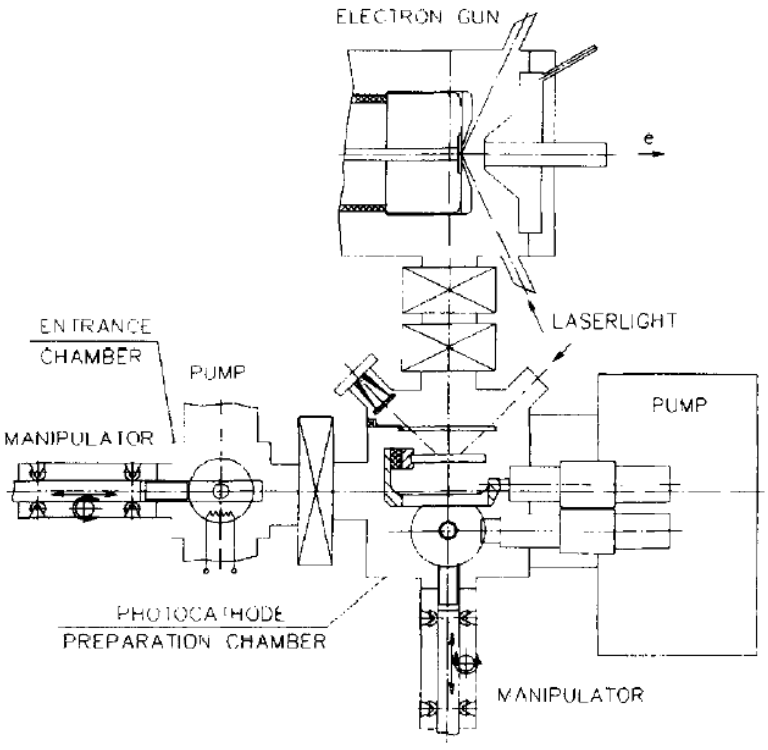

Figure III.B.2.5.3: A sketch of BINP's DC photocathode gun.

III.B.3 SUPER-CONDUCTING RF LINAC

Both the e-cooling and the prototype ERLs have linac based on a high current 5-cell super-conducting 703.75 MHz RF cavities equipped with effective HOM dumping system. The prototype has only one 703.75 MHz SRF cavity.

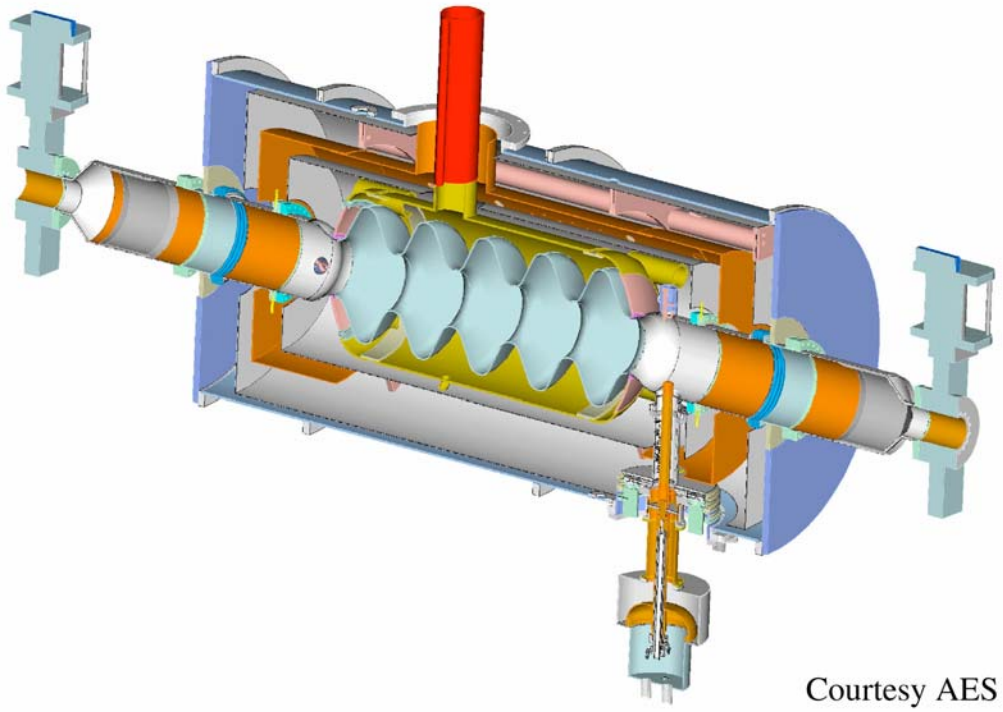

Fig. III.B.3.1 A 3-D view of the 5-cell SRF cavity design with complete cryomodule.

In the e-cooling ERL linac has four 703.75 MHz SRF cavities accelerating the beam to 54.7 MeV. The bunch length is approximately 4 cm or 15 degrees of 703.75 MHz. Because of the cosine dependence of the accelerating field, the off-crest electrons gain less than on-crest electrons. Hence, electron bunch has intrinsic energy spread, which is corrected by three 2111 MHz SRF cavities. The third harmonic cavities are phased to decelerate the beam. The combined functions of the fundamental and 3rd harmonic cavities provide for increased range of uniform accelerating gain. The 703.75 MHz cavities will operate at 15 MV/m, the 2111 MHz cavities will operate at the gradient 8 MV/m. The resulting energy spread of the electron beam at the exit of the linac is $4 \cdot 10^{-4}$.

It is important to notice that the 2111 MHz cavities should be located in the middle of the linac. Placing them at the end of the linac would create a problem: the beam would

lose all energy during the deceleration in the 703.75 MHz cavities and would not reach the end of the beam dump.

III.B.3.1 Phasing of the cavities

First, the accelerating cavities should be phased with the electron gun to accelerate the fresh beam. In addition, the overall time lapse for the returning beam should be equal to an odd number of the RF cycles to be decelerated. This feature is identical for both ERLs: the e-cooler's and the prototype. Still, the e-cooler has multiple linac cavities operating both the fundamental and third harmonics of 703.75 MHz. Furthermore, the electron beam in the e-cooler ERL must be stretched to match the length of the ion bunch. It imposes additional requirements for the phasing and the longitudinal kinematics in the ERL:

> During the acceleration, the over-all phase must be set of-crest so that the beam at the end of the linac has a correlated energy spread (a chirp) of about ±1%. In this case, passing through the stretcher elongates the bunch to about 1 nsec. Finally, the low frequency RF cavity (operating at ~ 235 MHz, a sub-harmonic of the fundamental frequency sufficiently) will take the energy chirp off to reduce the resulting energy spread in the cooler.
>
> It is also important to notice that after interaction with ions electron beam is bunched to its original duration via bunching low frequency RF cavity and the buncher – a copy of the stretcher. The energy chirp of about ±1% introduced by the bunching cavity has opposite sign of that in the stretcher – hence, the same lattice provides for bunch reduction instead of the stretching. The resulting short electron beam enters the linac in decelerating phase.

The returning beam must be decelerated by depositing into each cavity the same amount of energy it took during the acceleration. Each 5-cell 703.75 MHz cavity is fed by individual RF transmitter with maximum RF power of 50 kW. Most of this power will be used for maintaining the constant accelerating gradient, i.e. to compensate for fast oscillations of the resonant frequency of the SRF cavity caused by micro-phonics, vibrations and acoustic noise. Only small potion of this power (~20%) can be used to compensate for a phase mismatch of the returning beam. With a beam current of 200 mA and an energy gain of 15 MeV per cavity it corresponds to the maximum phase mismatch of ±2 degrees (i.e. about ±2 mm in the distance)

Table III.B.3.1.1 Energies of accelerating and decelerating electron beam between the cavities in the ERL linac: injection energy 4.5 MeV, e-cooling energy 54.68 MeV

Energy	*accelerating*	*decelerating*
E_1 (MeV)	17.04	42.13
E_2 (MeV)	29.59	29.59
E_3 (MEV)	42.13	17.04

One component contributing into the mismatch is the difference in velocity of the accelerating and decelerating beams in the region between the cavities. The maximum difference is between the first and second and between the third and forth cavities: it corresponds to a change of 1º in RF phase per 3.15 meters of length.

III.B.3.1.1 Longitudinal stability

The typical instability in longitudinal direction is the Robinson instability, when a small deviation of the beam energy from the designed energy caused exponential run-off. The stability criterion depends on the sign of the momentum compaction factor (longitudinal dispersion – the correlation of the particle energy with the round-trip time) and the effective decelerating phase. In the prototype ERL, the sign on the momentum compaction factor can be chosen either positive or negative – hence the possibility to operate with decelerating phases of-crest in both directions.

The present design of the e-cooling ERL (including stretcher, de-bunching cavity, bunching cavity and compressor) has slightly negative momentum compaction factor, i.e. particle with higher energy has faster round trip time compared with an elercton having the nominal energy. In order to overcome the Robinson instability the bunch receiving too much energy during acceleration must deposit less energy during the decelerating. Detailed studies show that with the proper adjustment of the accelerating gradient of the bunching cavity, the phase of –0.3 degrees provides for stable operation of the e-cooler ERL.

III.B.3.2 The 5-cell SRF cavity

This chapter describes an optimized design of a cavity aimed at energy-recovery linac operation at an unprecedented level of current. The 5-cell 703.75 MHz SRF cavity is designed to operate with very high average electron beam currents from hundred mA to few amps. This requirement imposes a number of specific technical solutions including a very large aperture of the vacuum pipe with provides high efficiency coupling of all cavity's higher order modes (HOMs) to the dedicated ferrite absorber. This feature is the key for stable operation of the ERLs with high current electron beams.

A first prototype design of 5-cell SRF cavity has been approved for manufacturing. The production is a joint effort of and Advanced Energy Systems and BNL's Collider-Accelerator Department [III.B.7].

Specifically, the HOMs are one of the dominating factors influencing the performance and operation of a cavity:

• Multi-pass, multi-bunch instabilities driven by high impedance dipole modes resulting in beam-breakup.

• Power loss into the HOMs, which must be removed safely from the cavity and cryogenic system.

III.B.3.2.1 Design criteria

Several factors influenced the choice of key parameters of the cavity:

- A frequency choice of 703.75 MHz was made due to both physics and engineering issues. This is the 25th harmonic of the RHIC bunch repetition frequency with 360 buckets. A small loss factor from HOMs and the possibility of a larger aperture were important criteria. Also, engineering issues such as availability of high power CW klystrons and chemical cleaning facilities played an important role. A potential future use of this cavity in a linac-ring version of eRHIC (electron-ion collider) was also considered.
- A five cell structure with a large aperture of 19 cm was chosen in the original design [III.B.8]. This choice was made in order to optimize the cavity for the best possible damping of higher order modes. However, after further investigation, the aperture of 17 cm was found to provide higher acceleration efficiency while effectively damping all HOMs.
- Ferrite absorbers have proven successful in single cell cavities (CESR & KEKB). Following the Cornell design, we adopted the use of ferrites in a 5-cell linac cavity. We will demonstrate that such HOM absorbers are adequate to damp all modes in our multi-cell cavity that might lead to beam instabilities. We plan to use two ferrite absorbers located along the beam pipe at room temperature. We also plan to install HOM couplers which may prove useful if we find unexpected trapped modes that weakly couple to the beam pipe.

III.B.3.2.2 Geometry

The cavity geometry was constructed by the ``Build Cavity code'' [III.B.10], a graphics interface software to Superfish. It allows the user to specify multi-cell cavity parameters and optimizes the cavity geometry through a series of Superfish runs. The new design of the 17 cm aperture with 24cm beam pipe diameter is Fig. III.B.3.2.2.1

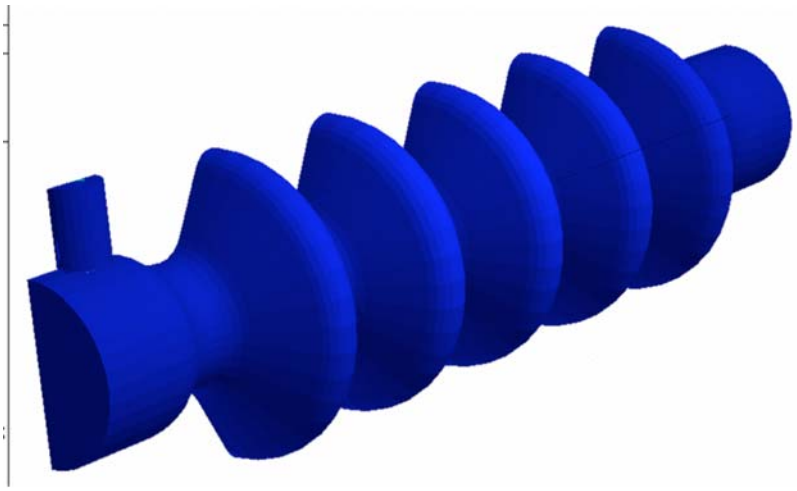

III.B.3.2.2.1. Five cell cavity design with 17 cm iris and 24 cm beam pipe.

Ferrite absorbers are 24 cm in diameter and 20 cm in length located outside the cryostat at room temperature. The ferrite material used is Ferrite-50 and is being manufactured by ACCEL according to the Cornell design [2.1.14]. Various parameters of the five-cell cavity are shown in Table III.B. 3.2.2.1. The optimum iris diameter of 17 cm is compared to an earlier choice of 19 cm.

Table III.B.83.2.2.1 Cavity Characteristics

Diameter(cm)	*17 cm*	*19 cm*
Freq (MHz)	703.75	703.75
G (Ω)	225	200
R/Q (Ω)	807	710
Q @ 2K°	$4.5 \cdot 10^{10}$	$4 \cdot 10^{10}$
E_p/E_a	1.97	2.10
H_p/E_a(mT/MV/m)	5.78	5.94
Cell to cell coupling	3%	4.8%

For the calculation of Q at 2K°, we assume R_{BCS} = 3 nΩ and $R_{residual}$ = 2 nΩ.

Field flatness and surface fields for the fundamental modes, calculated using 2D FEM code [III.B.11], are shown in Fig. III.B.8.1.2.

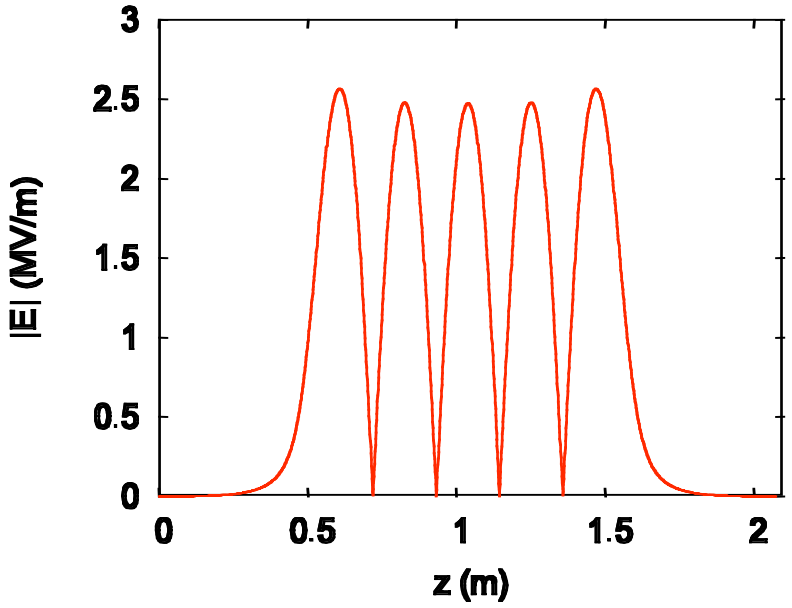

III.B.8.1.2 Field profile of fundamental mode, peak-to-peak 96.5 %.

III.B.3.2.3 Higher Order Modes

Rigorous analysis of modes in a cavity is necessary to develop an efficient design. The complex structure of multi-cell cavities often cause modes to be trapped inside the cavity, thus limiting the performance due to beam instabilities. There are two main reasons for HOMs to become trapped inside the cavity structure:

- Small irises may result poor cell to cell coupling and cause HOMs to get trapped inside structure.
- It is also possible to find HOMs below the cutoff frequency of the beam pipe, preventing the mode from propagating out of the structure. These modes exponentially decay in the beam pipe before they reach the ferrite absorbers.

It is very important to carefully analyze such trapped modes and to modify the cavity structure to propagate them. It is common practice to use HOM couplers to couple out some harmful modes that exist in these complex structures. A preliminary design for couplers is underway. However, we propose a cavity design that will demonstrate the possibility of a high current operation with just ferrite absorbers placed in the warm section, thus minimizing cryogenic losses and simplifying critical engineering issues.

III.B.3.2.4 Analysis of Trapped Modes

III.B.3.2.4.1 Loss Free Case

In this method, two different boundary conditions (electric/magnetic) at the cavity ends are used to solve the eigenvalue problem in MAFIA. The corresponding frequencies are calculated and the influence due to change in boundary conditions is used to infer the presence of possible trapped modes. The factor k given in equation 1, is a measure of relative field strength between the middle cells and end cell.

$$k = \frac{1}{2}\left(\frac{f_{mag} - f_{ele}}{f_{mag} + f_{ele}}\right); \qquad \log(k) \approx \begin{cases} 0: & untrapped \\ \infty: & trapped \end{cases}$$

THIS CALCULATION WAS PERFORMED FOR 3 DIFFERENT CONFIGURATIONS AND THE RESULTS ARE SHOWN IN FIG. III.B.3.2.4.1.1. IT IS CLEAR FROM THE PLOT THAT THE CONFIGURATIONS USING 17 CM IRIS WITH 24 CM BEAM PIPE DIAMETER IS IDEAL TO PROPAGATE ALL MODES, ESPECIALLY THE LOW FREQUENCY ONES WHICH CONTRIBUTE TO INSTABILITIES. A SIMILAR CALCULATION USING BOUNDARY CONDITIONS WERE ALSO PERFORMED FOR MONOPOLE MODES AND FIG. 2.1.0.3.1.1 SHOWS LOG(1/K) AS A FUNCTION OF FREQUENCY. THE *R/Q* VALUES FOR THE CAVITY MODES CAN BE EASILY COMPUTED USING P-MODULE IN MAFIA. IT IS MOST DESIRABLE TO DESIGN A CAVITY WITH HIGH FUNDAMENTAL *R/Q* WHILE KEEPING THE *R/Q* FOR DIPOLE MODES AS LOW AS POSSIBLE. WE FIND THAT *R/Q* VALUES FOR DIPOLE MODES ARE QUIET SMALL FOR OUR GEOMETRY.

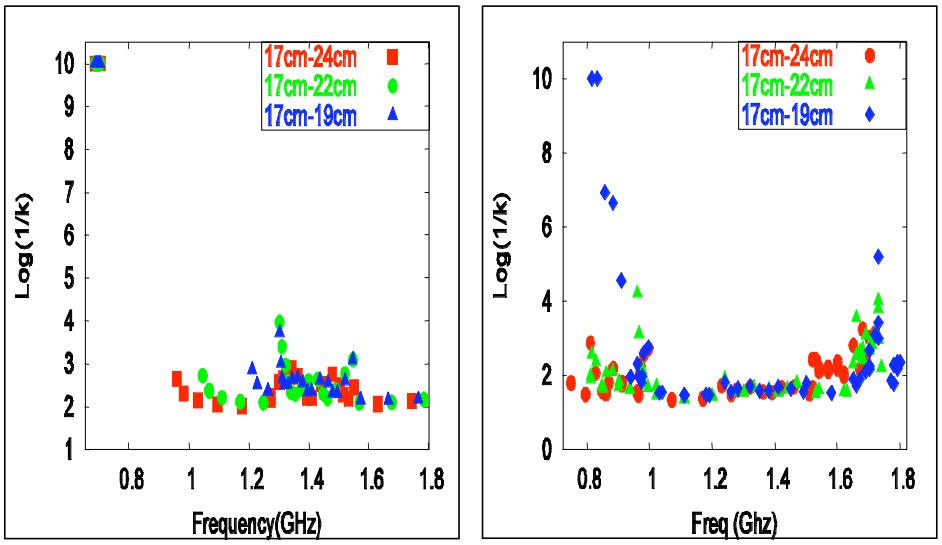

FIG. III.B.3.2.4.1.1. ANALYSIS OF TRAPPED MONOPOLE AND DIPOLE MODES IN 17 CM GEOMETRY. NOTE FUNDAMENTAL PASS BAND AT 0.7 GHZ WITH HIGH VALUES.

III.B.3.2.4.2 LOSS CASE

In the case with losses, the calculations become significantly complicated and long. E-module offers two different possibilities for solvers, a complex invariant of the generic solver and the inverse solver. We use the inverse solver as recommended by the user's manual and also due to the fact that the generic solver failed to give coherent results with complex shapes such as ours. We performed a calculation of dipole Q's with both generic (SAP) and inverse solvers without beam pipe modifications and found that they agree pretty well, as shown in Fig. III.B.3.2.4.2.1.

The discrepancy around 2 GHz is due to simulation accuracy. To calculate accurate results around 2 GHz, one has to calculate modes to much higher frequency.

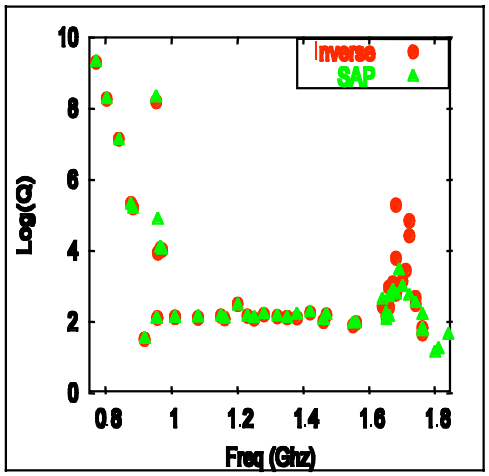

FIG. III.B.3.2.4.2.1. DIPOLE Q COMPARISON OF INVERSE AND SAP SOLVERS IN MAFIA USING 19 CM GEOMETRY.

III.B.3.2.4.3 Quality Factor (Q) of modes

Using the inverse solver we can determine the real and imaginary frequencies of the cavity modes and calculate their *Q's*, given by

$$Q = \frac{F_{real}}{2F_{imag}}$$

The Q values of the dipole modes can give a direct indication of possible trapped modes. Since small geometry changes do not change R/Q significantly, one can take advantage of this fact to cleverly shape the cavity to damp Q significantly without changing R/Q by a large amount. This allows one to have a better control over multibunch instabilities at high current operations. We investigate such a possibility of modifying our cavity design to damp Q's of dipole modes.

Detailed calculations using the original 19 cm geometry were performed and a 4 TE_{11x} like modes (740-760 MHz) and 3 TM_{11x} like modes (950-970 MHz) were found to have frequencies below the cutoff frequency of the beam pipe.

The cutoff frequency for a cylindrical waveguide is given by

$$f_c = \frac{c}{\pi D} X$$

where c is the speed of light and X is the root of the Bessel function or its derivatives as appropriate. Table III.B.3.2.4.3.1shows cutoff frequencies for a few diameters of interest.

Table III.B.3.2.4.3.1 Cutoff frequencies for different types of modes.

D(cm)	*TM01(MHz)*	*TE11(MHz)*	*TM11(MHz)*
17	1350.94	1034.11	2152.5
19	1208.74	925.28	1925.9
24	956.92	732.51	1524.7

It is clear from the above Table that an increase in aperture to 24 cm is required to propagate the TE modes, but a further enlargement to propagate the TM modes is not feasible. HOM couplers would be required to extract these modes. MAFIA calculations using different apertures were performed and Fig. III.B.3.2.4.3.1 demonstrates the Q behavior as a function of aperture.

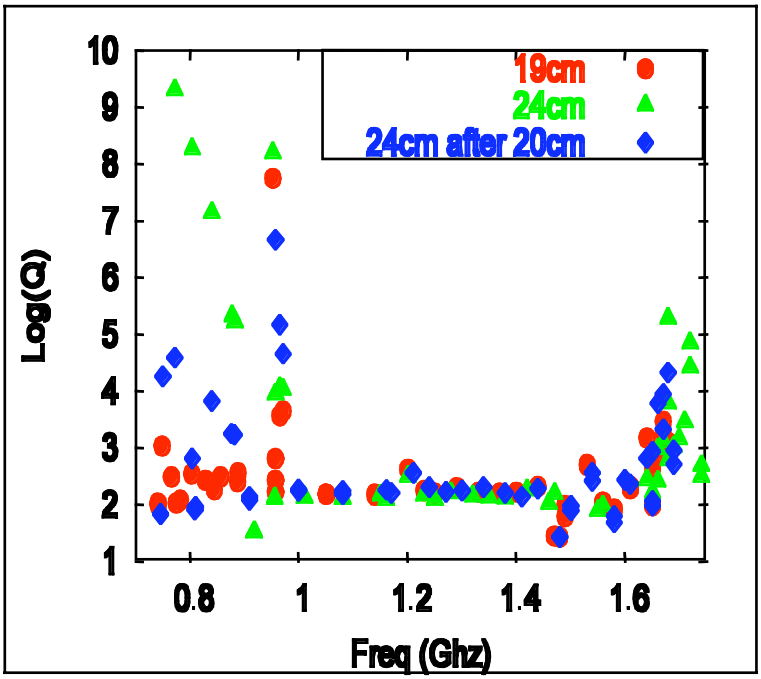

Fig. III.B.3.2.4.3.1. Dipole Q dependence for 19 cm geometry.

The results from the 19 cm geometry prompted us to investigate a new cavity design with a smaller iris. The motivation was to increase the fundamental mode efficiency at the cost of trapping a few more HOMs that can be extracted using the HOM couplers. However, calculations with the new 17 cm geometry revealed quite spectacular results. The shunt impedance was increased by 10% and a beam pipe modification to 24 cm revealed a virtually HOM free cavity. Fig. III.B.3.2.4.2.2 shows Q of dipole modes as a function of aperture and unlike the 19 cm geometry all modes are sufficiently damped. Q and R/Q values of particular modes interest are also shown in Table III.B.3.2.4.2.1.

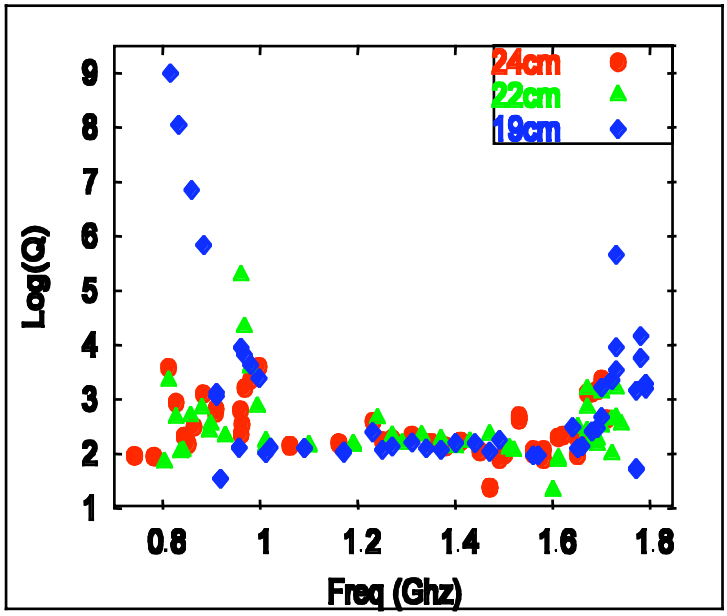

Fig. III.B.3.2.4.3.2. Dipole Q dependence for 17 cm geometry.

Table III.B.3.2.4.2.1. R/Q and Q values for some dipole modes of interest.

Freq (MHz)	*R/Q (Ω)*	*Q*
862.6	30.16	632.2
882.2	54.65	2499.8
906.9	41.71	1133.05
967.1	3.52	3213
979.2	3.74	4608
995.7	1.72	8088.54

The loss free analysis using different boundary conditions reveal the same phenomena as shown in Fig. III.B.3.2.4.2.1. Unlike the 19 cm geometry, we did not find any TM like modes below the cutoff frequency in 17 cm geometry. Thus, an increase in beam pipe to 24 cm was sufficient to propagate all dipole modes out of the cavity structure to be absorbed by the ferrites. This is evident from the Q values of the dipole modes. Since minor geometrical changes do not affect R/Q significantly, one can expect a big rise in beam break current in the new design.

This improvement can probably be attributed to two factors.

- In a complex cavity structure, the EM modes are not purely TM or TE but probably a superposition. In the 19 cm geometry, 3 modes have a dominant TM part which prevents them from propagating through the beam pipe. However, similar modes in the 17cm geometry might have a dominant TE part, allowing them to propagate through the 24 cm aperture.
- It is also possible for a cavity with poor coupling between middle and end cells to cause a mode to be trapped. A smaller iris improves coupling and might detrap some harmful modes. However, we did not find any significant evidence to attribute the trapped modes to coupling.

III.B.3.2.4.4 Comparison to Other Codes

A calculation using HFSS [III.B.12] was performed to crosscheck MAFIA results. Since HFSS only computes in 3D, the exact input used in MAFIA was replicated in 3D in HFSS and dipole Q's were computed. We were able to extract the dipole Q's of particular modes of interest. Fig. III.B.3.2.4.4.1 shows that the values agree pretty well between MAFIA and HFSS. This is additional proof that our cavity structure is indeed HOM free.

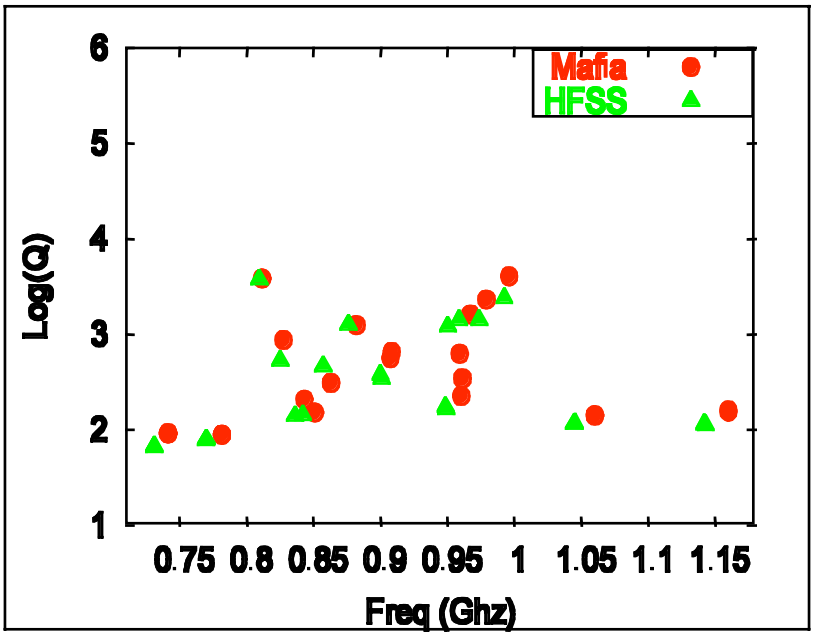

Fig. III.B.3.2.4.4.1. Dipole Q's comparison between Mafia and HFSS for select modes.

Mesh Dependence

For all the cavity calculations above we use 10^5 mesh points with the auto-mesh feature. In a simple comparison analysis, we vary the number of mesh points and measure the dependence of Q values of dipole modes as a function of mesh points. Since the cavity structure under consideration for e-cooling has a 17 cm iris with a 24 cm beam pipe, we use this geometry for calculating Q's with the aid of inverse solver. Fig.

III.B.3.2.4.4.2 shows that Q values start to converge at 10^4 mesh points. We use 10^5 mesh points to be on the safe side.

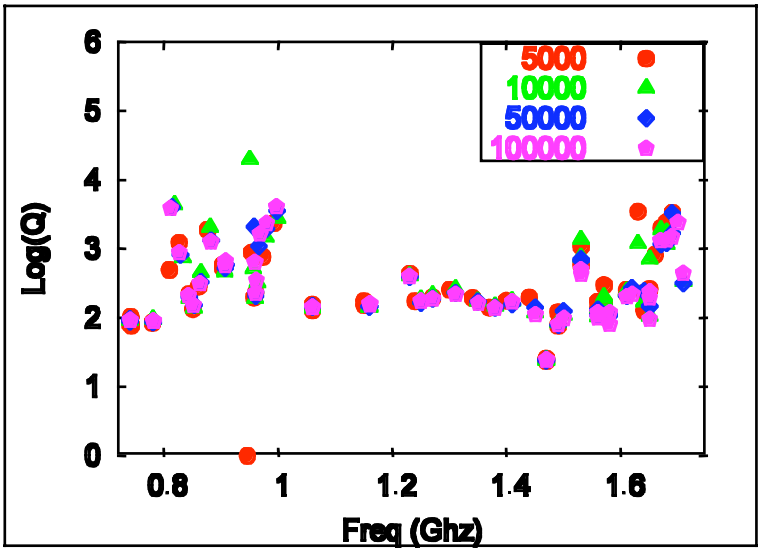

Fig. III.B.3.2.4.4.2. Dipole Q's as a function of mesh points for 17 cm geometry.

ε and μ and Dependence

For all calculations with losses, ε and μ used were small. Table III.B.3.2.4.4.1 shows properties of ferrite proposed for the cavity at frequencies of 1 GHz and the values used in MAFIA calculations.

Table III.B.3.2.4.4.1 Ferrite properties.

	R/Q (Ω)	*Q*
Epsilon	(30.0, -10)	(10.0, -0.33)
882.2	(2.0, -100)	(2.0, -0.5)

Large imaginary values such as ferrite-50 yield inaccurate results because the solvers are unable to converge. However, we performed a calculation of Q values for dipole modes of interest with small increase in imaginary parts of epsilon and mu to understand the dependence. Fig. III.B.3.2.4.4.3. demonstrates that dipole Q's decrease with an increase in imaginary ε and μ values, indicating that the real cavity with high loss ferrites should perform better than in simulation.

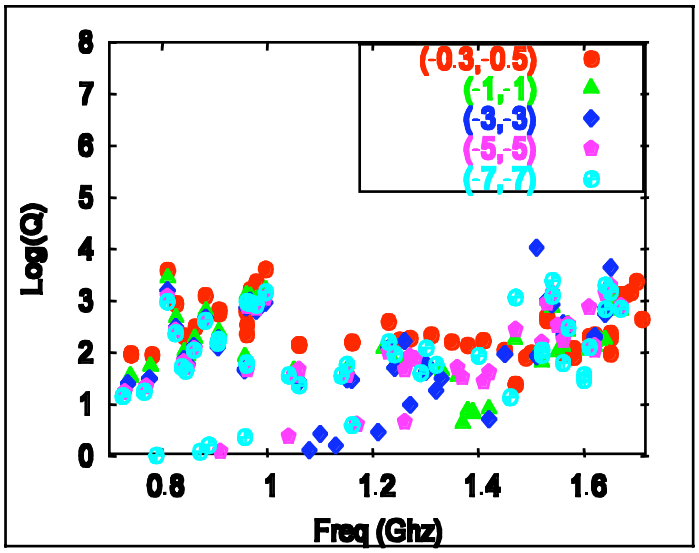

Fig. III.B.3.2.4.4.3. Dipole Q dependence on epsilon and mu of ferrite in 17 cm geometry.

III.B.3.2.4.5 Ferrite Location

The ferrites are not perfectly matched to the characteristic impedance of the beam pipe, resulting in some reflections and field variations as a function of position. From the proposed design, if one relies completely on ferrites to absorb the HOM power, it is important to match ferrite location to that of the maximum of the field strength. However, given the finite length (20 cm) of the ferrite, one cannot find an ideal location where every mode is to be matched perfectly. Since some modes have higher Q than others, one should choose a location with lowest Q configuration for all modes. This is under investigation, and the final location will probably be determined from test cavity results.

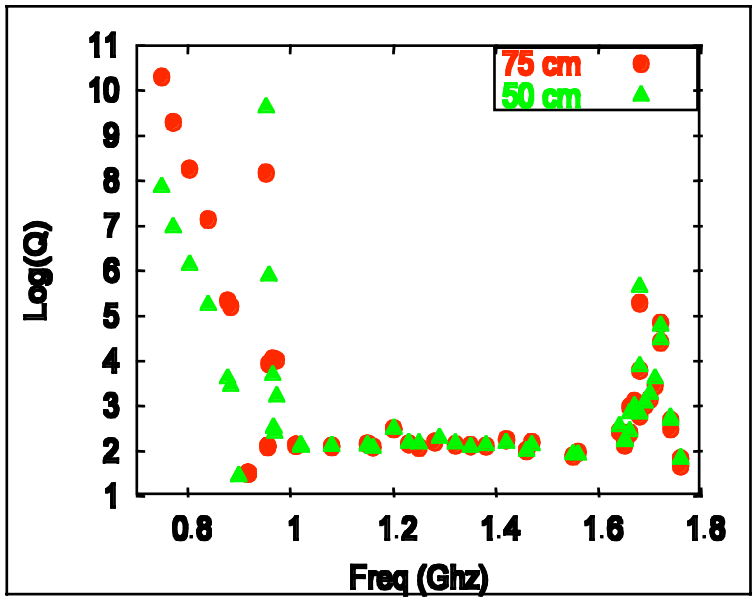

Fig. III.B.3.2.4.5.1 Dipole Q dependence on ferrite location for 19 cm geometry.

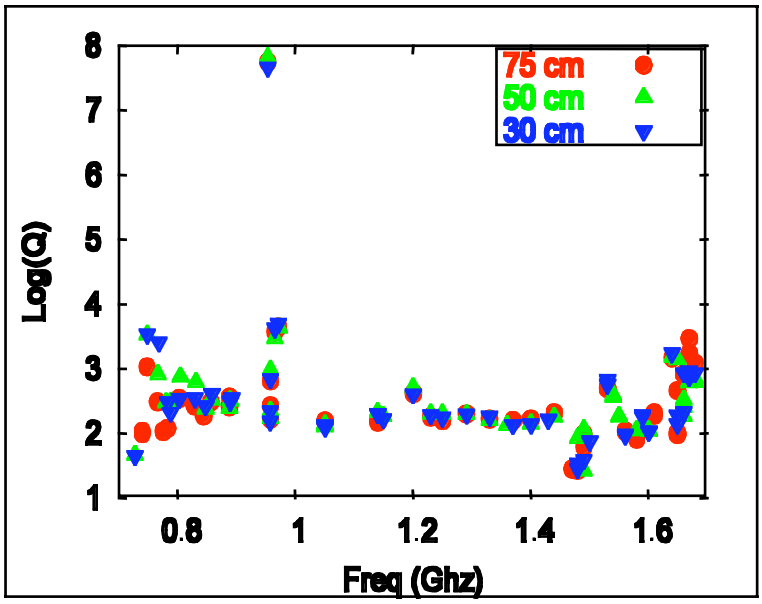

Fig. III.B.3.2.4.5.2 Dipole Q dependence on ferrite location for 17 cm geometry.

Another factor to consider is the proximity of the ferrite to the cavity. It is desirable to place the ferrite close to the end cell in order to absorb the maximum power from exponentially decaying trapped modes that do not manifest themselves clearly in simulations. Fig. III.B.3.2.4.5.1 demonstrates how location of the ferrite location affects Q values of trapped modes. This calculation was performed using the previous design with a 19 cm cavity iris with two different ferrite locations without any beam pipe modifications. It is clear from the plot that Q values are significantly lower when the ferrite is placed closer to the end cells. However, the same cavity iris with a 24 cm beam pipe shows no effect on the location because most of the modes are able to propagate to the ferrite and get absorbed. Ultimately, cryogenic issues determine how close the ferrite can be placed and possibly forcing one to use HOM couplers to extract any trapped modes.

III.B.3.2.4.6 Time Domain Calculations

Boundary conditions play an important role in simulating HOM propagation accurately. In frequency domain, one is limited to closed boundary conditions to solve for the modes in a resonator. However, Mafia's time domain module [III.B.9] allows one to specify waveguide like boundaries. The calculations in time domain are performed for a 3D structure using only half the cavity taking advantage of the symmetry of the cavity, the fundamental coupler and the ferrite. Addition of HOM couplers with entail the use of full 3D structure increasing the computation time which will not be discussed in this paper.

Two ports at either end of the cavity are defined such that all waves above the cut-off frequency of the waveguide propagate without any reflection thus representing an

infinitely long waveguide. To accomplish such boundaries, a 2D cross section of the ports in interest is considered for which eigenmodes are computed upto a desired frequency, which in our case is 2 GHz. These waveguide modes are loaded into the 3D computation domain which then allows one to define the boundaries as perfectly transmitting (waveguide) ports.

A Gaussian bunch of the desired length is launched into the cavity structure with monitors to record the wakefields generated in the structure. The bunch can be launched in the center of the beam tube to excite azimuthally symmetric modes (monopole), or launched off-center with appropriate boundary conditions to excite transverse modes (dipole). Mafia computes the longitudinal wake $W_{\|}(x,y,s)$ as a function of bunch coordinate (s = ct) which is given by

$$W_{\|} = \frac{1}{q}\int_{-\infty}^{\infty} E_z(x, y, (s+z)/c)dz$$

A Fourier transform of the longitudinal wake normalized by the bunch spectrum yields the broadband impedance given by

$$Z_{\|} = \frac{1}{q}\int_{-\infty}^{\infty} W_{\|}(x, y, s)e^{-i\frac{\omega}{c}s}ds$$

where

$$I(\omega) = qe^{-\frac{1}{2}\left(\frac{\sigma_s\omega}{c}\right)^2}$$

In the case where the bunch is launched off-center, the transverse wake is related to the longitudinal wake given by Panofsky-Wenzel theorem. Therefore the impedance for transverse modes is given by [III.B.13]

$$Z_{\perp} = \frac{Z_{\|}(x, y, s)}{kr^2}$$

where $k = \omega/c$ and r is the bunch offset from the center of the beam tube.

Simulations

The broadband impedance spectrum of the both short-range and lone-range wakefield is quite useful in understanding the behavior of HOMs. Since the goal of this simulation is to investigate high Q dipole like modes, long-range wake computations upto to 300m is required to observe any high Q modes slowly decaying long after the passage of the bunch. Sometimes, longer computation is required if the finer frequency resolution is required. If a mode is still ringing, the spectrum of that mode is broadened and true impedance of this mode has to be determined with the aid of two different time domain runs [III.B.14]. Fig. III.B.3.2.4.6.1 shows longitudinal wake for the bunch traveling on-

axis. The impedance spectrum is dominated by the fundamental mode and rest of the spectrum contains modes with significantly smaller impedance.

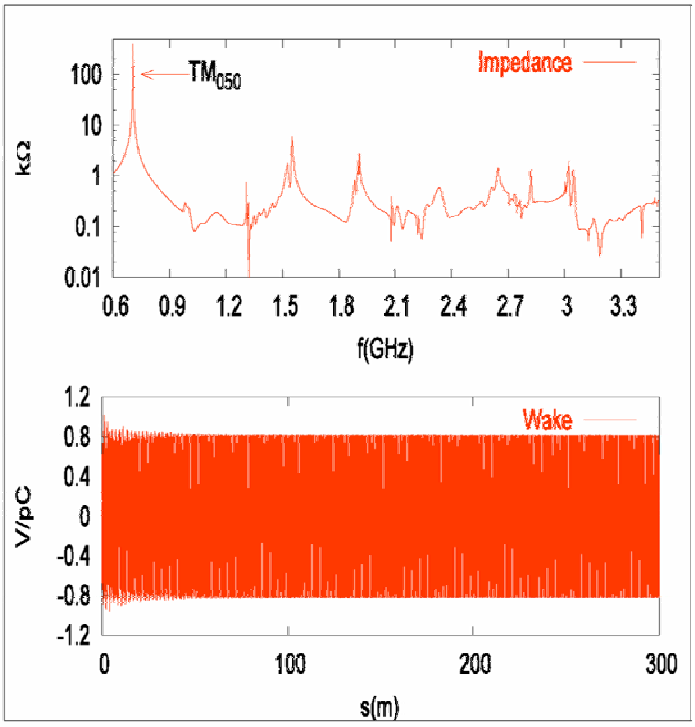

Fig. III.B.3.2.4.6.1. Wake function and Impedance spectrum for monopole modes 17 cm geometry.

A similar calculation for transverse deflecting modes can be performed by displacing the bunch by an offset (3 cm). From Fig. III.B.3.2.4.6.2 we can see that wake function is exponentially decaying except for a few modes that show beating effect. This can be clearly seen in the impedance spectrum as two bands near 0.9 GHz and 1.8 GHz. The Q factors of these modes are estimated in Table III.B.3.2.4.6.1 and compared to that of frequency domain simulations.

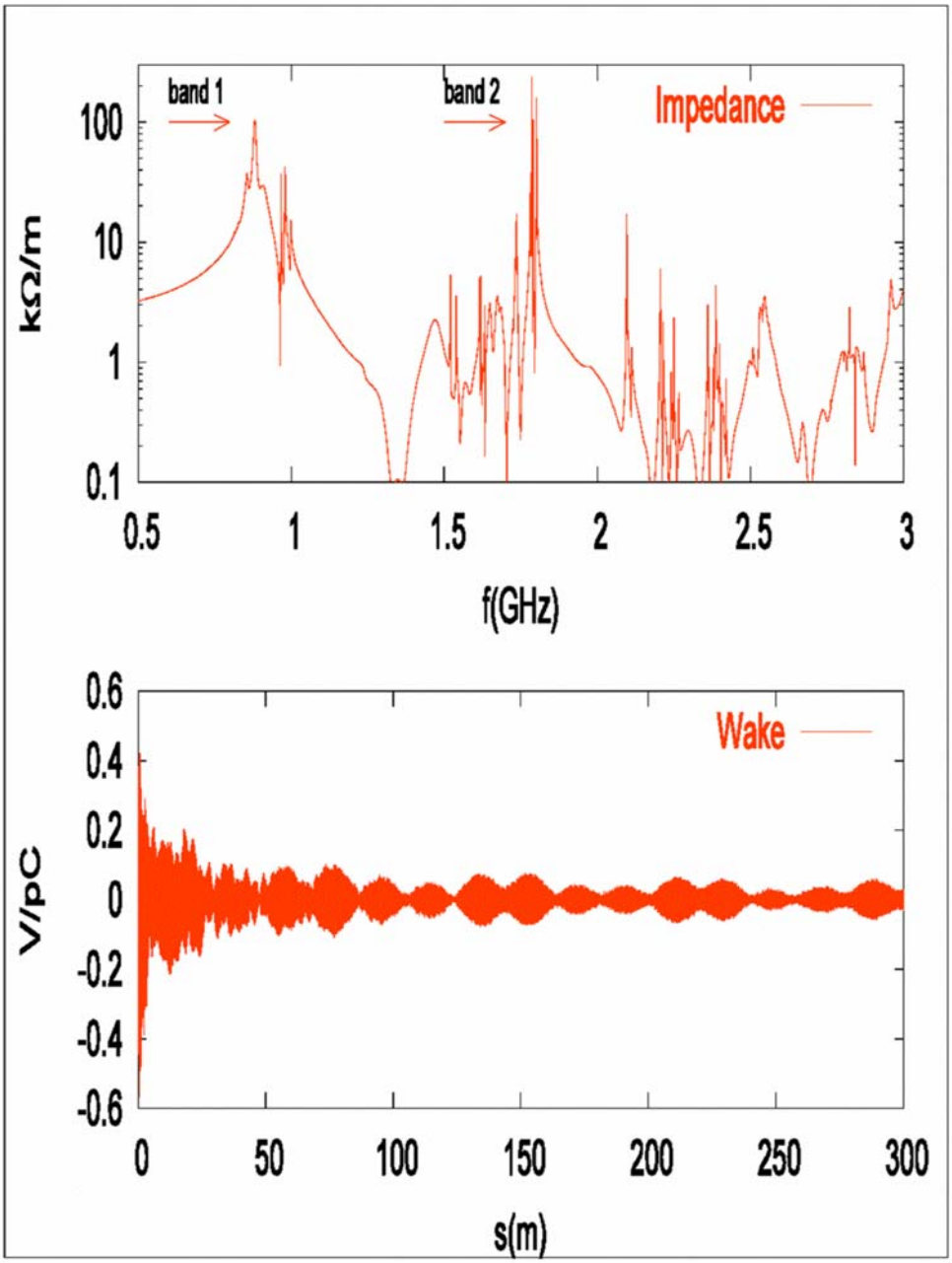

Fig. III.B.3.2.4.6.2. Wake function and Impedance spectrum for dipole modes 17 cm geometry.

Table III.B.3.2.4.6.1 Q comparison for select modes between frequency domain and time domain.

Freq (MHz)	$Q_{freq\text{-}domain}$	$Q_{time\text{-}domain}$
862.6	311	244
882.2	1250	< 110
967.1	1606	< 483
979.2	2304	< 244
1787	NE	1276
1791	NE	1790
1802	NE	1287

The Q factors estimated in time domain values are smaller due to truncation of wake computation before all the stored energy in the cavity has decayed. This causes artificial broadening of the peaks and hence the lower Q values. However, the complex frequency domain is known to yield Q factors, which are higher than in real conditions due to closed boundary conditions [III.B.15]. Also, ferrites can only be simulated as low loss materials and we expect much better damping which will be tested in a copper prototype of the niobium cavity in the near future. The band of modes between 1.7-1.8 GHz shows impedances much larger than what we estimate from a similar ABCI calculation [III.B.18] in 2D. The field profiles of these modes are being analyzed carefully to resolve the discrepancies.

III.B.3.2.4.7 Longitudinal Loss Factor

One of the major issues in SRF cavity design is power dissipated in the HOMs. High current and high bunch charge implies a huge HOM power that has to be absorbed by Ferrite absorbers or extracted through HOM couplers. When this power becomes large it becomes a major cryogenic challenge, so it is imperative to keep HOM power loss to a minimum. The total HOM power is given by:

$$P_{HOM} = f_{beam} k_{loss} q^2$$
$$P_{total} = \sum_n P_n$$

where f_{beam} is the beam repetition frequency at a bunch charge q, and k_{loss} is the loss factor which is given by

$$k_{loss} = \frac{1}{2\pi} \int_0^\infty Z_r(\omega) d\omega$$

In the neighborhood of the resonance frequency, the integral simplifies to the following expression.

$$k_{loss} \approx \frac{\omega_n R_n}{4Q_n}$$

where loss factor was calculated using ABCI, using a single bunch with a RMS length of 1 cm. Loss factor results are displayed below in Fig. III.B.3.2.4.7.1.

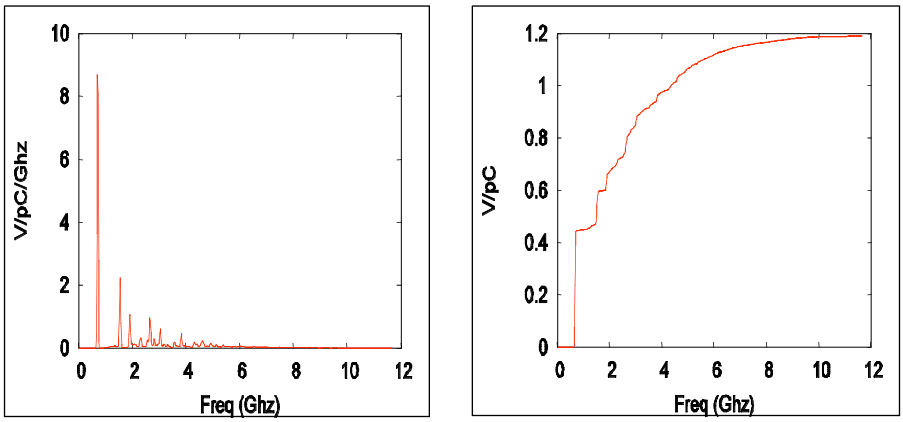

Fig. III.B.3.2.4.7.1. Longitudinal loss factor frequency spectrum (left) and integrated (right).

Another important factor to consider is wall losses due to the fundamental mode in the beam pipe. Since part of the beam pipe is at 2K, it becomes crucial to minimize this loss for CW operation to be feasible. Preliminary calculations from the cryogenic group [III.B.20] indicate a maximum loss of 25 watts to be tolerable for a sustained CW operation. One can calculate this power loss from MAFIA. Results for a beam pipe length of 20 cm made of copper after the end cell with our present configuration show a total wall loss of 12 watts on both sides of the cavity. We expect to intercept this power at liquid nitrogen temperature. The copper tube, also serving as a shielding for the stainless steel bellows, will be anchored to the radiation shield and thermally isolated from the niobium pipe. The electrical path for HOM power and beam image currents will be provided by a small capacitive element.

III.B.3.2.5 Superstructure – combination of two 5-cell cavities

A superstructure using the current five-cell design as shown Fig. III.B.3.2.5.1 is being investigated. Superstructure may not be necessary the electron cooler greatly but future projects such as eRHIC (10 GeV linac) will benefit greatly with the numerous attractive features of a superstructure [III.B.21]. Copper model testing will be conducted for the five-cell as well as a superstructure to investigate the advantages and limitations.

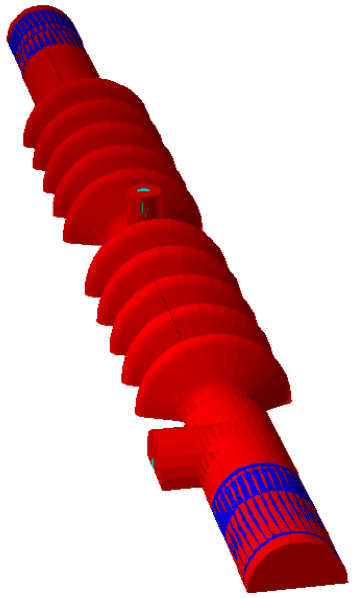

Fig. III.B.3.2.5.1. 3-D model of Superstructure comprising of two 5-cell cavities and two ferrite absorbers. This design promises to combine the higher average accelerating gradient with effective dumping of HOMs.

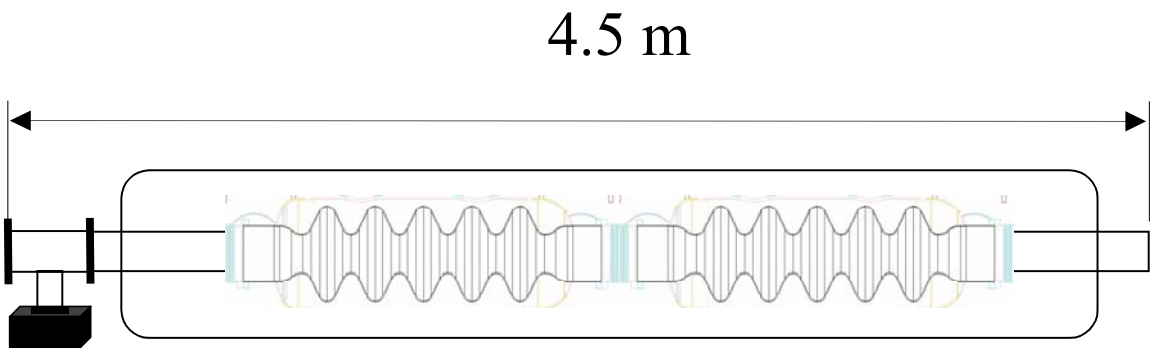

Fig. III.B.3.2.5.3. 3 A superstructure comprising of two 5-cell cavities provides economical solution of using one cryostat for two cavities.

III.B.4 RETURNING LOOP

The returning loop plays very important role in the ERL – it defines the global ERL parameters influencing the beam stability such as the momentum compaction factor and one turn matrix. It also serves matching function of the electron beam for its specific functions. In the e-cooling ERL the beam should be carefully matched into the cooling solenoid to preserve the low transverse temperature of the electron beam.

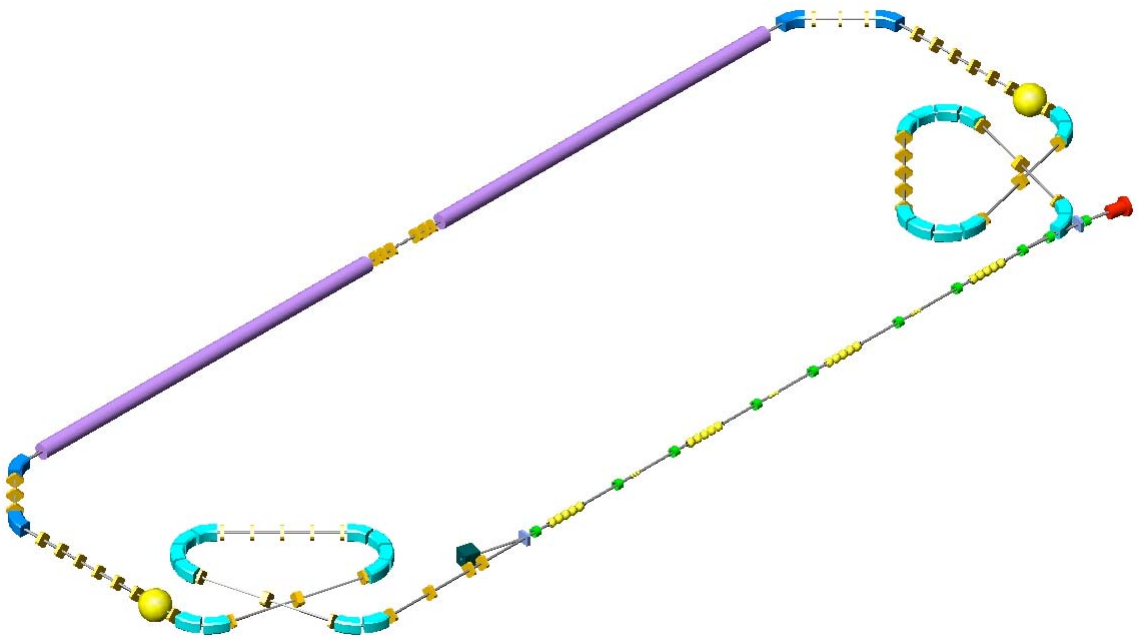

Figure III.B.4.1: Layout of the ERL for electron-cooling facility

Fig. III.B.4.1 illustrates the present working layout of the proposed electron cooling ERL. III.B.4.2 shows the top view of the ERL. The loop transports the electron beam, stretches its bunch length, matches it into the solenoid and merges it with the ion beams. The electron bunches are then shortened and decelerated in the linac to recover the energy. After the energy is extracted from the beam, it is dumped.

In order to obtain a minimum transverse temperature of the electrons in the cooling solenoid the electron beam must be magnetized, i.e. it must rotate around the longitudinal axis in a field-free space. The rotation must be such that the fringe field of the cooling solenoid “un-rotates” the beam. According to Busch’s theorem the product of rotation speed and beam cross section is a constant of motion, if only axial fields are involved. Non-axial fields can only destroy the rotation. Therefore the rotation must be produced by a longitudinal field on the cathode. Such beam is called “magnetized”.

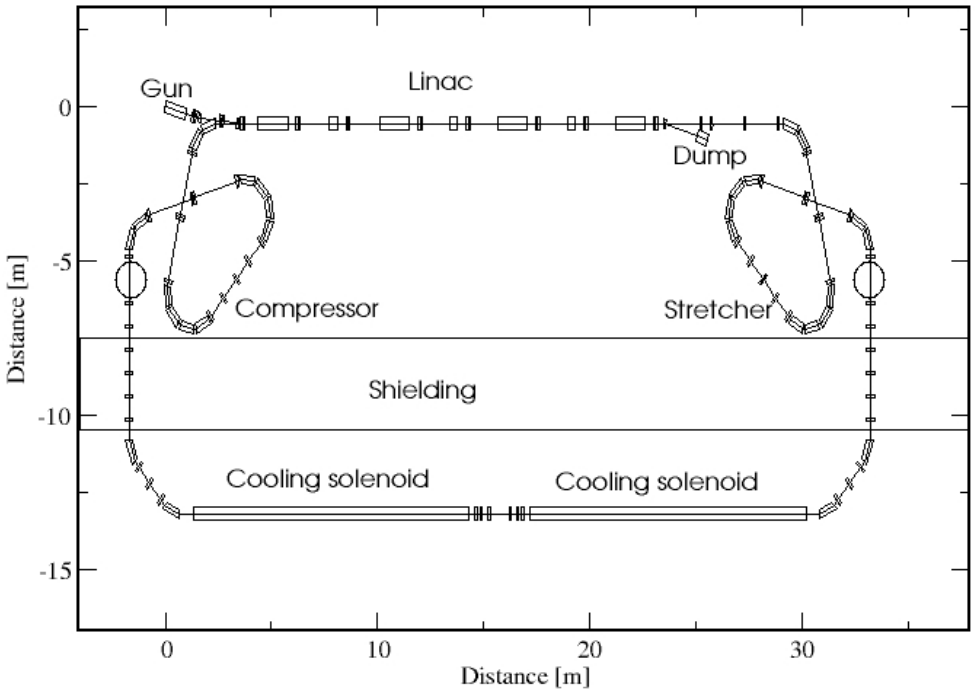

Figure III.B.4.2: Top view of the cooler

III.B.4.1 Beam Transport from the Linac to the Cooling Solenoid

After the linac the beam energy is reasonably high and quadrupoles are more efficient for focusing compared with solenoids. Four quadrupoles match the round beam coming from the linac into the stretcher. The stretcher fulfills two functions: it matches the electron bunch length with that of the ions by stretching the beam from 4 cm to 15 cm and, together with a 200 MHz de-bunching cavity, lowers the energy spread to less than $2*10^{-4}$ by rotation in longitudinal phase space.

A second matching section with 7 quadrupoles is used to match the phase advance to maintain magnetization. Two dipoles and a quadrupole triplet form the achromat that merge the electron beam with the ion beam.

The lattice of the stretcher has bilateral symmetry. Each half consists of two dipoles to create dispersion, a telescope with three quadrupoles to enlarge the dispersion, four dipoles which create large momentum compaction and a quadrupole section to match the slopes of the Twiss functions in the symmetry point to zero. By changing the quadrupole strength in the telescope the momentum compaction can be modified in a wide range. The maximum value of longitudinal dispersion is 60 m. The lattice functions of the ERL for e-cooler are shown if Fig. III.B.4.1.1 The maximum β-function is 15 m, the maximum transverse dispersion is 16 m.

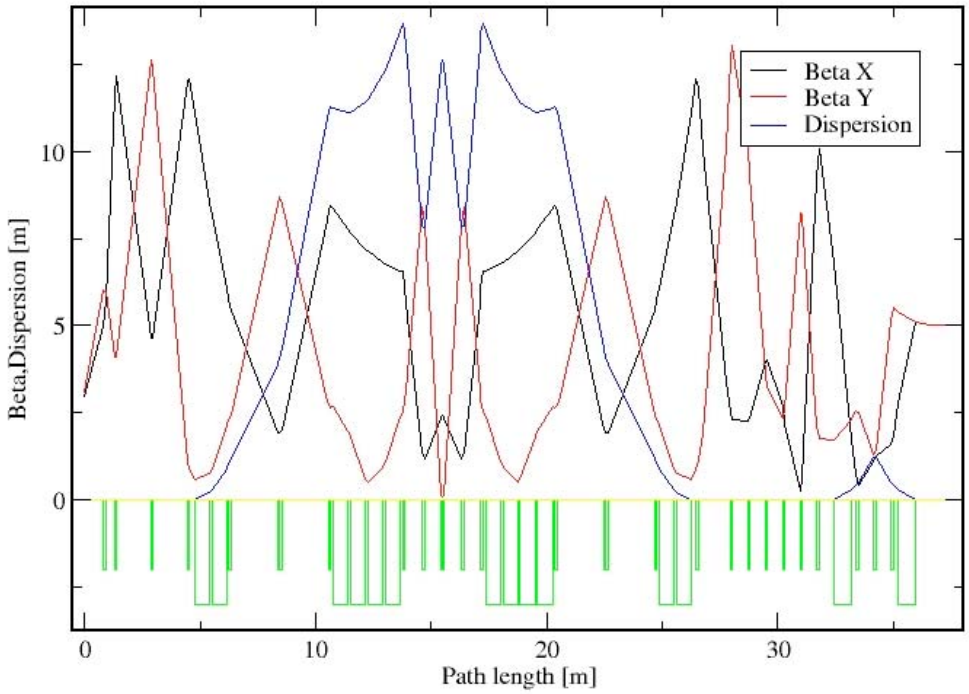

Fig. III.B.4.1.1: Optics of the beam transport between linac and cooling solenoid. The horizontal and vertical beta functions are shown in black and red, respectively. The dispersion is in blue, the tall green boxes show the location of dipoles; the short boxes indicate the quadrupoles.

The cooling solenoid is for engineering reasons build in two sections. It is necessary to match the optics between the sections to maintain the beam magnetization. This is normally accomplished using extra solenoid coils. By using quadrupoles instead and choosing a phase advance of $180^o/360^o$ it is possible to invert the beam rotation. This allows opposing fields is the solenoids, which cancels the coupling of the transverse motions of the ion beam. The quadrupoles will be implemented as ironless super-conductive coils inside the solenoid cryostat.

In the ideal case with rectangular fields one can find an optical solution with six quadrupoles. Real fields decay over a distance comparable to the aperture of the magnet. In this case eight quadrupoles are necessary. Each quadrupole will have a quadrupole and a skew quadrupole winding.

The beam transport from the cooling solenoids back to the linac is symmetric to the transport described so far. A 200 MHz cavity produces the opposite momentum spread so that the bunch length shrinks in the compressor. However, there are no matching quadrupoles between the compressor and the linac because they would interfere with the low energy beam transport. Instead the second half of the compressor is modified so that

the beam converges into the injection region. Figure below shows the β-functions as they would propagate in a drift with the length of the linac. The focusing of the solenoids (which are optimized for the low energy beam) and the RF focusing of the cavities is excluded in this simulation.

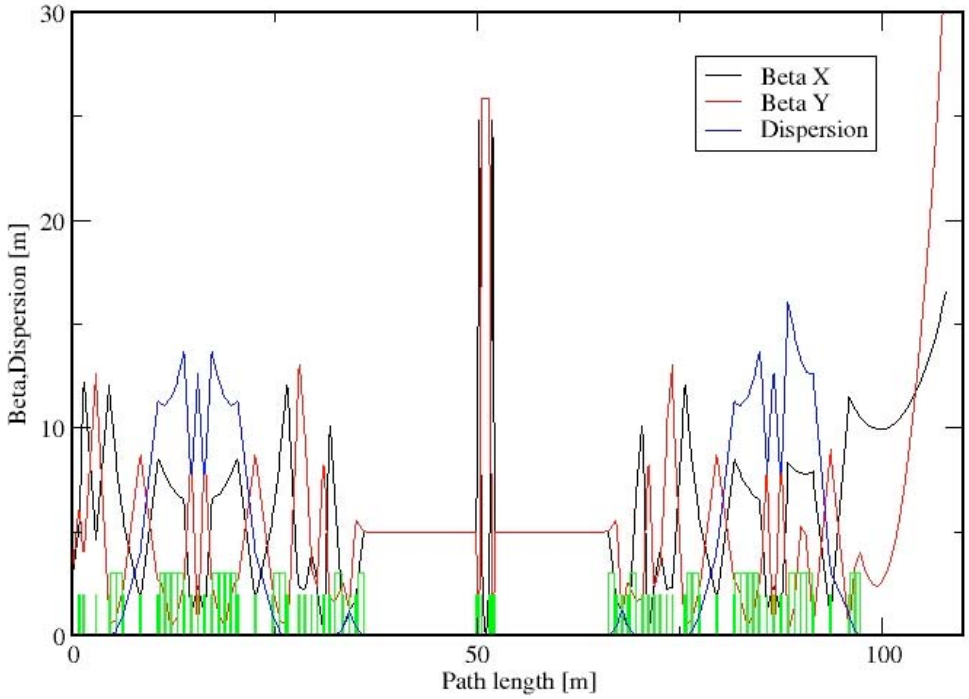

Fig. III.B.4.1.2: The complete high energy beam transport from the end of the linac back to the entrance of the linac.

Figure III.B.4.1.3 shows the size of 100 % of the beam in the high energy beam transport. The normalized emittance of 500 mm mrad is taken from the PARMELA calculation shown in Fig. III.B.4.1.2 and is valid for a 2 Tesla cooling solenoid. This emittance is an order of magnitude larger than the emittance in the rotating frame and emittance grows linear with the field of the cooling solenoid.

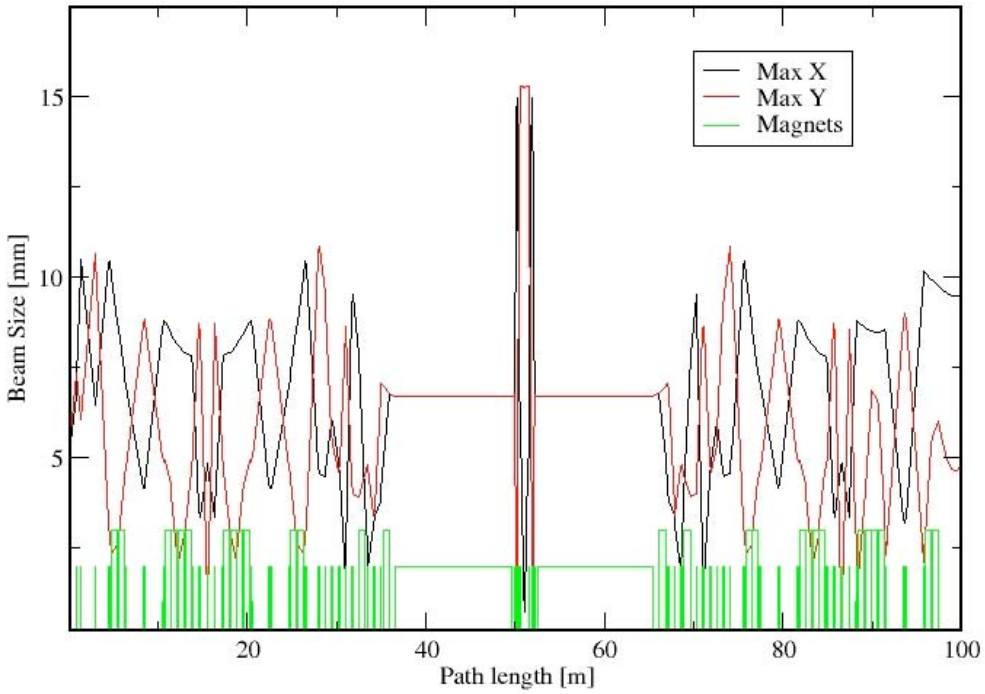

Figure III.B.4.1.3: Beam size in the high-energy beam transport.

III.B.4.2 Return Loop for ERL prototype

In the prototype ERL the accelerated e-beam goes further through a re-circulating loop comprising of two 180^{o} arcs and a straight section. The circumference of the entire ERL loop will be about 20 meters and will be determined after final lattice design is frozen. It is important that the time of flight of electron from the exit of the SRF cavity till the its entrance must be equal to the exactly integer number and a half of RF cycles – this insures that after passing through the re-circulating loop the accelerated beam returns in decelerating field with exactly same amplitude (but opposite sign).

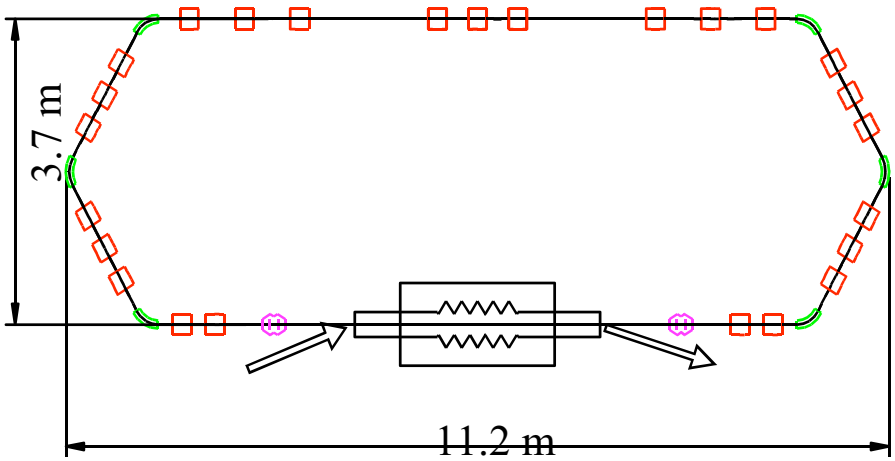

Figure III.B.4.2.1: A sketch of the ERL layout for Bldg. 912.

Each arc has achromatic lattice, which comprises of three bending magnets and up to six quadrupoles (number of quadrupoles is to be finalized later). This structure provides adjustable longitudinal dispersion (so-called R_{56}) while remaining achromatic. A sample of possible β- and D– functions are shown in III.B.4.2.2.

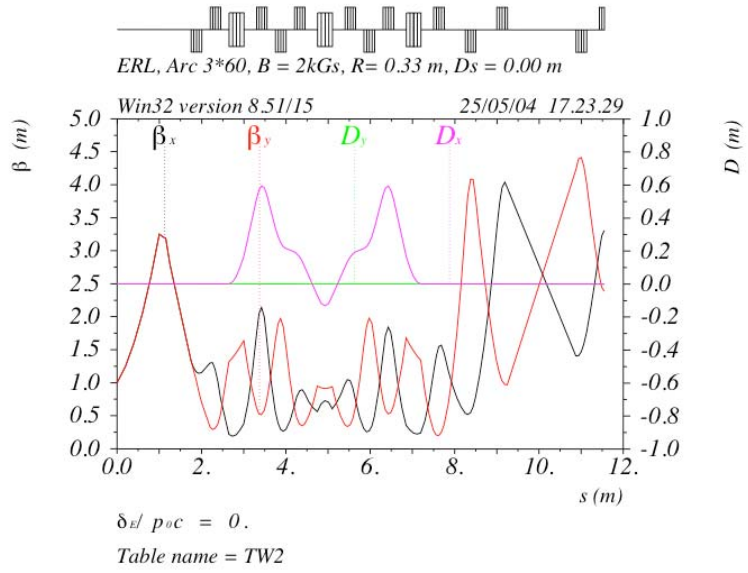

Figure III.B.4.2.2: Lattice functions of the ERL operating in isochronous mode. The ERL has bilateral symmetry. Hence, the only one half of the ERL is shown.

All magnets in the arcs have the same field and magnetic field. They also have similar design, with exception of the septum magnet used for merging the beams. The straight section will have from six to twelve quadrupoles, which will provide for complete control of the elements of the one turn matrix, including elements m_{12} and m_{34}, which will determine threshold of the transverse beam brake-up instability. This feature in combination with control of m_{56} is extremely for this test facility – it will allow to compare theoretical models and predictions with direct experiment.

$$\begin{bmatrix} x \\ x' \\ y \\ y' \\ -c\delta t \\ \delta E/E \end{bmatrix}_{s2} = \begin{bmatrix} m11 & \boldsymbol{m12} & \ldots & \ldots. & \ldots & \eta_x \\ m21 & m22 & \ldots & \ldots & \ldots & \eta_x' \\ \ldots & \ldots & m33 & \boldsymbol{m34} & \ldots & \eta_y \\ \ldots & \ldots & m43 & m44 & \ldots & \eta_y' \\ \ldots & \ldots & \ldots & \ldots & m55 & \boldsymbol{m56} \\ \ldots & \ldots & \ldots & \ldots & \ldots & m66 \end{bmatrix} \cdot \begin{bmatrix} x \\ x' \\ y \\ y' \\ -c\delta t \\ \delta E/E \end{bmatrix}_{s1}$$

In addition, there are a half-dozen of solenoids, a half-dozen of quadrupoles and nine vertical trim-dipoles in the injection line, between SRF and the arcs and in the beam-dump channel. Trim dipoles are used for chicanes, beam-dump and for compensation of vertical displacement of returning e-beam. The solenoids will be used for emittance compensation and e-beam focusing in the injector and for the focusing beam into the beam-dump. The rest of them will be used to match the electron beam with the arcs of the ERL.

The goal of the lattice design is to keep the values β-function in the ERL well below 10 meters and to keep the beam diameter within 1 cm (0.4") in all-around the machine. Possible exception from this rule will be the injector part before the chicane and the beam at the entrance and inside the beam dump.

III.B.5 BUNCH INSTABILITIES

III.B.5.1 TRANSVERSE MULTI-BUNCH INSTABILITIES

The energy recovery mode and high currents contribute strongly to coupled bunch instabilities due to poorly damped higher modes that limit the cavity performance. The low frequency dipole modes are particularly dangerous and can lead to beam breakup. Our new design of 17 cm iris and 24 cm beam pipe geometry looks very promising. We find most of the dipole Q's to be small with a few of the order of 10^3, but still does not pose any significant threat. This remains to be checked in the high frequency range (above 2 GHz), but contributions from high frequency modes to beam break up are

usually small. Also, we find that R/Q values are small for all modes which indicate high threshold currents for beam breakup.

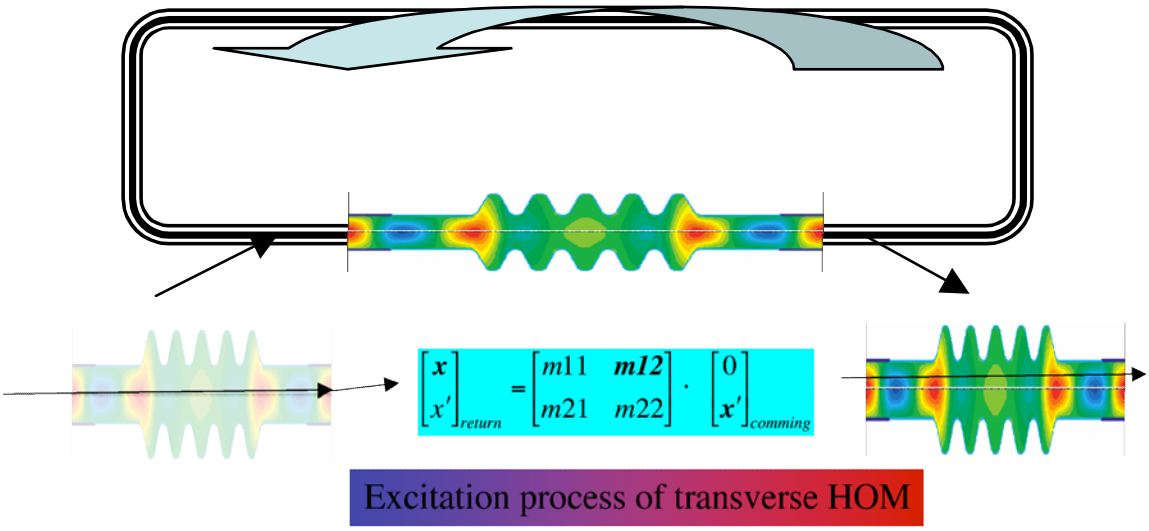

Fig. III.B.5.1 The transverse beam breakup instability is highly sensitive to the one-turn matrix elements:

$$m_{12} = \sqrt{\beta_{1x}\beta_{2x}}\,\sin\Delta\psi_x$$
$$m_{34} = \sqrt{\beta_{1y}\beta_{2y}}\,\sin\Delta\psi_y$$

The transverse angular kick of the electron bunch in the cavity by the field of transverse HOM causes the displacement of the e-beam at the entrance of the cavity proportional to m_{12} element in the transport matrix after passing through the loop. If the HOM field excited by the displaced beam exceeds the loss of the field caused by the HOM dumping, the beam became unstable.

This is oversimplified picture of the process. For exact calculation we use the TDBBU simulation code developed in Jefferson Laboratory [III.B.16] to calculate beam breakup thresholds from R/Q, Q, and corresponding frequencies, along with other beam parameters as input.

For e-Cooler ERL we simulated each cavity as two drifts with an energy gain of 13.5 MeV with the HOMs placed in between the drifts. Using each dipole mode in both polarizations with a 15 MHz Gaussian distribution, we obtain a threshold current of 1.8 A (see Fig. III.B.5.2). Work is underway to accurately build cavity matrix and optics for the beam to propagate around the ring. In principle this should increase the threshold currents. A sister simulation software called MATBBU [III.B.17] was recently acquired from Jefferson Lab, which solves an eigen-value problem to determine the threshold limits. Results from MATBBU show a threshold current of 1.85 A. Fig. Fig. III.B.5.2 shows transverse beam position as a function of time calculated by TDBBU for a current of 1.8 A. The initial (artificial) transverse kick decays, showing that 1.8 A is stable operation current.

The prototype has only one 5-cell cavity and should have even higher threshold of the instability. We will use the flexibility of its lattice to increase values of m_{12} and m_{34} and to benchmark the simulation with the experiment for this SRF cavity.

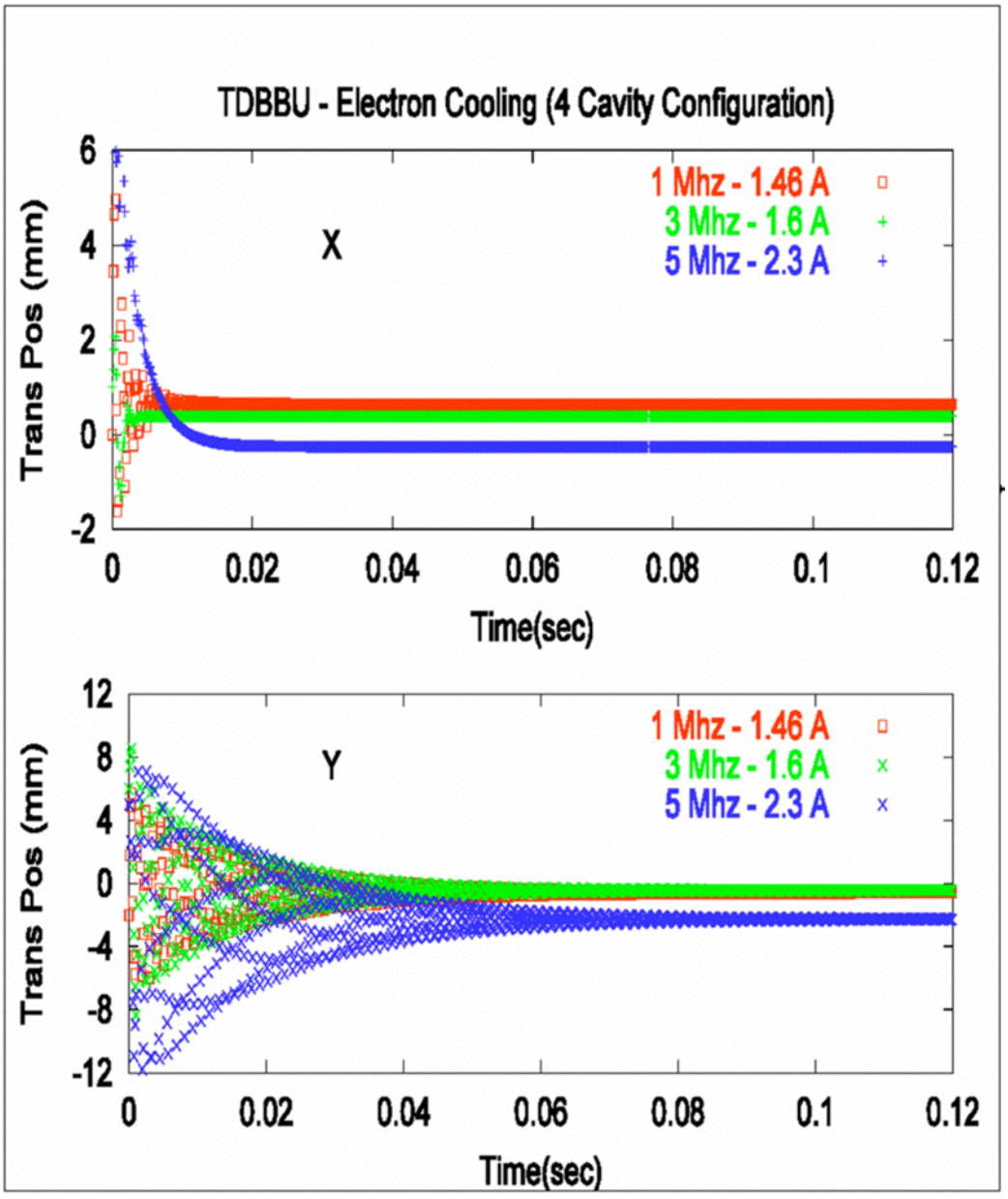

Fig. III.B.5.2 Beam breakup simulation using TDBBU with Gaussian distribution for HOMs.

REFERENCES:

[III.B.1] This solution was found by J.Kewish

[III.B.2] D. Janssen, et al., Nucl. Instr. and Meth. A507 (2003) 314.

[III.B.3] D. H. Dowell S. Z. Bethel and K. D. Friddell, NIM A 356, (1995), 167

[III.B.4] R. Calabrese et al. NIM A 340, (1994), 109

[III.B.5] A. Shih et al. J. Appl. Phys. 82, 1860 (1997)

[III.B.6] X.Y.Chang, et al., *Compensation for bunch emittance in a magnetization and space charge dominated beam*, to be published

[III.B.7] *Advanced Energy Systems*, USA.

[III.B.8] Dong Wang et. al., PAC 2003, Portland, May 2003.

[III.B.9] *The MAFIA Collaboration*, MAFIA Version 4.0, CST GmbH, Darmstadt, Germany.

[III.B.10] Paolo Pierini, *Build Cavity Manual*, Milan, Italy.

[III.B.11] J. Sekutowicz, Proceedings of Linear Accelerators Conference, Tsukuba, Japan, 1994.

[III.B.12] *Frequency Structure Simulation (HFSS),* ANSOFT Co., Pittsburgh, PA, USA.

[III.B.13] F. Marhauser et.al., *Numerical Simulations of HOM damped cavity*, PAC 2001.

[III.B.14] Derun Li and Robert Rimmer, *Beam Impedance Calculations and Analysis of HOMs using MAFIA in Time Domain*, PAC 2001, Chicago.

[III.B.15] R. Schuhmann, T. Weiland, PRST-AB, Vol. 3, 122002(2000).

[III.B.16] TDBBU was written by G.A. Krafft at Jefferson Laboratory.

[III.B.17] MATBBU was written by G.A. Krafft at Jefferson Laboratory.

[III.B.18] Y. H. Chin, *ABCI Version 8.1*, CERN, Geneva.

[III.B.19] Chojnacki et. al., Proceedings of the Particle Accelerator Conference, 1997.

[III.B.20] Mike Iarocci, Private Communication.

[III.B.21] J. Sekutowicz, PRST-AB, Vol.2, 062001 (1999).

to be added:

III.B.X MAIN PROCESSES IN THE ERL

XXXX Dispersion-free injection system for space charge dominated beams

XXXX Acceleration and deceleration in the SRF linacs

XXXX Lattice for the ERL – additional tims

- *Transverse dynamics*
  - *Introduction*
  - *Stability of transverse motion*
- *Longitudinal dynamics*
  - *Introduction*
  - *Stability of longitudinal motion*
  - *Feedbacks*

Bunching and de-bunching of electron beam

Robinson Instability

IV. R&D requirements for the RHIC electron coolers.

Electron cooling for RHIC is an enormous technical challenge. It may be argued that electron cooling has been known for many years and is practiced in many machines around the world. It is also true that the physics of cooling takes place in the reference frame of the ions (and electrons) bunch, which is independent of the energy of the machine. However, there are a number of differences between this electron cooler and any other built so far:

6) The RHIC cooler will be by far the highest energy cooler, requiring electron energy of over 50 MeV as compared to the few hundred KeV of any previously built cooler (the only exception is the recycler cooler of FNAL, which is under construction and will have 4.3 MeV electron energy).
7) The RHIC cooler is the only machine planned for cooling bunched beams.
8) The RHIC cooler will be the first instance in a collider will be directly cooled.
9) The RHIC cooler will operate with electrons that are much "hotter" then previous coolers.
10) The RHIC cooler will use a very long, high-field, ultra-high precision solenoid.

There are various implications stemming from these observations. The first one is rather obvious. The electron beam technology of this cooler will be different than any other, requiring high-energy, high-current and low-emittance (temperature) electron beams. That requires a very bright electron source. The other one becomes obvious when one considers that the cooling solenoid has to provide 5 Tesla field over two 13 meter sections with a precision (angular deviation of the magnetic field) smaller than 8x10-6 as measured at any point along the magnet. This is a very challenging magnet. The next point becomes obvious when one considers the electron accelerator, which has to provide a C.W. beam at over 50 MeV and over 0.2 amperes, providing a challenge even to superconducting energy recovery linacs. Finally, all of these considerations put together mean that the present state-of-the-art of electron cooling simulations must be considerably improved.

The Collider-Accelerator Department concluded that R&D should be taken along the following fronts:

5) An electron source based on a 703.75 MHz laser-photocathode RF gun (photoinjector) must be developed to demonstrate that the electron beam can be prepared with the required emittance, bunch charge and average current. This research may be broken further down to the following components:
    a. High quantum-efficiency, long-lived photocathode R&D.
    b. High average-power, 9.4 MHz repetition frequency laser must be developed.
    c. A high electric field, CW operation RF gun has to be developed.

d. The above-mentioned elements must be brought together in an operating gun.

6) Energy recovery linac R&D must be pursued to accelerate (and then decelerate for energy recovery) the electron beam without emittance or energy-spread degradation.
7) A high-precision superconducting solenoid R&D must be carried out.
8) Electron cooling simulation codes, providing better predictions of the performance of electron coolers must be developed.
9) R&D will be carried out towards the development of the cooler solenoid.

A detailed R&D plan is presented in this design report. The Collider-Accelerator Department is taking aggressive action to execute this research program. This work is done in close collaboration with other national laboratories such as Jefferson Laboratory, industries such as Advanced Energy Systems in Medford NY and Tech-X in Boulder, CO., and international institution such as the Budker Institute of Nuclear Research in Novosibirsk, Russia, the Joint Institute of Nuclear Research in Dubna, Russia and the Gesellschaft für Schwerionenforschung in Darmstadt, Germany.

IV.1 R&D Plan

Electron cooling of RHIC will increase the integrated luminosity by close to an order of magnitude and make it possible to operate RHIC for electron-ion collisions in eRHIC. The proposed electron beam-cooling scheme for RHIC uses a single pass, energy-recovery superconducting linac to generate the 52 MeV, 100 mA to 300 mA electron beam needed to extract the transverse and longitudinal energy spread from the circulating ions. The electron beam is "magnetized" to reduce the cooling time. Generation of the necessary transverse and longitudinal brightness requires the development of a CW laser photocathode RF gun as the injector. Energy transfer between the "cold" electron beam and the "hot" ion beam takes place in a highly uniform solenoid magnet to maintain particle alignment. The electron accelerator is a superconducting, energy-recovery linac.

IV.1.1 R&D GOALS

Electron cooling for RHIC is an enormous technical challenge. While electron cooling has been known for many years, it was never anywhere near the conditions in RHIC.

1. At 54 MeV the RHIC cooler will be by far the highest energy cooler as compared to the few hundred KeV of any previously built cooler.
2. The RHIC cooler is the only machine planned for cooling bunched beams and requires a very high average electron current due to the high ion energy.
3. The RHIC cooler will be the first instance in a collider will be directly cooled.
4. The solenoid required is of unprecedented precision-length combination.
5. The RHIC cooler will be the first to use relatively "hot" electrons for cooling.

Accordingly, the R&D plan for the electron cooling of RHIC comprises the following areas:

1. R&D of a CW electron gun capable of a high bunch-charge, low emittance and high average current. In particular, R&D will be carried out on the
   - 1.1. Superconducting gun cavity, including its electron beam dynamics performance, its cathode insertion port, its SRF characteristics, its performance under high HOM load, its main power coupler, cryostat, tuner etc.
   - 1.2. Photocathode suitable for very high current at low laser power. The photocathode should also be long-lived and must not contaminate the SRF gun cavity.
   - 1.3. Laser for driving the photocathode with the proper pulse energy, repetition rate, pulse width, mode purity and high stability in all parameters.
   - 1.4. An alternate scheme of delivering the needed high-current, low-emittance beam will be investigated. This alternate approach may be based on either bunch manipulations to overlap a few gun bunches on each RHIC ion pulse, or a DC photocathode gun followed by a low frequency buncher-accelerator section.
   - 1.5. A backup plan is in place to investigate the potential performance of a DC gun, operated with a very long electron bunch at the gun, followed up by a low frequency RF system comprising acceleration and bunching.
2. R&D of a CW, superconducting, energy-recovery linac capable of accelerating the high current and handle the large high-order mode (HOM) power with a good preservation of phase-space volume. The program will also include
   - 2.1. Study of the effects and possible solutions of the kick delivered by the fundamental power coupler.
   - 2.2. Prototype copper cavities will be built and tested for various properties, in particular the frequencies, R/Q and Q of the HOMs.
   - 2.3. HOM dampers will be studied experimentally.
3. Electron beam dynamics studies for generating, accelerating and matching the electron beam under conditions of a magnetized beam and high brightness.
   - 3.1. These studies will employ at least two programs capable of space-charge and magnetized beam calculations to verify the critical dynamics of large-charge, magnetized beams.
   - 3.2. Experiments will be carried out to test the emittance compensation of magnetized beams.
   - 3.3. Sensitivity studies will be made to study effects of errors and establish tolerances.
4. Studies of electron cooling theory in the regime of RHIC (bunched beam, high electron temperature) and
   - 4.1. Development of reliable electron cooling simulation codes, aimed at achieving the ability to calculate cooling in the RHIC regime with better than a factor of 2 precision.
   - 4.2. Benchmarking of the codes by comparison to other codes and by experiments in available storage rings are a must.

4.3. Studies of IBS in RHIC and development of models that are appropriate for use with electron cooling simulation codes under electron cooling conditions.

4.4. Simulations of RHIC with all effects, such as

4.4.1. Cooling

4.4.2. IBS

4.4.3. Beam-Beam

4.4.4. Collective instabilities

5. Development of a prototype ~5 Tesla superconducting solenoid with precision in the few ppm range. The program will include

5.1. Development of magnetic measurement systems capable of providing the necessary resolution in magnetic error determination.

5.2. Construction of a prototype solenoid to study the intrinsic precision of the magnet, the efficacy of the correcting system and the performance of the magnetic measurement system. This prototype solenoid will be long enough to establish the interior field and study of the correction system for a sufficiently long path.

5.3. A support system for the magnet.

6. Electron beam diagnostics will be developed for:

6.1. The ERL section, including

6.1.1. Position Measurement

6.1.2. Phase Measurement

6.1.3. BBU/Energy Feedback

6.1.4. Beam Transfer Function

6.1.5. Energy Spread

6.1.6. Loss Monitors

6.1.7. BPM Sum Signal Current Monitors

6.1.8. Injection Line Current Monitors

6.1.9. Differential Current Monitor

6.1.10. Profile Monitors - Flags, wire Scanner, Scraper, synchrotron Light

6.2. The ion beam, including

6.2.1. Position

6.2.2. Recombination rate monitor

6.2.3. Relative electron-ion position along the solenoid

IV.2 R&D Milestones

The milestones for this extensive program are as follows (exact dates depend on funding rate):

Energy Cooling R&D Major Milestones	**Estimated Completion Date**
Develop & Procure the SC 5-cell RF cavity	August 2005
Building 912 Utility Modification Complete	April 2005
Assemble SRF Cavity to Associated Components & Test	August 2005
Development, Design & Procurement Magnets & Power Supp.	November 2006
High Power RF System tested	November 2005
SC Electron Gun delivered	November 2006
Photocathode System Development, Procurement & Test	March 2006
Assemble & Test of RF Gun & Associated Systems	February 2007
Control Room operational	May 2006
Design & Procurement of Gun-to-Dump Vacuum System	March 2006
Beam Dump Procurement	April 2006
Beam Instrumentation - Develop, Design, Procure & Test	August 2006
Assemble Photocathode, RF Gun, Cavity & Beam Dump for test	July 2007
ERL Installation	September 2007
Subsystems Tests Complete	July 2007
Receive Approval to Run	November 2007
System Shakedown	December 2007
System Running Begins	December 2007
Demonstration of 200 mA	Early 2008

Superconducting 5T solenoid prototype

Initial studies of correction coils completed	June 2004
Magnetic design of solenoid complete	August 2004
Magnetic design of correction coils completed	November 2004
Magnet construction completed	March 2006

Electron beam optics and dynamics simulations

Emittance compensation and magnetized beam	December 2003
Start-to-end beam dynamics of a cooler	December 2004
Design of prototype energy recovery linac	June 2005
Cooling software and theory	
Phase I BETACOOL and SIMCOOL codes	December 2003
Phase I Benchmarking of Vorpal codes	December 2003
Phase II BetaCool and SimCool codes	April 2005
Phase II Vorpal code – results for RHIC parameters	January 2005
Phase III BetaCool, SimCool, UAL	December 2005
Phase I First benchmarking with cooler ring experiments	September 2005

IV.3 C-AD Machine Advisory Committee Review

The C-AD Machine Advisory Committee (MAC) reviewed the R&D plans for electron cooling of RHIC on March 10-11, 2004. The MAC members were Oliver Boine-Frankenheim, GSI; Alexander Chao, SLAC; Jean-Pierre Delahaye, CERN; David McGinnis, FNAL; L. Merminga, JLAB, and Ferdinand Willeke, DESY, who chaired the committee. The MAC report was congratulatory to the efforts of C-AD on electron cooling, stating also that:

- A RHIC luminosity upgrade program has been developed which is based on high energy bunched beam electron cooling. This novel technique which presents a considerable challenge in accelerator physics and in accelerator technology is addressed by an aggressive R&D program.
- A high-energy (54MeV) electron cooling scenario based on a high current (100mA) Energy Recovery LINAC (ERL) has been developed that can be regarded as one of the most complex and challenging accelerator projects.
- The committee is impressed by the amount of work which has been done in a rather short time, especially in view of the fact that previously there was no cooling expertise residing in BNL.

The MAC proceeded to make a number of suggestions concerning the electron cooling R&D program. The Collider-Accelerator Department is adopting these remarks completely. In Table IV.3.1 we enumerate the remarks of the MAC and the department's response to these.

MAC comment / recommendation	C-AD response	Responsibility
The committee considers an improved agreement between experimental and calculated cooling times a challenging but mandatory task, which has a direct impact on the possible luminosity improvement factor. The committee suggests • strengthening the effort in the laboratory to support the corresponding activities and • encourages strongly further collaboration with other electron cooling laboratories.	Improved agreement between experimental and calculated cooling times is one of the main tasks of the RHIC electron Cooling Group. • Additional resources will be given to this effort as budget permits. • Since the MAC report BNL signed an additional MOU on electron cooling R&D, with GSI.	I. Ben-Zvi
The committee suggests furthermore including studies of the effect of transverse kicks from the super conducting RF cavities on the beam	A study of the effects of the transverse kicks has been started by simulations. Experimental test will be	R. Calaga

emittance.	carried out in the R&D ERL.	
The committee however can see that a large detailed study program still needs to be performed. The committee is concerned about whether there is sufficient understanding of the interplay of IBS, beam-beam effects, wake fields and bunched beam electron cooling.	A study of the dynamics of RHIC in the presence of an electron cooler has been planned and will be carried out by December 2005.	A. Fedotov
The committee would like to recommend intensifying the effort in performing systematic comparison of theoretical models with experimental results obtained at existing electron cooler rings for the cooling forces and equilibrium beam parameters. Still it is unclear whether a satisfactory agreement with theory can finally be reached. Therefore the efforts should also focus on the scaling of experimental results obtained at low energy to the high-energy RHIC parameters.	Systematic comparisons of theory and experiment are planned and will be part of the collaboration with GSI. Initial program will be completed by December 2005, additional experiments will be planned following this initial phase.	A. Fedotov
Of concern are also collective instabilities in the cooled beam. The experience in existing cooler machines shows, that the cooling efficiency can be limited by collective instabilities induced by ring impedances. An accompanying study should collect the relevant instability thresholds for the expected cooled beam parameters (Gold ions and protons) in RHIC. A broadband feedback system might be required to fight against (low to medium frequency) collective instabilities.	Collective instabilities will be part of the RHIC beam dynamics study with a cooler section as described above.	A. Fedotov
However there are possible areas of concern which were not covered sufficiently by the presentations to the committee such as:	Not all effort in the group were described in the review due to the shortage of time. However: • The beam	V. Litvinenko

• Electron beam diagnostic systems, • Diagnostics of the cooled ion beam, and • A study plan for the ERL prototype	diagnostics part of the electron cooling group has been strengthened • A study plan for the ERL prototype is being prepared.	
The committee would like to mention that in view of the challenges to be met, the human resources dedicated to the accelerator physics and overall design issues appear to be quite small.	Human resources will be added as budget permits. the electron cooling project enjoys a top priority in the C-AD.	T. Roser
In view of the scale of the CW photo-injector with CsK2SB cathode development, the committee proposes that • alternative designs be considered. • The project management should consider strengthening the electron source team.	A significant effort is put into the photocathode development • An alternate design (using a secondary emission enhanced photocathode) has been developed. • The electron source team will be strengthened.	T. Rao
As these BBU simulation results depend critically on the magnitude of higher order mode (HOM) damping, the committee believes that it is important to perform measurements on a prototype RF cavity with HOM dampers to verify the expected quality factors of HOM experimentally.	HOM measurements will be started in June 2004 on a prototype RF cavity which is nearing completion.	R. Calaga
More generally, the committee wishes to stress the importance of early prototyping of hardware components, including ferrite absorbers, and novel diagnostic devices.	Ferrite absorbers will be tested in August 2004. Novel diagnostics will be tested as soon as possible, but possibly only in the R&D ERL.	R. Calaga V. Litvinenko
Control of phase and amplitude of the RF fields in RF cavities with high loaded Q can be challenging, depending on the required phase and amplitude stability. The design of a proper control algorithm may require	A control group has been established. Specifications will be developed and the RF control will work to meet these specifications. This work will be completed by 2006.	A. Zaltsman

simulations and may require testing. The committee suggests that specifications on the required phase and amplitude stability of the RF fields be worked out, and work on RF controls that meet the specifications be initiated.		
A solenoid system with a sophisticated field error compensation system was presented to the committee. The proposed solenoid production technique appears to be quite adequate. However it remains unclear to the committee whether the proposed plan for verification of the field direction with a precision of 10^{-5} rad is adequate. In view of the required field precision, the committee is concerned about the medium and long term mechanical stability of the long solenoids. o The committee suggests developing an alternative high precision measurement of the solenoid field direction. o The committee suggests furthermore starting to work on supports for the cooler section since the required mechanical stability of the long solenoid might be difficult to achieve.	A significant effort is devoted to the solenoid and its measurement system. It includes efforts to develop two alternative measurement systems. Work on the design of the cooler support section is planned.	A. Jain

Table 4.3.1 C-AD Machine Advisory Committee recommendations on electron cooling of RHIC and the corresponding responses in the C-AD electron cooling R&D plans.

2.0 Major Systems

2.1 SRF Cavity System

A NEW SHORT TECHNICALLY ORIENTED VERSION WILL BE SUBMITTED SOON

NEED 2.1.1.1

NEED 2.1.1.2

2.1.1.3 Ferrite Absorbers

Ferrite absorbers have proven successful in damping higher order mode (HOMs) in single cell cavities (CESR & KEKB). The Cornell ferrite design is being adopted in the five-cell linac cavity. Among commonly known RF absorbing materials, two satisfy beamline requirements: nickel-zinc and lossy dielectrics such as silicon carbide. Ferrites have the advantage of complex permeability μ as well as complex permittivity ε. Complex μ is necessary since the absorber located on the wall must have strong interaction with the magnetic field characteristic of most HOM's.

A similar Cornell design has been effectively tested up to 10.8 kW of HOM load, two loads typically associated with each cavity [2.1.1.3.1]. The ferrite are cooled by water flowing through the copper tubes brazed onto the surface of the heat sink of the ferrite as shown in Fig. 2.1.1.3.1.

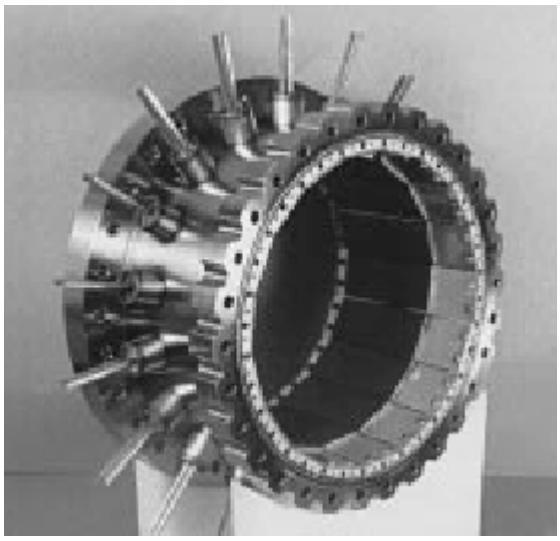

Fig. 2.1.1.3.1 HOM ferrite absorber

References

[2.1.1.3.1] E. Chojnacki et.al., *Beamline RF load development at Cornell*, PAC 1999, NY.

2.1.1.4 HOM COUPLER

Higher order mode (HOM) couplers have been widely used in superconducting cavities to absorb the HOM energy stimulated by the beam. The ERL cavity will have

two HOM couplers at one of the cavity ends to supplement the ferrite HOM damper. The design details of the coupler are shown in Fig. 2.1.x.1. The dimensions of the HOM coupler shown in Fig. 1 are in inches. The outer envelop (i.e. the cylinder), the tuner and the output coupling port are shown schematically in the left part of Fig. 1. The diameter of the inner surface of the cylinder is 50 mm. The tuner on the top part is adjustable up and down. The output is coupled by a capacitance between it and the inner conductor. The protrusion of the tip of the HOM coupler into the coaxial line is 0.917" (23.3 mm).

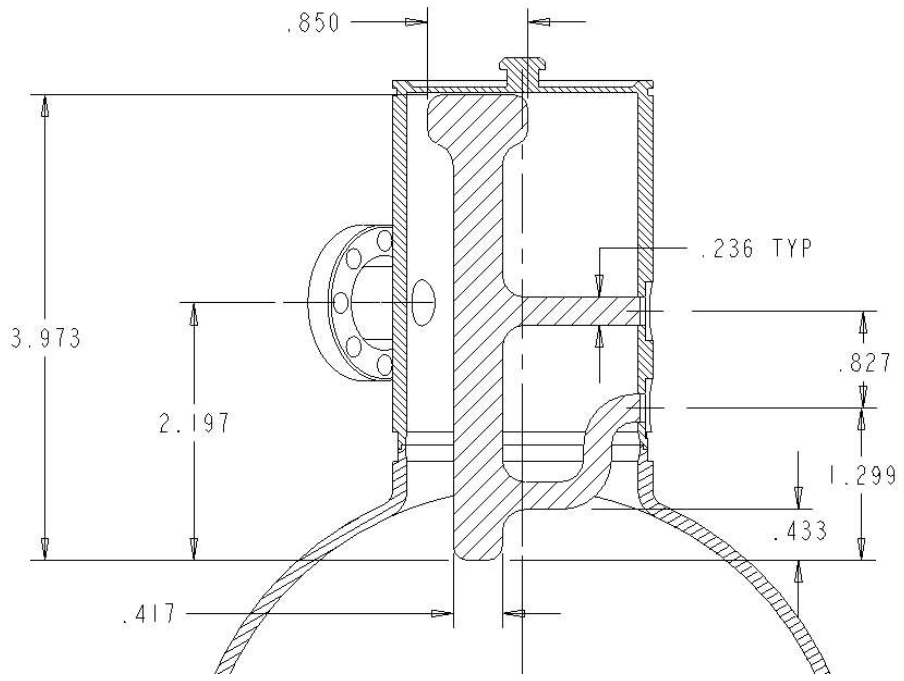

FIG. 2.1.x.1. Design and dimensions of the HOM coupler for the ERL cavity.

The purpose of the HOM coupler is to absorb as much as possible the HOM energy stimulated by the beam. Meanwhile it should absorb as little as possible the fundamental mode energy in the cavity. The effectiveness of the coupler was measured in the test set-up shown in Fig. 2.1.x.2. The main body of the set-up is a coaxial line, onto which the HOM coupler was mounted. Both the line and the coupler are connected to a network analyzer (Agilent 8753ES) for measuring the forward scattering coefficients at the HOM output.

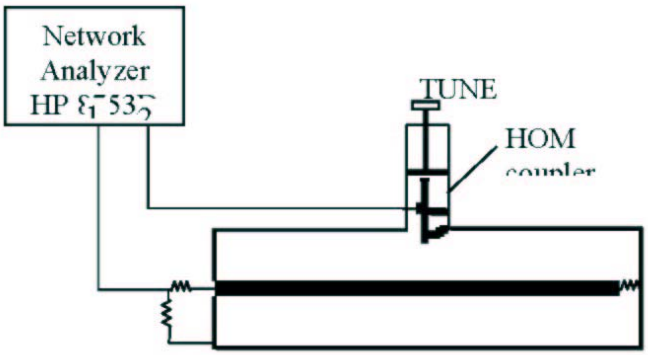

Fig. 2.1.x.2. Test setup to measure absorption by HOM coupler.

Fig. 2.1.x.3 shows a typical S21 response, with its amplitude at the top of the figure and its phase at the bottom. The measurement of S21 in this set-up is expected to have a minimum (a notch) at the fundamental frequency, and to have rather large values at high frequencies. This has been done by the adjustment of the tuner at the top of the tuner. It was seen that the "notch" is at 707 MHz with S21 of -100 dB and is very sharp. S21 at high frequency is around -20 dB, or 80 dB higher than that of the fundamental frequency. The paramount HOM was found from MAFIA computations to be around 950 MHz and its S21 exceeds the fundamental mode by about 50 dB .

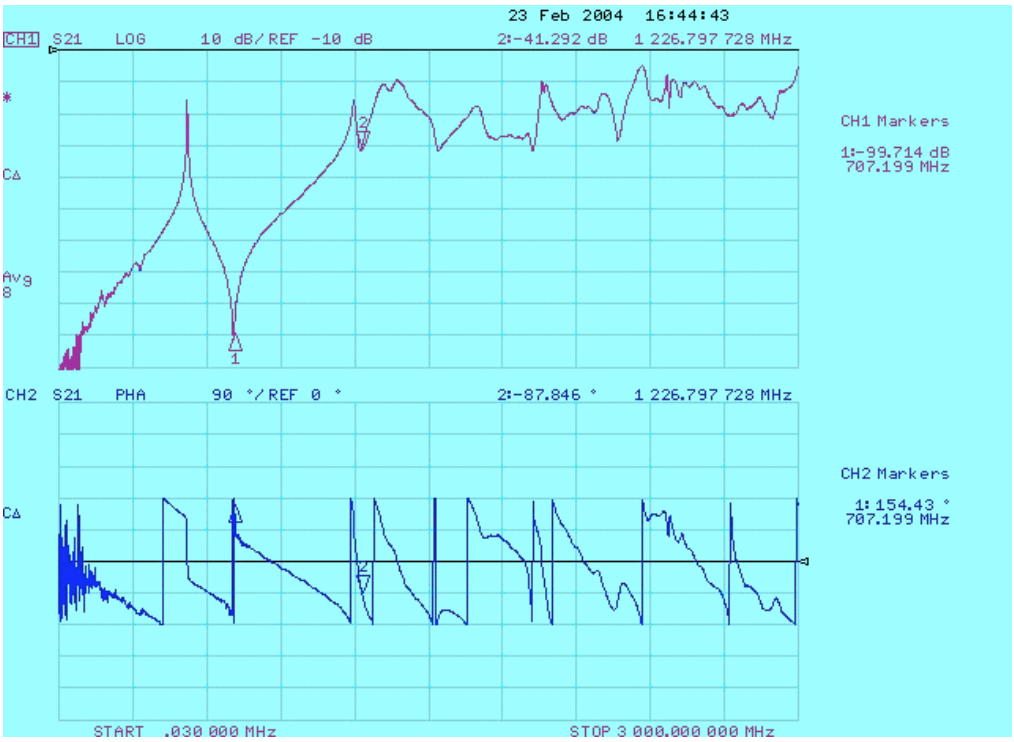

Fig.2.1.x.3. The measured S21frequency response via network analyzer HP8753D, note the "notch" is at 707 MHz. The curve on the bottom is its phase.

Destructive heating of the coupler has been observed at other laboratories and must be prevented by precise tuning of the notch to the fundamental frequency. The notch is narrow sharp in the superconducting structure and results in an extreme mechanical sensitive to the position of the tuner, possibly a limiting disadvantage.

REFERENCES:

[2.1.x.1] J. Sekutowicz, *Higher Order Mode Coupler for TESLA,* Report TESLA 94-07 (DESY,1994).

[2.1.x.2] Y. Zhao and H. Hahn, *HOM Coupler Measurement and Simulation,* BNL-Report C-A/AP/ * (2004, in preparation)

2.1. Superconducting RF Cavity
2.1.0 Design Considerations
2.1.1 Niobium Cavity Cryomodule
  2.1.1.1 Nb Cavity
  2.1.1.2 Helium Vessel
  2.1.1.3 Ferrite Absorbers
  2.1.1.4 HOM Couplers
  2.1.1.5 Transition Pieces
  2.1.1.6 RF Shielded Valves
2.1.2 First Copper Cavity
  2.1.2.1 Test Equipment
2.1.3 Second Copper Cavity

Probes for (relative) for the measurement of higher-order mode power can be used for the purpose of beam position tuning. Preliminary solution involves the insertion of a double-sided conflat between the cavity flange and the ferrite HOM absorber flange. Four radial holes (~6mm dia) at 90 degrees around the circumference can then terminate in short tubes and mini-CFs, permitting insertion of short electric field probes. Space in the layout will be provide for this.

2.2

2.2.1 ERL SC Gun HLRF System

HLRF system for the superconducting gun will provide 1 MW of RF power. It consists of 1 MW CW klystron, lead garage to shield from the x-rays generated by the klystron, transmitter and power supplies, circulator to provide the match to the klystron, 1 MW dummy load, power splitter to limit the maximum power to the RF window to 500 kW and all waveguides.

2.2.2 ERL SC Cavity HLRF System

HLRF system for the superconducting cavity will provide up to 50 kW of RF power to the cavity. It consists of 50 kW transmitter, circulator, dummy load and waveguides. Amplifier is standard, stand-alone digital TV transmitter.

2.2.3 ERL LLRF System Description

The LLRF control system proposed for the Bldg. 912 ERL is a modern mixed analog – digital system. It will be designed to provide robust, independent control of field amplitude and phase for both the ERL cavity and the photocathode gun, as well as beam energy and phase regulation loops. The system will be based primarily on proven hardware designs; however, there will be significant R&D effort required due to the frequencies involved and the very tight energy and phase regulation specifications. The system will also be designed with future RHIC compatibility in mind. Operator control of the system will be provided via standard C-AD controls interfacing and custom operator screens.

2.3 Injector System

TO BE REPLACED BY NEW SHORT TECHNICALLY ORIEINTED VERSION SOON

2.4 Cryogenic System

The cryogenic system consists of a 5-cell RF cavity and a superconducting gun. Both the 5-cell cavity and the superconducting gun, each with a power coupler, are to be operated at 2.1 K. The power couplers require 5 K cooling. End flanges of the cavity also need to be cooled at 5 K for reducing heat input to the 2.1 K system. An 80 K heat shield with multi-layer superinsulation is used to minimize thermal radiation.

Due to the small scale of the experiment, an open system using liquid helium is selected instead of a closed cycle helium refrigerator. The flow schematic for cooling the cavity and the RF gun is given in Figure 2.4.1. A room temperature vacuum pumping station is used to create the 0.04 bar pressure for 2.1 K operation. Supercritical helium at 4.5 K and 3 bar is used to cool the power couplers and the end flanges. Liquid nitrogen will be used to keep the heat shield between 80 and 100 K.

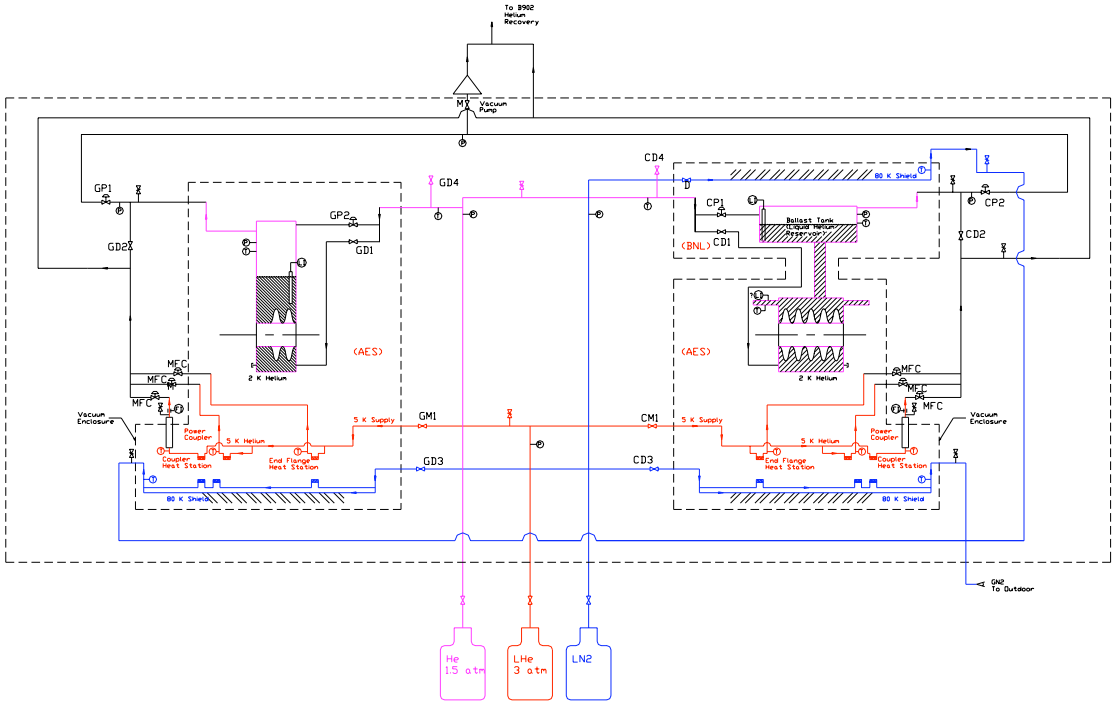

Figure 2.4.1: Flow schematic for cooling ERL experiment in B912

Parameters and heat loads of the ERL experiment are given in Table 1. The heat loads are extrapolated from similar cryogenic systems[1] and are believed to be on the conservative side. The static heat load consists of heat conduction and thermal radiation. The dynamic heat loads result from RF operation. Total heat load and pressure requirement for the ERL experiment are given in Table 2. Depending on the duty cycle, allowance for the 2.1 K dynamic load is no more than 25 W. The 4.5 K dynamic heat

loads are assumed to be the same as the couplers used in the SNS project[1]. The liquid helium volume and projected operating time for test are also given.

TABLE 1: PARAMETERS AND HEAT LOADS OF THE ERL EXPERIMENT

	5 cell Cavity	RF Gun
Cells	5	2
Length	~ 1.5 m	< 1 m
2 K static heat load	< 25 W	< 25 W
2 K dynamic heat load	< 20 W	< 15 W
4.5 K load for couplers – static, 4.5 K, 3 bar	~ 0.05 g/s	~ 0.05 g/s
4.5 K load for couplers – dynamic	~ 0.025 g/s	~ 0.025 g/s
Shield heat load	200 W	200 W

Table 2: Cryogenic system parameters

Temperature	2.1 K	4.5 K	80 – 100 K
Pressure	0.04 bar	3.0 bar	~ 1.2 bar
Static load	< 50 W	~ 0.35 g/s	400 W
Dynamic load	< 25 W	~ 0.15 g/s	-
Total load	< 75 W	~ 0.5 g/s	400 W
Liquid required	~ 10 L / hour	~ 15 L / hour	~ 10 L / hour
Liquid Capacity	650 L	250 L	250 L
Time for operation	~ 15 hours	~ 15 hours	> 15 hours

2.4.1 BALLAST TANK

In the ERL experiment, the cavity will be filled with liquid helium before pump down to 2.1 K. Ample liquid helium above the 2.1 K devices must be provided to account for the expense of liquid helium during 2.1 K pump down.

For the 5-cell cavity, a helium reservoir "Ballast Tank" about 500 Liters (liquid volume) will be installed. With an estimated 150 L liquid helium volume in the vessel around the 5-cell cavity, total liquid volume is about 650 L before pumpdown. When the cavity is pumped from 4.5 K to 2.1 K, there is approximately 300 L of liquid helium left. This leaves about 150 L of liquid helium above the cavity available for the experiment. The tank shall be designed with additional volume for phase separation. The volume of the tank is estimated at 650 L. Proper mechanism for liquid carry over prevention needs to be incorporated.

For the superconducting gun, there will not be a separate Ballast Tank. Helium vessel for the superconducting gun shall have an appropriate volume above the gun for 2.1 K pump down.

2.4.2 2.1 K VACUUM PUMP

The proposed vacuum pump station consists of booster pump and duplex liquid ring pumps by Kinney Vacuum. These types of pump have been successfully used in other national laboratories.

The capacity of the pump skid is 38 SCFM at 10 Torr. The mass flow as a function of temperature is given in Figure 2.4.2. The suction pressure is assumed to be 2/3 that of the saturation pressure of helium. Both BNL calculation and estimation from Kinney are given.

The cooling capacity as a function of temperature is given in Figure 2.4.3. Cooling capacities calculated from saturated liquid and liquid at 4.5 K are given. The capacity with 4.5 K liquid feed is about 2/3 that with liquid at saturation temperature.

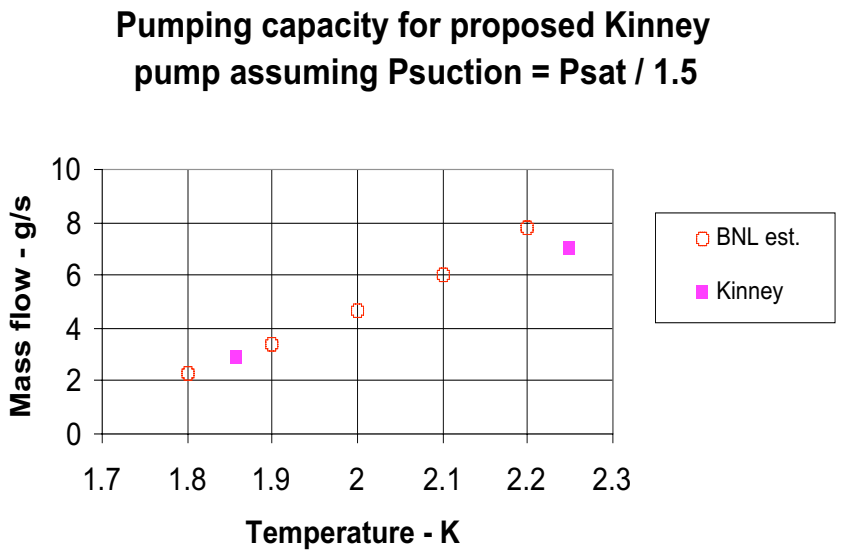

Figure 2.4.2: Mass flow as a function of temperature for the proposed vacuum pump

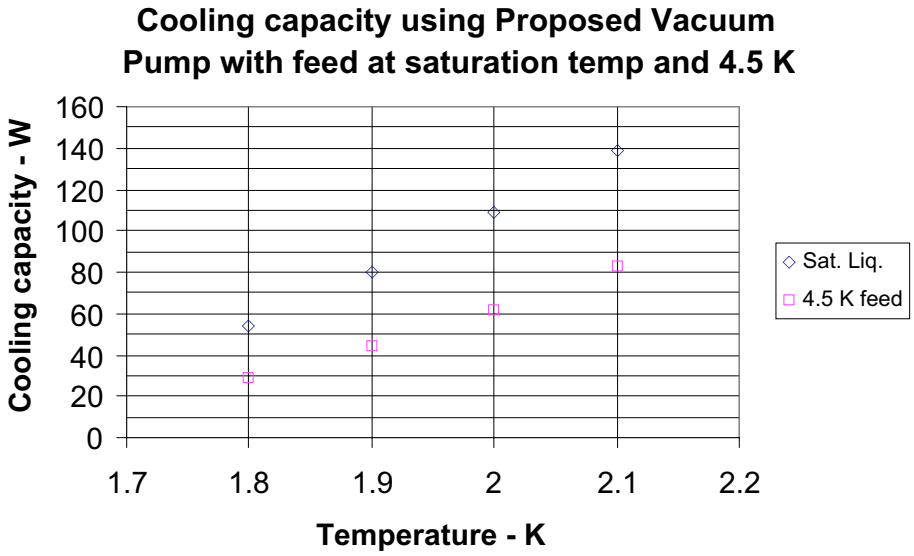

Fig. 2.4.3: Cooling capacity as a function of temperature for the proposed vacuum pump with saturation liquid and 4.5 K liquid feed.

2.4.3 WARM PIPING

A top view for the layout of the ERL experiment in B912 is given in Figure 2.4.4. Both warm piping and transfer lines need to be provided according to the flow schematic given in Figure 2.4.1.

The largest line is 10 inch IPS for the low pressure return from the cavity and gun to the suction of the 2.1 K vacuum pump marked pink in Figure 2.4.4. Other lines will be shown and explained at a later time.

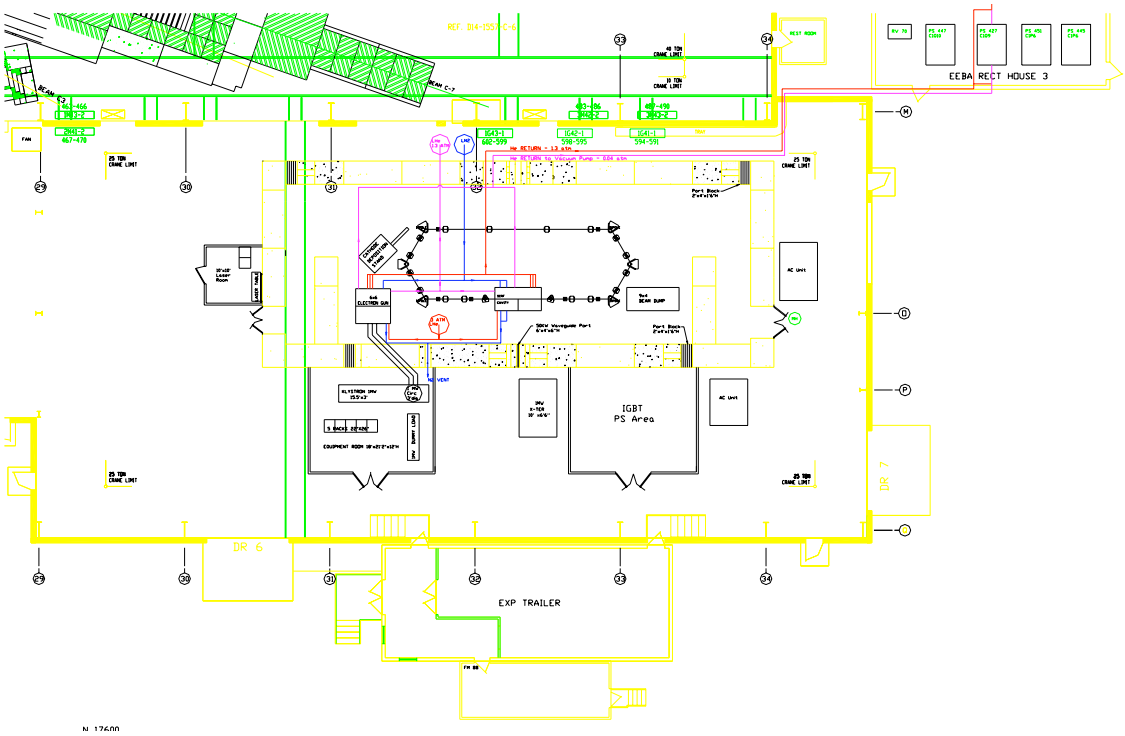

Figure 2.4.4: Layout of ERL experiment in B912

2.4.4 TRANSFER LINE

To avoid transporting effort, liquid helium for the cavity and gun will be transferred from lines connected to the outside of the concrete block wall. For cooling power couplers and end flanges, a 250 L dewar will be brought to the experimental area to minimize heat loss associated with transfer.

The transporting dewars will be shipped to the connecting point outside the concrete block wall. Cavity and gun will be cooldown according to the required rate. The cooldown will continue until liquid helium reaches the top of the Ballast Tank for the cavity or the helium reservoir for the gun. The system is then isolated and ready for 2.1 K pump down.

For cooling the power couplers and end flanges, a 250 L dewar with a design pressure of 4 to 5 bar will be used. The dewar will be transported to area near the cavity. Transfer lines will be connected to the cryostat to provide 4.5 K helium at 3 bar.

The liquid nitrogen dewar of about 250 L will be used for cooling the thermal heat shield of the cavity, the Ballast Tank and the gun. A transfer line will be used to simplify transporting of cryogen in and out of the experimental area.

REFERENCES:

[2.4.1] C. Rode, et al., *The SNS Superconducting Linac System*, Proceedings of the 2001 Particle Accelerator Conference, Chicago.

2.5 Vacuum Systems

Vacuum level of 10^{-11} *Torr* is needed in the RF gun for the quantum yield and life time of the photocathode. Vacuum in SRF is normally at 10^{-12} *Torr* owing to the large cryopumping provided by the 2^{o} K surface. Otherwise, a clean ultrahigh vacuum of low 10^{-9} *Torr* is sufficient for the operation of ERL, and to minimize gas migration and particulate contamination to the cavities.

Most ERL beam pipes will be made of stainless steel with 5cm aperture. Except at the two chicane regions, the chamber design is rather conventional. The six dipole chambers, curved by 60^{o}, will have a rectangular cross section of 1.5cm (H) x 3cm (V) with two tangential ports for the exit of synchrotron light. For beam diagnostics, thin Sapphire windows will be used at the exit ports to minimize the attenuation of the infrared light. No water cooling of the dipole chambers is necessary for the little synchrotron radiation power generated by the relatively low energy beam. The 5cm diameter pipes for quadrupoles will be welded to bellows and BPMs, and mounted on the magnet pole face to precision align the BPMs. To minimize HOM losses, the bellows and the pump ports will be shielded, and the steps will be tapered. The RF gun and the beam dump, and the associated chicane chambers will have to be carefully engineered for the successful merge and extraction of the beam, respectively.

The ERL will not be *in-situ* baked except at the RF gun region. Nevertheless, UHV practice will be used through out to eliminate any possibility of hydrocarbon contamination which is detrimental to the performance of the photocathode and SC cavities. All the chamber components will be made of UHV compatible metal or alumina ceramic. They will be thoroughly cleaned and degassed in a vacuum furnace prior to assembly, reducing the outgassing and contamination. Sputter ion pumps will be used to pump and maintain the 10^{-9} *Torr* vacuum in ERL. Due to the small aperture and linear conductance, ion pumps of ~20 *l/s* positioned every two meters will provide satisfactory pressure level in ERL as shown in Fig. 2.5.1. Pump spacing of less than two meters might not be practical due to the presence of various beam components and length of vacuum chambers. The ion pump current can and will be used to measure the pressure distribution in ERL. The combination of titanium sublimation pumps and ion pumps will be used to achieve 10^{-11} *Torr* vacuum in the photocathode gun region.

In the beam dump, additional lump pumps are needed to handle the gas load from the thermal outgassing and the electron stimulated desorption (ESD). The thermal outgassing of Cu surface at 100^{o}C is approximately 10^{-10} *Torr.l/s.cm*^{2} [2.5.1] after a short period of beam conditioning/baking, or a total outgassing of ~10^{-6} *Torr.l/s* for the 10,000 cm^{2} dump surface. Assuming an ESD yield _ ~ 10^{-3} [2.5.2] after modest beam dose, the total gas flux is ~ 3×10^{-5} *Torr.l/sec* for a 200mA beam. Therefore, pumping speed of > 10^{3} *l/s* is needed to maintain a 10^{-8} *Torr* vacuum in the beam dump, where either cryopump or NEG pumps supplemented by ion pump may be used. Gate valves will bracket SRF and will isolate the injector and the beam dump when the needs arise. No additional valve is envisioned at the ERL. A thin-wall (~75 μm) beryllium window to separate the ERL and

the beam dump was evaluated and found to have excessive temperature [2.5.3] if relying solely on convection cooling.

Pirani and cold cathode gauges will be used as primary vacuum measurement, and will be supplemented by the ion pump current readouts. Cold cathode reading together with the arc detector will trip the RF power and protect the coupler window in the RF gun. Portable residual gas analyzers may be used to analyze the gas composition when problem arises. All the vacuum electronic devices will be located outside the ERL. These devices can be operated through front panel switches and will communicate with the PLC based control system through serial network for remote monitoring and control. PLCs will provide the logic for the operation of the sector gate valves, other vacuum devices and ERL subsystems with hard wired I/O.

[2.5.1] G. Moraw, Vacuum, 24, p125 (1974).
[2.5.2] J. Gomez-Goni and A.G. Mathewson, J. Vac. Sci. Technol., A15, 3093 (1997).
[2.5.3] C. Pai, ANSYS Anaysis, May, 2004.

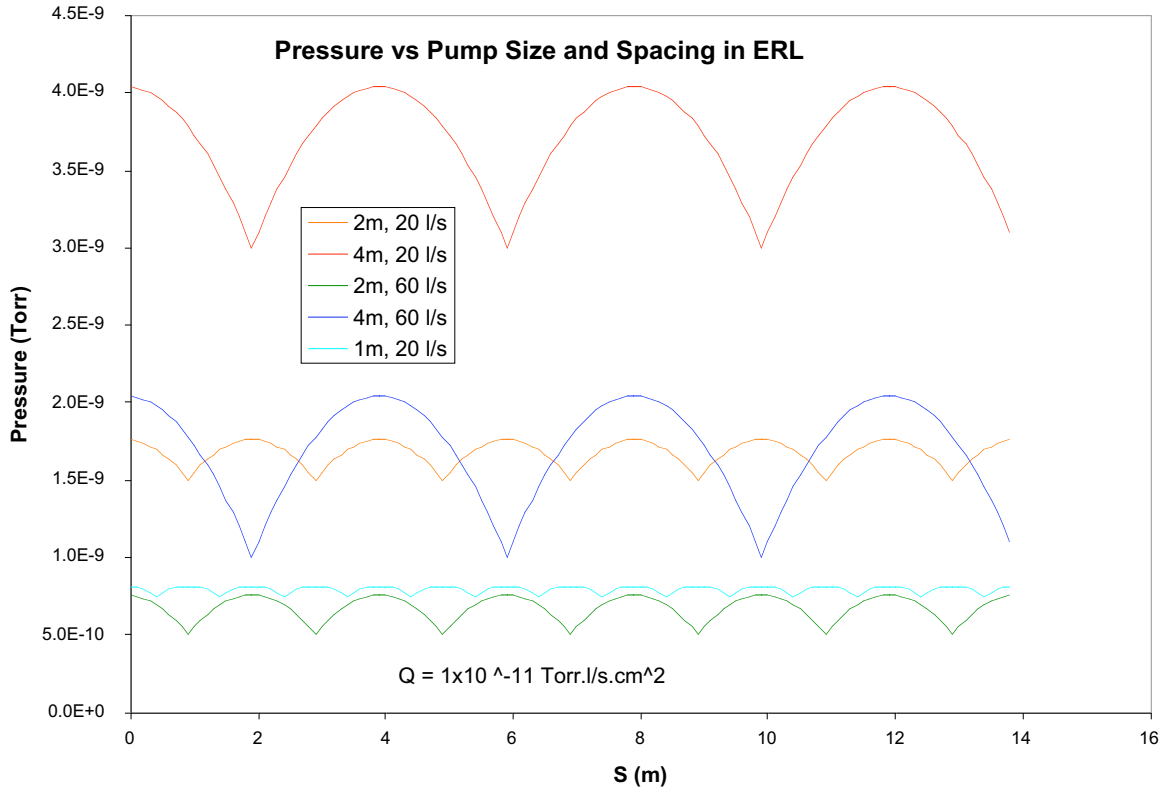

Fig. 2.5.1. Pressure distribution in ERL versus pump size and spacing, assuming a uniform outgassing of $1x10^{-11}$ *Torr.l/sec.cm*^{2}, with 50% H_2 and 50% H_2O, typical of a not *in-situ* baked UHV system.

2.6 NEED

2.7 Magnet Electrical

2.7.1 MAGNET POWERING DESIGN CONCEPT

The magnet powering concept is to maximize the use existing power supply designs, and control those units with BNL standard Power Supply Interfaces (PSIs) and Power Supply Controllers (PSCs).

There will be three types of power supplies. The main dipoles and quads will be powered by larger, more precise (100 ppm), unipolar power supplies. The trim windings of the main dipoles and quads will be powered by smaller, less precise (1000 ppm), bipolar power supplies. The chicane magnets and solenoids will use unipolar power supplies, also in the 1000 ppm range. All models will use standard PSIs and PSCs with 16 bit DACs and ADCs.

2.7.2 CONTROLLING THE POWER SUPPLIES

Each power supply will be controlled by its own PSI. This interface provides electrical isolation between the power supply and the control system, as well as isolation between power supplies. The PSI communicates with the PSC using a pair of fibers. Each PSC can control up to six PSIs. The PSC normally resides in a VME crate with the interface computer and timing boards.

The PSI provides one analog set point from a 16 bit DAC, which can be configured as either unipolar or bipolar. There are four analog read backs that are quantized by 16 bit bipolar ADCs. Fifteen command bits are available. A sixteenth bit is used for internal calibration. Sixteen status bits

There are many other hardware features that make this a useful interface. Read and write triggers may be either hardware or software initiated. Each channel in the PSC has a circular buffer of over 5000 records. This allows historical information in the event of a fault. Also, the PSC is designed to be able to operate without a VME crate. By using a serial port of laptop computer, the power supplies can be fully tested even without the control system being active.

With hundreds of these units in use or currently being installed, there exists a large software base at BNL for this device.

Figure 2.7.1 shows a typical application of the PSI and PSC. In this case, eight bipolar corrector power supplies are in one rack.

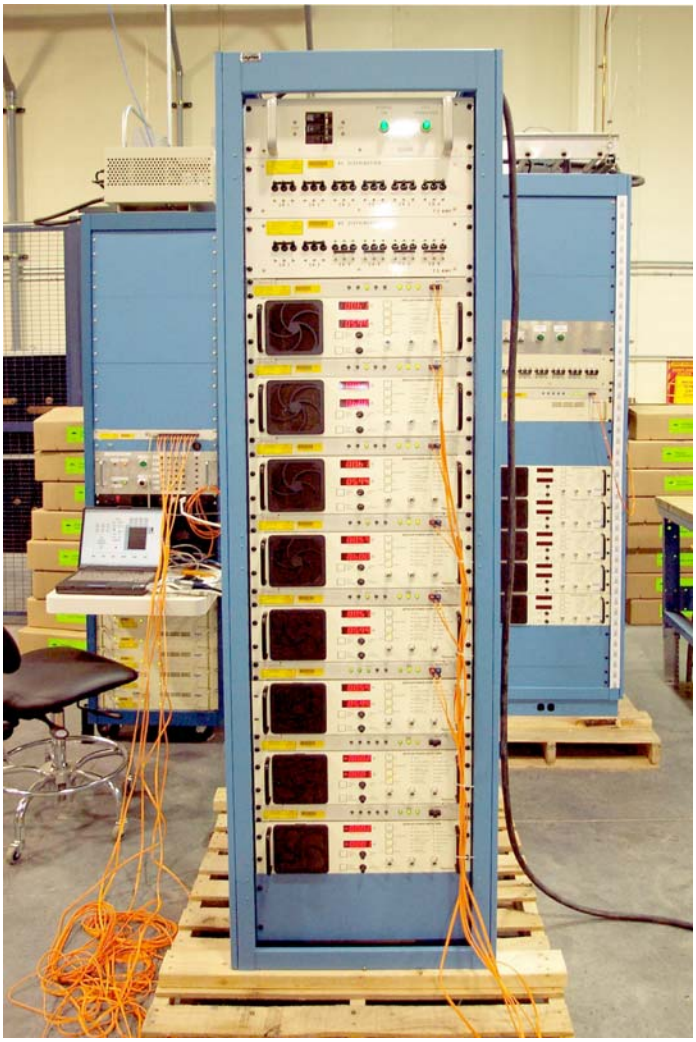

Fig. 2.7.1 Eight bipolar power supplies using PSI / PSC control.

2.7.3 LARGE UNIPOLAR POWER SUPPLIES

The main dipole and main quadrupole magnets will be powered by high precision unipolar power supplies. These units will be stable to within 100 ppm. As there are no ramping requirements, the bandwidth of the power supplies can be low. This gives flexibility in the selection of topology. A simple twelve pulse phase controlled power supply can be used. A unipolar switch mode design would also be considered.

All power supplies will have circuitry to monitor thermal switches and flow switches if the magnets are water cooled. In addition, leakage currents to earth ground will also be monitored. Every unit will also have security enabling circuits.

The power supplies will be internally protected as well, monitoring output voltages, currents, line condition, thermal switches on power components, and flow switches on

water cooled elements. Any fault will shut down the equipment and report the status back through the PSI / PSC.

There are six identical main dipoles in the ring. These will all be connected in a series circuit and energized by a single power supply. The thirty main quadrupoles will be energized in pairs, which will require fifteen power supplies.

2.7.4 BIPOLAR POWER SUPPLIES

In addition to showing the control elements, Figure 2.7.1 also shows typical bipolar correction power supplies. These units use a switch mode pre-regulator directly off the line, followed by a linear H-bridge. They are designed to interface directly with a BNL PSI. Hundreds of these units have already been produced, and they are used at Oak Ridge National Lab, and BNL. They are also be evaluated for LHC applications at CERN.

The bipolar units needed for this project are in the range of 5W to 100W, which are much smaller than the 1500W units shown in Figure 2.7.1. At these lower power levels, linear bipolar power supplies may be more economical.

There are two general areas of application in the ERL for the bipolar power supplies. First, each of the six main dipole magnets and each of the thirty main quadrupole magnets have trim windings. Thirty six bipolar supplies will be used to individually power these windings. Each of the six dipole trim windings provides horizontal steering. But, the quadrupole trim windings can be configured as a quadrupole correction, vertical steering, or horizontal steering.

Second, bipolar supplies will be used individual steering elements, as is the case with the beam dump steering magnet and trim windings for the chicanes.

2.7.5 SMALL UNIPOLAR POWER SUPPLIES

Lower power, less precise unipolar power supplies will be used for the chicane magnets and the solenoid magnets.

Each of the three chicanes (input, output, and phase tuning) consists of four magnets which will be powered in a series circuit by one small unipolar power supply.

There will be five solenoid magnets. These will be powered in three circuits by small unipolar power supplies.

2.7.6 POWER SUPPLY SUMMARY

Table 2.7.1 summarizes the inventory of power supplies needed for this project. By minimizing the number of different models of power supplies, the project can be supported with less spare equipment. Spare units are not listed in this table.

Table 2.7.1 Power Supply Summary

Function	Type	Number of Magnets	Number of Required Power Supplies	Power Supply Rating
Main Dipole	Unipolar	6	1	
Dipole Trim	Bipolar	6	6	
Main Quad	Unipolar	30	15	
Quad Trim (quad or steering function)	Bipolar	30	30	
Solenoid	Unipolar	6	3	
Input Chicane	Unipolar	4	1 Main	2 A @ 40 V
	Bipolar		2 Trim	1 A @ 5 V
Output Chicane	Unipolar	4	1 Main	2 A @ 40 V
	Bipolar		2 Trim	1 A @ 5 V
Phase Tuning Chicane	Unipolar	4	1 Main	2 A @ 40 V
	Bipolar		2 Trim	1 A @ 5 V
Dump Steering	Bipolar	1	1	1 A @ 5V

2.8 Electron Beam Dump System

As its name suggests, the beam dump is where electron bunches end up while depositing energy unrecovered by the ERL. The process of removing unrecovered energy must not have any adverse effects on the ERL system like outgassing or backstreaming electrons. Electron beam dumps are widely used in various applications ranging from radiation generating devices like klystrons and traveling wave tubes to EBIS sources and electron beam coolers, as well as to large machines that include LINACs and electron colliders. Energy of discarded electrons range from a few electron volts to 10's of GeV.

This beam dump has a couple of unique issues that determine the design concept: cascade showers and special need for high velocity turbulent cooling.

2.8.1 Physics Issue: Cascading

Most electron beam dumps are basically energy disposal devices. Just like in proton or heavy ion beam dumps, particles are stopped in solid materials, which are cooled (usually by water). For electrons with energy exceed 1.022 MeV, there is the phenomenon of cascading that must be dealt with. These electrons, when passing through solid material generate gamma rays, which in turn produce electron - positron pairs. The positrons annihilate and generate more gamma rays that produce more electron – positron pairs, thus resulting in cascade showers.

Angular dependence of cascade showers on beam energy is rather strong. The higher the energy, the less the angular spread. In the energy range of 30 – 40 GeV (like at SLAC), cascade showers are directed forward in the direction of beam propagation and have practically no energy spread. Beam dumps in this energy range are long solid tubes of water cooled low Z materials. They are easy to design and fabricate since there is low power per unit length of dissipation.

In the energy range of 1.022 MeV to 10 MeV, cascade showers spread laterally. Therefore, deposited electron beams must be spread out to power levels of below 500 W/cm^2 to prevent burning holes. But, this level of power density removal requires very challenging cooling techniques. Therefore, spreading beam deposition to below 100 W/cm^2 is preferable.

2.8.2 Beam Dump Constraints & Requirements

A maximum total power of 1 MW must be removed based on the following electron beam parameters and electron beam energy/average current options:

Total power 1 MW

	Option A	Option B
Electron energy	5 MeV	2 MeV
Average current	0.2 Amp	0.5 Amp

Entry beam height 50 inches (127 cm); beam dump should be insulated either from its support structure, or the support structure should be insulated from the floor (which ever is easier and cheaper).

The beam pipe has 4" diameter, and the ERL system pressure is 10^{-9} Torr.

2.8.3 Beam Dump Description

Figure 2.8.1 is a sketch of the beam dump. The beam will impinge on a flat water-cooled, copper plate measuring approximately 36x48 sq. in. This large area is to insure that local boiling of the cooling water does not occur. The beam will be spread over this large surface area by rastering it with magnetic field coils. One set of coils will be for vertical scanning and the second set for horizontal scanning.

The rectangular beam dump will be attached to the end of a stainless steel scan chamber. The half angle of the scan chamber is approximately 12 degrees. This relatively small angle is desirable to limit scattering (reflection of the electrons from the copper) of the electron beam into the sides of the chamber. Even with this small angle some reflected electrons are anticipated and consequently water-cooling channels would be added to the stainless steel scan chamber. The spot size is also easier to control with the small angle deflection when there is a large energy spread in the beam.

The beam dump will have an overall length of approximately 9 feet. The width of the device will depend on the mounting orientation and could range from 4 to 5 feet depending on the preferred orientation of the 36 inch by 48 inch copper plate. Likewise the overall height will be dependent on the copper plate orientation and required beam centerline height. A separate stand supporting the dump will be bolted to the floor through an insulator. There will be some adjusting features that will allow the dump to be matched up to the beam line. It is suggested that a flexible bellows be installed between the beam line and beam dump to allow for thermal expansion. The weight of the beam dump is expected to be approximately 6000 pounds and an additional 1500 pounds for the support structure.

Average cross section of the copper beam dump plate is approximately 1 inch thick, and it has approximately 80 percent copper and the water channels constitute about 20 percent of its volume. This thickness and ratio is approximately the same for a beam dump option where the electron beam impinges on an aluminum plate.

Average cross section of the stainless steel scan chamber walls is approximately .375 inches thick and it has approximately 94 percent stainless steel and 6 percent water by volume.

Pros and cons of the aluminum plate choice are as follows:

- Less radiation is generated by an electron beam impinging on aluminum.
- The aluminum option is cheaper.

- But, aluminum sputters easily, short lifetime.
- Aluminum vapor may have adverse chemical effects on other components of the ERL system.

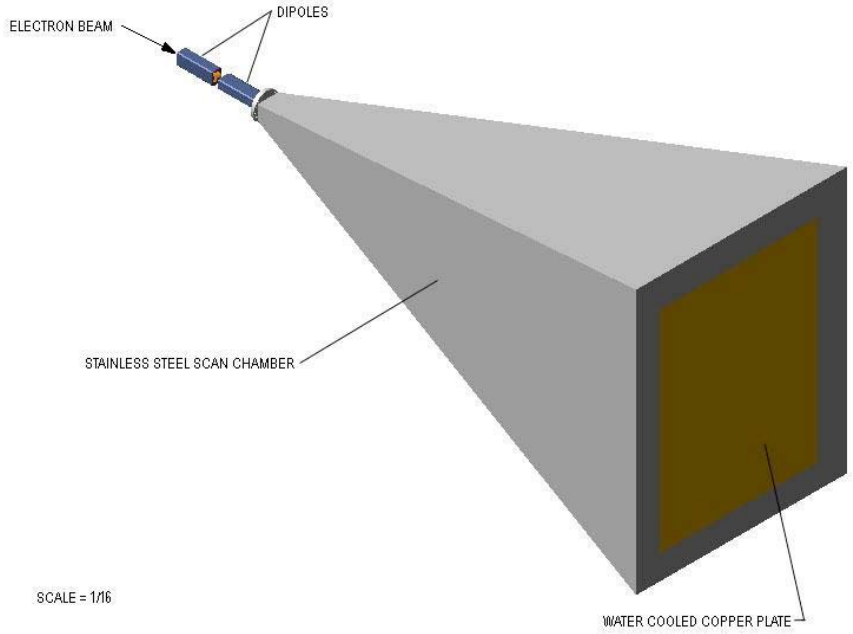

Figure 2.8.1 Beam dump layout

2.8.4 Rastering

The rastering system comprises a pair of dipole magnets driven by amplifiers and protective interlocks. The interlocks are critical. If either of the amplifiers, field coils pairs or interconnecting cables fails, the 1 MW beam will dwell in a small area and failure of the beam dump will happen in seconds. The ideal waveform is a saw tooth: a linear ramp from negative to positive with a fast fly back to the negative value. This shape can be used to prevent the doubling up of the power at the extreme deflection if just a triangular waveform is used. However, this fast fly back dramatically increases the frequency response requirements of the amplifiers. Another way to achieve this is to "step" the horizontal sweep.

The vertical sweep will probably be triangular and the horizontal will be a stair step at a frequency of about 20 kHz.

2.8.5 Cooling

Due to the high density of the deposited power, high speed turbulent water flow is needed. The 1 MW heat load concentrated over the surface area of 36 by 48 inches requires a very high velocity water source that can deliver at least 400 gallons per minute through the beam dump. The minimum pressure drop required across the beam dump plate for creating sufficient heat transfer is 120 psid. In order to have a film temperature of no more than 60 F above that of the cooling water (i.e., a low temperature difference between the water in the center of the tubing passages and the edge); cooling must be done at a temperature differential of no more than 15 – 20 F, hence the requirement for a very high water flow. Therefore a special Water Cooling Pumping System that is specifically designed for this kind of service should be included. This Water Cooling Pumping System requires between 100 and 150 gallons per minute of facility water be delivered to it from the 912 facility cooling system. This Pumping System shall be 4 feet by 4 feet by six feet high and shall require a 480 Volt 3 phase 60 amp service outlet. The facility water pressure drop through the primary side of the Water Cooling Pumping System shall be approximately 50 psi.

2.8.6 Vacuum System

Vacuum pumps will have to be installed on the scan chamber to control the pressure rise when the beam is on. Pumping requirements can be determined from the wall temperature, which is expected to be 200 F plus the maximum water temperature (90 F), i.e., about 300 F. For pumping, roughing and gauges, three ports with 6" conflate flanges on the scan chamber bottom, and four ports with 2.75" conflate flanges on the side are needed.

2.8.7 List of Components and Controls

Components:

1. Beam dump plate
2. Stainless steel beam dump chamber
3. Beam dump support
4. Support insulator
5. Beam pipe insulator
6. 2 dipole scanning magnets with laminated magnet cores
7. 2 amplifiers each requiring a DC power supply
8. 2 bipolar low voltage scanning waveforms. The vertical sweep will probably be triangular and the horizontal will be a stair step at a frequency of about 20 kHz.
9. Interlocks
10. Bellows
11. 2 turbomolecular pumps
12. 2 vacuum valve

13. 2 mechanical pumps
14. Vacuum gauges, at least 2
15. Water flow meter
16. 2 water temperature sensors

Readouts, Cables & Controls

1. Bipolar low voltage-scanning waveforms for x and y scanning; 2 signals.
2. On/off control for raw DC power supplies. 2 signals
3. Redundant methods to check the actual current output to the current input into the coils. 4 signals
4. Several warning/fault signals are available from the amplifiers; want to monitor at least 2 from each.
5. Total beam dump current.
6. Beam current signal from beam pipe insulator
7. Signal from interlocks
8. Signals from pumps and valves. 6 signals
9. Vacuum gauge readouts. 2 signals
10. Water flow readout
11. 2 water temperature readouts

Total number of signal and control cables: at least 30

2.8.8 Cost and Schedule

The projected beam dump is $158,000 FOB Brookhaven, NY and can be provided in 8 to 10 weeks after receipt of order. This cost includes $40K for water pumping system. A rough estimate for the rastering system and protective interlocks is $40k. The total cost FOB BNL is $ 198,000. Ceramic insulated vacuum section with 6" conflate flanges costs about $500.

Cost of solid-state amplifiers for needed for rastering is approximately $20k each plus the cost of waveform generators and DC power supplies. Total cost is about $50k.

Installation and operation at 912 can be done by BNL personnel or on a time and material cost basis by the company providing the beam dump. One possible scenario is to start with a surveyor team to determine dump position, followed by a rigger team, and person from company providing the beam dump assisted by a BNL technician to make the final connections. The cost of person from company providing the beam dump (including travel) is about $ 2,500. One technician for a day is $827, two surveyors for two hours $221, and 2 riggers for one day $1237. 3.5% escalation for FY05 is included in the cost.

Grand Total = $ 253,285; price does not include contingencies.

2.8.9 Aluminum Beam Dump Option:

The Beam Dump Assembly can also be constructed using an aluminum chamber and aluminum beam absorption plate. This assembly would be an all welded construction that would be attached to a conflat flange with a suitable adapter. The cost of the Aluminum Beam Dump Option is $139,000 FOB Brookhaven, NY and can be provided in 8 to 10 weeks after receipt of order.

Aluminum does not last as long as copper. Therefore, it is not a viable option for the RHIC E-Coolers, which require prolonged operation over many years. But, aluminum dump may be suitable for the ERL. Its advantages are substantially lower radiation and a lower cost.

2.9 Beam Diagnostics

General Information

Table 1 is a brief compilation of ERL machine parameters used in the preliminary design of the various beam diagnostics systems [1,2,3]. As suggested by the table, the ERL will operate in either of two modes. In the first (high bunch charge) mode, the 9.383/28.15 MHz bunch frequency is appropriate for electron cooling of 120/360 bunches in RHIC (although other bunching frequencies are under consideration). In the second, every bucket of the 703.75MHz RF will be filled for low emittance studies. The additional dynamic range required by these two modes adds only minimal complication or expense. However, some forethought is required as a result of the sparse spectrum with the 703.75MHz bunching frequency. This makes it more difficult to work away from the RF frequency,

Table 1 Machine Parameters

Parameter [units]	high chg	low emit
inj energy [MeV]	3-5	3-5
beam energy [MeV]	15-20	15-20
rms bunch length [ps]	~20	~20
RF frequency [MHz]	703.75	703.75
revolution freq [MHz]	9.383	9.383
bunching freq [MHz]	9.4/28.15	703.75
charges/bunch	~1e11	4e9
beam current [mA]	~150/450	500
rms energy spread	10e-3	10e-4
εx, εy [mm-mrad]	30	1-3
beampipe dia [cm]	6	6
energy recovery [%]	99.95	99.95
current recovery [%]	99.9995	99.9995

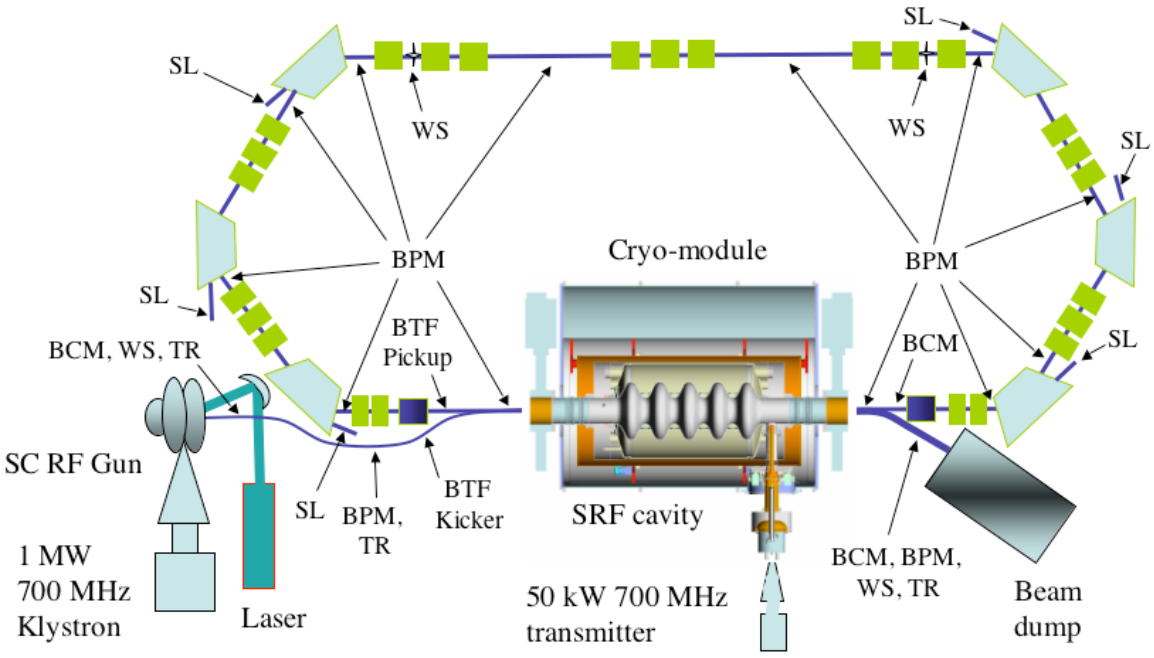

Figure 1 Ring layout showing Diagnostics

and imposes more stringent demands on RF shielding. Our intent is to provide flexibility where possible (for instance, by using programmable synthesizers to generate local oscillator frequencies) to permit avoiding the RF fundamental when operating with the 9.383/28.15MHz bunching frequency. Processing at 14.07MHz looks particularly attractive, as this will permit the same LO frequency for either e-cooling or high current mode, and the resulting 56.3MHz clock frequency for BPM I/Q demodulation is comfortable for the intended digitizer.

Figure 1 above shows a Ring layout including locations of specific Diagnostics devices. Diagnostic device types, quantities, and their preliminary accelerator physics specifications are shown in the Table 2 below. In consideration of budget limits, the present plan is to defer the wire scanners, scraper, and streak camera until some time after initial low-current operation of the ERL.

Table 2 - Diagnostics Devices and AP Specifications

Device	Qty	Range	Accuracy	Resolution	Comments
Position/Phase					
BPM (button)	14	1/2 pipe rad	500μ	1μ (av)/100μ	Dual plane
Phase	14	+/- 180 deg	+/- 2 deg	0.2 deg	BPMs w/ I/Q
HOM probes	2				Mini-CF antennas
BBU/Energy Feedback	1				Sample scope
Beam Transfer Function	1				Include BTF kicker
Loss					
BLM (PMT)	10	1-1000 rem/h	30%	0.1μa loss	10μsec shutdown
Current					
Current	12		5%	1%	BPM sum signal
Current	2		1%	0.1%	Bergoz PCTs
Differential	1		10^{-4}	10^{-5}	2 toroids w/ null
Profile					
Flags	2		0.2σ	0.1σ	Phosphor + TR
Wire Scanner - profile	4	Full aperture	0.2σ		SEM mode
Wire Scanner - halo	4			10^{-6}	BLM mode
Scraper	1		0.2σ		SEM + BLM
Synch Light	6		0.2σ	10μ	Every bend mag
Energy Spread	-		$3x10^{-4}$	10^{-4}	Dispersive locations
Longitudinal Profile	?		10psec	5psec	Diodes + zero cross

2.9.1 POSITION AND PHASE

Given the small quantity of position monitor pickup electrodes required and the transient nature of the facility, the possibility of purchasing an existing design from a commercial vendor was investigated. It appears that the 'large aperture' LHC button is suitable for our ERL application. Specifications include 10pF capacitance, 34mm button diameter, and 61mm beampipe diameter. The vacuum interface is a 2.75 Conflat flange with an N-type connector. A budgetary estimate of price and delivery (with cryogenic-driven material and testing requirements relaxed relative to those specified for the LHC) has been received from the vendor. The preliminary design of the position monitor electronics assumes the parameters of this button. There is a possibility that the buttons on either side of and immediately adjacent to the SRF cavity will be located in the large

aperture beampipe. In that case, the need to modify the button radius will be investigated. All calculations assume the 61mm beampipe diameter.

Recent experience with BPM electronics within the Collider-Accelerator Department includes the design and production of hardware and software for the Spallation Neutron Source [4,5]. From a technical and engineering point of view that is restricted to the perspective of beam diagnostics for the ERL, these electronics are a good fit and could be adapted to the ERL application with minimal effort. However, when viewed from the perspective of the support effort required from the Controls Group (including implications for a possible upgrade path for the RHIC BPM electronics), the situation is not so clear. Figure 2 below shows two possible architectures. The upper data path situates the electronics and software for a single BPM in a PC running Linux, communicating with the Control System via Internet Protocol as managed by a SNAP server. This implementation is a minimal modification of the SNS BPM electronics. The lower data path has the electronics packaged in VME. It requires new board layouts and a significant effort in the development of new software, and suffers from the disadvantage that the additional complication of a DSP is required for data decimation before delivery to the VME bus, and also from the data rate limitations of that bus. However, it does not require that the Controls Group maintain the PCs running Linux.

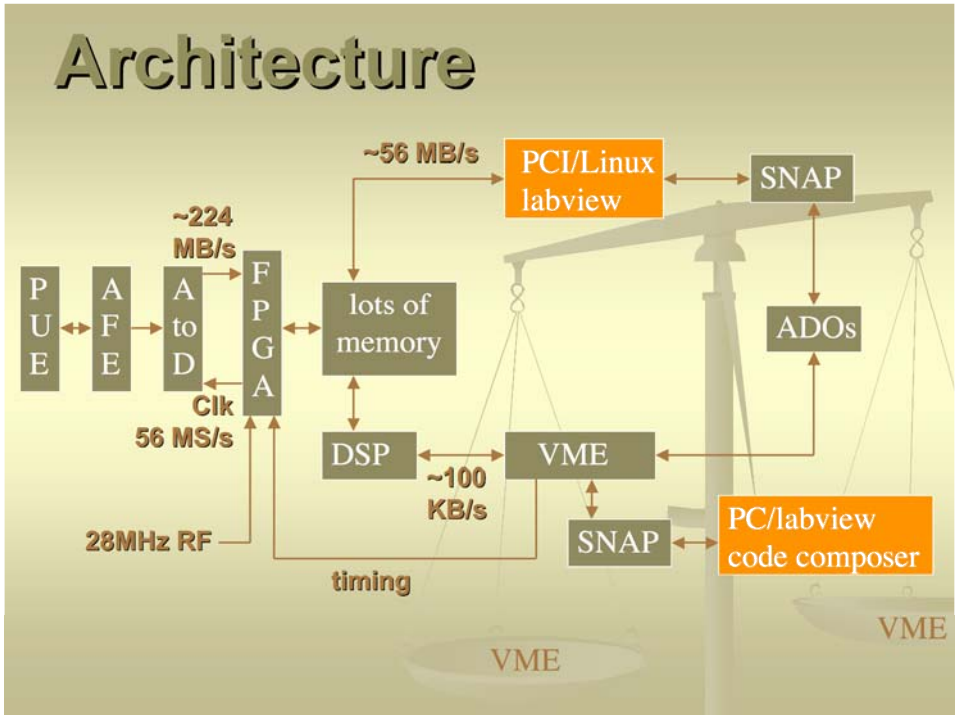

Figure 2 Two possible BPM electronics architectures. The upper data path utilizes the PCI bus, and the lower the VME bus.

IN AN EFFORT TO GAIN A LARGER PERSPECTIVE, THE WORLD COMMUNITY OF BEAM INSTRUMENTATION SPECIALISTS WAS CANVASSED, BOTH VIA A LITERATURE SEARCH OF RECENT WORKSHOP PROCEEDINGS AND THROUGH DIRECT INTERPERSONAL

COMMUNICATION. A CLEAR TREND EMERGED FROM THIS SEARCH, DEMONSTRATING A REMARKABLY BROAD WORLD-WIDE CONVERGENCE IN THE APPROACH TO BPM ELECTRONICS. THIS CONVERGENCE IS DRIVEN BY THE RECENT AVAILABILITY OF FAST (~100MS/S) HIGH RESOLUTION (14 BITS) DIGITIZERS, COUPLED WITH THE EVER-INCREASING POWER OF DIGITAL PROCESSING. THE TYPICAL ARCHITECTURE COMPRISES HIGH-FREQUENCY (HUNDREDS OF MHZ) BANDPASS FILTERING, BEAM PHASE SYNCHRONOUS MIXING TO IF (~10MHZ), FURTHER FILTERING, A LINEAR VARIABLE GAIN CHAIN (WITH THE OPTION OF HIGH-RESOLUTION VARIABLE DELAY ALSO OFTEN PRESENT), BEAM PHASE SYNCHRONOUS DIGITIZATION, I/Q DEMODULATION, AND FURTHER DIGITAL SIGNAL PROCESSING [6-13]. THERE IS ALSO CLEAR MOVEMENT AWAY FROM THE LIMITATIONS OF VME AND INTO PCS FUNCTIONING AS NETWORK-ATTACHED DEVICES. THIS ALSO DESCRIBES VERY WELL THE ARCHITECTURE OF THE SNS BPM ELECTRONICS.

Table 3 - Calculated BPM Electronics Performance

Parameter [units]	value
Button voltage [V]	290
Cable loss [dB]	2.6
RF filter voltage [V]	1.8
IF filter voltage [V]	0.5
Thermal noise [μV]	3
Losses [dB]	7
Amp noise figure [dB]	4
Contingency [dB]	6
Resolution [μm]	<1
Phase resolution [deg]	<0.1

AFTER EXTENSIVE DISCUSSIONS, THE GUIDANCE FROM DEPARTMENT MANAGEMENT WAS THAT THE CHOICE OF ARCHITECTURE SHOULD BE DE-COUPLED FROM ANY FUTURE UPGRADE PATH. GIVEN THAT, PLUS THE FACT THAT QUANTITIES ARE SMALL AND THE CONTROLS GROUP ALREADY SUPPORTS A SIGNIFICANT NUMBER OF PCS RUNNING LINUX, OUR PRELIMINARY CHOICE OF ARCHITECTURE CONTINUES TO BE ESSENTIALLY THAT OF THE SNS BPM ELECTRONICS. THE INTERFACE TO TIMING IS ENCODER LOGIC EMBEDDED IN A GATE ARRAY IN EACH DATA ACQUISITION MODULE. THE TIMING DECODER GATE ARRAY BOARD ALSO PROVIDES THE INTERFACE TO THE PCI BUS, SERVES AS A MOTHERBOARD FOR THE ANALOG ELECTRONICS AND DIGITIZERS, AND PERMITS THE POSSIBILITY OF FAST PRE-PROCESSING IN A GATE ARRAY BEFORE DELIVERY OF DATA TO LABVIEW. THE FOLLOWING DESIGN CALCULATIONS ARE BASED ON SUCH ELECTRONICS. IN THE EVENT THAT THE DECISION IS ULTIMATELY MADE TO REPACKAGE THESE ELECTRONICS IN VME, THE DESIGN CALCULATIONS SHOULD REMAIN VALID.

Table 4 - Measurement Resolution

measurement	analog res (one bunch)	digital res (one bunch)	digital res (w/ avg)
position	~1μ	5μ	0.3μ (256 smpl)
phase	~.01 deg	.02 deg	.001 deg (256 smpl)
current	10^{-5} single 10^{-8} 2^{16} smpl	5 x 10^{-4}	10^{-6} 2^{16} smpl

DESIGN

CALCULATIONS[14] FOR A SINGLE BUNCH WERE ACCOMPLISHED USING A MATHCAD PROGRAM ORIGINALLY DEVELOPED AT SLAC[15], AND MODIFIED FOR ERL PARAMETERS AND TO SIMPLIFY FILTER CALCULATIONS. BEAM PARAMETERS WERE TAKEN FROM THE HIGH CHARGE COLUMN OF TABLE 1. TABLE 3 SHOWS THE RESULTS OF THESE CALCULATIONS. IT IS ASSUMED THAT WE ARE USING 20M LONG LRM400 COAXIAL CABLES TO BRING THE SIGNALS OUT TO THE ELECTRONICS. AFTER THE CABLE THE SIGNAL IS FILTERED WITH A 3-POLE BESSEL BANDPASS AT A REVOLUTION LINE CLOSELY ADJACENT TO THE 703.75MHZ RF FREQUENCY, MIXED TO 14.1MHZ, AGAIN BESSEL FILTERED, SYNCHRONOUSLY DIGITIZED WITH A 56.4MHZ CLOCK, AND I/Q DEMODULATED. WITH GENEROUS ALLOWANCES FOR LOSSES IN THE PROCESSING CHAIN, AMPLIFIER NOISE FIGURE, AND CONTINGENCY, THE ANALOG SINGLE BUNCH POSITION RESOLUTION OF ~1μ EASILY MEETS THE 100μ AP SPECIFICATION. IN LOW EMITTANCE MODE (~4X10^9 CHARGES/BUNCH) ANALOG RESOLUTION WILL BE A FEW TENS OF MICRONS. WITH THE LARGE BUNCH CHARGE, SHORT BUNCH LENGTH, AND AMPLE BUTTON SIZE FOUND IN ERL, SINGLE BUNCH RESOLUTION WILL BE LIMITED BY DIGITIZER RESOLUTION. IF WE ASSUME THAT WE HAVE 11 EFFECTIVE BITS FROM OUR 14 BIT DIGITIZER, IN TABLE 4 WE SEE ACTUAL MEASUREMENT RESOLUTION FOR SINGLE BUNCHES AND WITH AVERAGING. WITH I/Q DEMODULATION, 256 SAMPLES CORRESPONDS TO ~10USEC. IN THE INTEREST OF BEAM STABILITY, SOME OF THE ANALOG POSITION RESOLUTION MAY BE SACRIFICED FOR THE SAKE OF ADDING ADDITIONAL ATTENUATION IN THE SIGNAL PATH, TO DIMINISH EXCITATION OF THE BEAM BY REFLECTIONS BACK TO THE BUTTONS FROM THE HIGH FREQUENCY BESSEL FILTER. CABLE LENGTHS WILL ALSO BE ADJUSTED TO LAND REFLECTIONS IN EMPTY BUCKETS, WHEN POSSIBLE. AN ALTERNATIVE POSSIBILITY IS TO REPLACE THIS FILTER WITH A DIPLEXER. CALIBRATION AND VERIFICATION OF SIGNAL PATH INTEGRITY WILL BE ACCOMPLISHED WITH A BUILT-IN TIME DELAY REFLECTOMETRY CAPABILITY.

IN ADDITION TO USUAL REQUIREMENTS FOR POSITION MONITORING, AN ERL-SPECIFIC REQUIREMENT IS TO HAVE THE ACCELERATED AND DECELERATED BEAMS ON A COMMON CENTER AS WELL AS TO HAVE THAT COMMON CENTER CENTERED IN THE SRF CAVITY, TO MINIMIZE EXCITATION OF HIGHER-ORDER TRANSVERSE MODES RESPONSIBLE FOR THE BEAM BREAKUP (BBU) INSTABILITY. THIS MEASUREMENT WILL UTILIZE THE POSITION MONITORS IMMEDIATELY BEFORE AND AFTER THE SRF CAVITY. IN LOW DUTY CYCLE OPERATION THE TIME SEPARATION (ONE TURN OR ~100 NS) OF THE LOW AND HIGH ENERGY PASS THROUGH THE PICKUP WOULD IMPOSE A NOT-UNREASONABLE LOWER LIMIT ON POSITION MONITOR ELECTRONICS BANDWIDTH, SO THAT INDEPENDENT POSITION

MEASUREMENT AND CORRECTION OF BOTH BEAMS IS FEASIBLE. EARLY IN COMMISSIONING CENTERING OF THE ALIGNED BEAMS ON THE SRF CAVITY MIGHT THEN BE ACCOMPLISHED BY RELIANCE ON SURVEY DATA. HOWEVER, DURING NORMAL HIGH-CURRENT OPERATION TIME SEPARATION IS LESS THAN 1NS AND THIS MEASUREMENT IS THEREFORE NOT POSSIBLE WHEN MOST CRUCIAL. ALIGNMENT OF THE TWO BEAMS RELATIVE TO EACH OTHER DURING NORMAL OPERATIONS MIGHT BE ACCOMPLISHED VIA A METHOD [2] (NOT YET DEMONSTRATED IN PRACTICE) THAT WOULD CENTER THE TWO BEAMS RELATIVE TO EACH OTHER BY LOOKING AT THE BPM OUTPUT AT THE RF FUNDAMENTAL AND SECOND HARMONIC AND TUNING TO MINIMIZE THE FUNDAMENTAL AND MAXIMIZE THE SECOND HARMONIC. TUNING OF TRANSVERSE POSITION IN THE SRF CAVITY MAY THEN BE FACILITATED BY MONITORING OF HIGHER-ORDER-MODE POWER[16]. FOR THIS PURPOSE, SHORT MINI-CONFLAT MOUNTED ELECTRIC FIELD PROBES WILL BE INSTALLED AT FOUR LOCATIONS AROUND THE CIRCUMFERENCE OF LARGE CONFLAT SPACERS INSERTED AT BOTH ENDS OF THE SRF CAVITY, BETWEEN THE CAVITY AND THE HOM ABSORBERS.

The requirement for phase measurement is driven by the need to have the bunches properly phased through the SRF cavity in both the acceleration and deceleration passes, to minimize momentum spread in the accelerated beam (crucial for electron cooling) and to maximize energy recovery from the decelerated beam. Our intent is to I/Q demodulate the outputs of all BPMs, which will provide a measurement with better than 0.1 degrees of phase resolution. Absolute phasing for the acceleration pass can be accomplished by utilizing a dipole for momentum analysis. If we ignore for the moment the effect of the beam-splitting dipole immediately downstream of the SRF cavity (as well as phase offsets due to momentum-dependent path length variations) and consider the momentum dependence of beam position immediately downstream of the first 60 degree bending dipole, for the values assumed below the position offset due to momentum will be

$$\delta x = (4\rho/3)(\delta p/p) \sim 1\mu$$

where

ρ = bending radius (assume 1m)

$\delta p/p$ = momentum difference (assume 10^{-6})

Or in other words, with these conditions our 1μ single bunch position resolution can resolve the position effect of a momentum difference of 10^{-6} immediately after the first dipole. This corresponds to ~0.1 degrees of SRF cavity phase at the peak of the voltage profile. By sweeping the cavity phase and noting the phase that corresponds to minimum beam deflection, calibration of the phase monitors can then be accomplished within the required 2 degrees of absolute phase. A possible concern here is whether the dipole field will be sufficiently stable to permit this measurement, and if not whether multiple phase sweeps can be accomplished uncorrelated with dipole variations to extract the needed data.

Phasing for the deceleration pass will be accomplished by adjusting path length with a small chicane, and can be monitored in a variety of ways. In a method similar to that used for the accelerated beam, beam position can be measured in the dump beamline. A second possibility is to directly monitor the SRF cavity drive power, a minimum in the required power indicating good phasing.

POSSIBLE ONSET OF THE BBU INSTABILITY WILL BE MONITORED WITH A STRIPLINE PICKUP. DATA ACQUISITION WILL BE ACCOMPLISHED IN PARALLEL WITH A FAST (20GHZ BW) SAMPLING SCOPE, AS WELL AS WITH A SPECTRUM ANALYZER. ATTENTION WILL BE GIVEN TO CABLE SELECTION AND LENGTH TO MINIMIZE THE EFFECT OF DISPERSION. WITH THE ADDITION OF A STRIPLINE KICKER AND POWER AMPLIFIER, THIS PICKUP WILL ALSO BE USED FOR BEAM TRANSFER FUNCTION MEASUREMENTS, AND IN PARTICULAR TO EXPLORE PARAMETERS RELATED TO THE BBU INSTABILITY.

THE PICKUP AND DATA ACQUISITION SYSTEM FOR ENERGY FEEDBACK REMAIN UNDER DISCUSSION. ONE POSSIBILITY IS TO USE THE BBU STRIPLINE PICKUP, EITHER WITH THE FAST SAMPLING SCOPE OR ANOTHER DATA ACQUISITION SYSTEM. A SECOND POSSIBILITY IS TO USE THE STANDARD BPM ELECTRONICS (AS OUTLINED ABOVE IN THE PARAGRAPH ON PHASE CALIBRATION) WITH ADDITIONAL GATE ARRAY PROGRAMMING, AND WITH PROPER ATTENTION TO REAL-TIME COMMUNICATION WITH THE RF PHASE INPUT TO INSURE ADEQUATE LOOP BANDWIDTH. A THIRD POSSIBILITY IS THAT A COMPLETELY INDEPENDENT DATA ACQUISITION SYSTEM WILL BE DEVELOPED.

2.9.2 LOSS MONITORS

The beam loss monitor system is important for beam tuning, minimizing activation, equipment protection, and as a general diagnostic. Three possible choices for loss monitor detectors are photomultipliers[17], diodes[18], and long (coaxial cable) ionization chambers[19]. The initial intent was to provide PMTs for fast and high-sensitivity measurements (including detection for the Halo Monitors), and cable ion chambers to ensure a calibrated measurement and complete coverage. Budgetary limitations are pushing the design in the direction of a single loss monitor system, and our preliminary choice is a PMT-based system. There remain concerns about the importance of complete coverage for adequate machine protection, and this decision will be examined in greater detail. Space will be reserved in the layout wherever possible for installation of 7/8” heliax cable immediately adjacent to the beampipe.

The loss budget goal for the ERL is 1uA, primarily derived to keep residual levels below 100mR/hr and allow hands-on maintenance. As in many high power machines, the maximum intensity achievable is limited by beam losses. Prompt ionizing radiation sources include, electrons, gamma & x-rays, and some neutrons. Simulations of 1uA local loss result in levels on the order of 1-10kRads/hr at 1 meter. The electron beam has

enough power to damage the vacuum chamber if it is not adequately protected. A distributed loss monitor system based on 10 fast photomultiplier tubes is proposed, it will be able to rapidly shut the beam down when beam loss exceeds a programmable threshold. Each loss detector will have a built in self-test, and programmable bias voltage control for gain adjustment. Experience on nuclear physics machines indicates that losses as low as 100 nA are detectable by these methods. A scintillator will be included at locations such as wire scanners and halo scrapers where higher sensitivity is required. The response time of the signal processing electronics will be of the order of 1us. Shutdown within 10us of beam loss detection is anticipated. The loss signal will be processed using integrating electronics for equipment protection, and a linear and/or logarithmic technique for diagnostics & beam tuning. Similar systems have been used extensively at existing machines such as CEBAF at JLAB.

2.9.3 CURRENT MONITORS:

By virtue of the BPM processing architecture, current measurement from the sum signals of all BPMs will be available essentially for 'free'. The button measurement will be calibrated by Bergoz Parametric Current Transformers (PCTs) [20] to meet the accuracy requirement, and will be compensated for the non-linear response of the buttons to beam offsets. The calculated current resolution of ~10nA easily meets the AP specification. Absolute accuracy of the current measurement from the button pickups is estimated to be a few percent before calibration by the PCT.

The differential current measurement (the difference in currents between the accelerated and decelerated beams) will assume increasing importance as commissioning proceeds and beam current increases, both as a measure of the efficiency of current recovery and as a possible input to the machine protect system. In principle this could be accomplished by measuring the power requirement of the SRF cavity, but proper calibration of such a measurement is not straightforward, and in addition it presumes that the low and high energy beams are accurately anti-phased. A simple and elegant method is to utilize the two toroids in the injection and dump lines, and to link those toroids with a figure eight winding. The output of one toroid is used to drive a nulling current through the figure eight, and the output of the second toroid is then the differential current measurement. This overcomes the dynamic range problem of measuring a small current difference in the presence of a large current signal.

This method of nulling requires that the sensor have DC response. If one looks at RF (say for instance at a possible first revolution line at 9.4MHz) the method is confounded by phase shift of the nulling signal between the toroids, as well as by coupling of the beam signal between the toroids by the nulling winding. Available DC sensors include squids, the DC Current Transformer (or DCCT, which Bergoz calls the PCT), and Hall effect devices. The effort to implement a squid in this application cannot presently be justified, despite the tremendous potential gain in accuracy and resolution. The PCT gains DC response by modulating the core into saturation with a square wave, and looking for second harmonic output due to DC offset. Flux (Barkhausen) noise due to the square wave modulation causes the S/N to be ~80dB above thermal. Despite this, with filtering to limit bandwidth to ~50Hz (20msec response time based on machine protection

requirement) the extended range version of the PCT should have a resolution of better than 1μA. As mentioned above, the differential measurement becomes crucial with high beam current. For 100mA beam current the AP specification of 99.9995% current recovery requires measurement resolution of better than 0.5μA. This suggests that the differential current specification should be investigated in greater detail, perhaps to remove the machine protection requirement from the highest resolution range to permit more bandwidth narrowing.

2.9.4 PROFILE MONITORS:

Profile measurements are required to gain information about lattice functions as well as longitudinal and transverse emittance. Profile measurements are crucial to the purpose of the ERL, and in some cases require precise knowledge of lattice functions. Every effort should be made to provide the best possible diagnostics for profile measurements, and we should take advantage of all possibilities to make higher management aware of this important priority and urge that it be adequately funded.

2.9.4.1 Flags

Phosphor screens and optical transition radiation viewers will be used to measure transverse beam profiles and position in the transport from the rf gun, and transport to the dump. This semi-destructive measurement will be made with reduced currents or when running in pulsed mode to avoid damaging the foil/phosphor. Resolution of 50-100 microns is expected. OTR emitted light will be analyzed at beam currents above 10mA. Fluorescence from the phosphor screens will be used at the lower currents where low OTR light levels are expected. CCD cameras with appropriate lenses and filters, and external trigger capability will feed a frame grabber digitizer with variable gain to capture the images. All video signals will be routed through a multiplexer to a common frame grabber. Image analysis software will be written to process the data and generate beam parameters.

2.9.4.2 Wire Scanners & Scrapers

Profile measurements at injection, extraction, and two locations in the ERL ring will be made using wire scanners. Each location will have a full aperture scanner that provides a secondary emission signal from a wire. A limited range halo scanner that relies on resulting loss measurements will be used to resolve enhanced details of the beam in the halo. Horizontal and vertical scrapers will be installed to localized beam losses. The scraper jaw will be electrically isolated to allow a secondary emission signal to be collected. Nearby dedicated beam loss monitors previously described will also be used to measure scattered electrons. Motion control for all will be based on stepper motors, and confirmation measured by position transducer.

2.9.4.3 Synchrotron Light Monitors

The critical wavelength for synchrotron emission from a typical ERL 60^{o} dipole with 20cm bend radius, and 15MeV beam is about 500nm, and 284nm at 20MeV. CCD

cameras located near each of the 6 dipoles will be mounted off axis to prevent radiation damage. The image will be viewed via a mirror mounted near the viewing port of the vacuum chamber of each dipole. Attenuators will be used to prevent camera saturation during high power running. A video multiplexer feeding a frame grabber digitizer with variable gain will capture the images. Image analysis software will be written to process the data and generate beam parameters. We anticipate resolution on the order of 10 microns.

Longitudinal Profile Measurement

The above discussion of profile monitors dealt with transverse profile measurement. In addition it is necessary to measure longitudinal profile of the ~20ps bunches, as well as beam energy spread. During initial commissioning direct measurement of longitudinal profile will be accomplished with a borrowed streak camera, and with either a button pickup or the BTF stripline pickup monitored by a fast (20GHz BW) sampling scope and a spectrum analyzer[21]. In addition, we are investigating the possibility of monitoring longitudinal profile with fast (a few ps) photodiodes, at low energy looking at transition (low current) or diffraction (high current) radiation from the flags, and at high energy looking at synchrotron light. At low energy resolution will be limited to a few ps by $1/\gamma$ broadening of the radiation cone (in quadrature with the photodiode rise time).

Indirect measurement of energy spread can be accomplished by measuring transverse profiles in dispersive regions and comparing with non-dispersive regions, and information regarding longitudinal profile can be gained by inducing additional momentum spread by scanning the RF phase while measuring transverse profiles[2,22]. In particular, applying the zero-crossing method to the main SRF cavity and measuring profiles in the dump line will permit measurement of bunch length from the injector (though the comments below on energy spread measurement must be taken into consideration). In addition, with normal SRF cavity phasing to the injector, adjusting the chicane for +/- 90 degrees phase shift of the recirculated bunch (rather than the usual 180 degrees) might permit bunch length measurement of the high energy beam by the same method, with transverse profile taken from the synchrotron light monitor. The zero-crossing method is recognized as the fiducial to which all other longitudinal bunch measurements are calibrated, and resolutions of ~10fs have been achieved [2].

This method requires measurement of transverse profiles in a dispersive region. A possible lattice for the ERL is shown in Figure 3. The figure shows lattice functions for half the ring, from downstream of the SRF cavity to the midpoint of the opposite straight section. The ring lattice is symmetric about the midplane, so that one obtains lattice functions for the second half by following the figure backwards from the end. As the figure shows, dispersion will be ~0.2m downstream of the first and second dipoles, and again downstream of the fifth and sixth dipoles.

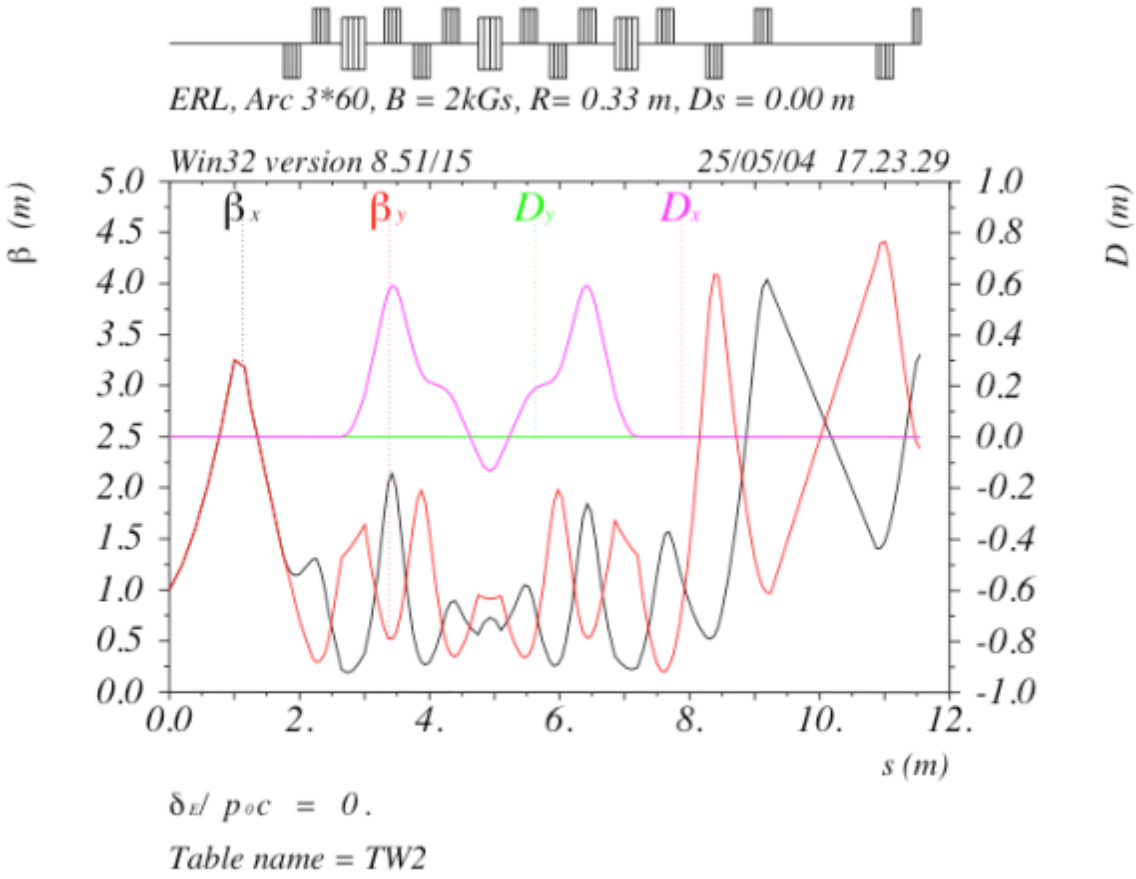

Figure 3 A possible ERL lattice

To specify the profile resolution needed to meet the AP requirement of 10^{-4} resolution in the energy spread measurement, we consider the two sources of transverse beam size in a dispersive location and calculate beam size using beam parameters from Table 1 and lattice parameters from Figure 3:

$\sigma_{beam} = (\sigma_\beta^2 + \sigma_\delta^2)^{1/2}$ = rms beam size ~920μ

where

$\sigma_\beta = (\varepsilon\beta/\gamma)^{1/2}$ = rms size due to emittance and beta function ~870μ

ε = emittance ~30mm-mrad

β = beta function at the pickup ~1.0m

γ ~40

$\sigma_\delta = D\,\delta p/p$ = rms size due to momentum spread and dispersion ~ 300μ

D = dispersion at the pickup ~ 0.3m

$\delta p/p$ = momentum spread ~ 10^{-3}

With these parameters, transverse emittance dominates the beam size, the contribution due to momentum spread being only 50μ. Similarly, the 10μ measurement adds in quadrature, so that the contribution of measurement resolution to the measured beam size can be ignored. With the lattice parameters shown in Figure 3, we can measure energy spread with a resolution of ~10^{-1}. To meet the AP specification of ~10^{-4} resolution one

could consider a special lattice[24] with a dispersion of ~30m, as well as signal averaging to improve the measurement resolution. Other possibilities (for instance, spectral analysis of Compton back-scattered microwave radiation) are also under active investigation.

REFERENCES:

[2.9.1] P.R. Cameron et al., *Beam Diagnostics for the BNL Energy Recovery Linac Test Facility*, BIW 2004, Oak Ridge.

[2.9.2] G.A. Krafft and J-C Denard, *Diagnostics for Recirculating and Energy Recovered Linacs*, BIW 2002, Brookhaven.

[2.9.3] P. Piot et al., *Performance of the Electron Beam Diagnostics at Jefferson Lab's High Power Free Electron Laser,* PAC 1999, New York.

[2.9.4] W. Dawson et al., *BPM System for the SNS Ring and Transfer Lines*, BIW 2002, Brookhaven.

[2.9.5] K. Vetter et al., *RF Beam Position Monitor for the SNS Ring*, BIW 2004, Oak Ridge.

[2.9.6] Hamburg Workshop on Digital Receivers in Beam Instrumentation, Jun 2004. http://desyntwww.desy.de/mdi/Conferencesold/Aumuehle/CARE-N3-Aumuehle-Agenda.html

[2.9.7] R. Webber et al., *FermiLab Recycler Ring BPM Upgrade Based on Digital Receiver Technology*, BIW 2004, Oak Ridge.

[2.9.8] P. Duperrex et al., *Latest Diagnostic Electronics Development for the PROSCAN Proton Accelerator*, BIW 2004, Oak Ridge.

[2.9.9] J. Denard et al., *Overview of the Diagnostics systems of SOLIEL and DIAMOND*, DIPAC 2003, Mainz.

[2.9.10] G. Naylor et al., *Beam Position and Phase Measurement using a FPGA for Processing Pickup Signals*, DIPAC 2003, Mainz.

[2.9.11] R. Ursic, *Reconfigurable Instrumentation Technologies, Architectures, and Trends*, BIW 2002, Brookhaven. See also the I-tech web site at http://www.i-tech.si/

[2.9.12] B. Chase and K. Meisner, *Digital Receiver for BPM and Phase Detection Processing at FNAL*, BIW 2002, Brookhaven.

[2.9.13] Extensive documentation including (but not limited to) digital receiver development at FNAL is available at http://beamdocs.fnal.gov/cgi-bin/public/DocDB/DocumentDatabase
This site is an excellent resource for the beam instrumentation specialist, and a fine example of well-documented work.

[2.9.14] M. Kesselman et al., *Design Calculations for the ERL BPM system*, available at RHIC e-cooling web site
http://www.agsrhichome.bnl.gov/eCool/

[2.9.15] S. Smith, *Beam Position Monitor Engineering*, BIW 1996, Argonne.

[2.9.16] M. Wendt et al., *Beam Based HOM Analysis of Accelerating Structures at the TESLA Test Facility LINAC*, DIPAC 2003, Mainz.

[2.9.17] K. Mahoney et al., *Overview of the Jefferson Lab Machine Protection Beam Loss Monitor*, HPS Winter Meeting, 2000, Virginia Beach, VA. http://www.jlab.org/accel/ssg/papers_Pres/sspres/beamloss/sld001.htm

[2.9.18] G. DiPirro et al., *DAFNE Beam Loss Monitor system*, DIPAC 2003, Mainz.

[2.9.19] P. Michel et al., *Beam Loss Detection at Radiation Source ELBE*, DIPAC 2003, Mainz.

[2.9.20] see the Bergoz web site
http://www.bergoz.com/pct/d-pct.htm

[2.9.21] A. Freyberger et al., *Energy Spread Monitoring for the JLAB Experimental Program: Synchrotron Light Interferometers, OTR Monitors, and Wire Scanners*, BIW 2004, Oak Ridge.

[2.9.22] L. Vos, *Electromagnetic Bunch Length Measurement in LEP*, EPAC 1998, Stockholm.

[2.9.23] B. Yang, *Optical System Design for High-Energy Particle Beam Diagnostics*, BIW 2002, Brookhaven.

[2.9.24] I. Barzov et al., *Phase I Energy Recovery Linac at Cornell University,* EPAC 2002, Paris.

2.10 Control System

The ERL control system shall be an extension of the RHIC controls system [2.10.1]. To the maximum degree possible, solutions chosen for the ERL system shall be appropriate for the RHIC e-Cooling facility. The basic elements of the system will comprise a networked family of front-end interfaces connected via Ethernet to ERL control console workstations and to central C-AD servers.

2.10.1 NETWORK & LINKS

Existing fiber optic infrastructure in building 912 will provide access to the C-AD controls subnet, with switched 100Mbit Ethernet on copper to individual front-end nodes and console computers. The standard controls interface infrastructure will comprise VME chassis, CPU, utility link interface, battery-backed SRAM, event decoder/delay modules, remote power reset, and terminal server (for serial port access to CPUs). Some engineering may be needed for module redesign driven by parts obsolescence. Software support for an updated CPU will also be needed.

The C-AD Real-Time Data Link (RTDL) will be delivered via fiber to provide the facility-standard, time-of-day reference for all front-end chassis. This time base will be common to all logged data. Pulse timing will be provided by a local version of the standard Event Link system with provision for **TBD [nx16]** encoded events. It will provide a standard real-time clock and asynchronous, software- or hardware-initiated encoded event signals for triggering equipment.

A fast beam inhibit system will be required to protect the equipment from uncontrolled operation of the high power beam. It will be patterned after the present RHIC/AGS systems. Equipment will indicate, *"operation permitted"*, by sending a fail-safe current signal to one of 16 input channels. The system will be modular so that additional inputs may be added economically. Redundancy will be provided as needed to drive *critical devices* used to shut off the system. New software will be required to manage the specifics of the ERL system.

2.10.2 CONTROL CONSOLE

A work console composed of standard 19-inch racks with writing shelf attachments will be provided in the facility control room. Each of 3 "seats" will be equipped with a Linux workstation and 4 flat-panel monitors, configured as a single continuous display resource. Rack space will be provided at the console for some other rack-mounted equipment, telephone, and the access control system panel display and key-tree. A color printer will also be provided. General purpose and project-specific application software for operating and monitoring the equipment and beam characteristics will be provided. It is expected that a majority of the required services will be met by existing software tools for simple device control, sequencing, data logging, comfort displays, alarms, and e-log. In addition, the RHIC *post mortem* system, that comprises automatic data recording by

front-ends after an *abort*, and display and summary tools, will be adapted for ERL fast beam inhibit response.

2.10.3 INJECTOR AND RF SYSTEM INTERFACES

The custom-configured, commercial laser system will be specified to be compatible with standard RHIC VME interfaces for state control and monitoring. Motion control will be provided for 2 axes of mirror alignment. VME digitization will be provided for photodiode signals, and CCD camera images will be captured via a Firewire-to-Linux configuration in use at the Booster.

A custom module will provide timed signals to control the intensity of the laser beam by means of an electro-optical switch system. This module will support both a single-shot mode and a normal mode beginning with a graduated sequence of progressively higher intensity commands to provide proper initiation of energy recovery in the ERL. This module will require a 9.4 MHz clock signal from the RF system. Front-end software will need to be developed for this module.

The RF system controls interface shall be at the Ethernet connection. Controls chassis and custom DSP-based VME control modules are part of the RF system (WBS 2.2). Control of the high-power RF system equipment will be implemented using networked PLCs that are likewise included in the RF system. The Controls contribution to this effort will comprise standard VME modules for timing and link interfaces, and database support.

2.10.4 MAGNET ELECTRICAL INTERFACES

All magnet power supplies with the exception of the dump rastering system power supplies will be controlled via the PSC-PSI interface system developed to BNL specifications for the SNS project and already in use at NSRL (BNL). This system is described in more detail in section 2.7. Software effort will be needed for database setup and configuration of standard control and monitoring tools.

2.10.5 BEAM INSTRUMENTATION INTERFACES

Beam instrumentation interfaces will be patterned after existing AGS or RHIC systems with the system interface at the VME front panel. Engineering will be needed for any new module updates, along with database, driver and interface software development.

The BPM system interface will be located at the chassis backplane, and interface modules will be adapted from PCI-based SNS systems to BNL-standard VME as part of the beam instrumentation system (WBS 2.9). Front-end software will need to be developed for this new module.

2.10.6 BEAM DUMP AND OTHER SYSTEM INTERFACES

The power system for the beam rastering magnets will need non-standard controls interfaces. A PLC interface will be used for state control and monitoring. A commercial VME waveform generator will provide synchronized, programmed reference signals for current control. A networked oscilloscope will provide current waveform readout. In addition, a VME DSP module will be configured to measure and compare the time varying coil input and output currents and provide output interlock signals to the fast beam inhibit system.

Networked PLC interfaces are also included in the vacuum system (WBS 2.5). It is assumed that a PLC-based monitoring system will also be provided as part of the cryogenic system (WBS 2.4). Control system server resources will apply standard time stamps to the data and export it using standard protocols. Engineering is required for database support and for software for data collection and alarms.

Existing C-AD systems will be extended for UPS, power and building temperature monitoring. Software engineering effort will be required for database and alarm configuration.

REFERENCES:

[2.10.1] D.S. Barton, et al., *RHIC control system*, Nuclear Instruments and Methods in Physics Research A 499 (2003) 356-371.

2.11 Solenoid:

2.11.1 OVERVIEW OF THE COOLING SOLENOID:

The solenoid for the cooling section in RHIC is required to operate at a field of 2-5 Tesla. Due to the high field requirement, the solenoid will be superconducting. The most challenging requirement of the solenoid is in terms of the transverse fields on the magnet axis, which must be well below 1×10^{-5} of the axial field. It is anticipated that such a precision will not be achieved by mechanical tolerances alone. Consequently, the magnet incorporates an array of dipole correction coils to correct the deviations of the local solenoid field from a straight line. These dipole coils provide a maximum transverse field of only about 10^{-3} Tesla, and are normal conducting. To minimize the resistive heating, the correctors are placed inside a double walled heat shield at ~80 K. Finally, a magnetic shield is placed surrounding the solenoid in order to minimize field leaking out of the solenoid to the outside, and more importantly, to shield the solenoid field from external stray fields which may be well above the tolerable limit. A schematic of the cross-section is shown in Fig. 2.11.1. A conceptual 3-D view is shown in Fig. 2.11.2.

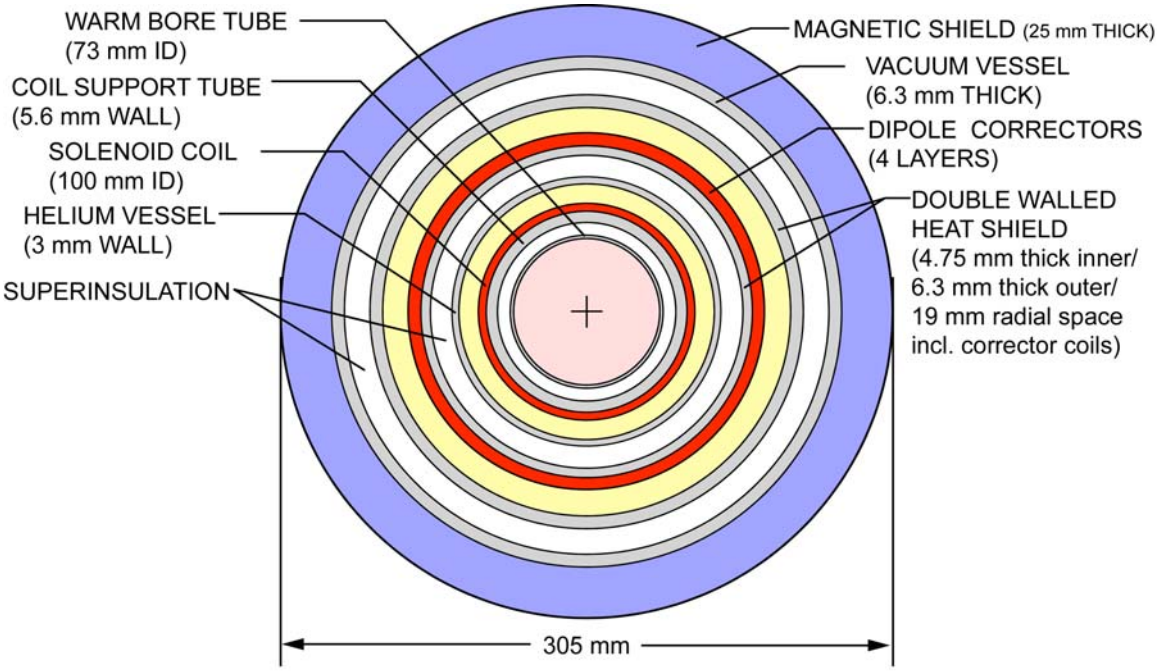

Fig. 2.11.1 Cross section of the cooling section solenoid.

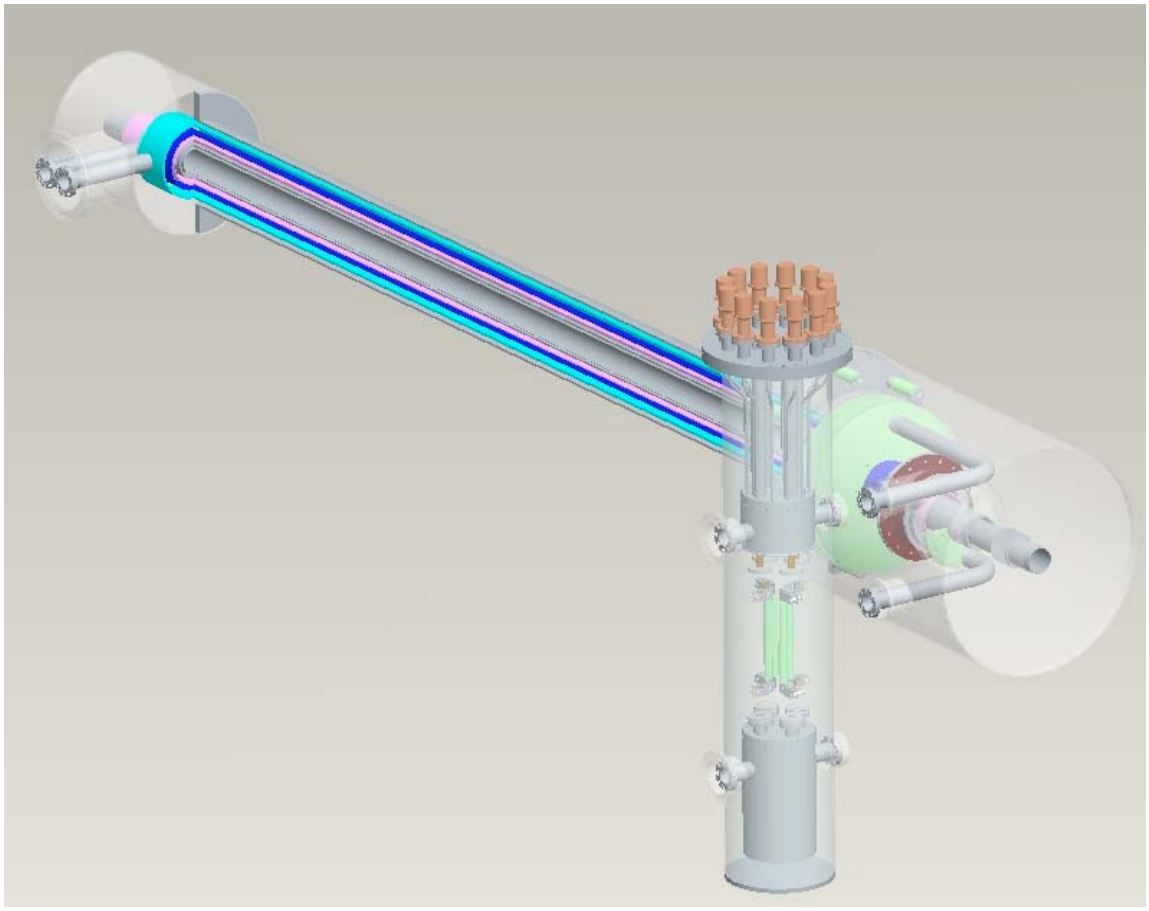

Fig. 2.11.2 A conceptual 3-D view of the electron cooler solenoid.

2.11.2 THE SOLENOID COIL:

A R&D prototype solenoid is currently being developed. This solenoid will be approximately 3 meters in length, with a coil inner diameter of 100 mm. In order to take advantage of inexpensive, off-the-shelf commercial superconductor, the prototype solenoid is designed using a 2.4 mm × 1.6 mm rectangular wire with a copper to superconductor ratio of approximately 7:1. The small width of the wire allows for a small winding pitch, which keeps the transverse fields caused by the tilt of the turns well within the required tolerance. The large copper to superconductor ratio of this conductor is also helpful in protecting the magnet during a quench. The critical current (I_c) of this conductor is roughly 2 kA at 2 Tesla and 1.5 kA at 3 Tesla field, dropping further to 1.1 kA at 4 Tesla.

In order to bring out both the power leads on the same end of the magnet, one must use an even number of layers in winding the coil. With only two layers of the chosen conductor, the ultimate quench field (short sample limit) is 2 Tesla. Such a solenoid could be operated reliably at fields below 1.5 Tesla or so. Adding another two layers increases the short sample limit to 3 Tesla, with safe operation possible in the 2 to 2.5 Tesla range. Further increase in the number of layers produces diminishing returns,

while significantly increasing the inductance of the magnet. For example, doubling the number of layers from 4 to 8 increases the short sample limit from 3 Tesla to only 4.3 Tesla, but increases the inductance four times. For these reasons, the prototype solenoid coil will be limited to 4 layers, with a design operating field of 2 Tesla at 1 kA, with ample quench margin. The transverse fields on-axis are calculated to be below 1×10^{-5} of the axial field, except in about 0.5 meter region near the solenoid ends. Fig. 2.11.3 shows the calculated axial and transverse field profiles on the axis of a 2-meter long solenoid. In practice, the field errors will be dominated by mechanical winding errors, as well as straightness of the coil support tube. The transverse fields due to a finite winding pitch are expected to be small compared to such errors.

For off-axis points, a radial field is present wherever there is a variation in the axial field strength. For perfectly built long solenoids, the radial field is significant only near the ends. Fig. 2.11.4 shows the axial and radial fields at radii of 5 mm and 2 mm in a 2-meter long solenoid. In reality, there may be significant radial fields at off-axis points, even well away from the ends, due to variations in the turn density along the length of the solenoid. For this reason, uniformity of winding is of utmost importance for this solenoid.

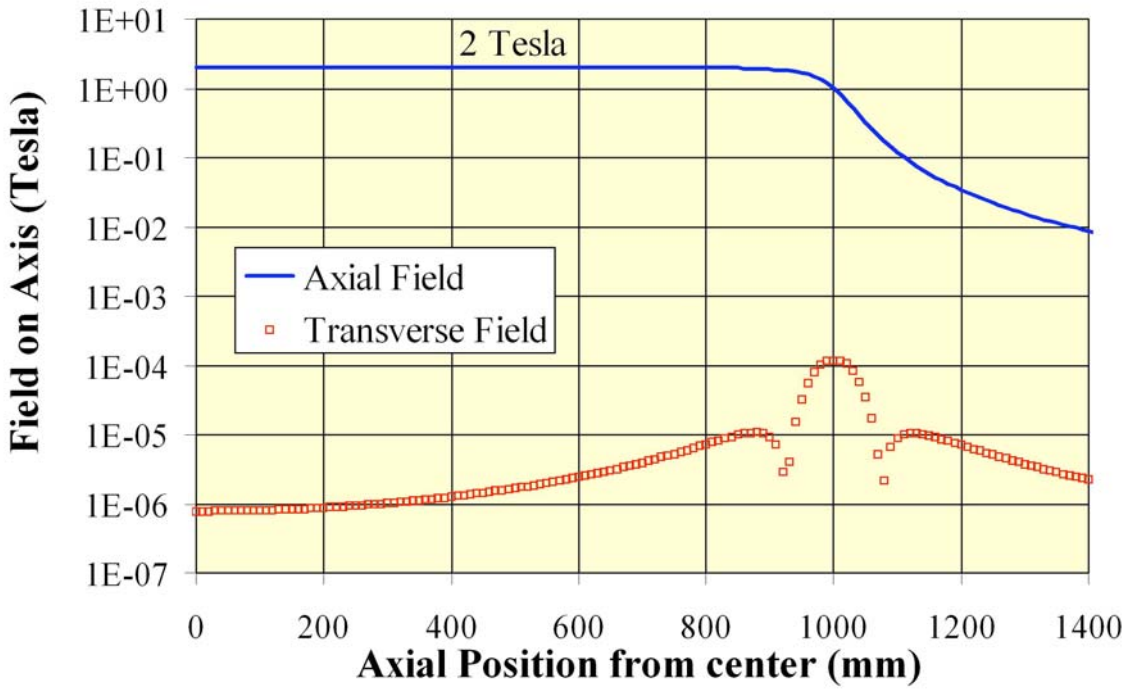

Fig. 2.11.3 Axial and transverse fields calculated on the axis of a 2-meter long, 4 layer solenoid designed for 2 Tesla field. The transverse field is generated due to a finite tilt of the turns.

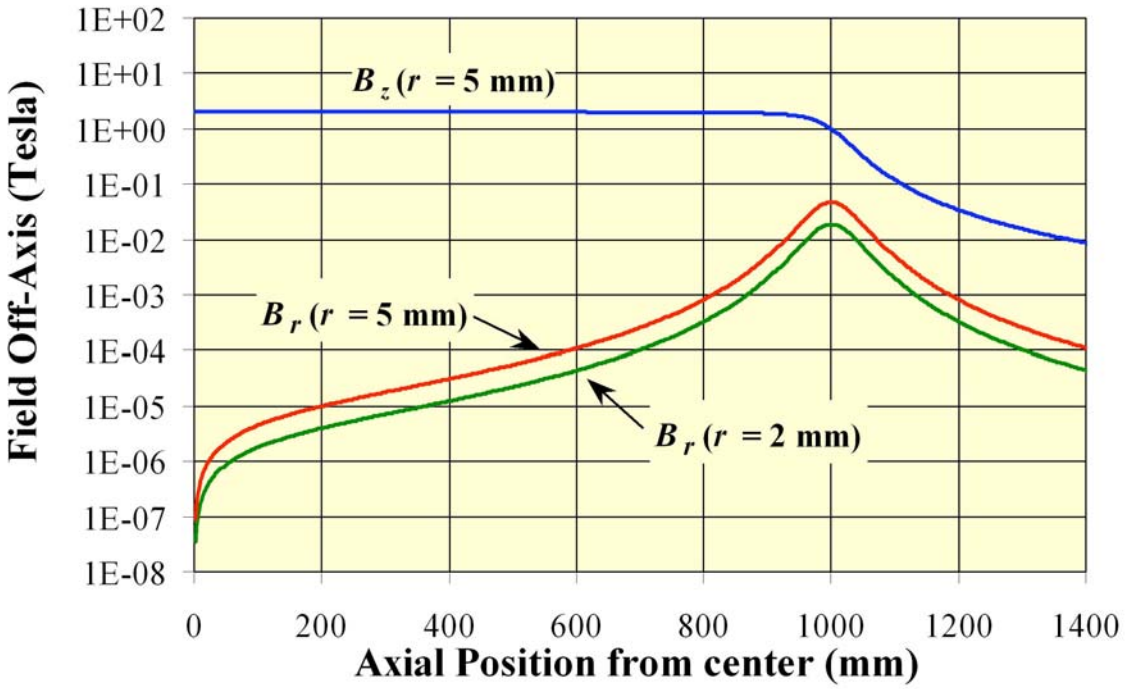

Fig. 2.11.4 Off-axis radial and axial fields in a 2-meter long, 4 layer solenoid designed for 2 Tesla field. The calculations are for purely azimuthal turns. The effect of the helical nature of the windings is negligible at these radii.

2.11.3 DESIGN OF THE DIPOLE CORRECTORS:

In practice, the on-axis transverse fields will be dominated by winding errors in the construction of the solenoid, and the ability to keep the coil support tube straight. Even for a perfectly wound solenoid, a tolerance of transverse field less than 1×10^{-5} of the axial field implies a tube straightness of 0.1 mm over a length of 10 meters. It is unlikely that such a tolerance will be achieved with mechanical alignment alone. To compensate for the transverse fields generated by various construction errors, it is necessary to include in the design an array of dipole correctors.

Based on cooling physics considerations, it was determined that the transverse field tolerance must be met at all points along the solenoid length. In other words, it is not sufficient to simply cancel out the transverse fields in an integral sense. To achieve correction locally, the dipole correctors must be very short, comparable in length to the solenoid coil inner diameter. This implies a rather large number of correctors, and it is desirable to produce them in the most economical way. Also, given the fact that these correctors will be required to produce only very small fields $\sim10^{-5}$ to 10^{-3} Tesla, superconducting corrector coils is not a good option due to persistent current effects.

Each dipole corrector has a length comparable to the diameter. The field harmonics of such short magnets are minimized only in an integral sense. Such short length corrector magnets have been developed earlier at other laboratoies using printed circuit technology [2.11.1]. This technology appears to be well suited for correctors required in

the electron cooling solenoid. A design has been developed for a 150 mm long, 159 mm inner diameter dipole corrector using a two-layer printed circuit board. The pattern width is chosen to be 1 mm, which allows to put 60 turns per pole. The corrector produces ~1.2×10^{-3} Tesla field in the center with excitation at 2 A. The calculated field profile of the corrector is shown in Fig. 2.11.5. Three prototype printed circuit correctors have been fabricated and tested for satisfactory field quality. Fig. 2.11.6 shows the printed circuit boards mounted on a tube.

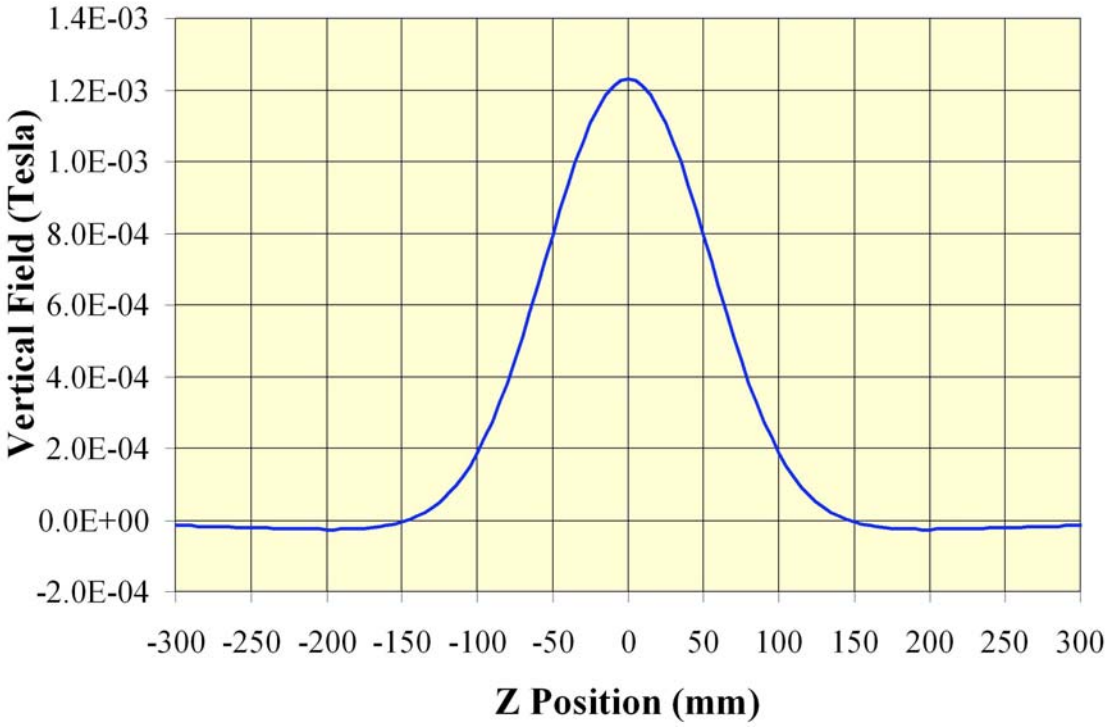

Fig. 2.11.5 Calculated transverse field profile of a dipole corrector at 2 A

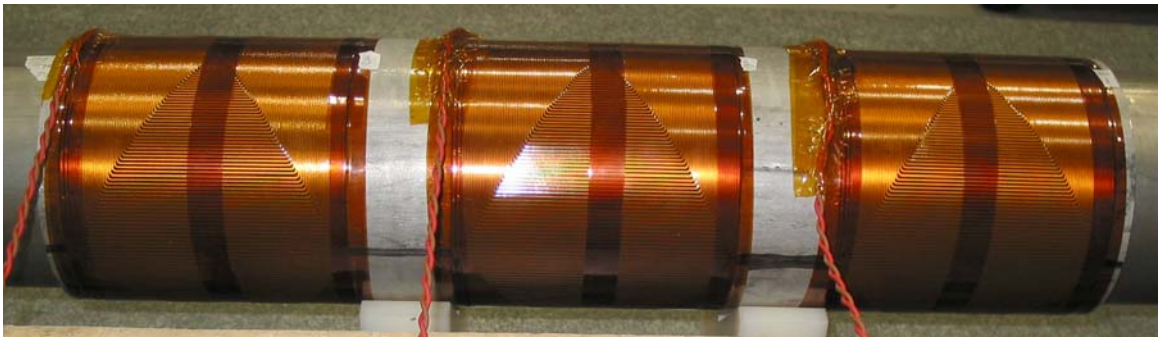

Fig. 2.11.6 Prototype printed circuit dipole correctors.

For dipole correctors of length 150 mm, a reasonable separation between adjacent elements is about 160 mm, allowing space for printed circuit board edges and leads. The

combined field profile from an array of 5 such correctors, each excited at 2 A, is shown in Fig. 2.11.7. The red (dashed) curves denote the field profile from each of the correctors, and the blue (solid) curve shows the superposed field from all the correctors. It can be seen that in the region between two correctors, there is a "valley" which can not be filled. This would limit the ability to correct transverse fields uniformly along the length. Therefore, another layer of similar correctors, offset by half the pitch, is needed for effective correction in one axis. This doubles the total number of dipole correctors that will be needed. Roughly, a total of 25 correctors are needed per meter length of the solenoid for correcting the transverse fields in both the horizontal and the vertical directions.

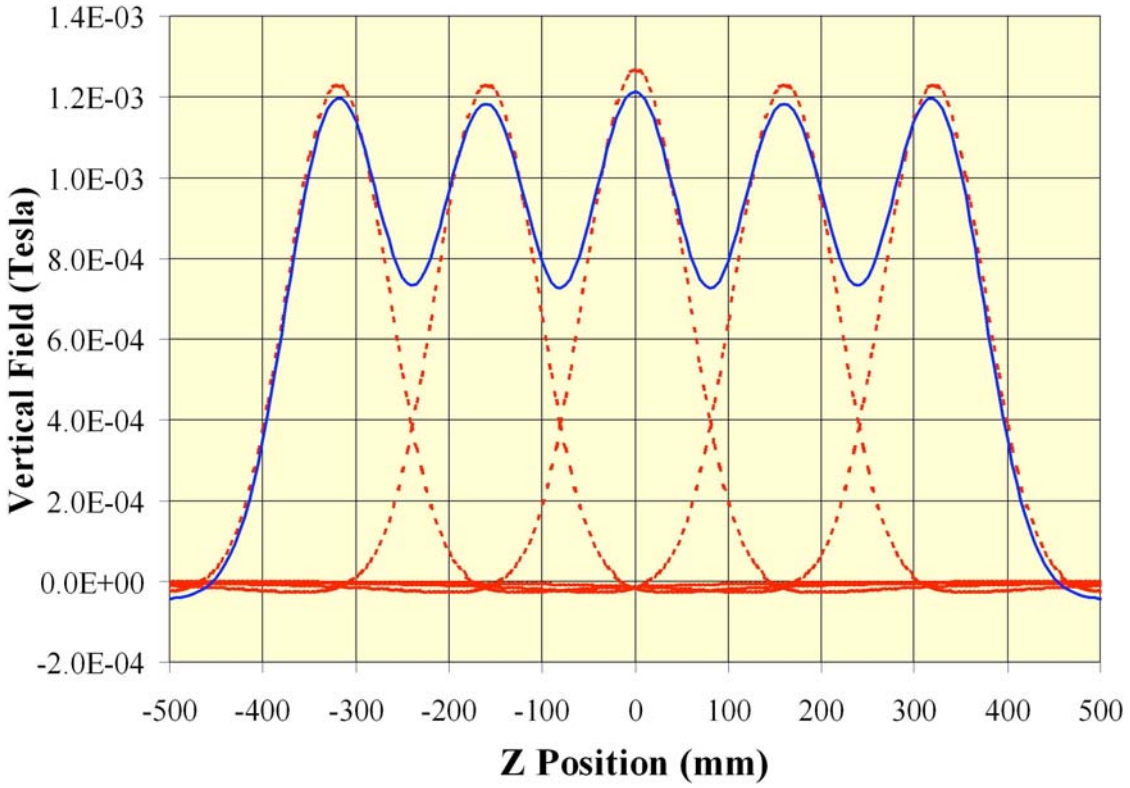

Fig. 2.11.7 Computed field profile from an array of five 150 mm long dipole correctors, separated by 160 mm center-to-center. The red (dashed) curves show the field profile from each of the correctors and the blue (solid) curve is the total field profile.

The printed circuit boards for the dipole correctors use a pattern width of 1 mm and 4 oz. copper (~ 130 μm) thickness. For room temperature operation, the resistance of each corrector is about 12 Ohms resulting in roughly 50 W of power dissipation per corrector, or 1250 W per meter length of the solenoid. To minimize the dissipated power, it is planned to mount the dipole correctors inside a double walled heat shield at ~80 K (see Fig. 2.11.1). It is estimated that the power dissipation will be reduced by a factor of about 6 as a result of low temperature operation of the correctors.

2.11.4 FIELD CORRECTION ALGORITHM

Numerical studies have been carried out to verify feasibility of correcting reasonable field errors with the dipole correctors described in the previous section. For the purpose of these studies, a "typical" error profile of the transverse field as a function of axial position is synthesized by adding sinusoidal profiles ranging in wavelength from 200 mm (twice the coil inner diameter) to 4 meters, with arbitrary strengths and phases of each wavelength. The strengths are chosen to produce a net transverse field in the 10^{-4} Tesla range. The currents in all the dipole correctors are then adjusted to produce transverse fields which cancel the synthesized fields. As can be seen from Fig. 2.11.5, field from a single corrector spills over significantly into the neighboring correctors. Consequently, it is necessary to optimize the currents in all the correctors simultaneously. An unconstrained optimization tends to use extremely high values of currents of opposite sign in neighboring correctors. To avoid this problem, the optimization is constrained to use the least amount of current in each corrector by applying a penalty function.

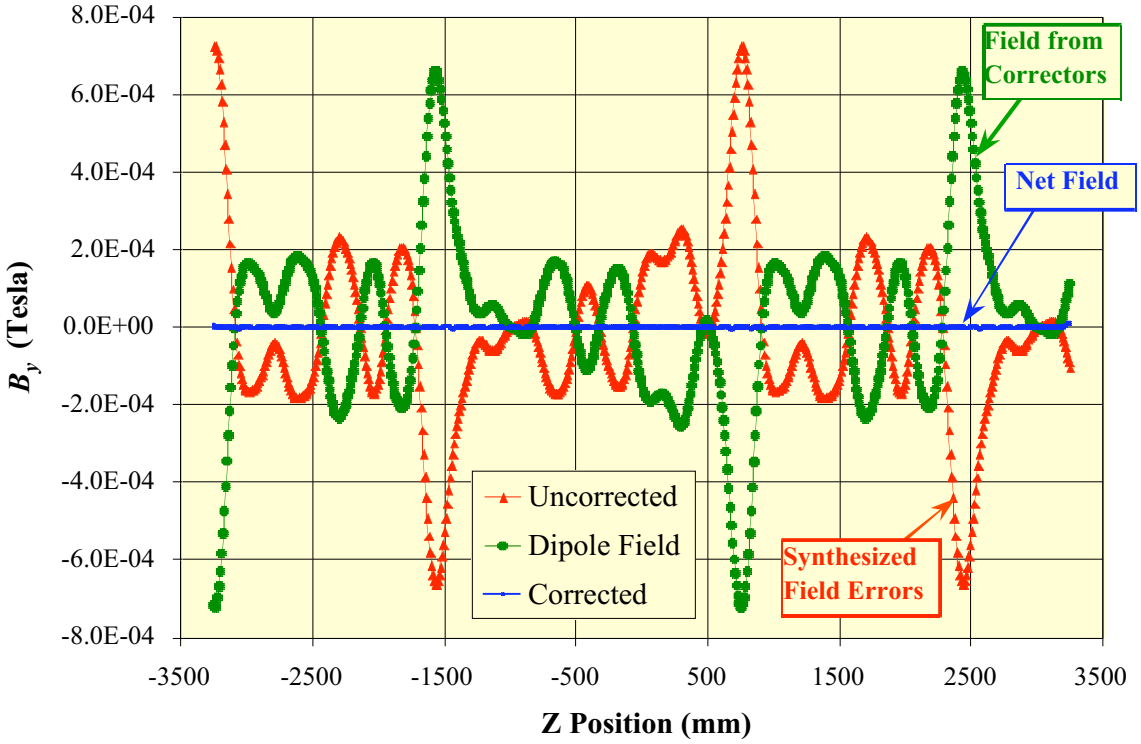

Fig. 2.11.8 Correction of a synthesized field error profile using two layers of dipole correctors. The net field is below 5×10^{-6} Tesla everywhere, except at the two ends.

Fig. 2.11.8 shows the syntesized transverse field profile, along with the field profile generated by two layers of dipole correctors powered with the optimized currents. Each layer consists of 150 mm long dipoles separated by 160 mm center-to-center distance. The second layer is offset with respect to the first by 80 mm (half of the pitch). The net field is below 5×10^{-6} Tesla everywhere, except at the two ends. The maximum current

used in any corrector is less than 1 A in this case. These simulations show that it is possible to correct arbitrary error profiles with wavelengths 200 mm or longer using two layers of the 150 mm long dipoles. With a limit of 2 A, it should be possible to correct transverse fields up to $\sim 1 \times 10^{-3}$ Tesla using these correctors. Similar simulations also confirm that a single layer of correctors is not adequate for compensating the field errors.

2.11.5 THE IRON SHIELD:

In order to minimize the field leakage from the solenoid, and of more importance for the electron cooling application, to shield the solenoid field from external stray fields, it is necessary to provide some form of shielding around the solenoid. For example, the earth's field itself is larger than the amount of transverse field than can be tolerated. Any magnetic material placed outside the solenoid will attract the flux from the solenoid ends, and will tend to saturate. Consequently, the shield material should not only have a high permeability, it should also have a high saturation field. It is planned to use a 25 mm thick warm iron shield around the solenoid, as shown in Fig. 2.11.1.

The effect of the iron shield on the solenoid field distribution is studied using finite element calculations with OPERA-2d. Fig. 2.11.9 shows the 10 mT boundary near one of the ends in a 2 Tesla solenoid. It is clearly seen from this figure that the flux leaking out of the solenoid is greatly reduced in the presence of the shielding. Also, the maximum field in the iron is well below the saturation field, thus keeping the permeability high.

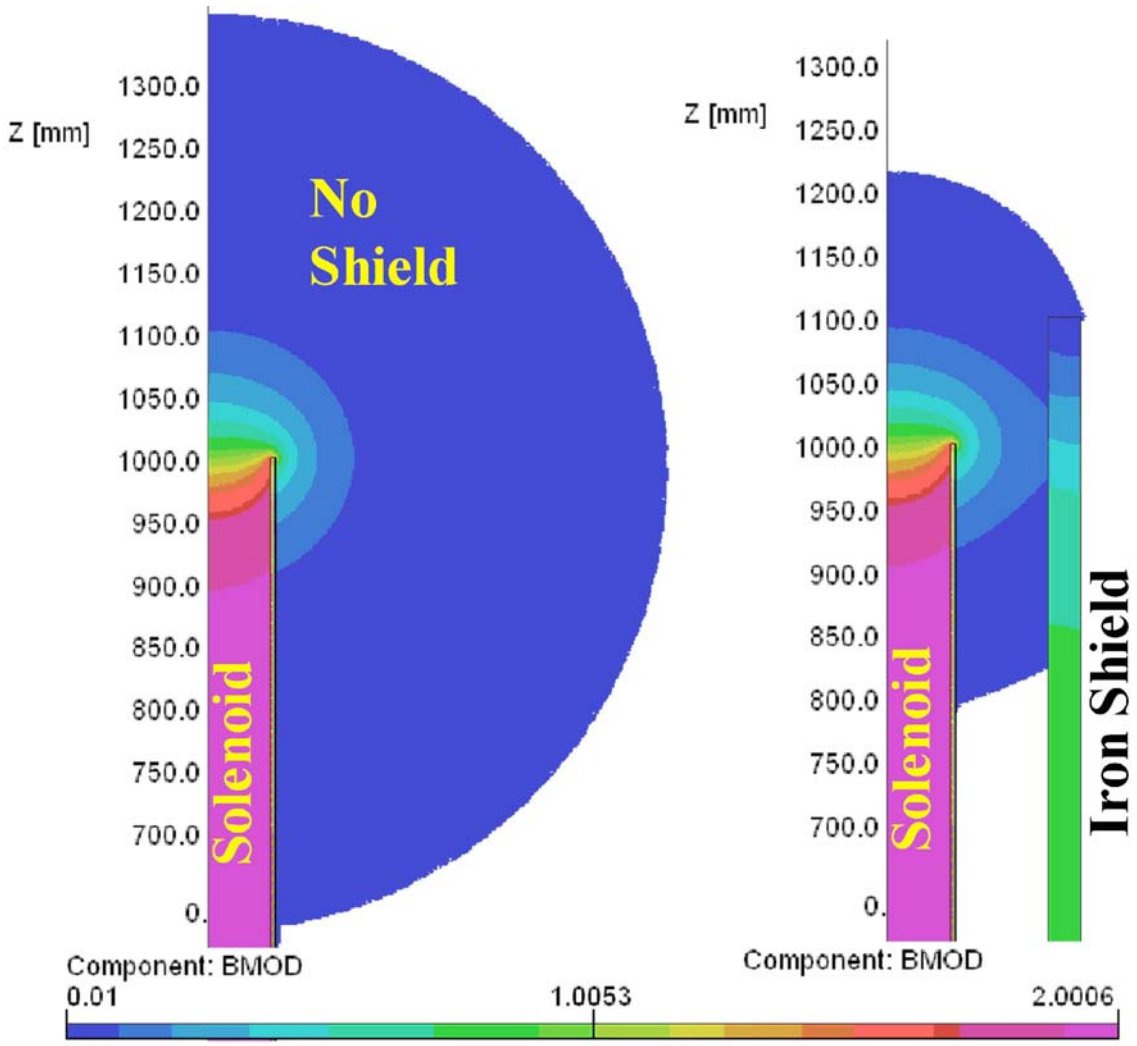

Fig. 2.11.9 10 mT boundary in a 2-meter long, 2 Tesla solenoid with and without a 25 mm thick iron shield. The iron shield extends 100 mm beyond the end of the solenoid.

The effect of the shield on the field profile inside the solenoid is illustrated in Fig. 2.11.10. The axial field becomes considerably more uniform in the presence of the shield. This also means that the off-axis radial fields are reduced over most of the end region, with only a slight increase very close to the edge of the solenoid.

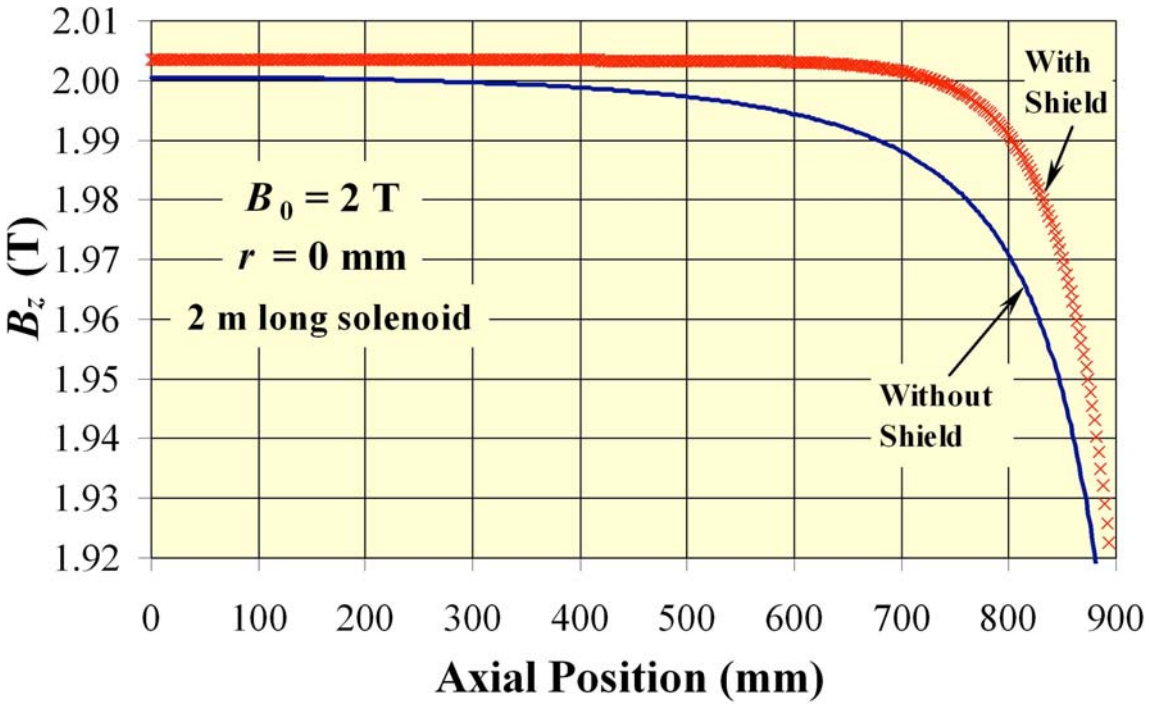

Fig. 2.11.10 Effect.of the iron shield on the axial field profile.

The shielding from external fields is also studied using OPERA-2d. The quantity of interest is the attenuation provided for low transverse fields originating from sources external to the magnet. This is to be evaluated under operating conditions, where the iron shield also carrries flux from the solenoid. This is strictly a 3-D problem, requiring extensive computational effort. As can be seen from the field map in the iron (Fig. 2.11.9), the flux density inside most of the shield length is more or less constant at ~1 Tesla. Thus, one could obtain the shielding effect from a 2-D calculation, where the iron shield is assumed to have a constant relative permeability of about 2000. In the OPERA-2d model shown in Fig. 2.11.11, the iron shield is placed in an external dipole field of 10 mT, created by a 60 degree dipole coil. As can be seen from Fig. 2.11.11, the region inside the shield is protected from the external field. The attenuation factor at the center of the solenoid is calculated to be ~100. Thus, the shield is adequate to protect the solenoid field quality from external fields up to ~ 10 Gauss.

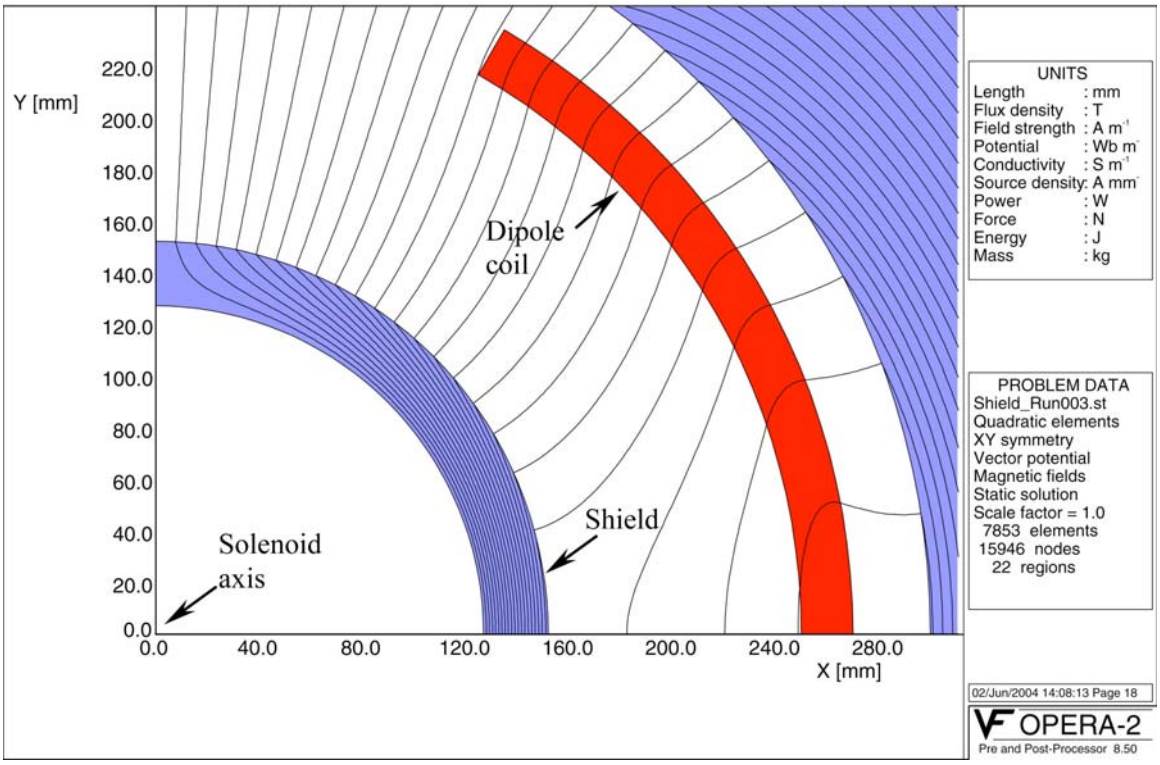

Fig. 2.11.11 Field lines showing the shielding effect of the iron shield in an external dipole field. For the purpose of these calculations, the external dipole field is generated by a 60 degree dipole coil.

2.11.6 QUENCH PROTECTION:

Table 2.11.1 lists the main magnet parameters relevant for quench protection. The inductance and stored energy for a 3 m-long prototype are 0.078 Henry and 40.5 kJ respectively.

Table 2.11.1: Magnet parameters relevant for quench protection.

Magnet parameter	Value	Unit
Coil ID/OD	100/115.5	mm
Turns/length/layer	390	turns/m
N. of layers	4	–
Operating Current @ 2 T	1020	A
Operating Current @ 2.5 T	1275	A
Short sample quench limit	2.94	T
Current limit	1500	A
Inductance/length @ 2 T	0.026	H/m
Stored energy/length @ 2 T	13.5	kJ/m

Given the low inductance, and the high copper content of the conductor (with a copper to non-copper ratio of 6.9:1), the magnet can be protected with a simple energy extraction. The schematic of the circuit is shown in Fig. 2.11.12.

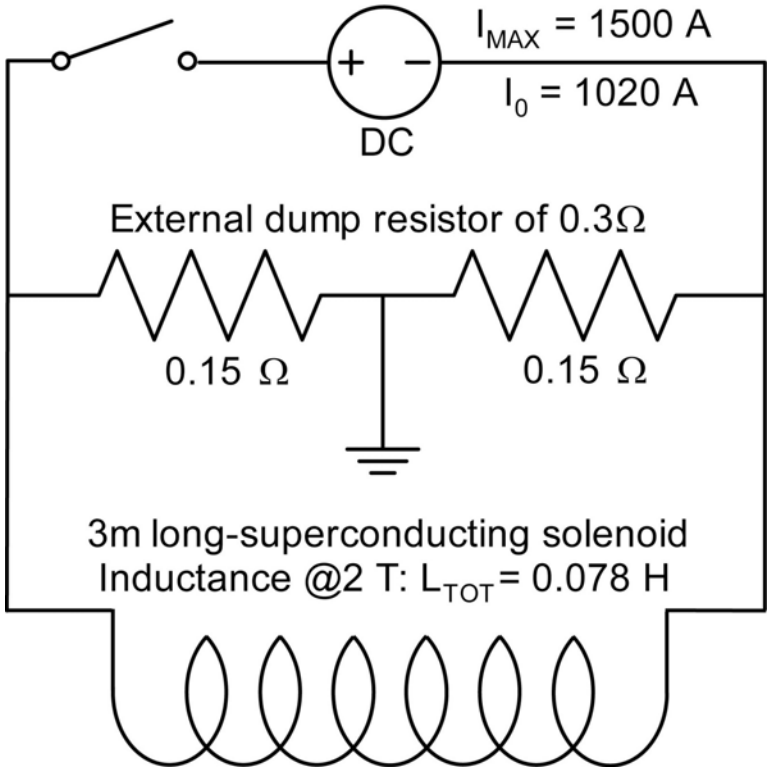

Fig. 2.11.12: Schematic of the quench protection circuit.

2.11.7 QUENCH CHARACTERISTICS:

The quench process was simulated using a numerical code, suited for adiabatic solenoids, namely the QLASA program [2.11.2]. The coil was modeled as a series of "unit cells" representing the conductor cross section. In this study, the unit cell includes all the insulation (conductor insulation, and layer-to-layer insulation). Instead of Kapton, G10 material properties were used, since they are available in the electronic material property library automatically connected with the simulation program. Fig. 2.11.13 shows the adiabatic quench integral (also known as MIIts curve) versus the hot spot temperature, calculated for the insulated conductor at 2 Tesla field.

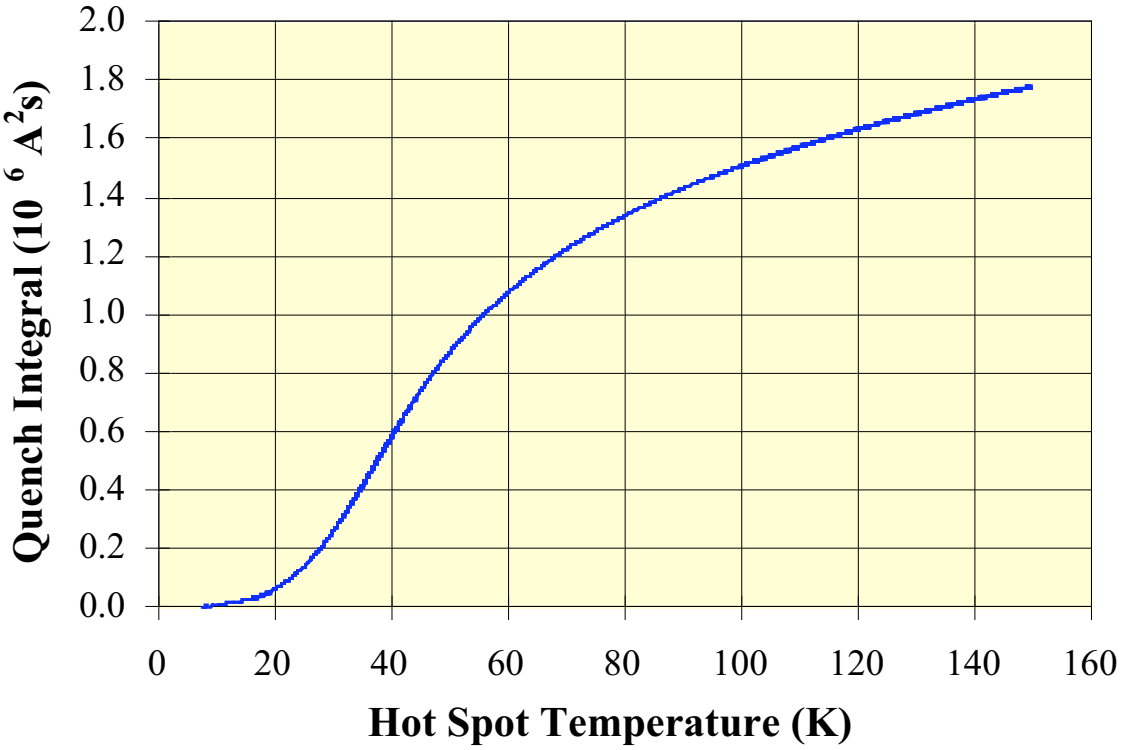

Fig. 2.11.13 Adiabatic quench integral (also known as "MIITs") in 2 Tesla field for the cable cross-section, including the entire insulation fraction (18.5%).

Using the circuit in Fig. 2.11.12, we obtained the quench characteristics shown in Fig. 2.11.14 for the 3-m long prototype at 1275 A initial current (corresponding to 2.5 T bore field). The simulations assume a power supply shut off delay time of 6 ms, due to a 5 ms quench detection time, plus 1 ms switch delay time.

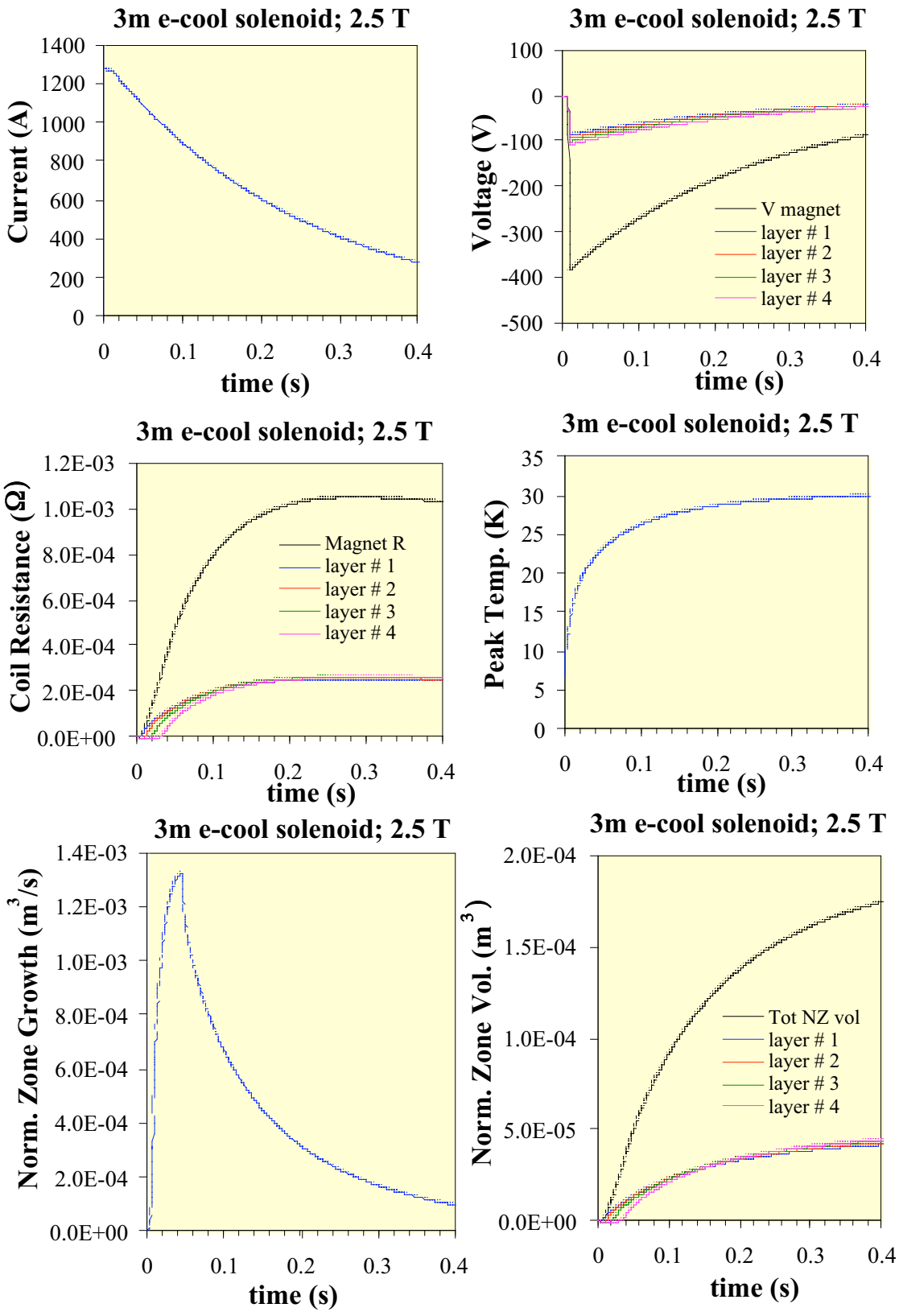

Fig. 2.11.14 Quench characteristics for the 3-m long prototype solenoid at 2.5 Tesla.

Table 2.11.2 summarizes the main simulation results for the prototype and for the full length magnets. The voltage across each of the dump resistors is half the voltage across the magnet leads, because the connection to ground is placed in the middle of the resistors. The other circuit components are electrically floating. Even if the internal magnet voltage were to reach about a hundred volts more than the calculated value across the leads, the voltage would still remain below 500 V (for the 2.5 T bore field). Table 2.11.2 reports also the main results for a quench at the magnet short sample limit of 2.9T/1500 A.

Table 2.11.2: Main quench characteristics for model and full scale magnet.

Magnet length	---------- 3 m ----------		---------- 13 m ----------	
Initial field/current	2.5 T/1275 A	2.9 T/1500 A	2.5 T/1275 A	2.9 T/1500 A
Peak temperature (K)	30	34	60	85
Peak coil voltage (V)	-380	-450	-380	-450
Peak voltage across dump resistors (V)	380/2	450/2	380/2	450/2
Decay time (s)	0.3	0.26	1.4	1
Quench Integral (10^6 A^2 s)	0.21	0.3	0.91	1.2

2.11.8 CONSTRUCTION DETAILS:

The superconducting wire will be wound onto a support tube which also serves as the inner helium vessel. The coil windings will be secured to the support tube by a combination of epoxy impregnated fiberglass tape and pre-tensioned epoxy impregnated fiberglass roving. In addition to the fiberglass wrap, the magnetic coil forces will be supported by a series of supports between the coil, outer helium vessel, heat shield, cryostat, and warm yoke. In addition, axial supports are planned in the ends of the solenoid due to the large axial forces (~7 kN at the ultimate field of 2.94 T) in the coil end regions. These supports will also be linked to the external magnet structures. Both axial and radial external supports will still permit the adjustment of coil center via spaced positional guides.

A warm bore tube is provided (see Fig. 2.11.1) as a part of the magnet system for placing a moving probe for carrying out measurements of field direction. The clear bore available for measurements is estimated to be approximately 73 mm in diameter.

The large number of independently powered dipole correctors implies a large number of power leads. Each layer of correctors is envisioned to have all the lead pairs distributed azimuthally in a layer of leads on top of each corrector layer. For the short prototype, it should be possible to bring out all the leads on one end of the solenoid. For the full length solenoid, each layer may have up to approximately 200 leads. In order to lay out so many leads, it may be necessary to bring out half of the leads on each end of

the solenoid. The corrector leads will be rated for 2 A, whereas the main solenoid lead will be rated for well above the normal operating point.

Magnet cooling will be provided by the 4.2 K helium gas used on the RHIC machine, with power bus diverted from the helium flow before introducing helium to the cooling solenoid. Helium flow will also be required for the gas cooled leads. Heat load from the solenoid coil leads will be minimized by the use of HTS leads between 80 K and 4.2 K.

The prototype is envisioned to contain all the major elements of the final magnet, with the exception of a reduced length of about 3 meters.

2.11.9 MAGNETIC MEASUREMENTS:

The axial field profile, as well as the variation of local field direction are the quantities of interest in characterizing the field quality in the solenoid. The axial field profile can be measured relatively easily using NMR probes for the central region and using precision Hall probes in the end regions of the solenoid. The position of the probe can also be measured accurately using a laser interferometer.

The most stringent requirement on the field quality, however, is in terms of the local field direction, which must not deviate from a straight line path of the ion beam by more than a few micro-radians. In order to achieve this tolerance, it is necessary to carry out mesurements of the field direction with a resolution of about 1 micro-radian.

The technique commonly employed for measurement of field direction in electron cooling solenoids is based on a “magnetic needle and mirror” system [2.11.3-4], shown schematically in Fig. 2.11.15. A magnetic needle is attached to a mirror, which is free to rotate around two axes transverse to the solenoid axis. A laser beam is bounced off the mirror and the reflected spot position is recorded. At any axial position of the mirror, the magnetic needle is aligned to the solenoid field and the position of the reflected laser spot can be used to determine the field direction. A prototype system for field measurements is currently under development at the Superconducting Magnet Division, BNL. It is planned to use a high resolution CCD camera as the detector to achieve the required resolution. The prototype solenoid will be used to characterize the system, and to make further improvements that may be necessary. A prototype gimbal mount for the mirror and the magnetic needle is shown in Fig. 2.11.16.

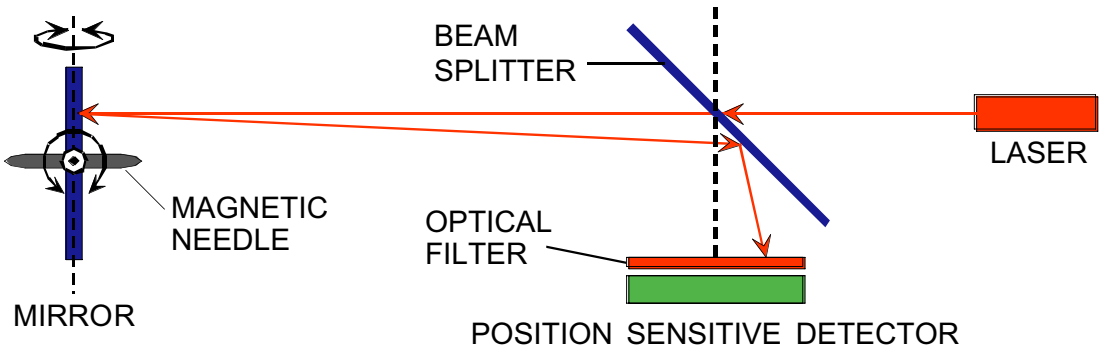

Fig. 2.11.15 Schematic of a "needle-and-mirror" system to measure the field direction of a solenoid. (Based on Ref. [2.11.3]).

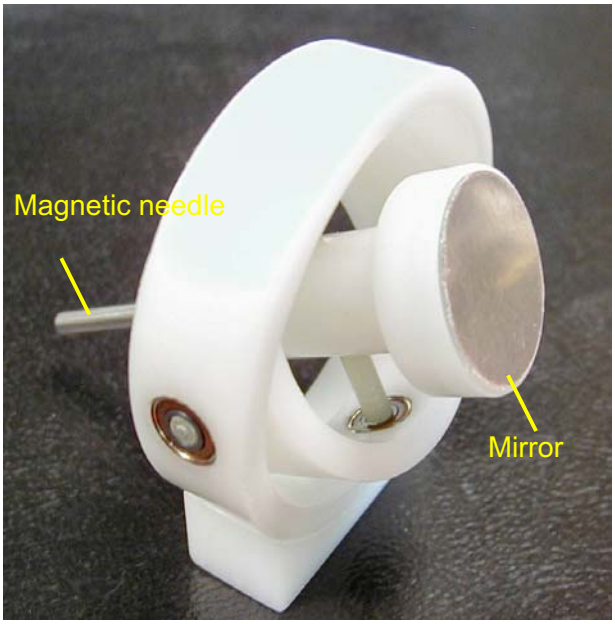

Fig. 2.11.16 A prototype gimbal mount for the "needle-and-mirror" probe.

2.11.10 REFERENCES:

[2.11.1] W. W. Zhang, et al., *Design and field measurements of printed-circuit quadrupoles and dipoles*, Phys. Rev. Special Topics – Accelerators and Beams, Vol. **3**, 122401 (2000).

[2.11.2] M. Canali, L. Rossi, *Dynque: A Computer code for Quench Simulation in Adiabatic Multicoil Superconducting Solenoid*, Report INFN/TC_93/06, June 1993.

[2.11.3] C. Crawford, A. Sery, V. Shiltsev, A. Aleksandrov, B. Skarbo, and B. Sukhina, *Magnetic Field Alignment in the Beam-Beam Compensation Device*, Proc. 1999 Particle Accelerator Conference, New York, pp. 3321-3.

[2.11.4] C. Crawford, E. McCrory, S. Nagaitsev, A. Shemyakin, V.Bocharov, A. Bubley, V. Parkhomchuk, V. Tupikov, and S. Seletsky, *Fermilab Electron Cooling Project: Field Measurements in the Cooling Section Solenoid*, Proc. Proc. 2001 Particle Accelerator Conference, Chicago, pp. 195-7.

2.12 ERL Conventional Facilities at Building 912

The North East Building Addition (NEBA) of building 912 has been selected as the preferred location for the construction of the ERL for R&D. This newest addition to the 912 complex is a high bay building, 140'x 70'overall, in good physical condition, equipped with a 25 ton overhead crane. There is an attached 20'x 50' counting house which will be utilized for housing experimental electronics and computer equipment. The building is close to available high voltage power required for the operation of the Klystron and has a number of available cooling towers that can be used for equipment cooling.

Inside the experimental hall a shielded area, 80'x 27'x 9-12' high will be constructed utilizing existing CAD shielding blocks. This area will provide 4 feet of concrete shielding around and above the ERL, Electron Gun, SCRF Cavity and beam dump for radiation protection. Approximately 2200 square feet of space is available inside the shielded area. Penetrations will be provided for the high voltage waveguides, helium transfer and recovery line, cooling water and experimental cables. Air conditioning and ventilation will be sized for the proper heat load.

In addition to the shielded area, 2 equipment rooms and 1 laser room will be provided to house essential experimental equipment. Each room will be a panel type, pre-engineered building with power and air conditioning sized for the equipment to be contained inside.

Unique power requirements for the operation of the high voltage power supply necessitate the upgrade and refurbishment of the existing 13.8 KV substation. High Voltage switchgear, circuit breakers and other electrical equipment will be refurbished or replaced. A new 4160 Volt transformer will be purchased and installed to supply power to the Klystron high voltage power supply.

The new high voltage equipment required to operate the ERL requires low conductivity de-ionized cooling water with a small amount of chilled, temperature controlled, water. A new closed loop DI water system will be designed and installed to provide equipment cooling utilizing the existing open cooling towers to dissipate the heat load. Smaller, stand alone chiller units will be purchased and installed to provide the limited amount of temperature controlled cooling water.

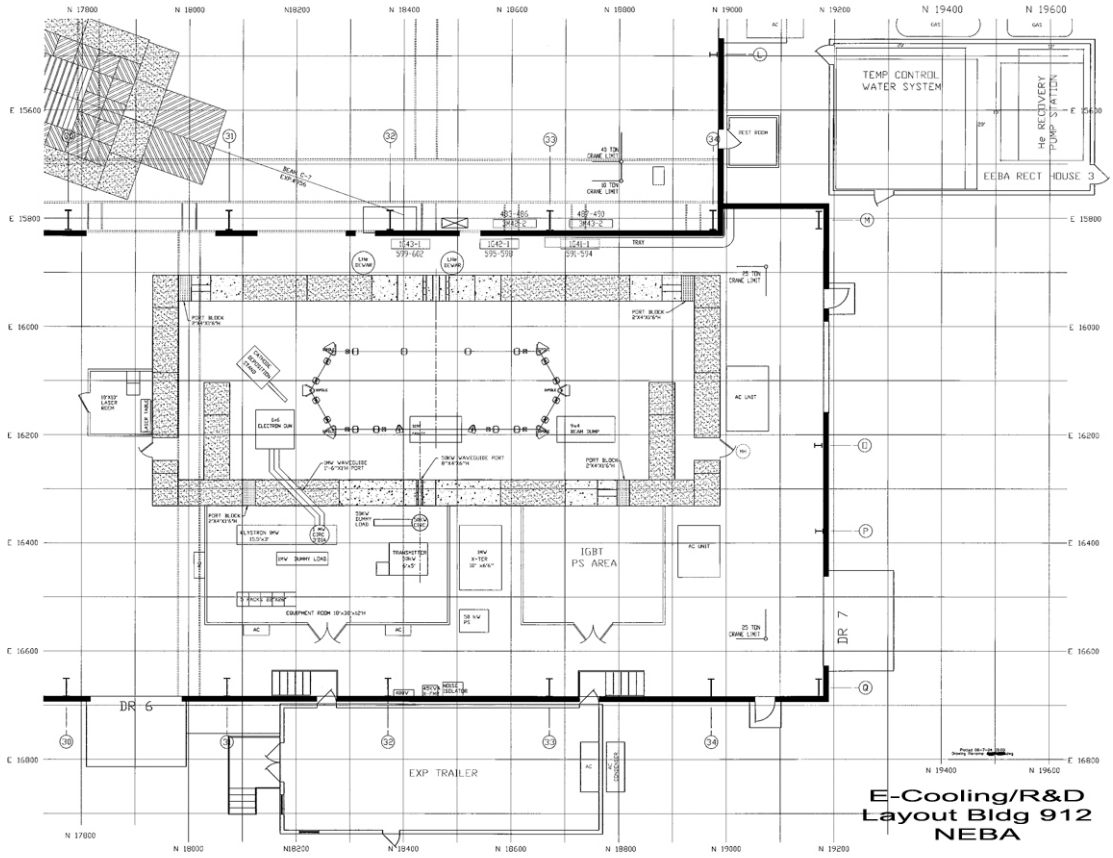

Fig. 2.12.1 Building 912 Layout

2.13 ECooler/ERL Access Control Safety (ACS) System

The proposed Access Control Safety system (ACS) for the eCooler and ERL facility will use Programmable Logic Controllers [PLC] as the basis of the system. In order to provide the required dual independent protection the area served by ACS has two independent PLC's [A and B divisions]. Each division independently provides full protection. All the I/O's (gate switches, critical devices, etc.) are redundantly monitored by both PLC systems. In addition, redundant monitoring of radiation level and ODH concerns will be incorporated in the safety system.
The Control Room (CR) operator interface utilizes touch screen displays [flat panels] on a command network that is connected through firewall machines to the separate divisions.

2.14 Cavity / Gun Installation

The superconducting rf Cavity will be received from Jefferson Laboratory having been chemically cleaned and then assembled. It will arrive with the 5-cell cavity encased in its

helium vessel. A copper-clad, stainless steel extension, ferrite damper, stainless steel aperture transition and rf-shielded, UHV, all metal gate will append each end of the cavity / He vessel assembly. Upon receipt, the cavity string (string, hereafter) will be removed from the shipping fixtures and placed on interim assembly stands. Since this cavity vendor's design borrows extensively from the SNS SCRF cavity design different stand combinations will be used on the string throughout the assembly process. The cavity installation tooling allows for the mounting of magnetic and thermal shielding while the cavity is suspended from Nitronic® rods. The rods provide ample support of the cavity while maintaining low heat transmission and precise cavity positioning during cryogenic operations. The cryomodule will be constructed around the string in-place in building 912.

It is expected that the construction / installation of the superconducting electron-gun will follow the same process as the cavity.